MULTI-AXIAL ACTIVE ISOLATION FOR SEISMIC PROTECTION OF BUILDINGS

BY

CHIA-MING CHANG

DISSERTATION

Submitted in partial fulfillment of the requirements
for the degree of Doctor of Philosophy in Civil Engineering
in the Graduate College of the
University of Illinois at Urbana-Champaign, 2011

Urbana, Illinois

Doctoral Committee:

Professor Billie F. Spencer, Jr., Chair
Professor Amr S. Elnashai
Professor Lawrence A. Bergman
Assistant Professor Junho Song

ABSTRACT

Structural control technology has been widely accepted as an effective means for the protection of structures against seismic hazards. Passive base isolation is one of the common structural control techniques used to enhance the performance of structures subjected to severe earthquake excitations. Isolation bearings employed at the base of a structure naturally increase its flexibility, but concurrently result in large base displacements. The combination of base isolation with active control, i.e., active base isolation, creates the possibility of achieving a balanced level of control performance, reducing both floor accelerations as well as base displacements. Many theoretical papers have been written by researchers regarding active base isolation, and a few experiments have been performed to verify these theories; however, challenges in appropriately scaling the structural system and modeling the complex nature of control-structure interaction have limited the applicability of these results. Moreover, most experiments only focus on the implementation of active base isolation under unidirectional excitations. Earthquakes are intrinsically multi-dimensional, resulting in out-of-plane responses, including torsional responses. Therefore, an active isolation system for buildings using multi-axial active control devices against multi-directional excitations must be considered.

The focus of this dissertation is the development and experimental verification of active isolation strategies for multi-story buildings subjected to bi-directional earthquake loadings. First, a model building is designed to match the characteristics of a representative full-scale structure. The selected isolation bearings feature low friction and high vertical stiffness, providing stable behavior. In the context of the multi-dimensional response control, three, custom-manufactured actuators are employed to mitigate both in-plane and out-of-plane responses. To obtain a high-fidelity model of the active isolation systems, a hybrid identification approach is used which combines the advantages of the lumped mass model and nonparametric methods. Control-structure interaction (CSI) is also included in the identified model to further enhance the control authority. By employing the H_2/LQG control algorithm, the controllers for the hydraulic actuators promise high performance and good robustness. The active isolation is found to possess the ability to reduce base displacements, as well as producing comparable accelerations over the passive isolation. The proposed active isolation strategies are validated experimentally for a six-story building tested on the six degree-of-freedom shake table in the Smart Structures Technology Laboratory at the University of Illinois at Urbana-Champaign.

ACKNOWLEDGMENTS

First and foremost, I would like to express my thanks to my advisor, Professor B. F. Spencer, Jr., for his advice, encouragement, and support on my research throughout my time at the University of Illinois. His academic insight and passion have greatly inspired me in many aspects. Having my Ph.D. study under his supervision is my most valuable asset towards my academic goals.

I sincerely appreciate the efforts of my committee members, Professor Amr Elnashai, Professor Lawrence Bergman, and Professor Junho Song for sharing their experience in different perspectives that significantly improved this dissertation greatly. All their support and comments are appreciated.

I would also like to thank Professor Chin-Hsiung Loh for his encouragement and support in the pursuit of my Ph.D. study at the University of Illinois. I would have never been able to make my dream come true without his help.

My dissertation research is generally based on the preliminary findings by the alumni of the Smart Structures Technology Laboratory. Thanks are owed to Doctor Kyu-Sik Park and Alan Mullenix. During the preparation period of my experiments, Charles DeVore spent a summer building all components of the active isolation system with me. All the work completed by him is really appreciated. I would like to thank Kenneth Dean Mitchell and Michael Davieau for tuning and calibrating the shake table that enabled me to duplicate earthquake records for my experiments. Implementing active isolation systems on a shake table always requires other trustable assistants who are able to execute the emergency procedure immediately if the systems are running unstably. For this reason, the help from Zhihao Wang and Pengfei Shi is really appreciated. In addition, I would like to thank all professional staff in the Shore Western

Manufacturing for consulting the hydraulic equipments in my experimental testing. I also acknowledge the donation of the ball-n-cone isolation bearings from the WorkSafe Technologies.

I would like to thank all of the SSTL members, Lauren Linderman, Brian Phillips, Sung-Han Sim, Shin Ae Jang, Jian Li, Nicholas Wierschem, Professor Jennifer Rice, Ryan Giles, Robin Kim, Hongki Jo, and Takehiko As-ai. Their academic excellence directly influenced and motivated me. I had a good time to work and party with all these colleagues. My life at Illinois would be dull if I never had them around. Thank you all.

This research in this dissertation has been supported by the National Science Foundation Grants CMS 03-01140 and CMS 06-00433 and the Taiwan National Science Council Grant NSC-095-SAF-I-564-036-TMS. These supports are gratefully appreciated.

I thank my parents for their continuous support when I encountered difficulties and challenges. All your encouragement is always my best remedy for hard times. I love you both.

TABLE OF CONTENTS

LIST OF FIGURES

LIST OF TABLES

CHAPTER 1 INTRODUCTION

1.1 Motivation

Natural hazards cause numerous deaths and cost society tens of billions of dollars each year. One of the major hazards, earthquakes, has resulted in tremendous economic and societal devastation in recent years. For example, the February 22, 2011, Christchurch, New Zealand earthquake, with a magnitude of 6.3, killed more than 100 people and damaged thousands of structures. Such severe loss drives researchers to continue working to more effectively protect civil infrastructure, and consequently, save lives.

Structural control is one feasible option to enhance structural performance against seismic events and avoid future collapses. Passive base isolation is one common type of structural control system that increases the structure's flexibility to mitigate the effect of potentially dangerous seismic ground motions. However, large base displacements resulting from the increased flexibility of the passive isolation system can potentially exceed the allowable limit of structural designs under severe seismic excitations, i.e., damaging seismic motes. The revisions to the Uniform Building Code (ICBO 1997) mandate the consideration of such large base displacements. Adding extra damping devices to an isolation system is a feasible approach to mitigate excessive base displacement.

Active isolation, consisting of a base isolation system combined with controllable actuators, is a potential alternative means to address the drawbacks of passive isolation systems. The efficiency offered by the base isolation system in reducing interstory drifts and floor accelerations can be combined with the adaptive active system to provide improved performance against a wide range of earthquakes. A few experiments for active base isolation systems have also been evaluated and verified by researchers (Yang et al. 1996, Riley et al. 1998, and Nishimura and Kojima 1998 and 1999). These experiments have successfully implemented active base isolation on structures using various controllers; however, the experiments employed actuators that were not appropriately scaled for the structural model, resulting in a system that had far too much authority. Moreover, the phenomenon of control-structure interactions were neglected in the implementation, resulting in substantially lower performance of the control systems. The experiments employed planar structures considering only unidirectional excitations; however, earthquakes have intrinsically multi-directional excitations. Further experimentation is needed to address these shortcomings before this technology will find wider acceptance.

In addition to active base isolation, other researchers have considered passive isolation systems combined with the controllable semi-active damping devices, such as MR dampers (Yoshioka et al. 2002, Madden et al. 2002, Sahasrabudhe and Nagarajaiah 2005a, Lin et al. 2007, and Shook et al. 2007). The semi-active devices replace the active devices in base isolation systems, providing a number of attractive features. Furthermore, a base-isolated building combined with two directional MR dampers has been experimentally evaluated against seismic excitations that proved the feasibility of this control combination (Shook et al. 2007). While this approach has been evaluated experimentally, demonstrating the applicability of the semi-active isolation systems, the performance was found to be less than that of the corresponding active isolation systems.

An ASCE benchmark control problem for an isolated building, which considered the excitation and associated responses in two directions, was proposed to evaluate the control performance through different combinations of control systems and different control strategies in simulation (Narasimhan et al. 2006). Many researchers applied their control strategies to this problem and proved the applicability of either active base isolation or the combination of passive base isolation with controllable damping devices against seismic excitations. Unfortunately, the practical implementation of a semi-active base isolation in multiple dimensions has been realized in only one demonstration project in Japan (Tsuchimoto et al. 2005). Hence, the gap between the theoretical approach and the experimental implementation of active base isolation has yet to be bridged.

To demonstrate the advantages of active isolation systems, the control implementation of these systems must be verified through the experimental testing against earthquake excitations. Since most of the previous studies only considered unidirectional excitations, active isolation systems with multi-axial active control devices need to be investigated under multi-directional excitations. This research develops and experimentally verifies active isolation systems for seismically excited buildings using shake table testing.

1.2 Overview of dissertation

This research focuses on the development and experimental verification of an active base isolation system for seismically excited buildings. First, a model building is designed to match the characteristics of a representative full-scale structure. All of the components for the active base isolation, such as isolation bearings and hydraulic actuators, have been appropriately designed and selected for the laboratory-scale testing which is able to portray full-scale implementations. To insure high-performance control can be achieved, accurate input-output relationships must be established to portray the behavior of the system; to this end, a simplified model for these systems is developed and the associated system identification approach is also investigated and established for building a control-oriented mathematical model. Additionally, the phenomenon of control-structure interaction is considered in the identified model and included in the control design as well. Robust H_2/LQG control strategies are designed with different considerations for achieving high performance. The efficacy of the developed control strategies is experimentally evaluated in both the time and frequency domain using a six degree-of-freedom shake table in the Smart Structures Technology Laboratory at the University of Illinois at Urbana-Champaign. Finally, all the developed control strategies are also validated for a wide range of seismic excitations.

Chapter 2 reviews previous studies related to active isolation. First, structural control technology and implementation are briefly addressed. Base isolation systems including smart base isolation and active base isolation are subsequently introduced. Finally, the issues and difficulties of active control implementation, particularly active isolation systems, are summarized.

Chapter 3 provides the design of active isolation. All components in the model active isolation systems are introduced, including two buildings, bearings, actuators, all sensors, digital processing systems, and the shake table. The reasons for employing these components in the active isolation are also presented, and specific concerns for the components are explained. Using all these components, the active isolation systems can be assembled and then implemented.

Chapter 4 develops a simplified model for the active isolation system. To obtain a precise model which can represent the system dynamics accurately, this research adopts the system identification technique to identify the system in accordance with the input-output relationship. Before applying system identification, the associated parameters, such as the numbers of states, poles, and zeros, should be determined in advance. Instead of determining these parameters of system identification by guessing, they can be determined using a simplified model for the active isolation system. Because the control design in this research depends on linear control theory, a linear time-invariant model is desired. The nonlinearities of the bearings and hydraulic actuators are linearized and coupled with a lumped-mass model of the building to yield this overall linearized model.

Chapter 5 describes the system identification procedure for active isolation systems in this research. This procedure consists of the single-input and multi-output (SIMO) system identification and the system combination from multiple SIMO system models to a multi-input and multi-output (MIMO) system model. The SIMO system identification includes two options: (1) the MFDID technique, which is developed for the frequency-domain models by Kim et al. (2005), and (2) the discrete-time method for transfer function models in the frequency domain. The goal of the system combination is obtain a minimum realization of the state-space model. Two examples based on the active isolation systems for the two-story and six-story buildings are provided to illustrate this system identification procedure, as well as address the quality of the identified models. Through this system identification procedure, a precise model can be obtained for use in the control design.

In Chapter 6, control design for the active isolation systems is presented based on the H_2/LQG control method. To enhance the performance as well as integrate the seismic effects into the control design, this chapter extends the standard H_2/LQG control method to accommodate an input/output shaping filter. After deriving the modified H_2/LQG control method, a procedure based on this method is also developed so that the designed controller can meet the control objective. Subsequently, the numerical loop gain and sensitivity transfer functions are used to ensure the performance and the robustness of the developed controllers. By employing this procedure, two examples using the active isolation systems of the two-story and six-story buildings are given. The controllers, which are determined in these examples, are applied in the experimental implementation as well.

Chapters 7 and 8 validate experimentally the active isolation strategies for a two-story and six-story buildings, respectively. The active isolation of the two-story building in this research relies more on the investigation of the active control strategies under unidirectional excitations, while the six-story building experiment is used to explore the efficacy of active isolation for bi-directional excitations. Both active isolation systems are investigated in the frequency-domain using the band limited white noise excitations, as well as the time-domain using historical earthquake excitations. In addition, comparison with the passive isolation and the zeroed control is also provided in these two chapters to better understand the behavior and performance of the active isolation systems.

Chapter 9 summarizes the research presented in this dissertation and provides recommendations and possible directions for future work on active isolation of buildings for seismic protection.

CHAPTER 2 LITERATURE REVIEW

This chapter presents a literature review of structural control technology and implementations, base isolation systems with additional damping devices or controllable actuators, and the need of implementations of active isolation.

2.1 Structural control technology and implementation

Significant earthquakes have occurred several times throughout the world in past decades. The magnitude 7.6 Northridge earthquake occurred in the U.S. on January 17, 1994 resulting in a \$20 billion loss across the west coast. The magnitude 6.8 Kobe earthquake in Japan occurred on January 17, 1995, killing 6,000 people and resulting in 200,000 collapsed structures. The Chi-Chi earthquake in Taiwan occurred on September 21, 1999, resulting in the deaths of 2,000 people and destroying 44,000 buildings. As a result of these events, the importance of protecting structures and people's lives has hastened the work of researchers and engineers in order to find solutions that would mitigate the effect of earthquakes.

Structural control technology has drawn the attention of researchers after the occurrences of several severe earthquakes. The basic idea behind structural control is that by adding extra components to the existing structural systems, these components play a role to reduce structural responses and ensure these structures survive during earthquake events. The additional components can either dissipate the structural kinetic energy or change the structural system functionality (e.g., shifting the natural period of structures). Moreover, some of these components can directly inject the additional energy required to protect structures against seismic forces. Hence, all means of structural control focus on the protection of structures through the same goal, avoiding structural responses that exceed the prescribed limits.

Passive control technology applied to structures is the conventional control technique for structural protection. Whittaker (1993) experimentally employed steel plate energy dissipation systems to reduce the interstory drifts. Constantinou (1992) experimentally and analytically investigated the mechanical characteristics of structures with fluid viscous dampers in order to reduce structural responses effectively. Soong and Dargush (1997) gathered all the passive control techniques with civil engineering applications. However, many challenges and difficulties still exist in passive control techniques (Soong and Constantinou 1994). These extra passive control devices (e.g. stiffness devices or viscous dampers) directly installed in structures naturally dissipate the externally induced energy but still increase the interstory drifts or the absolute floor accelerations of structures. Therefore, moderate modifications or control device replacements might be an improved solution in the application of structural control against seismic excitations.

Passive base isolation control is a technique used to employ a flexible device underneath the structure which shifts the dominant frequency of the structure away from the frequencies having significant magnitudes in excitations (Kelly et al. 1987; Kelly 1997). Base isolation bearings have been installed in many buildings to protect against earthquakes, e.g., Salt Lake City and County Building in 1989, Los Angles City Hall in 1990, San Francisco City Hall in 1999, Pasadena City Hall in 2004, and etc. Although base shears, floor accelerations, and interstory drifts are significantly reduced, the passive base isolation intrinsically induces larger base displacements (Kelly 1999; Nagarajaiah and Ferrell 1999; Buckle et al. 2002). Consequently, some buildings installed with base isolation bearings have performed far worse than promised and much worse than those buildings without base isolation systems due to restrictions on base displacements. Hence, effectively reducing the base displacements relative to the ground has become an issue for improvement of the base isolation functionality.

Active control is another structural control technique which uses the energy generated from the active control devices with an external power source to improve structural performance. Active control techniques are generally able to achieve higher control performance, as compared to passive control techniques (Soong and Constantinou 1994). An active control system requires structural information to complete the control mechanism, such as the structural responses (Soong and Manolis 1987). Additionally, the feedback loop used to accomplish the active control implementations closes up the control loop to include the structure itself and active control devices (Soong 1988). The active structural systems need to be reliable and workable, and the control algorithms need to include stabilizing characteristics (Fu 1971; Suhardjo et al. 1992; Rofooei and Tadjbakhsh 1993; Spencer et al. 1994; Kaufman et al. 1994; Casciati and Yao 1994; Meirovitch and Stemple 1997; Datta 2003). Numerous experiments have been conducted by researchers (Higashino and Aizawa 1993; Dyke et al. 1994a and 1994b; Chung et al. 1988 and 1998) and many real-world implementations have been applied to structures to protect against either wind or earthquakes (Kobori et al. 1998 and 1991; Soong and Constantinou 1994; Housner et al. 1997). Although many successful experiments and implementations prove the active control technology as a practical technique, some potential risks still exist in this real-time implementation; for example, the external energy injection from the active control devices might destabilize the system if the measurements of structural responses have been perturbed, the control laws are developed from a system model that misrepresents the true behavior of systems, the interaction between the structure and the control devices has been exclusively considered in the development of control laws, and so on. These details involved in the structural implementation of active control techniques continue to be an area of research interest.

Semi-active control is one control technique that cannot inject mechanical energy into the structural system, but has features that can be designed to optimally reduce structural responses. Unlike passive control techniques, semi-active control techniques have higher variability due to the different behaviors of the control devices when the power levels are changed, such as different stiffness and/or damping values (Tanida et al. 1991; Spencer and Nagarajaiah 2003). In contrast to active control techniques, semi-active control techniques do not have the potential to destabilize the system, indicating that no extra energy has been injected into the structures (Spencer and Sain 1997; Symans and Constantinou 1999; Spencer and Nagarajaiah 2003). Similar to active control, semi-active control techniques still require promising control laws to drive the semi-active control devices in order to improve the system response (e.g., adjusting the current levels to control the valve of the variable orifice damper (Feng and Shinozuka 1990) or the magnetorheological (MR) dampers (Dyke et al. 1996)). Numerous experiments have been done to validate the semi-active control techniques (Dyke 1996a and 1996b; Patten et al. 1999); furthermore, many implementations in structures have been realized over the world (Spencer and Nagarajaiah 2003). The results showed better control performance as compared to passive control techniques, while the control effectiveness of active control techniques still outperformed semi-active control. Hence, although the stabilizing features are implied in semi-active techniques, active control techniques exhibit the highest control performance among the three predefined control methods (e.g., passive control, active control, and semi-active control).

Each control method described in this subsection has had different attractive features in implementation. Passive control techniques rarely malfunction during earthquake events because of their simplicity. Active control techniques result in larger reductions in structural responses as long as the developed control laws are reliable and robust. Semi-active control techniques share the advantages of both previous control methods while achieving a moderate level of control performance. Given the relationship among the three control methods, researchers and engineers can seek the best performance by changing the detailed designs within each method or consider the possibility of using a combination of these control methods.

2.2 Base isolation systems

Passive base isolation, introduced in Section 2.1, ultimately results in the least reductions in the base displacements, i.e., the relative displacement between the base layer of the building and the ground. Similarly, the Uniform Building Code (ICBO 1997) revisions for base isolation systems requiring limits on base displacements potentially renders the need of additional techniques to be used in these systems (Kelly 1999; Yoshioka et al. 2002; Ramallo et al. 2002). Extra damping and controllable devices are feasible approaches to mitigate excessive base displacements due to base isolation systems in structures (Kelly 1999; Nagarajaiah and Ferrell 1999; Buckle et al. 2002). The following subsections will review all the feasible solutions regarding base isolation systems.

2.2.1 Smart base isolation

Smart base isolation is defined as a passive base isolation system which controls structures with variable semi-active control devices, i.e., orifice dampers or MR dampers (Spencer et al. 2000; Wongprasert and Symans 2005). The combination gives a stabilizing feature to structures, while the control mechanism can be adaptive to excitations (Makris 1997). The unacceptable base displacement responses in passive base isolation systems have been addressed several times in the previous sections; thus, the extra damping devices, such as semi-active control devices, provide the possibility to reduce the base displacements in the smart base isolation systems (Ramallo et al. 2002). This combination shares the advantages of semi-active control while still performing comparable to passive isolation system in structural responses, such as floor accelerations, interstory drifts, and base shear. However, the combination might not be always applicable to a wide range of seismic excitations. To seek improved control performance, a new combination of base isolation systems should be considered.

Many numerical and theoretical studies of smart base isolation systems have been investigated in the past decade. Ramallo et al. (2002) considered an isolated building with laminated rubber bearings and one MR damper at the base layer in order to reduce the base displacements as well as base shears and floor accelerations. Acceptable control performance was shown under moderate excitations, while lower control performance was exhibited under severe excitations. Madden et al. (2003) investigated the combination of an adaptive hydraulic damper and a sliding base isolated building. The sliding bearings in this study used the Bouc-Wen hysteretic model. The results proved that the combination of this smart base isolation system can effectively reduce the base displacements as well as interstory drifts. These numerical studies have demonstrated the applicability of smart base isolation systems, although a simulation might not sufficiently represent the true control performance in a practical implementation. Therefore, an overview on the experimental studies of these systems will be presented.

Numerous experiments on smart base isolation systems have been conducted in recent years. Yoshioka et al. (2002) verified a smart base isolation system employing laminated rubber bearings and MR dampers. The combination was realized in a single-story small-scale building under unidirectional excitations, and the results demonstrated acceptable control performance in the reductions of the base accelerations and displacements. Madden et al. (2002) experimentally proved the applicability of a sliding base isolated building with an adaptive hydraulic damper. In this study, the smart base isolation technique is validated for the first time, providing experimental evidence of the concept. Sahasrabudhe and Nagarajaiah (2005a) experimentally implemented a smart isolation system on a bridge between the deck and the piers. A variable stiffness device employed in the sliding base-isolated bridge was used to control the relative displacement between the deck and the piers and illustrated the applicability of this technique to bridges. Sahasrabudhe and Nagarajaiah (2005a) and Lin et al. (2007) employed different control strategies by applying smart base isolation with MR dampers to small-scale building models. In these studies, the control performance against near-fault earthquakes was examined and moderate reductions in structural responses were shown case by case. Moreover, Shook et al. (2007) considered a single-story building installed with bi-directional sliding bearings and planar MR dampers (e.g., MR dampers were placed in two directions) under bi-directional excitations. The control results exhibited similar performance in comparison to the previous studies, although two different directions for excitations were considered in this study. These studies have summarized the applicability of smart base isolation systems, which can promise the certain level of control performance. However, if higher control performance is desired in implementations, the type of damping devices might be reconsidered or substituted, such as hydraulic actuators.

As mentioned in this subsection, many studies of smart isolation systems have been investigated in recent years, and the results of these studies demonstrate the applicability and moderate control performance of these systems. To seek improved performance using this sort of control system, the control devices might be replaced or reconsidered for their applicability over a wide range of excitations as well as the previously drawn conclusions.

2.2.2 Active base isolation

Active base isolation denotes a passive isolation system combined with active control devices, such as hydraulic actuators. The passive isolation system in this combination provides the flexibility for the structural system, while actuators located at the base to mitigate large displacements. The combination shares the advantages of the passive isolation systems, i.e., reducing absolute floor accelerations, interstory drifts, and base shears, while at the same time limiting base displacements (Inaudi and Kelly 1990). High control performance is expected from this combination as compared to passive or smart base isolation systems (Yoshioka et al. 2002). To overcome the drawbacks of smart base isolation systems, active base isolation is the ultimate solution to the applicability for a wide range of excitations.

Active base isolation has drawn the attention of researchers for more than two decades. Inaudi and Kelly (1990) and Pu and Kelly (1991) proposed and experimentally verified the idea of active base isolation. Subsequently, many numerical studies were conducted by applying different control algorithms or employing different active control devices or isolation bearings into systems (Yang et al. 1992; Soong and Reinhorn 1993; Feng 1993; Yang and Vongchavalitkul 1994; Yoshida et al. 1994; Barbat et al. 1995; Yang et al. 1995; Fur et al. 1996; Loh and Chao 1996a; Loh and Ma 1996b; Lee-Galuser et al. 1997; Sener and Utku 1998). In these studies, the classic linear-quadratic-regulation control algorithm and the Lyapunov control algorithm were used most often (Inaudi and Kelly 1990; Pu and Kelly 1991; Loh and Chao 1996a; Yang et al. 1992; Loh and Ma 1996b; Fur et al. 1996). Some researchers focused on the numerical analysis of different isolation bearings, such as rubber bearings or sliding bearings (Yang et al. 1995; Feng 1993). Due to the complexity of the active control part in the active base isolation, some researchers investigated the realization of the active control loop, including the time delay or the uncertainties of the sensor measurements (Pu and Kelly 1991; Senser and Utku 1998; Barbat et al. 1995). Nonlinear behaviors inherently involved in the isolation bearings were also explored in some studies (Barbat et al. 1995; Yang et al. 1995). Different active control devices, such as active tuned mass dampers or active vibration absorbers (different from hydraulic actuators), were also considered (Loh and Chao 1996a; Lee-Galuser et al. 1997). Some studies also applied the idea to bridge structures in which the active isolation systems were placed between the deck and the piers (Reinhorn and Riley 1994; Yang et al. 1995; Park et al. 2003; Park et al. 2005). Although many numerical studies have been conducted in the research of active base isolation systems, few experiments were conducted during this time.

The limited number of active base isolation systems experimentally verified during the 1990’s are described in the following. Nagarajaiah et al. (1993) applied an active base isolation system to a single-span bridge on a shake table, in order to verify the control performance of the base displacements on the sliding bearings. Yang et al. (1996) employed the sliding mode control algorithm to control a sliding base-isolated, three-story building through shake table testing. Riley et al. (1998) developed a nonlinear controller to experimentally implement a hydraulic actuator for controlling a three-story, base-isolated building. Nishimura and Kojima (1998 and 1999) considered a building-like structure incorporated with an isolator and an actuator for verification of active base isolation. These experiments provided evidence of the applicability and feasibility of active base isolation systems. However, the experiments only considered the in-plane motions of structures under unidirectional excitations. Further considerations, i.e., out-of-plane motions of structures under multi-directional excitations, must be taken into account in the experiments of active base isolation systems in order to prove complete viability of this control technique.

To broaden the field of structural control, especially in base isolation, an ASCE benchmark control problem of a base-isolated building was developed for simulations (Narasimhan et al. 2006). In this control problem, three different types of isolation bearings, including elastomeric bearings, lead rubber bearings, and friction pendulum bearings, are optional to evaluate, and users can develop different control devices by using different control strategies (e.g., different measurements for feedback control, different control algorithms, or active/semi-active control devices) to examine their own approaches to the problem (Pozo et al. 2008). Several evaluation criteria, such as the resulting structural responses and the power consumption of control devices, are provided to compare the control performance between different control strategies. Nagarajaiah and Narasimhan (2006) also proposed some sample controllers to a linear isolation system in this control problem. In comparison to those studies in the 1990's, this control problem covered the three-dimensional behaviors of the structural system as well as in-plane and out-of-plane motions. Besides this benchmark control problem, Senser and Utku (1998) also investigated the dynamic behaviors of active base isolation systems in three-dimensional coordinates. Shook et al. (2007) investigated a smart base isolation system for a simple SDOF structure using two MR dampers in the two perpendicular directions under bi-directional excitation. However, up until now, the out-of-plane behavior of active and semi-active controlled base isolation systems still lacks comprehensive study and experimental verification. . Hence, experimental studies in active base isolation systems with multi-dimensional actuators under multi-directional excitations are still of need.

To bridge the gap between the practical implementation and the theory of active base isolation systems, successful experimental verification of a base-isolated system with multi-dimensional active control devices under multi-directional excitations is still needed. In the studies mentioned previously, the active control strategies encountered many difficulties including the time delay in the interface of the sensor measurements and the digital controller (Chung et al. 1988; Soong and Reinhorn 1993; Quast et al. 1995), understanding and modeling of the dynamic behavior of active control devices (Dyke et al. 1995), feedback control with a robust algorithm and available measurements of structural responses (Spencer et al. 1994; Dyke et al. 1994a and 1994b), control law realization by the digital controller (Dyke et al. 1994b; Quast et al. 1995). As for the planar motions of isolation bearings attached to the structures, only few experimental studies have considered the multi-directional excitations applying to the base isolated structures (Shook et al. 2007); therefore, further studies with consideration of the out-of-plane motions should be investigated. Many studies have addressed that the supplemental damping devices for the isolation systems might improve the performance a little (Kelly 1999; Nagarajaiah and Ferrell 1999; Buckle et al. 2002). For experimental verification, adequate setups, such as the selections of the active control devices and the isolation bearings, must be carefully prepared in order to correctly represent the behavior of the active base isolation system. According to the past research related to the implementation of active base isolation systems, numerous difficulties and challenges are waiting to be solved by researchers. A successful experimental implementation with complete considerations of experimental preparations and examinations will subsequently lead to the realization of active base isolation control in real-world structures.

2.3 Active isolation implementation

As described in the previous section, active base isolation systems produce the best control performance and are implementable; however, up to the present, only a limited number of experiments have completely implemented and proven this control technique. For this reason, the main objective in this research is the implementation of an active base isolation with multiple degree-of-freedom motions in order to verify this control technique against seismic excitations. This section subsequently presents a discussion of the relevant background of the experimental setup, the modeling of the active base isolation system, the control design and implementation, and the control performance evaluation.

2.3.1 Experimental research

An active base isolation system always consists of a structure, isolation bearings at the base, and the active control devices. In this research, the building structure is the main control subject to realize an active base isolation system. For the other elements of this problem including the isolation bearings, the active control devices, and other required equipments, the following discussion will carefully review the associated studies as well as provide potential solutions for the experimental instruments in detail.

The most interesting applications employing controlled base isolation systems in the laboratory use either buildings or bridges. For example, Inaudi and Kelly (1990), Yang et al. (1996), Riley et al. (1998) applied different active base isolation systems to a three-story, steel frame building. Similarly, Madden et al. (2002), Yoshioka et al. (2002), Wongprasert and Symans (2005), and Lin et al. (2007) applied smart base isolation systems to either a single mass building or a three-story, steel frame building. Although Nagarajaiah et al. (1999) and

Sahasrabudhe and Nagarajaiah (2005a) applied an active base isolation system or a smart base isolation system to bridges successfully, the limitation of the shake table capacity could give misleading results due to the required downscaling of the problem. The best option in this research is to use a building structure for testing an active base isolation system.

Structures used for dynamic tests in the laboratory are often small-scale models because of the limitations of space and shake table capacity. In order to represent the structural behavior and the experimental data of these tests accurately, the similitude technique should be applied to this type of problem (Chung et al. 1988). Accordingly, since the laboratory instruments might already exist (i.e., the shake table), the structural model should be designed based on the capacity of these instruments.

Several isolation bearings are available for implementation and application to structures (Naeim and Kelly 1999). First, Kelly (1997) introduced all types of rubber bearings, such as laminated rubber bearings, lead rubber bearings, high damping rubber bearings, and elastomeric bearings. Yang et al. (1996) and Riley et al. (1998) employed sliding bearings using Teflon/stainless plates to isolate the superstructure. Shook et al. (2007) employed a bi-directional roller-pendulum system with MR dampers to control a single-story frame. These bearings are all available options to be used in the experimental verification. However, if the bearings are down scaled (see the experimental setup in Yoshioka et al., 2002), the vertical stiffness of the laminated rubber bearings will be relatively small and may induce an instability problem. Hence, in addition to the laminated rubber bearings, the pendulum/friction type of bearings might be the best choice in terms of the vertical stiffness for the laboratory-scale tests.

Active control devices have been investigated and applied to experiments and real structures for many years (Soong and Reinhorn 1993; Soong and Constantinou 1994; Housner et al. 1997; Datta 2003; Spencer and Nagarajaiah). First, active tuned mass dampers have been wildly used in structures (Spencer and Nagarajaiah 2003), but most applications using these devices in active control are for the reduction of the responses induced by wind loadings. Although some buildings in Japan employed this technology to mitigate seismic responses (Kobori et al. 1991; Kobori et al. 1998) and some studies applied this control technique incorporated with isolation bearings (Loh and Chao 1996a), the experiment verification employing these control devices to active base isolation systems was rarely seen.

Hydraulic actuators were often used in active base isolation systems (Inaudi and Kelly 1990; Yang et al. 1996; Riley et al. 1998), which demonstrated their simplicity to install and control. However, the wrong capacity of the actuators employed in experiments may misrepresent the control performance of the active base isolation systems. For example, Inaudi and Kelly (1990) employed an actuator with the force capacity of 8 kips to control a 4,000 lb building, and Riley et al. (1998) used an 5,500 lb actuator to control a 6,370 lb building. These experiments presented a significant control performance of base displacement reductions but had fewer contributions from the isolation bearings. To represent the advantages of active base isolation systems effectively, the capacity of actuators should be selected carefully.

Digital controllers play an important role in the interface of the sensor measurements, the computation of the embedded control laws, and the input/output signal processing. The principle criteria to select the digital controllers for the applications of active control systems (or active base isolation systems) are the inherent time delay and the highest sampling rate, which could influence the system performance or distort the desired signals (Dyke et al. 1994a; Quast et al. 1995). Therefore, before the experimental implementation of active base isolation systems, these two key factors must be appropriate for the application.

Furthermore, since this research concentrates on active base isolation systems against earthquakes, the behavior of a shake table should be fully understood. The shake table is a motion simulator, which requires background knowledge of hydraulic actuators (Newell et al. 1995; Williams et al. 2001). In order to reproduce the earthquake records correctly, several preprocessing approaches should be considered, i.e., the tuning method to achieve the targeted accelerations using the input of the ground displacements (Spencer and Yang 1998). Due to the limitation of the shake table, the procedure to duplicate the ground motions will be varied case by case when different earthquake records are applied.

All the elements covered above are the basic requirements for the experimental implementation of an active base isolation system. Every component should be carefully determined before the tests; otherwise, the control implementation will be unstable and inapplicable or the control results will misrepresent the true behavior of the system.

2.3.2 System identification

To achieve high control performance in an active base isolation system, a control-oriented mathematical model for the entirely active base isolation system should be determined using appropriate system identification techniques. Many system identification techniques in most civil engineering applications are parametric in nature, seeking to determine or update physical quantities, such as mass, damping, and stiffness. For control purposes, specific values for the physical parameters of the structural system are not required; rather, an effective model that can accurately represent the dynamic relation between the various system inputs and the outputs is needed (Dyke et al 1994a and 1994b).

As mentioned previously, applying a system identification technique to develop an effective model of the active base isolation system can be challenging. The model needs to accurately portray the system's input-output behavior over the frequency range for which control is needed. According to this definition, the model of the system can be determined either in the time domain or the frequency domain. A model obtained by a time-domain system approach, such as the subspace system identification (van Overschee and de Moore 1994), can accurately describe the dynamic characteristics of systems in the time domain, but often cannot replicate detailed behavior in the frequency domain (e.g., zero locations). Bayard (1994) proposed a transfer function curve fitting method to identify a dynamic model which had 780 parameters over 0-100 Hz. Auweraer et al. (2001) modified this method to be faster using the total least-squared (LS) algorithm. Kim et al. (2005) developed a powerful tool for the frequency-domain system identification that allowed physical information about zeros at the origin to be considered. While these studies provided several ways to fit the transfer functions, the computational efficiency and the accuracy with respect to zeros of the transfer functions are limited. Mostly, these methods are applicable to a multi-input/multi-output (MIMO) system approach, but the model generated from the methods cannot be minimal (Dickinson et al. 1974). Hence, these methods still need some appropriate modification (e.g., combining several single-input/multi-output (SIMO) systems to be a minimal MIMO system) in order to correctly represent the system behavior.

Several approaches for system combination have been proposed previously. Dickinson et al. (1974) and Chen (1998) used a minimal realization method to cancel repeated modes after combining all SIMO systems into a MIMO system. Ober (1991), Dyke et al. (1994a and 1994b), and Chen (1998) employed a balanced realization method to combine SIMO systems by reducing the order of the systems and eliminating the noise order. However, these methods are only adequate for systems that can be very accurately identified and have relatively small nonlinearities; otherwise, the different natural frequencies and mode shapes will not be combined, and the system will then contain duplicate dynamics. Therefore, a new approach to improve the system combination is also a major task in this research.

The system approaches addressed in this section are mainly for use in the control design because most control algorithms require a mathematical model initially. A well-identified model cannot only give the dynamic behaviors of the whole system but also indirectly guarantee the robustness of the control design. Furthermore, improved control performance can be expected once the interaction between the control devices and the controlled structure is also included in the model (i.e., the control-structure interaction in Dyke et al. 1995). Hence, the system identification method should consider the physical representation of the system as well as include all the components involved in the system.

2.3.3 Control design and implementation

Controllers based on the control laws can be designed once the system model has been successfully identified. Note that the controllers defined in this section are the control laws/algorithms for use in driving the active control devices in an active base isolation system. The active control in structures is always in charge of stabilizing the structural system, indicating that all the poles must remain in the left-hand side of the complex plane after adding the control devices with the designed control laws. Most control algorithms used to stabilize a dynamic system robustly employ the feedback control technique, which utilizes the sensor measurements from the structural responses and the applied force, also referred to a close-loop control system

(Housner et al. 1997). Chen (1998) also stated that feedback control can reduce the effect of parameter variations and suppress noise and disturbances. Hence, active control using a feedback loop can be more reliable and robust, even powerful, despite the extra potential energy from the active devices that is always injected into the structure.

Many control algorithms have been developed and realized in active control structures or active isolation structures. Soong and Manolis (1987) applied the linear-quadratic-regulation (LQR) control algorithm to simulate an active control technique on a simple building, while Chung et al. (1988) demonstrated the idea on a building using a shake table test. Spencer et al. (1994) developed a frequency-domain optimal control algorithm based on the H_2/LQG control theory, and then Dyke et al. (1994a and 1994b) verified this control technique using acceleration feedback. Yang et al. (1992) employed the Lyapunov control algorithm to minimize a time dependent performance index, also called pole placement, on an active base isolation system, while Riley et al. (1998) carried out an experiment of an active sliding isolated building using this method. Yang et al. (1995) developed sliding mode control without an observer, which always indicates use of structural responses other than velocities and displacements, and then Yang et al. (1996) applied this control technique to an active isolation structure. The control algorithms which have been listed and reviewed in this subsection are categorized as the classic control algorithm, indicating that these methods always minimize the total energy of a control system in order to obtain a linear gain with respect to the state vector (e.g., consisting of displacement and velocity responses of structures in general. see Chen 1998). Although different methods utilize different procedures to solve the minimization problem of the total system energy, only a few researchers were able to exhibit very reliable and robust control laws in the control system because the gap between the numerical simulations and the experimental implementations still left many problems unresolved. As mentioned in Section 2.3.1 and 2.3.2, the real-time experiments should take into account the time delays and the hardware capability (e.g., high speed rate for computation, high sampling rate, and so on. see Quast et al. 1995 and Dyke et al. 1994a) as well as the control-structure interaction. Addressing these issues can lead the control implementation to be more robust and adaptive (Dyke et al. 1995). Based on these investigations, two key issues are addressed: 1) most classic control algorithms can be employed in the active control implementations of structures, while the procedures should be operated very carefully, given the series of considerations of control implementations; 2) most of this class of control algorithms generates a control gain with respect to the state vector but the responses in the state vector might not be available or might be difficult to measure. Therefore, while considering the requirements for real-time implementation, the classic control algorithms and an accompanying observer should be included in the control design and implementation.

Control designs with an observer, especially using the H_2/LQG control, have gradually been more popular in the field of structural control since the 1990's. Suhardjo et al. (1992), Spencer et al. (1994), and Yoshida et al. (1994) applied the H_2/LQG control algorithm in which the control gain was derived from the minimization of the LQR problem, and the observer was developed using the Kalman filter (details available in Spencer et al. 1998 and Chen 1998). Dyke et al. (1994a and 1994b) applied this control algorithm to a building using an active mass driver and an active tendon system, respectively. After these applications, many researchers validated this control algorithm in simulations as well as in experiments (Ramallo et al. 2002; Yoshioka et al. 2002; Park et al. 2003; Wongprasert and Symans 2005; Park et al. 2005; Nagarajaiah and Narasimhan 2006; Shook et al. 2007). Therefore, the wide acceptance of this control algorithm illustrated the viability and feasibility of its application in structural control, which includes all types of active/semi-active control techniques, such as active base isolation control. This research primarily continues working on this control algorithm and gives insights on this method.

To extend control performance while applying the H_2/LQG control algorithm, an earthquake spectrum, such as the Kanai-Tajimi spectrum (Soong and Grigoriu 1993), can be added to the system model in order to include information about the frequency content of earthquakes. This spectrum has been described in the form of a filter that can be easily converted into a state-space representation and directly appended to the model. The filter involved to form the system model functions as a shaping filter, which typically emphasizes the responses around the dominant frequency of the ground motions or translates the site effects to the structural dynamics. The details of the control designs with this shaping filter are available in the study by Yoshioka et al. (2002). This research also refers to this idea for examining the control performance of the active isolation building.

The applications of the H_2/LQG control and the shaping filter described previously mostly employed the structural parameters (mass, damping, stiffness) to form the state-space equation of motion; however, the system model for the control purpose does not require this information as mentioned in Section 2.3.2. Dyke et al. (1994a) and also followed the procedure of the system identification first, then designed the controller using the identified model. In the sort of models Dyke et al. utilized, the state vector in the state-space form is only used for the transition of the input/output relationship (e.g., the variables in a state vector are no longer the displacements and the velocities. see Chen 1998). To enhance the control performance and eliminate the modeling errors derived between the finite-element model and the real structure, this research only focuses on the control-oriented problem, which always depends on the input/output relationship.

The applicability of the controller developed from the H_2/LQG control algorithm can be verified for the specific system, such as an entire actively isolated building, before closing the control loop. Dyke et al. (1994b) demonstrated the details of the loop gain transfer function, which is defined by the relationship from the actuator command input to the controller command output. For example, the loop gain should be less than one at the frequencies where the model poorly represents the system behavior (e.g., the phases of the loop gain transfer function between the experimental data and those in simulation are mismatched), and the magnitude of the loop gain transfer function at higher frequencies should steadily roll off and be less than one. These steps ensure the stability of the whole system before implementing the active control. Hence, this procedure is discussed and included in this research.

Besides the development of the controllers and the controller check using the loop gain transfer functions, all the effects existing in the digital controllers must be considered before implementing all active control as addressed in Section 2.3.1. After all these considerations, such as time delay, required sampling rate, check of loop gain transfer functions, have been confirmed, the control techniques can be directly applied to the system and implemented in an active base isolation system.

2.3.4 Control performance evaluation

Passive base isolation, as addressed in Section 2.1, is vulnerable to large base displacements, which may induce lower stiffness and instability to the superstructure; smart base isolation systems described in Section 2.2.1 always exhibit moderate control performance and may be inapplicable to a wide range of seismic excitations. Hence, the control performance evaluation in this research relies on the improvement of the drawbacks in both control techniques.

Numerous evaluation criteria for the control performance of the active base isolation systems or the smart base isolation systems have been investigated and proposed by researchers. First, Narasimhan et al. (2006) defined many criteria in the base isolation benchmark control problem, i.e., peak and root-mean-squared (RMS) responses of base shears, base displacements, interstory drifts, absolute floor accelerations, and power consumptions from the control devices. For the experimental studies, Yang et al. (1996) observed the peak reductions in the interstory drifts of an actively isolated three-story building; Riley et al. (1998) evaluated the energy response reductions of an active base isolation system that were calculated as a function of interstory drifts and floor accelerations; Madden et al. (2002) focused on the reductions in the interstory drifts and base displacements for a smart base isolation system; Sahasrabudhe and Nagarajaiah (2005b) investigated the control performance on the base displacements and power consumption of a smart base isolation system; Lin et al. (2007) tried to reduce the absolute floor accelerations and the interstory drifts in a smart base isolation system; Shook et al. (2007) followed the criteria provided in the base isolation benchmark control problem and the results were varied for different excitations. However, most experimental studies on active base isolation systems always had poor control performance, while those on smart base isolation systems produced moderate performance. As a result, this research is seeking to mitigate the base displacements as well as the absolute floor accelerations.

Most studies in active base isolation systems only investigated the time-domain behavior, while rare studies addressed the control performance in the frequency domain. Dyke et al. (1994a and 1994b) applied active control techniques to a building in order to reduce the total energy over a band of frequencies. In this research, these types of analysis tools are also included and examined for an active base isolation system.

As mentioned previously, in order to appropriately represent structural responses in real structural systems, the similitude technique should be applied to small-scale experimental tests. Chung et al. (1998) applied this technique to an active control experiment by changing the interval time of earthquake records and defining the ratios for the structural parameters. In this research, the active isolation systems of the model buildings are small-scale buildings that should consider the similitude technique.

2.4 Summary

This chapter reviewed a number of analytical structural control studies, experimental control studies, and articles relative to the implementation of an active base isolation system. Many analytical studies have demonstrated the control performance of active base isolation systems; however, the experiments reported to date still cannot achieve the performance expected based on the numerical analysis. Moreover, most studies only considered in-plane motions and unidirectional excitations for shake table tests of active/semi-active base isolation systems. However, these previous studies only partially verified active base isolation systems experimentally. Further investigations of active base isolation systems should be conducted as well as a focus on the implementation of these systems in multi-dimensional motions under multi-directional excitations.

CHAPTER 3 DESIGN OF ACTIVE ISOLATION EXPERIMENTS

An active isolation system for buildings generally requires a building with the adequate dynamic characteristics, isolation bearings, active control devices, and components related to the operation of active control devices. Thus, this chapter presents the need to design or select all aspects of active isolation for buildings. The details in design of active isolation includes the building itself, the selection of isolation bearings, the design requirement of active control devices, the earthquake simulator, as well as the digital controllers for active isolation systems and the associated considerations.

3.1 Buildings

Buildings for base isolation control intrinsically require the fundamental natural frequency near the dominant frequency of excitations (e.g., earthquakes) when the buildings' base is fixed. This condition implies that the natural frequency of the fixed-base buildings for applying base isolation control should be within a certain range, where most earthquakes contain large components. Moreover, the performance of isolated buildings against earthquakes will be much more significant if the fundamental natural frequencies of these isolated buildings are outside the dominant frequency range of earthquakes. Hence, the buildings for active isolation should be relatively stiff before installing isolation bearings.

For the typical control objectives, the buildings themselves should always remain in a linear require. For example, the steel columns in buildings do not exceed the yield displacement during earthquake events where the isolation control has been applied to the buildings. Therefore, the buildings used for active isolation implementation should have high strength in order to ensure linear behavior during earthquakes.

This research considers two buildings with different heights. The two-story building, as shown in Figure 3.1(a), is the 1st stage of this study, which is mainly employed to simply explore the procedures for the active isolation implementation. The six-story building, as shown in Figure 3.1(b), is the 2nd stage in this research, which represents the general active isolation for buildings. Both frame buildings used in this control experiment are scaled models comprised of 45” x 28” x 1” steel plates for floors each weighing 360 lb. Each floor consists of six 100 ksi steel columns to support the plates. In order to further vary the structural systems, a number of braces are also available for tuning the structural characteristics, such as the natural frequencies. All column dimensions are listed in Table 3.1. Note that the column heights in the two-story building are exactly same as those in the first two stories of the six-story building.

Table 3.1. Dimensions of columns.

Floor	Height (in)	Width (in), *y*-direction	Thickness (in), *x*-direction
1	10.25	0.55	0.3125
2	12.5	0.55	0.3125
3 and 4	10.25	0.5	0.3125
5	10.25	0.4	0.3125
6	12.5	0.4	0.3125

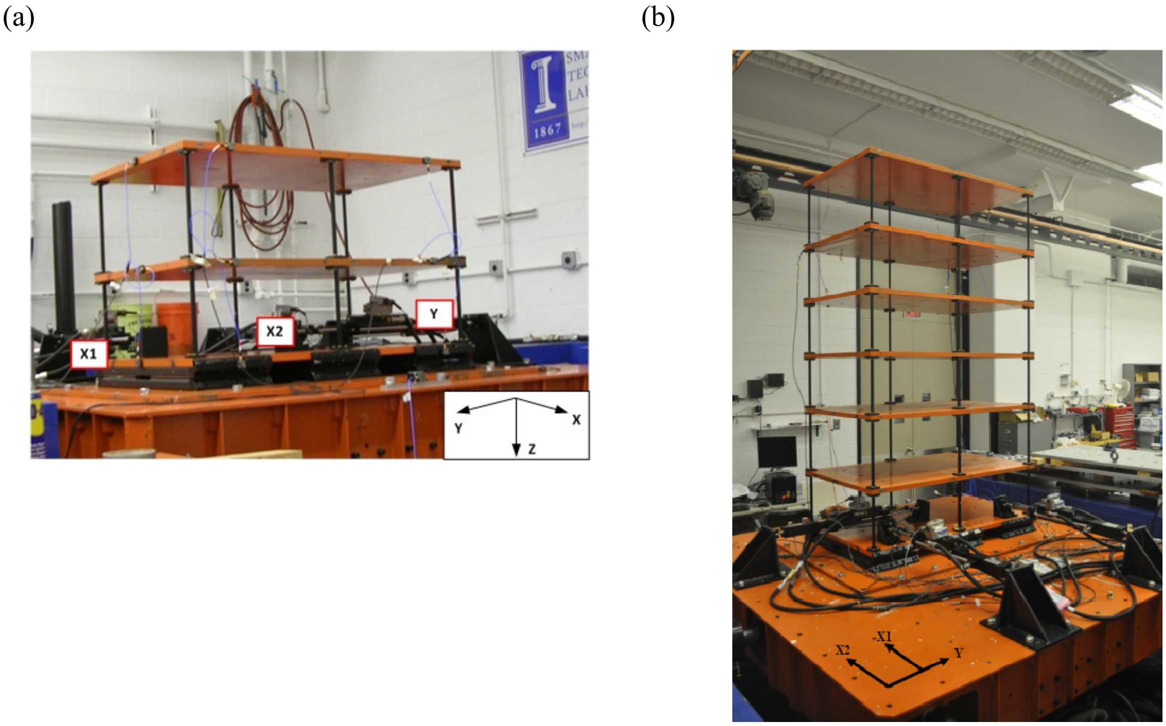

Figure 3.1. Active base isolation systems with (a) a two-story building and (b) a six-story building.

3.2 Isolation bearings

Two basic types of isolation bearings are commonly used in the structural isolation: elastomeric bearings (which are usually made of rubber) and sliders. Both types of bearings typically interpose structural elements with low horizontal stiffness between the structure and the foundation. Hence, the added flexibility shifts the fundamental natural frequency of buildings away from the dominant frequency of earthquakes.

Most isolation systems adopt steel-laminated rubber bearings to implement isolation control. This type of bearing is challenging to employ for laboratory-scale applications, because the low vertical stiffness can cause instability issues when the deformation of the bearings is sufficiently large. To avoid the potential problems, this research employs ball and cone isolation bearing, providing strong vertical stiffness.

The specific isolation bearings used in the active base isolation systems are the sliding type bearings from WorkSafe Technologies (2010), namely the ball-n-cone bearings. Figure 3.2 shows the bearings that consist of two identical conical-shaped plates (a diameter of 8.375") with a 1" ball in-between. The slope of the cone is 1:10. The total height of one bearing unit is 3 in. The active base isolation systems in this research use six bearings underneath the building. These bearings allow the building to move freely in the horizontally plane up to ±7" as well as provide very low damping and horizontal stiffness. Note that the lateral displacement of the top plate is equal to twice the ball displacement and the isolation units do not provide any vertical constraints.

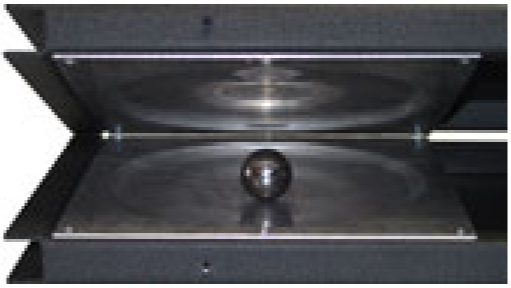

Figure 3.2. Isolation bearings used in active isolation systems (WorkSafe Technologies 2011).

3.3 Hydraulic actuators

As mentioned in Chapter 2, active control applications comprise a variety of control devices in the field of structural control. Depending on the applicability of structural systems, different mechanisms should be selected. For example, the active isolation systems in this research employ servo hydraulic actuators to control the isolated buildings. This type of active control devices is composed of two main components: a servo-valve and a hydraulic actuator. The servo-valve is commanded by an electrical input signal in order to allow the oil to move to and from the actuator chambers. The oil flow changes the pressure between two chambers which produces a force to move the piston and the specimen concurrently. Through this simple mechanism, the servo hydraulic actuator can offer the responding force based on the input signal and the supplied oil pressure.

The hydraulic actuators with Moog G761 series servo-valves (Moog 2011) are custom manufactured by Shore Western Manufacturing (2011) in order to meet the needs of this experiment, as shown in Figure 3.3. Each actuator has 500-lb dynamic force capacity with 8.76" in the full stroke. To avoid accidental over-travel, the stroke is limited to 8 inches. All actuators are hydraulically controlled by the SC-6000 controller, also designed by Shore Western Manufacturing. Proportional-integral-derivative control is also employed in the digital controller for commanding the actuators when moving to the desired displacements. Only the proportional gains of three actuators are tuned to be applicable for the real-time testing. Note that the details of these servo hydraulic actuators, with the associated parameters and modeling, will be addressed in Chapter 4.

Active isolation experiments in the previous studies employed actuators that were not scaled appropriately for the structural model. Typically, the base shear of buildings in the active isolation systems is carried by the bearings and the actuators. Ideally, an active isolation system should include contributions concurrently from the flexibility of bearings and the control capacity of the actuators. Thus, the more base shear the actuators take, the less contribution the bearings make. For example, in Inaudi and Kelly (1990), the actuator had a dynamic force rating of 8 kips, whereas the mass was only 4,000 lb. This actuator provided forces that are much greater than those that could be generated in the corresponding full-scale application. Moreover, Riley et al. (1998) employed a 5.5-kip actuator to control a 6,350-lb isolated building. These examples illustrate that fewer contributions of the passive base isolation can be expected if the capacity of the actuators is too big with respect to total mass of the active base isolation systems. A detailed comparison of these examples with the active base isolation systems used in this research is given in Table 3.2. Hence, use of these actuators in this research allows the laboratory-scale experiments to provide more information about the potential for full-scale implementation.

Because one of objectives in this research is the control of the horizontal motions, which includes two translational responses and one torsion response, multiple actuators are equipped at the base layer along with the bearings (see Figure 3.1). According to the configuration, one actuator, namely the *y*-actuator, is located on the strong axis of the buildings. The free end of this *y*-actuator is at the center of gravity of the buildings. The other two actuators, namely the *x*1-actuator and the *x*2-actuator, are located at 6.5” from both edge columns along the weak axis of the buildings. These two actuators are symmetrically placed with respect to the center of gravity of the buildings. Note that the free ends of the *x*-actuators are set off the center line of the *y*-direction.

Table 3.2. Comparison of actuators in active isolation systems

Variables	Study of Inaudi and Kelly (1990)	Study of Riley et al. (1998)	Actuators used in this study
Maximum operating pressure	3000 psi	3000 psi	3000 psi
Cross sectional area	Not available	1.90 in^2	0.25 in^2
Hydraulic flow rate	2.5 gpm	15 gpm	15 gpm
Maximum (dynamic) force	8.00 kips	6.35 kips	0.50 kips
Dynamic stroke	Not available	6 inches	8 inches

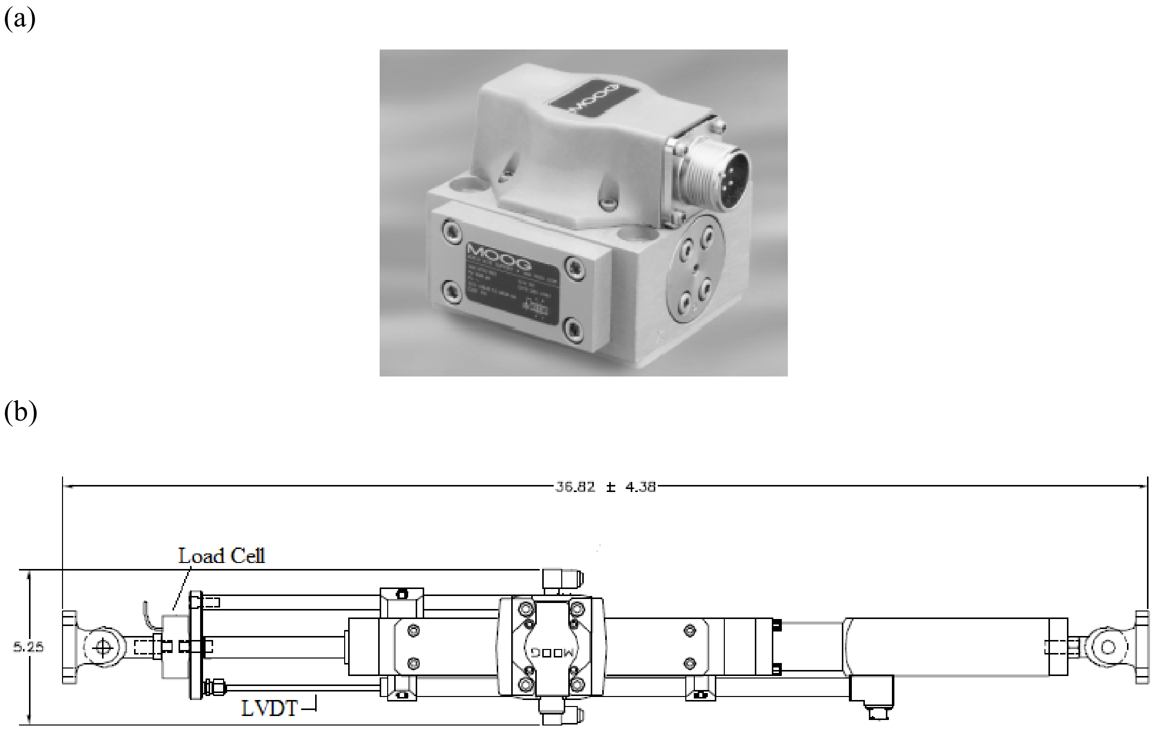

Figure 3.3. (a) Servo-valve (Moog 2011) and (b) Hydraulic actuator (ShoreWestern Manufacturing 2011).

3.4 Sensors

A number of sensors are installed on the model buildings for use in either the control implementation or in the determination of the control performance. Accelerometers are located at the edges of some floors along the actuators' directions (e.g., *y*-direction, *x*1-direction, and *x*2-direction). For instance, in the two-story building, the accelerometers are located at the base, 1st floor, and 2nd floor along the *y*-, *x*1-, *x*2-directions. In the six-story building, the accelerometers are located at the base, 2nd floor, 4th floor, 5th floor, and 6th floor along the *y*-, *x*1-, *x*2-directions. Additionally, two accelerometers are placed on the shake table in order to measure the ground accelerations. All the accelerometers are models 3701G3FA3G or 3711D1FA3G by PCB Piezotronics (2011), as shown in Figure 3.4(a). These two types of accelerometers have a ±3 g measuring capacity with a frequency range of 0-100 Hz. The sensitivities for the 3701G3FA3G and 3711D1FA3G are 1000 mV/g and 700 mV/g, respectively.

In order to fully investigate the behavior of the six-story building and the control performance, two additional wireless sensors are installed on the 1st and 3rd floors (see Figure 3.4(b)). Each wireless sensor is capable of measuring tri-axial accelerations. The data collected from the wireless sensors is independently recorded and uses different data acquisition schemes from wired accelerometers. The detailed specifications of the wireless sensors are available in http://shm.cs.uiuc.edu/.

In addition to acceleration, base displacement is also measured. The displacements along two perpendicular directions are measured using linear variable differential transformers (LVDT) or the Krypton K600-DMM system from Nikon Metrology NV (2011), as shown in Figure 3.3(b) and Figure 3.4(c), respectively. These LVDTs are located on the actuators, and the resulting LVDT readings can be viewed as the base displacements. While no actuators are attached to the buildings, the relative displacements between the building base and the ground are sensed by the Krypton system. Note that the setup in the two-story active isolation system does not include the measurements of the Krypton system.

The Krypton K600-DMM system is employed to measure the displacement from the position of infrared light-emitting diodes (LED) by means of linear charge-coupled device (CCD) cameras. Up to 256 LEDs can be used in a volume of up to 17 m^3 with a sampling rate of up to 3000 readings per second per LED. This system features measurements reliable to approximately 0.02 mm. The temperature compensation model, included with this system, can correct measurements within the range of 15° to 40 ° C. The dynamic reference in this system enables users to measure unstable parts. For example, the static coordinates of the target are set initially when the shake table is at the rest position. After the shake table turns into the working position, the original coordinates have changed. At this moment, users can redefine the coordinates based on the dynamic reference without calibrating the positions of the LEDs again. Hence, the Krypton K600-DMM fits the general purpose of the dynamic testing, particularly for the shake table testing.

The number of sensors used in the control implementation depends on the requirement of the control designs, but all the sensors provide the responses for evaluation of the control performance under different control strategies.

Figure 3.4. (a) PCB accelerometers (PCB Piezotronics 2011), (b) wireless sensor, and (c) Krypton K600-DIMM system (Nikon Metrology NV 2011).

3.5 Digital signal processing equipment

In this research, the data acquisition and the digital controller work independently with different equipment in accordance with the functionality. The data acquisition requires an anti-aliasing filter to avoid the frequency components above the Nyquist frequency corrupting the low frequencies. In contrast, the digital controller sends the control commands for the actuators based on the measurement inputs and needs a high sampling rate without any signal distortions, i.e., no anti-aliasing filter incorporated. Moreover, the investigation of frequency-domain responses, such as the transfer function responses, requires a function generator which can produce the band limited white noise (BLWN). All digital processing equipment is introduced in the following.

3.5.1 Data acquisition system

The main data acquisition (DAQ) system in the experimental setup is the NI-DAQ (National Instrument 2011). This tool consists of several modules that can acquire real-time responses for up to thirty-two channels. The inherent anti-aliasing filter, which allows users to define the cutoff frequency, ensures responses without the aliasing effect. For the six-story building system, the responses are always acquired using the NI-DAQ.

This NI-DAQ consists of an NI PCI-6052E data acquisition board, several cascaded NI SCXI-1141 lowpass elliptical filter modules, and several cascaded NI SCXI-1140 simultaneous-sampling differential amplifier modules. The NI PCI-6052E has a 16-bit input and output resolution and a maximum sampling rate of 333 kS/s. Each NI SCXI-1141 module has eight channels and the programmable 8th-order filters, which allow a sharp roll-off of responses. These are the anti-aliasing filters. The cut-off frequencies in these filters are assignable, ranging from 10 Hz to 25 kHz. These boards also condition signals ranging from ±50 mV to ±5 V and offer multiplexed and parallel modes of operation. Each NI SCXI-1140 module provides eight simultaneously sampled input channels, which feature the sample-and-hold timing conditions for the signals. This sample-and-hold timing feature among the cascaded modules is shared with each other, resulting in total thirty-two simultaneously sampled input channels available in this NI-DAQ.

A Labview program is the main platform to acquire and save data from the NI-DAQ. This program gives users the ability to set the programmable cut-off frequencies, sampling rates, measuring durations (or points) for each NI SCXI-1141 module, and the gain on each input channel.

3.5.2 Digital controller

A dSPACE DS1003 (dSPACE Inc., www.dspaceinc.com) parallel digital signal processing DSP board on a Texas Instrument TMS320G40 processor performing on a PC computer is used to generate the control commands for the actuators in accordance with the developed control strategies. A dSPACE DS2102 High-Resolution, 6-channel D/A Board and a dSPACE DS2002/DS2003 32-channel A/D Board are employed to convert the signals from digital to analog and analog to digital, respectively. These two boards have a resolution of 16 bits. Access to the input and output channels is provided by dSPACE connector panels which allow the signals to be connected via BNC ports. The high overall sampling rate and the high computation rates in the digital controller ensure the capability for real-time applications (Spencer et al. 1994; Dyke et al. 1994a and 1994b; Quast et al. 1995).

The developed control strategies are implemented in SIMULINK/MATLAB and then downloaded to the dSPACE processor using the Real-time Workshop (http://www.mathworks.com/products/rtw/). The other program used in the control implementation is COCKPIT which can monitor signals and change the parameters to or from the DSP board during testing.

3.5.3 Signal analyzer

To generate the band-limited white noise (BLWN) signals applied to the active base isolation systems for transfer functions, the dynamical signal analyzer of the Siglab (Spectral Dynamics 2007) is employed. The SigLab enables sophisticated measurements with time histories up to 15 M samples long, 128K samples per second on each channel, and power spectrums with a guaranteed 95 dB spurious free dynamic range. In addition, the SigLab performs measurements including transfer function magnitude, phase, and coherence using broadband FFT techniques or a swept sine wave, auto- and cross- correlation, and impulse response. This tool also contains a function generator, which can produce sinusoid waves, step functions, and BLWN signals, etc. Hence, the basic tests (e.g., the calibration of actuators, the tuning process for actuators, the signal testing for the digital controllers, and the transfer functions tests, etc.) always employ the

Siglab to obtain the specific responses in this research. Note that the time-domain responses for the two-story, actively base isolated building system are collected using the Siglab.

3.6 Shake table

As this research focuses on the seismic protection, a six-DOF shake table (ShoreWestern Manufacturing 2011), illustrated in Figure 3.5, is employed to simulate the earthquake records for all experiments. This shake table consists of six largely hydraulic actuators, denoted as X1, X2, Y, Z1, Z2, and Z3. The maximum displacement of the shake table in three translational directions is ±4” (*x*), ±2” (*y*), and ±2” (*z*), respectively. The total payload is two tons, resulting in the maximum accelerations of 2 g horizontally and 1 g vertically. The actions of the shake table are performed by the SC-6000 controller, which generates the functions and allows external inputs. To duplicate the earthquake records, the time histories of the displacement commands based on the six DOFs in the Cartesian space are required to preload into the SC-6000 before performing the wave forms.

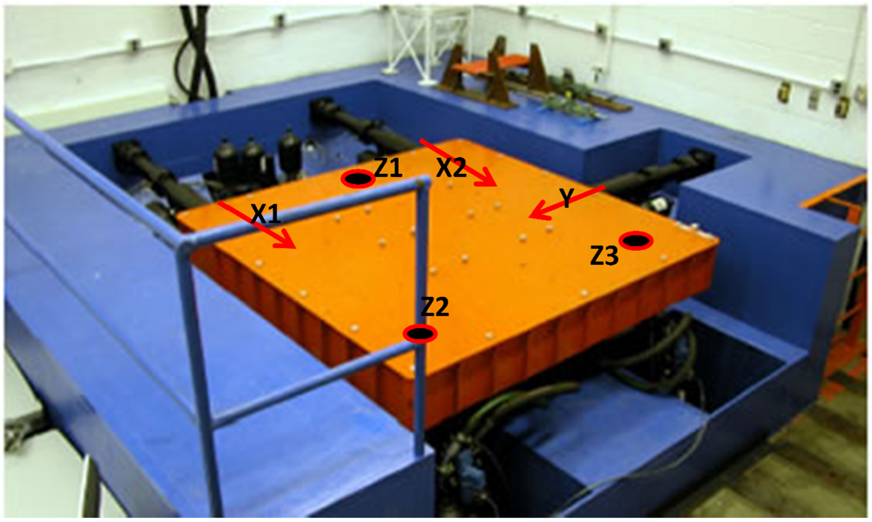

Figure 3.5. Shake table (ShoreWestern Manufacturing 2011).

3.7 Summary

In this chapter, two active isolation systems and the associated instruments have been introduced. Both buildings for these two systems were designed based on the basic isolation concept, which required the superstructure to be relatively stiff. Due to the laboratory-scale testing, the isolation bearings were carefully selected to avoid misleading the objective of active isolation (e.g., low stiffness and low damping) and producing unexpected responses (e.g., the vertical deformations). To consider the control implementation of these two active isolation systems in the horizontally planar motions, three actuators located in three different axes were installed at the base layer. By considering the availability in the practical implementations, acceleration responses were selected to be used in the control design as well as the evaluation of control performance. Because the isolation systems always exhibited large base displacements, these displacements were sensed by the LVDTs or the Krypton system for the control performance evaluation. Moreover, the digital signal processing systems were also carefully determined in order to meet the need of the experiments, such as the resolution of measurements, the requirement of data acquisition for different purposes, and the tests for different types of responses, etc. Through the assembly of these instruments, the two active isolation systems can be implemented using the shake table testing.

CHAPTER 4 FORMULATION OF A SIMPLIFIED MODEL

This chapter presents the numerical model of the active isolation systems which will give a preview of this control-oriented problem. For example, many researchers studying the active control applications obtain the structural model for control design directly based on the finite element (FE) method or the simplified lump mass approach. For control purposes, specific values for the physical parameters of the structural system are not required; rather, an effective model that can accurately represent the dynamic relationship between the various system inputs (e.g., the control commands of control devices and the excitations) and the outputs (e.g., the structural response) is needed. Ensuring the parameters, such as the numbers of states, poles, and zeros, in the system identification for the input-output relationship of the active isolation systems is the main objective for developing the mathematical model in this chapter.

In this chapter, the models of the buildings, the bearings, and the actuators are formed individually from the beginning. Following which, the overall system models with consideration of the control-structure interaction (CSI) are presented. Since the active isolation systems are intrinsically nonlinear, the difference between the linearized model and the real behavior of the systems is addressed. Two examples based on the two-story and six-story active isolation systems will be illustrated. The developed models will be comparable to the models from the system identification in Chapter 5.

4.1 Modeling of buildings

Consider, for example, the buildings in the active isolation systems shown in Figure 4.1. Due to the motions in the horizontal plane, the equation of motions includes three main components:

translational responses in the x- and y- directions and the torsions along the vertical direction. In this research, the buildings can be assumed to be shear-type structures because the column stiffness in the buildings is relatively strong and the floor plates are rigid enough. To simplify this problem, the structural systems are formed using the lumped mass approach. The assumptions made for the buildings' equation of motions are as follows:

- The buildings themselves are symmetric in both x- and y- directions.
- The torsion stiffness is derived from the translational stiffness of both directions.
- The mass of floor plates is uniformly distributed.
- The mass matrix is a diagonal matrix in accordance with the lumped mass approach.
- The stiffness matrix is derived from the shear-type formulation, e.g., no rotational forces.
- The damping matrix is formed by the modal damping method.

Therefore, the equation of motions for the multi-story buildings is given by

$$\mathbf{M}_s\left(\ddot{\mathbf{x}}_s-\mathbf{\Gamma}\ddot{\mathbf{x}}_b\right)+\mathbf{C}_s\left(\dot{\mathbf{x}}_s-\mathbf{\Gamma}\dot{\mathbf{x}}_b\right)+\mathbf{K}\left(\mathbf{x}_s-\mathbf{\Gamma}\mathbf{x}_b\right)=-\mathbf{M}_s\mathbf{\Gamma}\left(\ddot{\mathbf{x}}_g+\ddot{\mathbf{x}}_b\right) \tag{4.1}$$

with

$$\begin{aligned}
&\mathbf{x}_s=\begin{bmatrix}\mathbf{x}_{s,x}^T & \mathbf{x}_{s,y}^T & \mathbf{x}_{s,zz}^T\end{bmatrix}^T,\ \mathbf{x}_b=\begin{bmatrix}x_{b,x} & x_{b,y} & x_{b,zz}\end{bmatrix}^T,\ \ddot{\mathbf{x}}_g=\begin{bmatrix}\ddot{x}_{g,x} & \ddot{x}_{g,y} & 0\end{bmatrix}\\
&\mathbf{x}_{s,x}=\begin{bmatrix}x_{ns,x} & x_{ns-1,x} & \cdots & x_{1,x}\end{bmatrix},\ \mathbf{x}_{s,y}=\begin{bmatrix}x_{ns,y} & x_{ns-1,y} & \cdots & x_{1,y}\end{bmatrix}\\
&\mathbf{x}_{s,zz}=\begin{bmatrix}x_{ns,zz} & x_{ns-1,zz} & \cdots & x_{1,zz}\end{bmatrix}
\end{aligned}$$

where $\mathbf{x}_s$ and $\mathbf{x}_b$ denote the buildings' displacements and the base displacements; x, y, zz in the subscripts denote x-, y-, and torsion directions; the number subscripts indicate the floors; ns indicates the total number of stories; $\dot{\mathbf{x}}_s$ and $\ddot{\mathbf{x}}_s$ are the buildings' velocities and accelerations; $\dot{\mathbf{x}}_b$ and $\ddot{\mathbf{x}}_b$ are the base velocities and accelerations; $\ddot{\mathbf{x}}_g$ is the ground accelerations; $\mathbf{M}_s$, $\mathbf{C}_s$, $\mathbf{K}_s$

are the mass, damping, and stiffness matrices; $\mathbf{\Gamma}$ is a vector that couples each degree of freedom from the base absolute responses to the buildings.

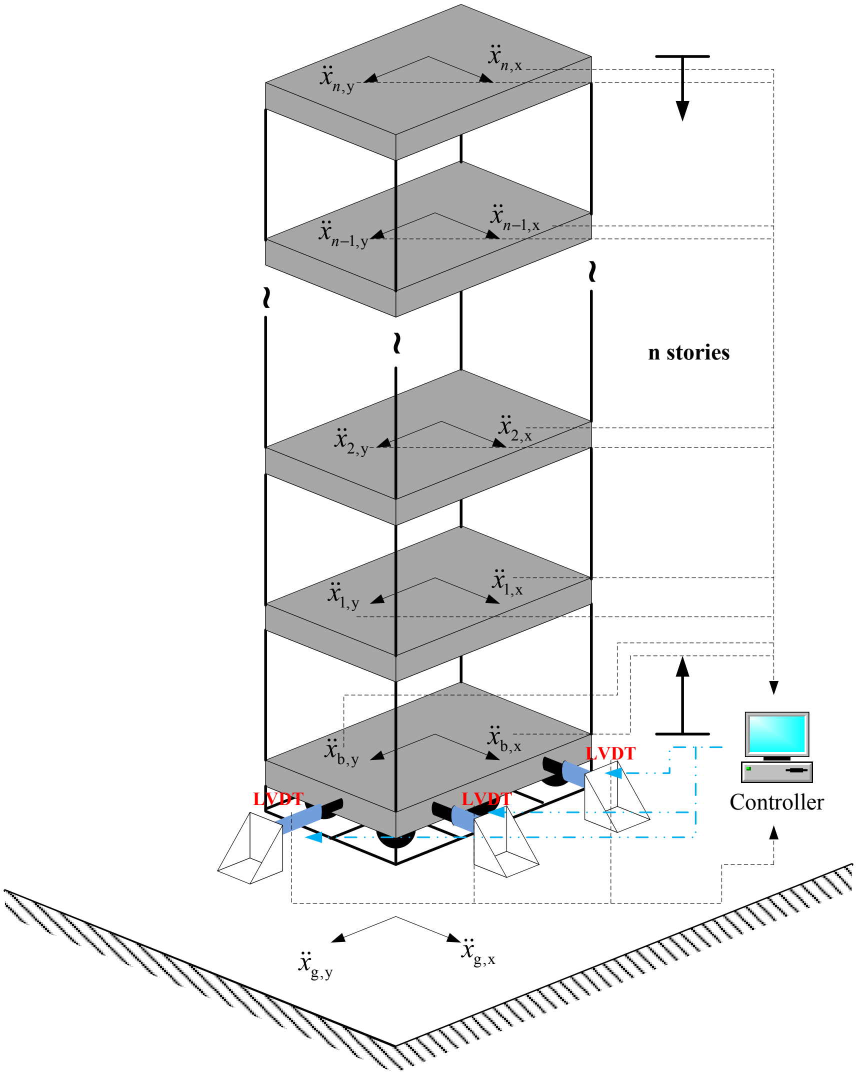

Figure 4.1. Illustration of active isolation systems.

4.2 Modeling of isolation bearings

As mentioned in Section 3.2, the isolation layer shown in Figure 4.2 employs the ball-n-cone bearings, which consist of two areas: 1) spherical area and 2) conical area. In the spherical area, the bearings provide a combined force from the re-centering stiffness and the friction force. In the conical area, the force is derived from the sliding force and the friction force due to the weight on the inclining surface (Vargas and Bruneau 2009).

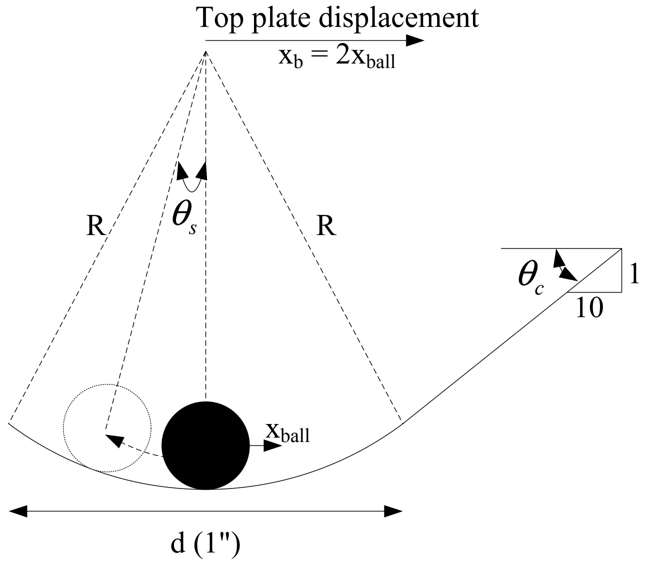

Figure 4.2. Sliding mechanism of ball-n-cone bearings.

4.2.1 Formulation for isolation bearings

According to the sliding mechanism shown in Figure 4.2, the force provided by the bearings to the buildings' bases are written in the form of

$$\begin{aligned} f_b &= N\sin\theta\,\mathrm{sgn}(x_b) + \mu N\cos\theta\,\mathrm{sgn}(\dot{x}_b) \\ x_b &= \sqrt{x_{b,x}^2 + x_{b,y}^2} \end{aligned} \tag{4.2}$$

with

$$\theta = \min(\theta_s, \theta_c),\ \theta_s = \frac{x_b}{2R}$$

$$N = m_{total}\,g\cos\theta - f_{BS}\tan\theta\,\mathrm{sgn}(x_b)\cos\theta$$

where f_b is the bearing total force; μ is the rolling friction coefficient normally ranging from 0.001-0.01 (Tsai et al. 2006); θ_c is the slope equal to 1/10; *R* is the radius of the spherical area; *N* is the normal force on the surface; m_{total} is the total mass of the superstructure, e.g., the total mass of the buildings; f_{BS} is the shear force between the bearings and the superstructure. Note that the bearing force in the *x*-direction is equal to $\frac{x_{b,x}}{x_b} f_b$; similarly, the bearing force in the *y*-direction is $\frac{x_{b,y}}{x_b} f_b$.

For the linear approach, the problem can be only focused on the spherical area, resulting in $\theta_s \to 0$. Because the rolling friction coefficient is very small, μ can be assumed to be zero. Additionally, the normal force can be assumed as $m_{total} g$. Therefore, the bearing force is rewritten as

$$f_b = \frac{m_{total} g}{2R} x_b \tag{4.3}$$

If the force in the *x*- or *y*- direction is only proportional to the displacement along this direction, the force can be divided into two terms, i.e., $f_{b,x} = \frac{m_{total} g}{2R} x_{b,x}$, $f_{b,y} = \frac{m_{total} g}{2R} x_{b,y}$. Note that all assumptions above would underestimate the bearing force. Therefore, the stiffness matrix $\mathbf{K}_b$ of the bearings can be formed in the equation of motions in accordance to these assumptions.

After forming the linear bearing force, the equation of motions for the isolation layer is given by

$$\left(\mathbf{\Gamma}^T \mathbf{M}_s \mathbf{\Gamma} + \mathbf{M}_b\right) \ddot{\mathbf{x}}_b + \mathbf{K}_b \mathbf{x}_b = -\mathbf{\Gamma}^T \mathbf{M}_s \ddot{\mathbf{x}}_s - \left(\mathbf{\Gamma}^T \mathbf{M}_s \mathbf{\Gamma} + \mathbf{M}_b \mathbf{\Gamma}^*\right) \ddot{\mathbf{x}}_g \tag{4.4}$$

where $\mathbf{M}_b$ and $\mathbf{K}_b$ are the mass and stiffness matrices of the bearings; $\mathbf{\Gamma}^*$ denotes the coupled effects from the ground accelerations to the response at the base layer. Note that the torsion stiffness also affects the bearings' stiffness matrix, which is contributed to by the two translational stiffness components.

4.2.2 Modeling of isolated buildings

After obtaining the equations of motions of both buildings and bearings, the linearized model of the isolated buildings (i.e., the isolated buildings stated here have no hydraulic actuators attached) is given by

$$\bar{\mathbf{M}}\begin{bmatrix}\ddot{\mathbf{x}}_s\\ \ddot{\mathbf{x}}_b\end{bmatrix}+\bar{\mathbf{C}}\begin{bmatrix}\dot{\mathbf{x}}_s\\ \dot{\mathbf{x}}_b\end{bmatrix}+\bar{\mathbf{K}}\begin{bmatrix}\mathbf{x}_s\\ \mathbf{x}_b\end{bmatrix}=-\bar{\mathbf{M}}\begin{bmatrix}\mathbf{\Gamma}\\ \mathbf{\Gamma}^*\end{bmatrix}\ddot{\mathbf{x}}_g \tag{4.5}$$

with

$$\bar{\mathbf{M}}=\begin{bmatrix}\mathbf{M}_s & \mathbf{0}\\ \mathbf{0} & \mathbf{M}_b\end{bmatrix},\ \bar{\mathbf{C}}=\begin{bmatrix}\mathbf{C}_s & -\mathbf{C}_s\mathbf{\Gamma}\\ -\mathbf{\Gamma}^T\mathbf{C}_s & \mathbf{\Gamma}^T\mathbf{C}_s\mathbf{\Gamma}\end{bmatrix},\ \bar{\mathbf{K}}=\begin{bmatrix}\mathbf{K}_s & -\mathbf{K}_s\mathbf{\Gamma}\\ -\mathbf{\Gamma}^T\mathbf{K}_s & \mathbf{\Gamma}^T\mathbf{K}_s\mathbf{\Gamma}+\mathbf{K}_b\end{bmatrix}$$

where this Eq. (4.5) is slightly reformulated from Eq. (4.2) and (4.4) due to the sensors' setup described in Section 3.4. For example, the accelerometers installed at the floor level are employed to measure the absolute accelerations, while the LVDTs or the Krypton are employed to measure the base displacements relative to the foundation. Additionally, this equation could be modified using Eq. (4.2) to consider the nonlinear behavior of the bearings.

The state-space representation is usually used in the response calculation as well as in the control problems. Hence, the passive isolation system (i.e., when the isolated buildings do not have any actuators attached) based on Eq. (4.5) is converted into a state-space representation given by

$$\begin{aligned}\dot{\mathbf{x}}_p &= \mathbf{A}_p\mathbf{x}_p + \mathbf{E}_p\ddot{\mathbf{x}}_g \\ \mathbf{y} &= \mathbf{C}_p\mathbf{x}_p + \mathbf{v}\end{aligned} \tag{4.6}$$

with

$$\mathbf{A}_p = \begin{bmatrix} \mathbf{0} & \mathbf{I} \\ -\overline{\mathbf{M}}\overline{\mathbf{K}}^{-1} & -\overline{\mathbf{M}}\overline{\mathbf{C}}^{-1} \end{bmatrix},\ \mathbf{E}_p = \begin{bmatrix} \mathbf{0} \\ -\mathbf{\Gamma} \\ -\mathbf{\Gamma}^* \end{bmatrix}$$

$$\mathbf{x}_p = \begin{bmatrix} \mathbf{x}_s^T & \mathbf{x}_b^T & \dot{\mathbf{x}}_s^T & \dot{\mathbf{x}}_b^T \end{bmatrix}^T,\ \dot{\mathbf{x}}_p = \begin{bmatrix} \dot{\mathbf{x}}_s^T & \dot{\mathbf{x}}_b^T & \ddot{\mathbf{x}}_s^T & \ddot{\mathbf{x}}_b^T \end{bmatrix}^T$$

where $\mathbf{y}$ is the measurement outputs with respect to the corresponding $\mathbf{C}_p$ and $\mathbf{v}$ is the measurement noise. The $\mathbf{C}_p$ could be modified by specifying the adequate entries. Therefore, the state-space representation is derived for the passive isolation systems. For the derivation of the active isolation systems, Eq. (4.6) will be also employed with the consideration of the control-structure interaction.

4.2.3 Effects of isolation bearings

In this section, Eq. (4.2) has shown the nonlinearity of the ball-n-cone bearings which are used in this research. To simplify the bearings into a linear problem, Eq. (4.3) provides the linear behavior only in the spherical area. However, this equation will be invalid if the base displacement exceeds the spherical area. The following addresses some aspects regarding the characteristics of the bearings:

1. If only considering Eq. (4.3), the interaction (e.g., the shear forces between the buildings and the bearings) has been neglected.
2. If the bearing balls move into the conical area and only the positive displacement is considered at that moment, the bearing force can be simplified into a function of normal

force on the conical surface, resulting in $f_b = N \sin\theta_c$. The rolling friction coefficient is assumed to be zero in this case.

3. If the diameter in the spherical area is small enough to be neglected, the bearing force will be simplified to $f_b = N \sin\theta_c \operatorname{sgn}(x_b) + \mu N \cos\theta_c \operatorname{sgn}(\dot{x}_b)$. Because the slope in the conical area and the rolling friction coefficient are very small, the bearing force f_b will approach zero. Accordingly, the floor accelerations of the buildings will be close to zero. Hence, very large base displacements can be predicted when the bearings perform based on this assumption.

Due to these aspects, the isolated buildings will exhibit high performance in reductions of the buildings' responses when the bearings stay in the conical area. Moreover, the bearing balls will have a high likelihood of moving around in the conical area because the spherical diameter of these ball-n-cone bearings is small. Therefore, the small bearing forces and the high nonlinearity which characterizes this type of bearing, as well as the large base displacement, can be expected using the bearings.

4.3 Modeling of actuator dynamics

Hydraulic actuators have been used in a wide number of engineering applications by virtue of the small size-to-power ratios and the ability to apply very large force, i.e., servo hydraulic actuators. However, hydraulic actuators also have a number of characteristics which complicate the development of high-performance closed-loop control due to their large nonlinearity. Before using actuators in a control problem, the understanding and recognition of these characteristics will improve the performance (e.g., by considering the control-structure interaction) and reduce the unexpected circumstances (e.g., the instability due to variations in the hydraulic parameters).

Most servo-valve actuators consist of a servo-valve and a hydraulic actuator. The servo-valve responds to an electrical input signal for a spool in order to change oil flow directions and oil flow rates. The changes in flow produce the pressure drop between the two chambers in the actuators, while the force caused by the pressure drop moves the piston and is then transmitted from the rod to the controlled object. This simple mechanism sketches the basic dynamics of servo-valve actuators in the motions and the force equilibrium. Hence, the relationship in these two dynamic characteristics to the whole control loop is the key for the modeling in this section.

As illustrated in Figure 4.3(b), the type of actuators employed in this research is the servo-valve hydraulic actuator with a double-rod cylinder. Typically a double-rod actuator has the same area in both chambers. The behavior of a double-rod actuator in a structural system has been investigated by Dyke et al. (1995). In this research, the actuator modeling is modified from the previous work in order to completely represent the dynamic behavior in a control-structure system.

To better understand the actuator's behavior, Figure 4.3(a) illustrates the flow path between the servo-valve and the hydraulic actuator from the beginning. The supplied oil pressure is generated from the pump and then passed to the actuator's chambers through the control of the servo-valve. To clearly express the path, a schematic block diagram shown in Figure 4.3(b) provides the sequential steps from the input command to the structural responses (e.g., the base displacements and velocities in the active isolation systems). According to this diagram, the interaction from the structural responses to the hydraulic actuator and the feedback loop implies the control-structure interaction (Dyke et al. 1995). As a result, modeling actuators should consider the responses of the structures, and the modeling of an active isolation system should include the actuator's model.

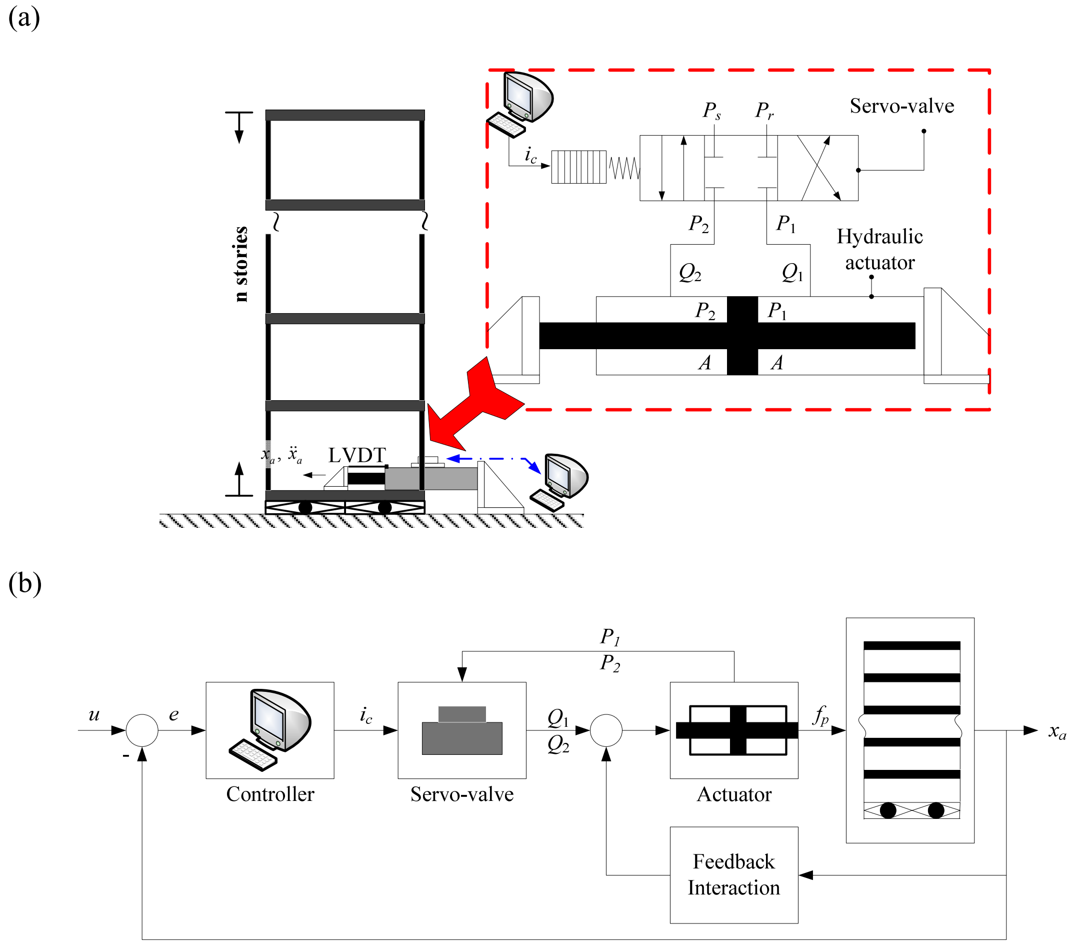

Figure 4.3. (a) Illustration of the servo hydraulic actuator and (b) the schematic block diagram of servo hydraulic actuator.

4.3.1 Servo-valve

As mentioned before, the spool in a servo-valve controls the flow paths and the flow rates. The opening displacement x_v of the spool determines the flow passage and volumes from the pump to the hydraulic actuator and depends on the command i_c. Typically, this displacement is a linear function of i_c for very low frequencies. However, a first-order model is more appropriate for a dynamic problem which is focused on the frequency up to 50 Hz (Carrion and Spencer 2007).

For example, considering a time constant τ_v for the servo-valve, the first-order system of the servo-valve is given by

$$\tau_v \dot{x}_v = -x_v + k_v i_c \tag{4.7}$$

where k_v is the valve gain. Since all servo-valves used in this research are manufactured by Moog (2011), the transfer function (see Figure 4.4) from the command to the spool displacement documented in the specification approximately performs a first-order system in the range of 0-50 Hz.

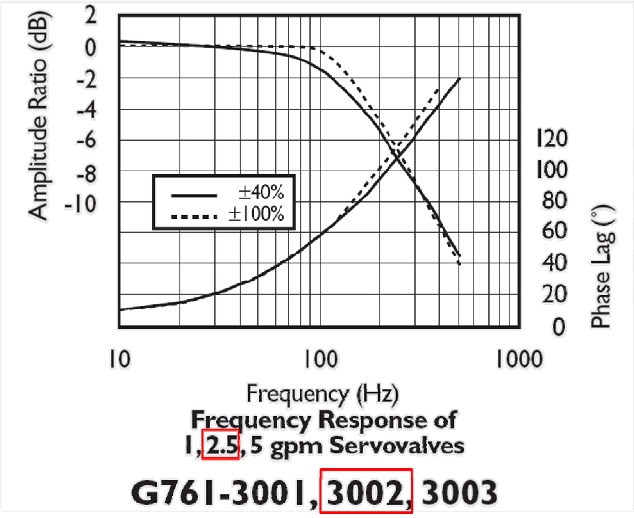

Figure 4.4. Servo-valve frequency response (Moog 2011).

The flow characteristics of the servo-valve, such as the relationship among the spool displacement, the controlled flow, and the pressure drop across the load are given by the flow equation (Merritt 1967) as

$$Q_1 = k_{q1} x_v \sqrt{\Delta P_1},\ \Delta P_1 = \begin{cases} P_s - P_1, & \text{when } x_v > 0 \\ P_1 - P_r, & \text{when } x_v < 0 \end{cases}$$
$$Q_2 = k_{q2} x_v \sqrt{\Delta P_2},\ \Delta P_2 = \begin{cases} P_2 - P_r, & \text{when } x_v > 0 \\ P_s - P_2, & \text{when } x_v < 0 \end{cases} \tag{4.8}$$

where Q_1 and Q_2 are the supplied flow rate to the forward chamber and the return flow rate of the return chamber, respectively; k_{q1} and k_{q2} are the flow gain coefficients of the servo-valve, in which the coefficients are typically a function of fluid density, the rate of change of the orifice area with the spool displacement, and the discharge of the valve orifices; P_1 and P_2 are the pressures inside the two chambers of the cylinder; P_s and P_r are the supplied pressure from the pump and the reference pressure, respectively. Assume that the spool is always moving around $x_v = 0$ and the acting forces at both sides of the piston are close to each other such that $P_1 A \approx P_2 A$, and then the nonlinear Eq. (4.8) can be simplified to a linear equation given by

$$\begin{aligned} Q_1 &= k_{q1}^* x_v - k_{c1}^* P_1 \\ Q_2 &= k_{q2}^* x_v + k_{c2}^* P_2 \end{aligned} \tag{4.9}$$

where k_{q1}^* and k_{q2}^* are the modified valve flow gains and k_{c1}^* and k_{c2}^* are the modified flow-pressure gains of the servo-valve. This equation is only valid for the operation of the servo-valve near the origin position ($x_v = 0$), but other applications might need to derive different functions for the flow rates.

4.3.2 Hydraulic actuator

A hydraulic actuator converts the hydraulic energy into mechanical forces or motions. To correctly describe the actuator behavior, the dynamics of the actuator need to be separately considered for both chambers. The position of the piston is determined by the equilibrium of the pressures in the two chambers with the additional pressure produced by the control load. The differential flow caused by the servo-valve moves the piston until the pressures are balanced. Therefore, the simple mechanism, which changes the pressures of the two chambers, can relocate the piston and then generate the corresponding force.

To represent the behavior of a double-rod hydraulic actuator as shown in Figure 4.3(a), the continuity equation is employed to portray the actuator dynamics for both chambers, given by

$$\begin{aligned} \frac{V_1}{\beta_e}\dot{P}_1 &= -A\dot{x}_a - C_t\left(P_1 - P_2\right) + Q_1 \\ \frac{V_2}{\beta_e}\dot{P}_2 &= A\dot{x}_a + C_t\left(P_1 - P_2\right) - Q_2 \end{aligned} \tag{4.10}$$

with

$$\begin{aligned} V_1 &= V/2 + Ax_a \\ V_2 &= V/2 - Ax_a \end{aligned}$$

where V_1 and V_2 are the control volumes of the first and second chambers, respectively; β_e is the effective bulk modulus; V is the initially total chamber volumes; x_a and $\dot{x}_a$ are the displacement and the velocity of the actuator head (i.e., the values are exactly same as the translational displacements and velocities of the isolated buildings at the free-end locations of the actuators in this research); C_t is the internal leakage coefficient of the piston. In Eq. (4.10), the external leakages to the reference tank are not considered. Hence, the force generated by the actuator piston, f_p, is given by

$$f_p = P_1A - P_2A + F_c\left(\dot{x}_a\right) \tag{4.11}$$

where F_c is the friction force as a function of the velocity. Due to the low-friction seals around the piston, this term of the friction force is negligible. As a result, the force acting on the control load only depends on the differential pressures on the both sides of the piston.

4.3.3 Servo controller

Hydraulic actuators are intrinsically unstable when the servo-valve is commanded without any controllers. Typically, the actuators have a difficulty achieving the desired position using the open-loop control, i.e., directly assigning the input commands for the servo-valve. Alternatively, a feedback loop using the error signal, *e*, works well when considering the measured displacements as one component of inputs such that

$$e = u - x_a \tag{4.12}$$

This error signal may be directly sent to the servo-valve; however, the displacement control may not perform effectively. One well-known control algorithm based on this closed-loop system, namely the proportional-integral-derivative (PID) control, is usually adopted in the actuator's control loop, given by

$$i_c = K_P e + K_I \int e dt + K_D e \tag{4.13}$$

where K_P, K_I, and K_D are the proportional, integral, and derivative gains, respectively.

The PID control in Eq. (4.13) should employ different gain values in different applications. For example, conventional pseudo-dynamic testing usually includes both proportional and integral gains for the servo controller, in order to reach the target displacement without overshooting. However, when considering a real-time dynamic problem (e.g., the active isolation problem in this research), only the proportional and derivative gains should be considered. In comparing these two problems, the integral gain slowly reaches the desired displacement as close to the target as possible, but in the mean time, the slow process would introduce a sufficient time lag which may not be adequate in the real-time applications. Furthermore, increasing the proportional gain would produce the response more quickly, while a large proportional gain may produce instability to the entire system. If the assigned proportional gain gives the response of oscillation around the target, an appropriate derivative gain can be employed to damp out the oscillation. To conclude, when considering the PID control for real-time applications such as the active isolation systems, only the proportional gain should be determined, while the derivative gain may be tuned if necessary.

4.3.4 Modeling of active isolation systems

After obtaining the equilibrium of forces on the piston, the system of one double-rod actuator is combined from Eqs. (4.7) - (4.13) given by

$$\begin{aligned} \begin{bmatrix} \dot{P}_1 \\ \dot{P}_2 \\ \dot{x}_v \end{bmatrix} &= \mathbf{A}_a \begin{bmatrix} P_1 \\ P_2 \\ x_v \end{bmatrix} + \mathbf{A}_i \begin{bmatrix} x_a \\ \dot{x}_a \end{bmatrix} + \mathbf{B}_a u + \boldsymbol{\varepsilon} \\ f_a &= \mathbf{C}_a \begin{bmatrix} P_1 \\ P_2 \\ x_v \end{bmatrix} \end{aligned} \tag{4.14}$$

with

$$\mathbf{A}_a = \begin{bmatrix} -\frac{2C_t\beta_e}{V} - \frac{2k_{c1}^*\beta_e}{V} & \frac{2C_t\beta_e}{V} & \frac{2k_{q1}^*\beta_e}{V} \\ \frac{2C_t\beta_e}{V} & -\frac{2C_t\beta_e}{V} - \frac{2k_{c2}^*\beta_e}{V} & -\frac{2k_{q2}^*\beta_e}{V} \\ 0 & 0 & -\frac{1}{\tau_v} \end{bmatrix},\ \mathbf{A}_i = \begin{bmatrix} 0 & -\frac{2A\beta_e}{V} \\ 0 & \frac{2A\beta_e}{V} \\ -\frac{k_v K_P}{\tau_v} & 0 \end{bmatrix},\ \mathbf{B}_a = \begin{bmatrix} 0 \\ 0 \\ \frac{k_v K_P}{\tau_v} \end{bmatrix},$$

$$,\ \mathbf{C}_a = \begin{bmatrix} A_1 & -A_2 & 0 \end{bmatrix}$$

$$\mathbf{x}_a = \begin{bmatrix} P_1 & P_2 & x_v \end{bmatrix}^T$$

where $\mathbf{x}_a$ is the state of the actuator and this equation represents the linearization of the actuator's behavior in accordance with the small movement at the actuator head such that $x_a \to 0$. Assuming this small movement, the dynamic chamber volumes are assumed to be static, i.e.,

$V_1 = V_2 = V/2$. According to Eq. (4.14), the linearized model of the actuator is formed as a function of the command and the control-structure interaction (e.g., the displacement and velocity of the piston or the control load).

To compare Eq. (4.14) to the 2nd-order actuator model in the work of Carrion and Spencer (2007), this 2nd-order model may be a special case for estimating the actuator parameters used in this research. Consider, for example, equal valve flow gains and flow-pressure gains for two chambers in Eq. (4.14). This equation can then be reduced to a two-state problem; i.e., the state vector is equal to $\begin{bmatrix} P_1 - P_2 & x_v \end{bmatrix}^T$, as seen in Carrion and Spencer (2007). Furthermore, if Eq. (4.7) is modified to a linear function (i.e., $x_v = k_v i_c$), the two-state problem will simplified to only one state, $P_1 - P_2$, as formulated in Dyke et al. (1995). According to these approximations, the order of the model for the double-rod actuator ranges from 1 to 3, which results in the poor to good accuracy, respectively.

Considering the model of the actuator with the interaction of the control load, the active isolation system can be obtained from Eqs. (4.5) and (4.14), given by

$$\bar{\mathbf{M}}\begin{bmatrix} \ddot{\mathbf{x}}_s \\ \ddot{\mathbf{x}}_b \end{bmatrix} + \bar{\mathbf{C}}\begin{bmatrix} \dot{\mathbf{x}}_s \\ \dot{\mathbf{x}}_b \end{bmatrix} + \bar{\mathbf{K}}\begin{bmatrix} \mathbf{x}_s \\ \mathbf{x}_b \end{bmatrix} = \begin{bmatrix} \mathbf{0} \\ \mathbf{b} \end{bmatrix}\mathbf{f}_a - \bar{\mathbf{M}}\begin{bmatrix} \mathbf{\Gamma} \\ \mathbf{\Gamma}^* \end{bmatrix}\ddot{\mathbf{x}}_g \tag{4.15}$$

with

$$\mathbf{b} = \begin{bmatrix} \mathbf{b}_{x1} & \mathbf{b}_{x2} & \mathbf{b}_{y} \end{bmatrix},\ \mathbf{f}_a = \begin{bmatrix} f_{a,x1} & f_{a,y} & f_{a,y} \end{bmatrix}^T$$

where **b** is a matrix of the actuators' force distribution, and $\mathbf{f}_a$ represents three actuators' forces. Due to the different behaviors of the three actuators, the parameters in Eq. (4.14) for the actuators should naturally be different. Thus, all parameters and variables associated with the three different actuators are not redefined in the equations but are only represented with different subscripts. To represent the active isolation systems in the state-space form, the original system in Eq. (4.6) is augmented to include the actuator model and the terms of the control-structure interaction in Eq. (4.14), given by

$$\begin{aligned}\dot{\mathbf{x}} &= \mathbf{A}\mathbf{x} + \mathbf{B}\mathbf{u} + \mathbf{E}\ddot{\mathbf{x}}_g \\ \mathbf{y} &= \mathbf{C}\mathbf{x} + \mathbf{v}\end{aligned} \tag{4.16}$$

with

$$\mathbf{A} = \begin{bmatrix} \mathbf{A}_p & \bar{\mathbf{M}}^{-1}\mathbf{b}_{x1} & \bar{\mathbf{M}}^{-1}\mathbf{b}_{x2} & \bar{\mathbf{M}}^{-1}\mathbf{b}_{y} \\ \mathbf{A}_{i,x1}\mathbf{T}_{x1} & \mathbf{A}_{a,x1} & \mathbf{0} & \mathbf{0} \\ \mathbf{A}_{i,x2}\mathbf{T}_{x2} & \mathbf{0} & \mathbf{A}_{a,x2} & \mathbf{0} \\ \mathbf{A}_{i,y}\mathbf{T}_{y} & \mathbf{0} & \mathbf{0} & \mathbf{A}_{a,y} \end{bmatrix},\ \mathbf{B} = \begin{bmatrix} \mathbf{0} & \mathbf{0} & \mathbf{0} \\ \mathbf{B}_{a,x1} & & \\ & \mathbf{B}_{a,x2} & \\ & & \mathbf{B}_{a,y} \end{bmatrix},\ \mathbf{E} = \begin{bmatrix} \mathbf{E}_p \\ \mathbf{0} \\ \mathbf{0} \\ \mathbf{0} \end{bmatrix}$$

$$\mathbf{x} = \begin{bmatrix} \mathbf{x}_p^T & \mathbf{x}_{a,x1}^T & \mathbf{x}_{a,x2}^T & \mathbf{x}_{a,y}^T \end{bmatrix}^T,\ \mathbf{u} = \begin{bmatrix} u_{x1} & u_{x2} & u_y \end{bmatrix}^T$$

$$\begin{bmatrix} x_{b,x1} \\ \dot{x}_{b,x1} \end{bmatrix} = \mathbf{T}_{x1}\mathbf{x}_p,\ \begin{bmatrix} x_{b,x2} \\ \dot{x}_{b,x2} \end{bmatrix} = \mathbf{T}_{x2}\mathbf{x}_p,\ \begin{bmatrix} x_{b,y} \\ \dot{x}_{b,y} \end{bmatrix} = \mathbf{T}_{y}\mathbf{x}_p$$

where the displacements and the velocities of the actuators' heads are exactly the same as those of the buildings at the same locations, i.e., $x_{a,y} = x_{b,y}$, $\dot{x}_{a,y} = \dot{x}_{b,y}$. All subscripts, $x1$-, $x2$-, and y, indicate the actuators as well as the directions. In the matrix, **C**, in Eq. (4.16) the measurements vary. For example, if the measurement output, **y**, contains the absolute accelerations of all floors and the base, the matrix, **C**, should have the partial components of $\bar{\mathbf{M}}^{-1}\mathbf{b}_{x1}$, $\bar{\mathbf{M}}^{-1}\mathbf{b}_{x2}$, and/or $\bar{\mathbf{M}}^{-1}\mathbf{b}_{y}$. Using Eq. (4.16), the active isolation systems with the control-structure interaction is completed by modeling in the time domain for the setup shown in Figure 4.1.

In addition to representing the active isolation systems in time domain, these systems can also be interpreted in the frequency domain, such as the transfer functions using the Laplace transform or the Fourier transform from the time-domain model. The frequency-domain representation can provide the comparison of the modal contributions from all modes, check the actuator behavior in a specific frequency range, and identify the changes in the pole locations and the phases when changing the variables in a system, etc. Furthermore, the frequency-domain models form a system intuitively from the loop, as shown in Figure 4.3(b). Hence, the frequency-domain model can help explain the system behavior as well as characterize the system dynamics.

Before deriving the active isolation systems in the frequency-domain, the minimal realization is introduced in order to address the difference of modeling in the time and frequency domains. The minimal realization is defined as the system that has a minimum number of controllable and observable states, while the system derived from the transfer functions often duplicates the poles (e.g., more than a pair of complex modes). When the system is obtained from the frequency-domain approach and then realized in the state-space representation, the redundant modes should be cancelled.

The active isolation systems are also derived from the frequency-domain approach in order to understand the contributions from the actuators. Instead of using the loop to form the actuators, the transfer function of the actuator based on Eq. (4.14) is first introduced in the *s*-domain from the Laplace transform (i.e., $s = i\omega$, where $i\omega$ is the complex frequency for the Fourier transform and *s* is the variable for the Laplace transform), given by

$$\mathbf{H}_{f_a\{u,x_a,\dot{x}_a\}}(s) = \left[h_{f_a u}(s) \quad h_{f_a x_a}(s) \quad h_{f_a \dot{x}_a}(s) \right] = \mathbf{C}_a \left(s\mathbf{I} - \mathbf{A}_a \right)^{-1} \left[\mathbf{B}_a \quad \mathbf{A}_i \right] \tag{4.17}$$

where $\mathbf{H}_{f_a\{u,x_a,\dot{x}_a\}}$ denotes the transfer function matrix from all inputs (e.g., *u*, x_a, $\dot{x}_a$) to the actuator force. Note that the transfer functions always use $\mathbf{H}_{ij}$ or h_{ij} to define the transfer function matrices (or vectors) and the transfer functions from the input *j* to the output *i*, respectively. Considering the transfer functions of the isolated building, Eqs. (4.6) and (4.15) are reused to develop the transfer functions from the actuator inputs and the ground excitations to the structural displacements and velocities, given by

$$\mathbf{H}_{\mathbf{x}_p\{\mathbf{f}_a,\ddot{\mathbf{x}}_g\}}(s)=\begin{bmatrix}\mathbf{H}_{\mathbf{x}_p\mathbf{f}_a}(s) & \mathbf{H}_{\mathbf{x}_p\ddot{\mathbf{x}}_g}(s)\end{bmatrix}=\left(s\mathbf{I}-\mathbf{A}_p\right)^{-1}\begin{bmatrix}\begin{bmatrix}\mathbf{0}\\ \mathbf{b}\end{bmatrix} & \mathbf{E}_p\end{bmatrix} \tag{4.18}$$

Therefore, by integrating Eqs. (4.17) and (4.18), the active isolation systems represented in the frequency-domain are derived as

$$\mathbf{H}_{\mathbf{y}\{\mathbf{u},\ddot{\mathbf{x}}_g\}}(s)=\begin{bmatrix}\mathbf{H}_{\mathbf{yu}}(s) & \mathbf{H}_{\mathbf{y}\ddot{\mathbf{x}}_g}(s)\end{bmatrix} \tag{4.19}$$

with

$$\mathbf{H}_{\mathbf{yu}}(s)=\mathbf{C}_p\left(\mathbf{I}-\mathbf{H}_{\mathbf{x}_p\mathbf{f}_a}(s)\mathbf{H}_{\mathbf{f}_a\mathbf{x}^*}(s)\mathbf{T}\right)^{-1}\mathbf{H}_{\mathbf{x}_p\mathbf{f}_a}(s)\mathbf{H}_{\mathbf{f}_a\mathbf{u}}(s) \tag{4.20}$$

$$\mathbf{H}_{\mathbf{y}\ddot{\mathbf{x}}_g}(s)=\mathbf{C}_p\left(\mathbf{I}-\mathbf{H}_{\mathbf{x}_p\mathbf{f}_a}(s)\mathbf{H}_{\mathbf{f}_a\mathbf{x}^*}(s)\mathbf{T}\right)^{-1}\mathbf{H}_{\mathbf{x}_p\ddot{\mathbf{x}}_g}(s) \tag{4.21}$$

$$\mathbf{x}^*=\begin{bmatrix}x_{b,x1} & \dot{x}_{b,x1} & x_{b,x2} & \dot{x}_{b,x2} & x_{b,y} & \dot{x}_{b,y}\end{bmatrix}=\mathbf{T}\mathbf{x}_p=diag\left(\mathbf{T}_{x1} \quad \mathbf{T}_{x1} \quad \mathbf{T}_{y}\right)\mathbf{x}_p$$

$$\mathbf{H}_{\mathbf{f}_a\mathbf{x}^*}=diag\left(\begin{bmatrix}h_{f_{a,x1}x_{b,x1}} & h_{f_{a,x1}\dot{x}_{b,x1}}\end{bmatrix} \begin{bmatrix}h_{f_{a,x2}x_{b,x2}} & h_{f_{a,x2}\dot{x}_{b,x2}}\end{bmatrix} \begin{bmatrix}h_{f_{a,y}x_{b,y}} & h_{f_{a,y}\dot{x}_{b,y}}\end{bmatrix}\right)$$

$$\mathbf{H}_{\mathbf{f}_a\mathbf{u}}=diag\left(h_{f_{a,x1}u_{x1}} \quad h_{f_{a,x2}u_{x2}} \quad h_{f_{a,y}u_{y}}\right)$$

where **y** is the measurement output with respect to the states of Eq. (4.6); *diag*($*$) denotes a diagonal matrix of the entries in which the diagonal can be rectangular. Again, $x1$-, $x2$-, and y-denote either the actuators or the measurements. When the transfer functions appear to be the inverse functions, e.g., Eqs. (4.20) and (4.21), the feedback loops and the control-structure interactions are implied in the transfer functions. As mentioned before, using Eq. (4.19) to realize the state-space model as Eq. (4.16) may not be minimal. Alternatively, Eq. (4.19), which has a minimal realization approach, can give an exact equation of Eq. (4.16).

4.3.5 Effect of servo hydraulic actuators

As mentioned in Sections 4.3.1 – 4.3.3, a servo hydraulic actuator contains the complex dynamics in both the servo-valve and the hydraulic actuator. Many of the nonlinear features in the actuators are approximated in the linearization or neglected with reasonable consideration. Aside from the nonlinear nature, the actuators also have a large extent of model uncertainties, which can be categorized as parametric uncertainties and uncertain nonlinearities. For example, the parametric uncertainties include the large variations of the bulk modulus due to the change of temperature and component wear, while the uncertain nonlinearities include the leakage or the friction which cannot be modeled exactly or does not have the nonlinear functions to describe. Moreover, the modeling technique in this research is based on the linear approach to develop the full model for the active isolation systems. The applicable range of the actuators through the linear approach would be limited; however, the performance of the linear approach would be guaranteed within a certain range of frequencies and movements. Through the system identification technique, a model of the actuators can deliver a high performance for the control applications if the identified model has the same form of the linearized model, i.e., the identified model has the same number of states as (4.16).

The actuator capacity would limit the performance in a control application. As mentioned in Section 3.3, different sizes of actuators in comparison of the isolated building weights are discussed. In Eqs. (4.10) and (4.11), the acting force is proportional to the working area. The large force would be generated because of the large working area, when the response of the actuator piston is small. In addition to the working area, the volumes of the chambers are key to the actuator's performance. When the supplied pressure and the supplied flow rate remain in certain values, the actuator, with small chambers, can respond to the command more quickly than to the one with large chambers. Moreover, the large stroke would allow the actuator to have more movement for a specific application, such as the active isolation. Ideally, the actuators for the active isolation system should feature a relatively small working area and chambers and a relatively large stroke.

Section 4.3 has addressed that when working with the servo controller only the proportional gain in the PID control is often employed for the real-time applications. Typically, before applying any control strategies on the actuators, a tuning process needs to be applied. The tuning process is used to assign an adequate value for the proportional gain by the trial-and-error method. An adequate proportional gain is determined when the actuator can achieve the step function as quickly as possible without overshooting too much. After the tuning process, the actuator can be then used in the real-time applications. The small proportional gain would usually soften the actuator's behavior, while the large one, as previously mentioned, would introduce instability into the system. Therefore, the tuning process should be conducted carefully and appropriately, and each application (i.e., when the control object is changed) may assign a specifically proportional gain.

Since the actuator has the inherently complex nonlinearity, the linear range in the frequency domain may vary case by case. A well-fabricated actuator with a high-performance servo-valve can extend the linear frequency range with respect to the load. The heavy load often requires more pressure inside the chambers of the actuator, and meanwhile, the linear frequency range would be decreased. If the control application is aimed at a very flexible structure, the actuator needs more stroke extending to reach the force balance, resulting in lower control performance. Before employing an actuator for real-time applications, the range for the linear control should be recognized in order to ensure a certain level of performance. Note that sometimes the higher proportional gain may solve the problem but may additionally introduce an instability problem.

4.4 Example: active isolation system of the two-story building

This section presents the active isolation system of the two-story building using the derived equations (4.16) and (4.19), in comparison with the experimental transfer functions. Although this research does not discuss the employment of the system identification to obtain the model until the next chapter, the modeling results provided in this section would help determine the number of poles (or states) and zeros for the system identification. To compare the performance of this linear model, other models, i.e., the model with only one state in Dyke et al. (1995) and the model with two states in Carrion and Spencer (2007), are also examined for this active isolation system. The details of the identified model and the experimental transfer functions will be provided in Chapter 5.

First, the model of the passive isolated building is derived from the structural properties and the linearized model of the bearings. In order to reduce the complexity, the lumped-mass model for the building, as in Eq. (4.1), is employed to develop the active isolation system. The mass matrix has every diagonal entry equal to 360 lbs, while the stiffness matrix is derived from the properties of high strength steels and the column dimensions listed in Table 3.1. The damping matrix of the building is obtained using the modal damping, equal to 1%. Due to the setup of sensors, only the base displacement and all floor accelerations including the base are selected in the measurement outputs, such as the vector **y** in Eq. (4.6). Moreover, because the sensors are placed along the center of the *y*-direction, the lumped-mass model only considers the translational degrees of freedom. Again, the linearized model of bearings employs Eq. (4.3), while only the force in the *y*-direction is considered in this section. As a result, the state-space model of the passive isolated building, which can be also represented as a transfer function of $\mathbf{H}_{\mathbf{y}\ddot{x}_{g,y}}$, has three states as shown in Figure 4.5. Because the structure is a low-rise building which usually behaves with shear-type, lateral dynamics, the numerical model shown in this figure performs closely to the experimental results in comparison with the transfer functions from the ground excitation (or the acceleration of the shake table) to the floor accelerations.

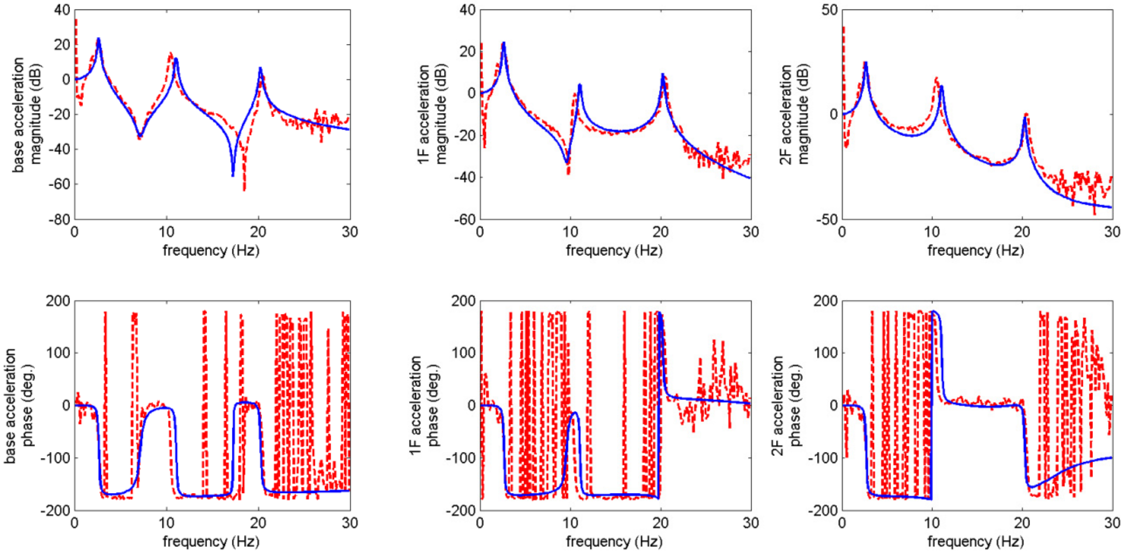

Figure 4.5. Comparison between the transfer functions of the isolated two-story building from the experiment (dash line) and the numerical model (solid line).

After the passive isolated building in the *y*-direction is determined with its numerical model, the active isolation system for this building can be modeled using the derived equations and compared with the other model proposed in the previous studies. The main objective for developing the model for the active isolation systems is to understand the number of states, the associated numbers of poles and zeros, and the effect of actuators on the performance of the isolated building. Thus, the same parameters, e.g., the numbers of poles and zeros, would be used in the system identification (described later in Chapter 5). According to Eq. (4.14), all parameters should be known in advance or obtained from the optimization process (e.g., the least-squares fitting over a time history); however, only the behavior of these models is concerned in this research in order to meet the objective. Therefore, the trial-and-error method is employed to obtain the model comparable to the experimental results. Figure 4.6 shows the results of the transfer functions of the base displacement and the base acceleration from (a) the actuator command and (b) the ground acceleration. As seen in this figure, the phase of the transfer functions from the numerical model performs closely to the experimental results, while the phases between the model and the experimental results produce a different behavior in the phase slopes. The magnitudes of the transfer functions from the numerical model are generally higher at high frequencies than the experiment results.

The model for the active isolation systems using Eq. (4.16) is also compared to the model developed in previous studies, such as the 1st-order model in Dyke et al. (1995) and the 2nd-order model Carrion and Spencer (2007). First, the 2nd-order model is introduced for the numerical model of the active isolation system. This model can be modified from Eq. (4.14) as

$$\begin{bmatrix} \dot{P}_1-\dot{P}_2 \\ \dot{x}_v \end{bmatrix} = \begin{bmatrix} -\dfrac{4C_t\beta_e}{V}-\dfrac{2k_c^*\beta_e}{V} & \dfrac{2k_q^*\beta_e}{V} \\ 0 & -\dfrac{1}{\tau_v} \end{bmatrix} \begin{bmatrix} P_1-P_2 \\ x_v \end{bmatrix} + \begin{bmatrix} 0 & -\dfrac{2A\beta_e}{V} \\ -\dfrac{k_vK_P}{\tau_v} & 0 \end{bmatrix} \begin{bmatrix} x_a \\ \dot{x}_a \end{bmatrix} + \begin{bmatrix} 0 \\ \dfrac{k_vK_P}{\tau_v} \end{bmatrix} u \tag{4.22}$$

$$f_a = \begin{bmatrix} A & 0 \end{bmatrix} \begin{bmatrix} P_1-P_2 \\ x_v \end{bmatrix}$$

where some compatible assumptions to Eq. (4.14) are made in this model, such as $k_c^* = k_{c1}^* = k_{c2}^*$ and $k_q^* = k_{q1}^* = k_{q2}^*$. After the 2nd-order model of actuators is derived, the active isolation system based on this actuator model is developed through the same procedure in Eq. (4.16). Figure 4.7 shows the results of the transfer functions for the base displacement and the base acceleration from (a) the input command of the actuator and (b) ground acceleration. In this figure, the phases from the experimental results and this numerical model are close to each other and are better than the transfer functions from the one using the 3rd-order state-space model for the actuator. The magnitudes of these transfer functions give the higher rolling-off rate at high frequencies.

Using the 1st-order state-space model to form the actuator (Dyke et al. 1995), the gain of the servo-valve becomes linear, resulting in another model of the actuator as

$$\begin{aligned}
\left[\dot{P}_1-\dot{P}_2\right] &= \left[-\frac{4C_t\beta_e}{V}-\frac{2k_c^*\beta_e}{V}\right]\left[P_1-P_2\right]+\left[\begin{matrix}-\frac{2k_q^*\beta_e k_v K_D}{V} & -\frac{2A\beta_e}{V}\end{matrix}\right]\left[\begin{matrix}x_a\\ \dot{x}_a\end{matrix}\right]+\left[\frac{2k_q^*\beta_e k_v K_D}{V}\right]u \\
f_a &= A\left[P_1-P_2\right]
\end{aligned} \qquad (4.23)$$

where the definition of all parameters is exactly the same as those in Eq. (4.22). Similar to the Figures 4.6 and 4.7, the comparison of the transfer functions of the experimental results and the numerical model are shown in Figure 4.8. This numerical model produces slightly poorer results in both magnitudes and phases. Since the trial-and-error method is employed for all cases, these three approaches for the active isolation system of the two-story building along the *y*-direction are acceptable to use in the system identification.

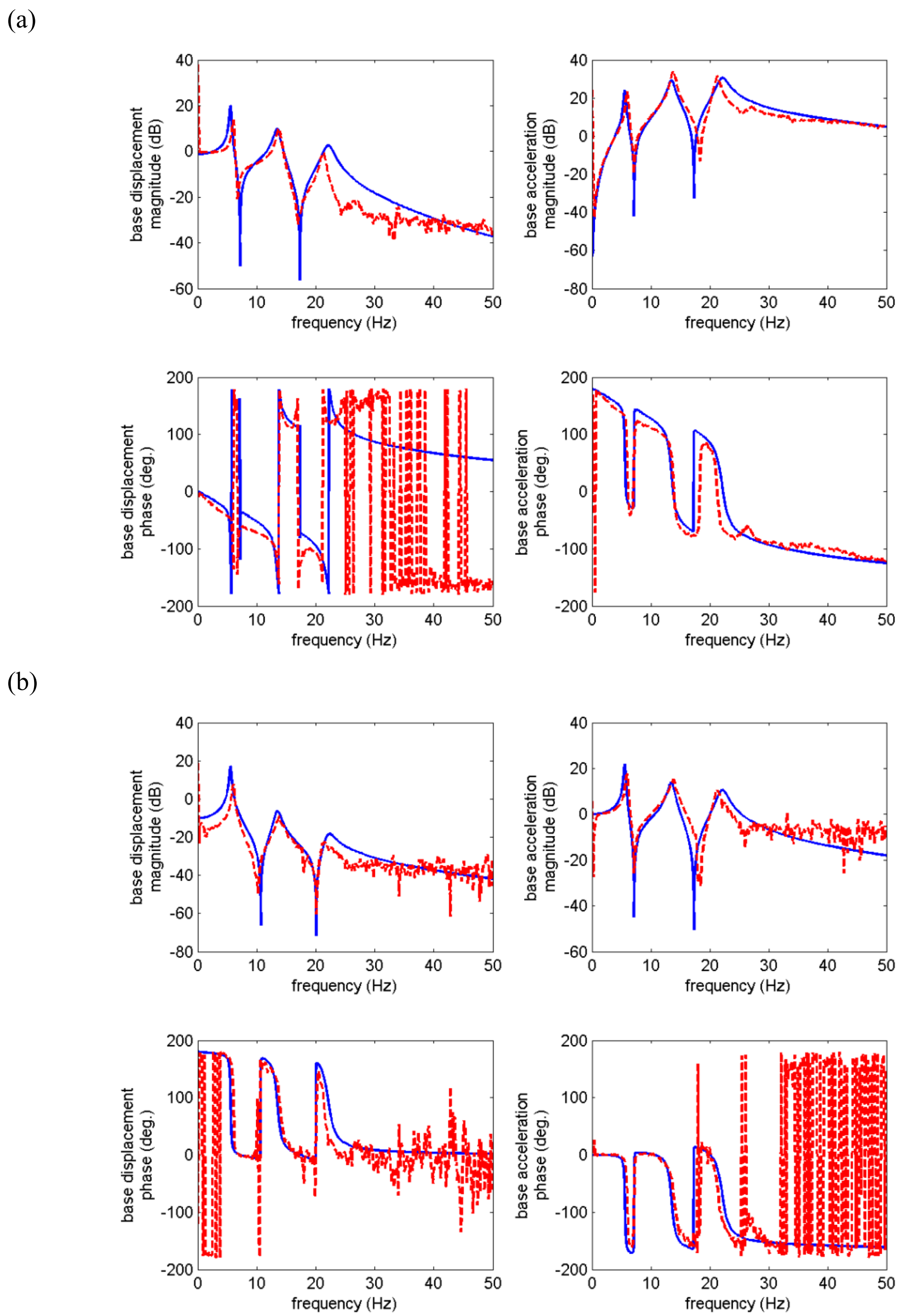

Figure 4.6. Comparison between the transfer functions of the experimental results (dash lines) and numerical model (solid line) using the 3rd-order actuator model.

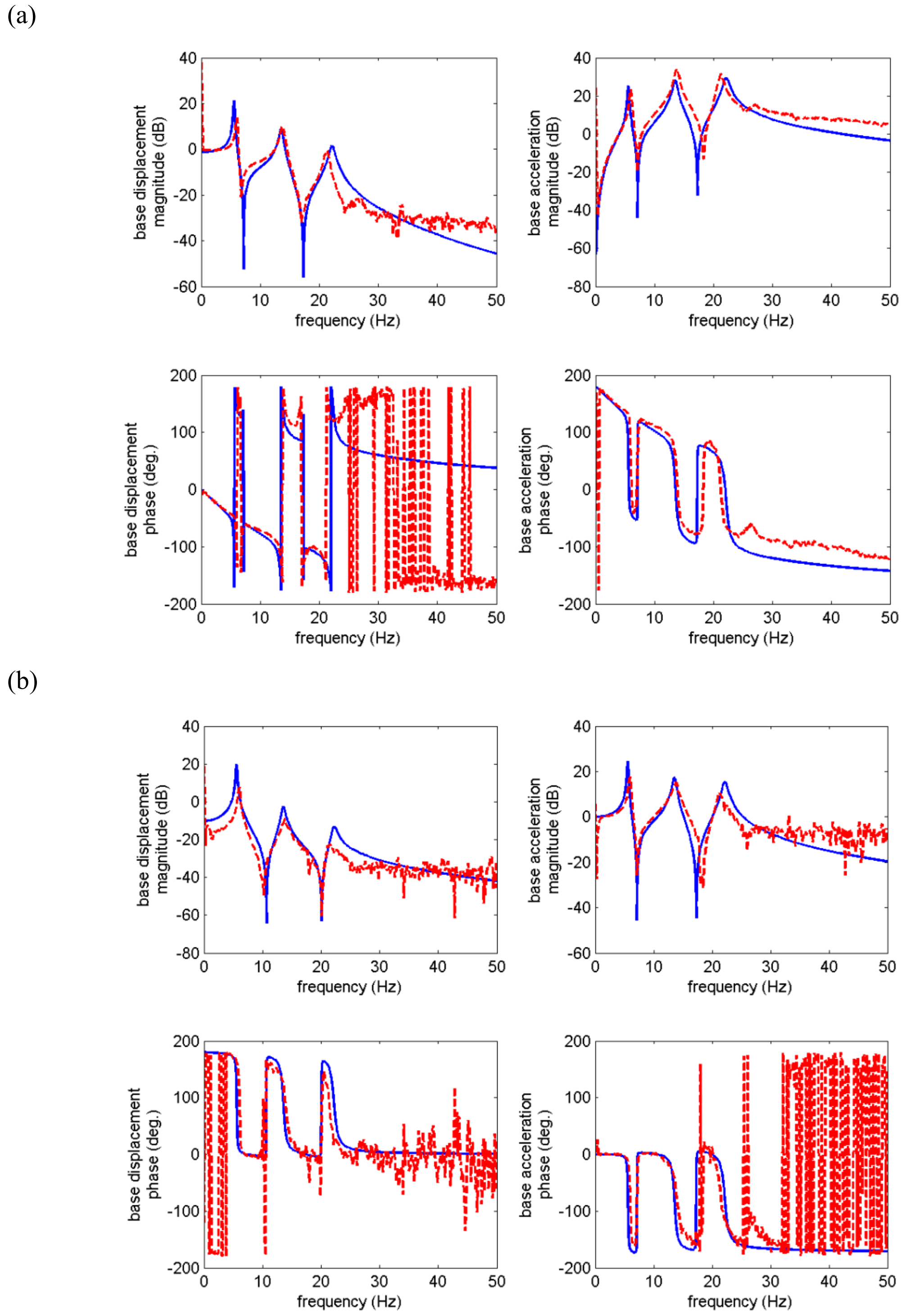

Figure 4.7. Comparison between the transfer functions of the experimental results (dash lines) and numerical model (solid line) using the 2nd-order actuator model.

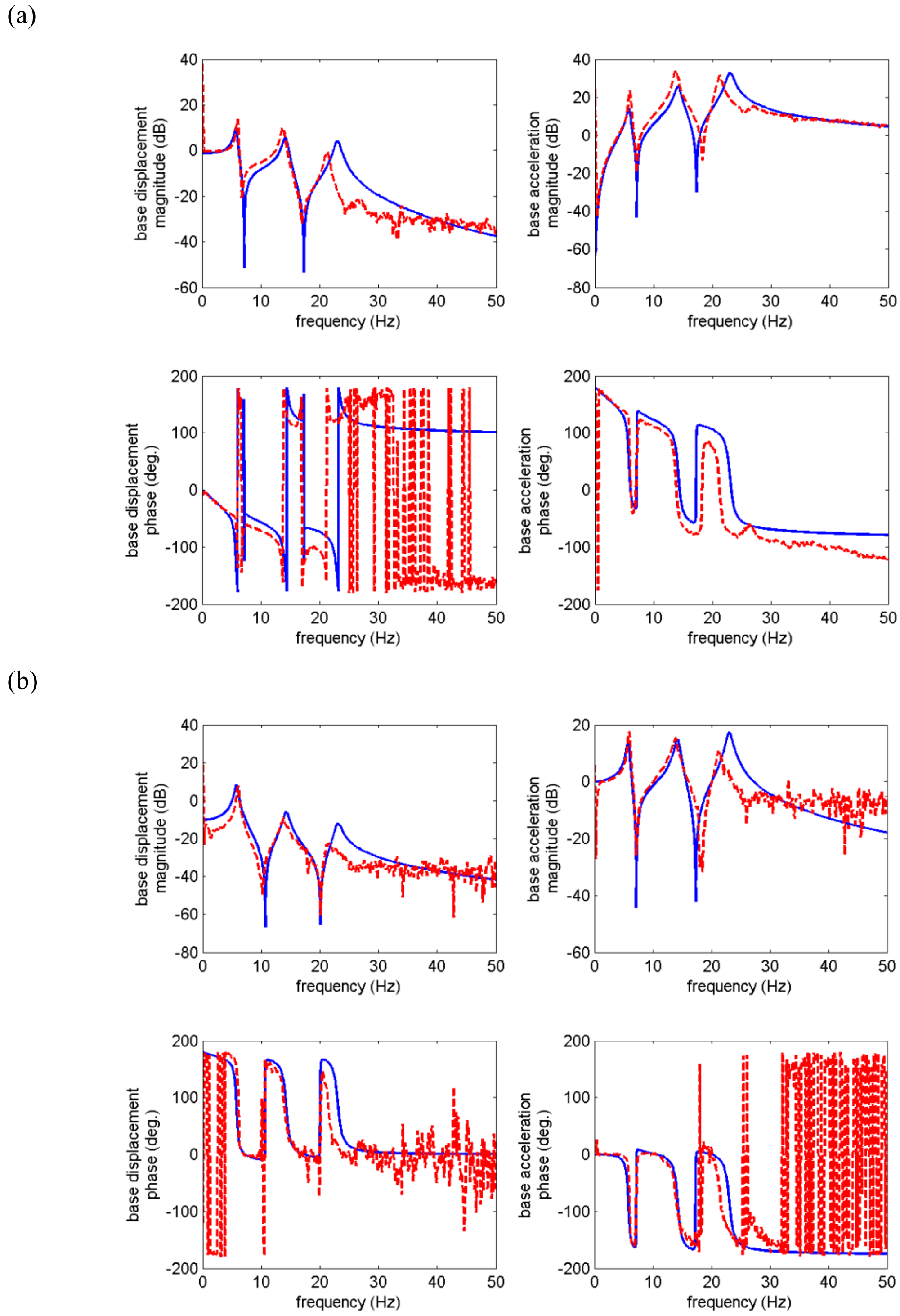

Figure 4.8. Comparison between the transfer functions of the experimental results (dash lines) and numerical model (solid line) using the 1st-order actuator model.

Because three models for the active isolation system of the two-story building are obtained through different actuator models, the parameters for each are listed in Table 4.1. Although these parameters exist in the theoretical relationship among models, i.e., the assumptions addressed in Eq. (4.22), the resulting model might have unstable behavior. For example, the model results in some unstable poles when using the physical mapping from the parameters in Eq. (4.14) to those in Eq. (4.22). Hence, this table shows the close relationship to the definition, while the slight difference is still illustrated amongst the individual cases.

Table 4.1. Parameters of the active isolation system model for the two-story building.

Parameter (Unit)	Actuator model		
	3^{rd}-order	2^{nd}-order	1^{st}-order
K_P (mA/in)	1	1	1
τ_v (ms)	5	6	Not applicable
k_{q1}^* / k_{q2}^* or k_q^* (in^3/s/mA)	22/18	10	10
k_{c1}^* / k_{c2}^* or k_c^* (in^3/s/psi)	25e-5/20e-5	2e-4	2e-4
k_v (mA/mA)	0.8	0.9	0.9
A (in^2)	0.2500	0.2500	0.2500
C_t (in^3/s/psi)	6e-4	1e-4	1e-4
V (in^3)	1.875	1.875	1.875
β_e (psi)	76800	115200	134400

As mentioned in Section 4.3.5, a large proportional gain for the servo controller may induce the instability problem. The model of the active isolation system using different proportional gains for the 3^{rd}-order actuator model is illustrated for the instability problem. Figure 4.9 shows the eigenvalues of the system matrix, e.g., the matrix **A** in Eq. (4.16), using the pole plot. If some eigenvalues are located at the region of positive real values, the system is intrinsically unstable. As a result, shown in Figure 4.9, some poles in the system model are shifted to the right when the proportional gain, K_P, is increased. Although the numerical model might incorrectly represent the system behavior, the poles will likely be unstable when increasing the proportional gain. Again, an adequately proportional gain should be tuned for the real-time applications.

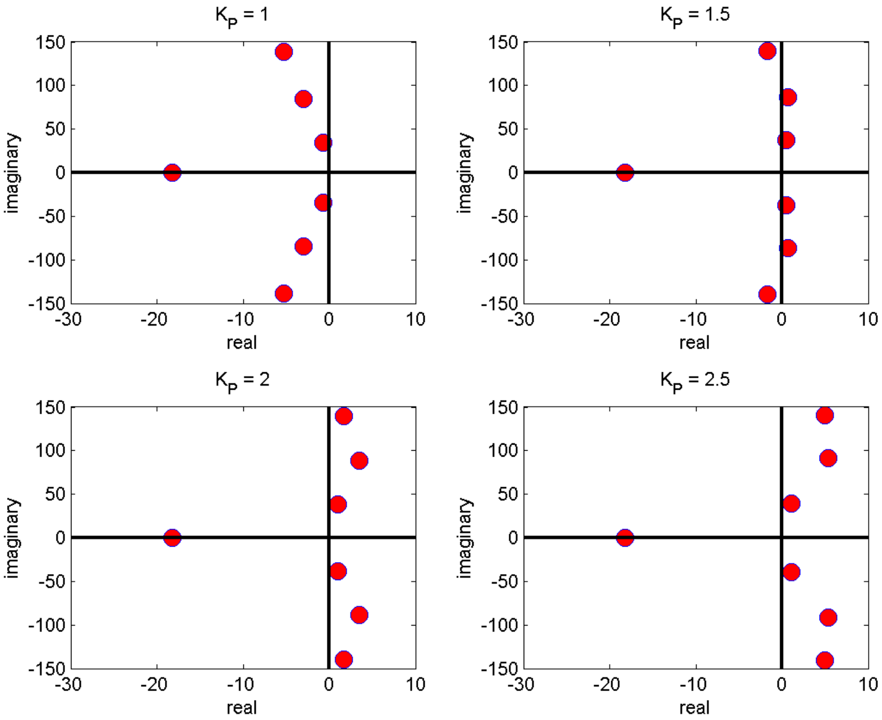

Figure 4.9. Illustration of an instability problem when tuning proportional gain.

4.5 Example: active isolation system of the six-story building

This section focuses on the numerical model for the active isolation system of the six-story building using different actuator models, such as Eqs. (4.14) and (4.22) – (4.23). Only the active isolation system in the *x*-direction is illustrated in this section. The primary objective is to investigate the difference between the experimental results and these numerical models, then determine the number of states as well as the numbers of poles and zeros. The model for the isolated building employs the same procedure as described in Section 4.4 for development. The parameters for both *x*-actuators adopt the values in Table 4.1 as a basis with some appropriate changes. Most of the changes in the parameters are due to the time constant in servo-valve decreasing with few milliseconds. Since the model in the *x*-direction has high complexity due to the torsion effect, some poles and zeros in this model may not match the experimental results. Through the observation of the magnitudes and the phases from transfer functions, the numbers of poles and zeros, which are adequate for the system modeling, can be determined for the active isolation system along the *x*-direction.

First, the model derived from the 3rd-order actuator model is investigated. Figure 4.10 shows the transfer functions of the base displacements and the second floor acceleration from the $x1$- and $x2$- actuator input commands (e.g., $\mathbf{H_{yu}}$ in Eq. (4.20)), as compared to the experimental results. Note that the base displacements and the second floor acceleration in the $x1$-direction are illustrated for the $x1$-acutator, while the same measurements in the $x2$-direction are illustrated for the $x2$-actuator. After comparing this with the transfer functions between the numerical model and the experiment, the results using the 3rd-order actuator model show good agreement in the phases, particularly the slopes in all transfer functions. Although some zeros and poles from the numerical model may not match the experimental results as mentioned before, the trend of the magnitude still represents the system acceptably.

The 2nd-order and 1st-order models for actuators are also investigated in order to determine the number of poles and zeros for the system identification. As the measurements are considered for the 3rd-order actuator model, the transfer functions of the same measurements are generated from these two actuator models for comparison. Figure 4.11 shows the results from the

2nd-order actuator model. The phases using this actuator model are decreased faster than the experimental results, while the magnitudes poorly represent the system at high frequencies. Similarly, Figure 4.12 presents the transfer functions from the 1st-order actuator model. The transfer functions from the numerical model misrepresent the system in both magnitudes and phases above 12 Hz. After investigating the active isolation system using different actuator models, only the 2nd-order and 3rd-order models for the actuators are similar to the system behavior in transfer functions. Although the 1st-order actuator model accurately represents the system for the active isolation system of two-story building in the *y*-direction, the complexity of the system creates challenges when employing this model for this active isolation system. While some poles and zeros in transfer functions for the cases using the 2nd-order and 3rd-order models of the actuators do not match the experimental results, the close behavior in phases would predict the success in obtaining the model using the system identification technique.

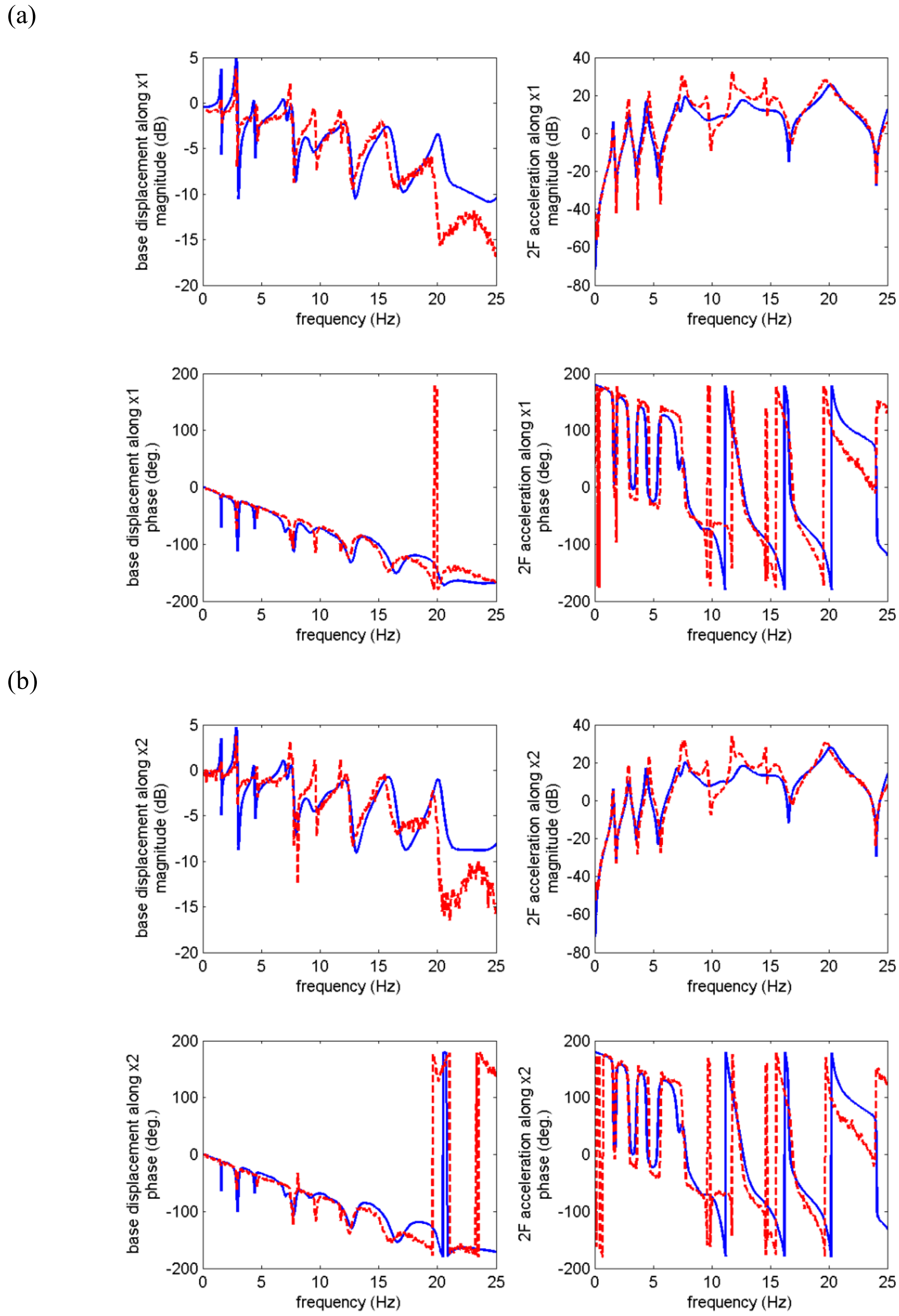

Figure 4.10. Comparison on transfer functions between experimental results (dash line) and numerical model (solid line) using 3rd-order actuator model from (a) *x*1-actuator and (b) *x*2-actuator.

(a)

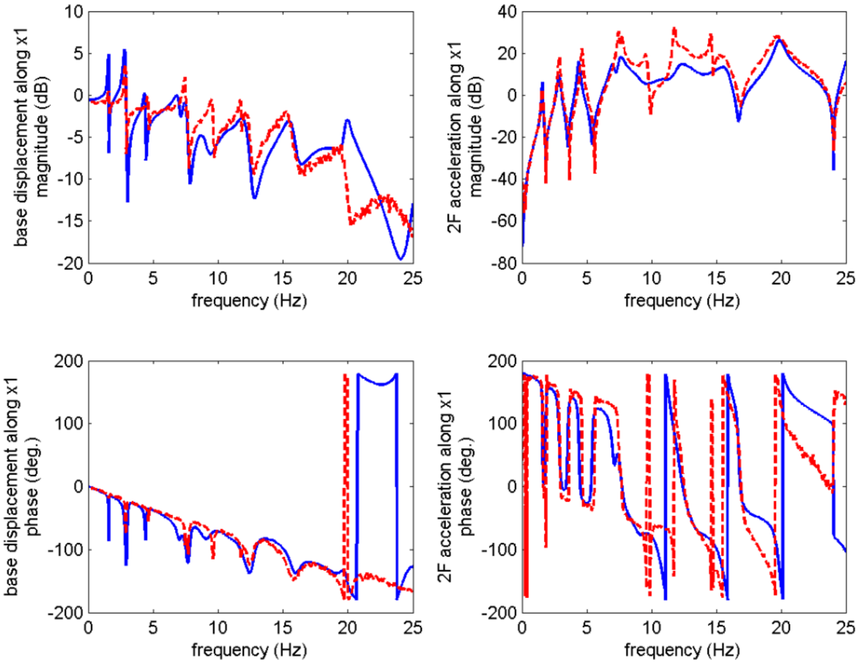

(b)

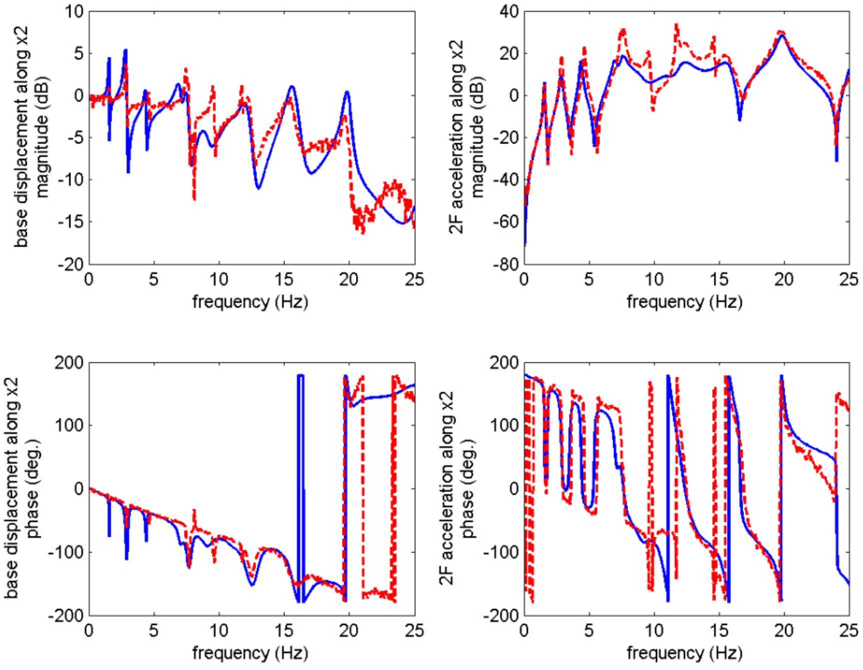

Figure 4.11. Comparison on transfer functions between experimental results (dash line) and numerical model (solid line) using 2nd-order actuator model from (a) *x*1-actuator and (b) *x*2-actuator.

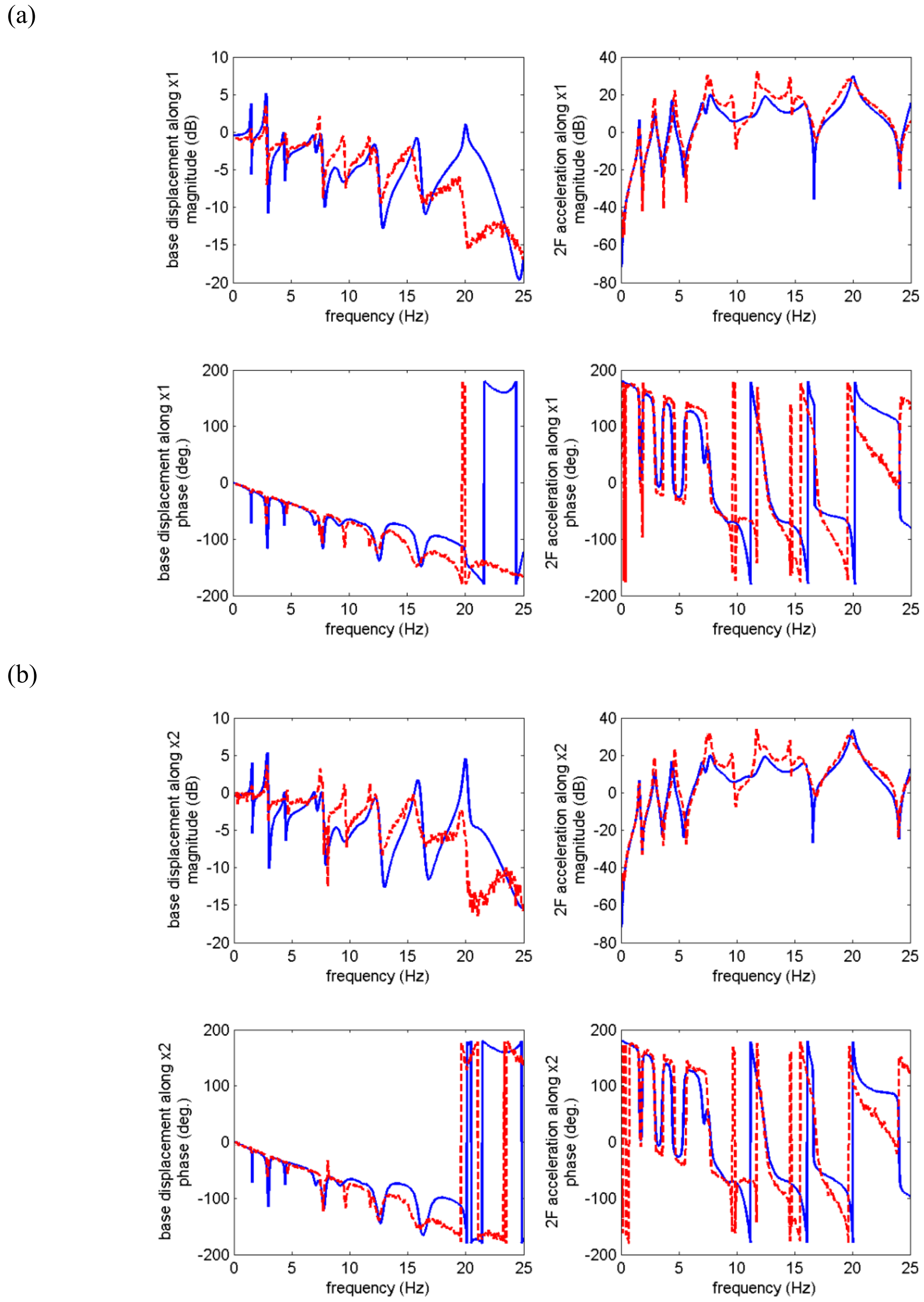

Figure 4.12. Comparison on transfer functions between experimental results (dash line) and numerical model (solid line) using 1st-order actuator model from (a) *x*1-actuator and (b) *x*2-actuator.

4.6 Summary

This chapter has modeled active isolation systems for buildings with the ball-n-cone bearings and the servo-valve hydraulic actuators. The buildings were simplified to the lump-mass, shear-type building models. The bearings were originally formulated from the nonlinear force equilibrium, while the model of the bearings for the isolated building employed the linear approach. A model of the double-rod, servo-controlled hydraulic actuators was developed to model the actuator dynamics as well as to construct the model of active isolation systems. A complete model of the active isolation systems was finally established using the linear approach for the bearings and the actuators. To illustrate the complexity of the system dynamics, two examples based on the active isolation systems for the two-story building and the six-story building were given. Consequently, the parameters of these two active isolation systems for the system identification were determined.

Since the objective in this chapter was the determination of parameters, e.g., the numbers of states, poles, and zeros, for use in system identification, the numerical models were developed to ensure these numbers. For example, due to the assumption of the shear-type buildings and the actuators' or sensors' locations, the numbers of states for the buildings are two times of the number of stories (e.g., $2 \times ns$ in Eq. (4.1)) for the y-direction and four times of the number of stories for the x-direction because of torsion. For the bearings, two states should be assigned for the y-direction, while the x-direction should have four states. As seen in Sections 4.4 and 4.5, the number of states in the actuator model varied case by case. The actuators for the two-story building have the number of states ranging from 1 to 3 for each actuator, while those for the six-story building should have at least two states. In addition, since the y-actuator is located at the center of gravity in the system and the sensors in the y-direction are placed along the center line of the building, the models of the active isolation systems can be divided into two parts, such that one is for the y-direction and the other is for the x-direction. As a result, one active isolation system should have $2(ns+1)+1 \sim 2(ns+1)+3$ states for the y-direction and $4(ns+1)+2 \sim 4(ns+1)+6$ states for the x-direction. Note that the number of poles is naturally equal to the number of states, but the number of zeros varies with the type of measurements and is determined directly from the numerical model itself.

CHAPTER 5 SYSTEM IDENTIFICATION

System identification is the critical issue in which a high-fidelity mathematical model is developed for use in control synthesis and analysis. As mentioned in Section 2.3.2, the system identification seeks to obtain a model describing the relationship between inputs and outputs, such as control device commands/ground accelerations and structural responses, respectively. This chapter presents the nonparametric system identification for the experimental transfer functions, in which both single-input and multi-output (SIMO) and multi-input and multi-output (MIMO) cases are introduced. Thus, the system identification technique that can identify the parameters for the numerical transfer functions (e.g., the MFDID technique in Kim et al. (1995)) is employed to identify the transfer functions for all SIMO systems with respect to all inputs. To quickly identify these SIMO systems, this research also provides the system identification approach for the discrete-time models. Due to the consideration of the minimal realization, the MIMO system is obtained by using the developed method from all SIMO system models. Two examples of the active isolation systems, the two-story building and the six-story building, are illustrated to employ the system identification procedure, resulting in the system models for the inputs of the actuator commands and the ground excitations. Finally, the identified models can then be used in the control design in Chapter 6.

5.1 Experimental transfer functions

In the identification of linear systems, the transfer functions are often used to portray the input/output behavior of the system in the frequency domain. Two experimental methods, the swept-sine and broadband approaches, are the fundamental methods used to obtain the nonparametric transfer functions. In this research, the broadband approach is employed to obtain the transfer functions because the swept-sine method barely reduces the measurement noise and requires more time than the broadband approach. Hence, the broadband approach is the experimental method primarily used to obtain the transfer functions from all inputs.

To determine the transfer functions using the broadband approach, the output responses are obtained from the input excitations over the frequency range of interest. The input excitations are basically stationary white noise; however, this type of noise cannot be generated experimentally. Instead, a band-limited white noise is employed to excite the systems. Thus, the transfer functions can be determined by the following equation as

$$\mathbf{G}_{\mathbf{yu}}(i\omega) = \mathbf{S}_{\mathbf{uu}}^{-1}(\omega)\mathbf{S}_{\mathbf{yu}}(\omega) \tag{5.1}$$

with

$$\mathbf{S}_{\mathbf{uu}}(\omega) = \mathbf{U}(\omega)\mathbf{U}^{H}(\omega),\ \mathbf{S}_{\mathbf{yu}}(\omega) = \mathbf{Y}(\omega)\mathbf{U}^{H}(\omega)$$

where $\mathbf{G}_{\mathbf{yu}}$ is a matrix of the transfer function from the input vector **u** to the output vector **y**; $\mathbf{U}(\omega)$ and $\mathbf{Y}(\omega)$ are derived from the fast Fourier transform (FFT) of **u**(t) and **y**(t), respectively; $\mathbf{S}_{\mathbf{uu}}$ is the matrix form of the auto-spectral density; $\mathbf{S}_{\mathbf{yu}}$ is the matrix of the cross-spectral densities between the input vector and the output vector; "*H*" denotes the Hermitian transpose also known as the conjugate transpose. The notation *G* or **G** is used to present the experimental transfer functions and *H* or **H** is used to present the rational polynomial transfer functions. During the experiment, several segments of the input/output signals with the same sampling points are employed to average the auto- or cross-spectral density to obtain accurate transfer functions. The Hanning window is also employed to avoid leakage. This step of averaging the spectral densities not only reduces the noise from the output signals but also averages out the nonlinearities in the system. In this procedure, the output noise is considered in the experimental transfer functions, while the input noise is assumed to be negligible. Although this equation only presents the case for the MIMO system, the SIMO system can also apply the same procedure to obtain the experimental transfer functions. Using this procedure, the transfer functions are experimentally determined for use in the system identification technique, which can convert these transfer functions into a system model.

5.2 Experimental system identification

Since this research identifies system models using the transfer function approach, the experimental transfer functions are first tested for each input. In Section 5.1, the experimental transfer functions have been briefly introduced. Basically, the experimental transfer functions are generated from the BLWN testing using Siglab or the predetermined white noise signals in this research. Moreover, different setups (e.g., the active isolation systems of the two- or six-story buildings) may have different procedures to obtain the experimental transfer function. Hence, all procedures for the experimental transfer functions are introduced in this section.

First, the procedure for the active isolation system of the two-story building in the *y*-direction is presented. The testing of this system originally obtained the experimental multi-input and multi-output (MIMO) transfer functions at one time. However, this method always results in bad-quality transfer functions. Alternatively, the experimental transfer functions of two single-input and multi-output (SIMO) systems are individually determined. Figure 5.1 illustrates the procedure for the *y*-actuator command input as well as the *y*-ground acceleration. For the *y*-actuator command input, the BLWN signals are generated directly from the Siglab with a band up to 50 Hz, while the shake table is at rest. As for the *y*-ground acceleration, the BLWN signals are preloaded in the ShoreWestern digital controller and then sent to the shake table, while the *y*-

actuator is always sent zero commands. Moreover, the BLWN signals for ground accelerations should also be modified because of the relationship between commands to the shake table and ground accelerations. In this research, the modified BLWN signals for generating ground accelerations are derived from the regular BLWN signals filtered by a Butterworth low-pass filter with a 5-Hz cutoff frequency, which is determined by the trend of the transfer function of this shake table. Note that this approach can roughly estimate BLWN ground accelerations. For precise BLWN ground accelerations, the method in Section 7.3 can be used. Through this procedure, the experimental transfer functions for both inputs can be determined.

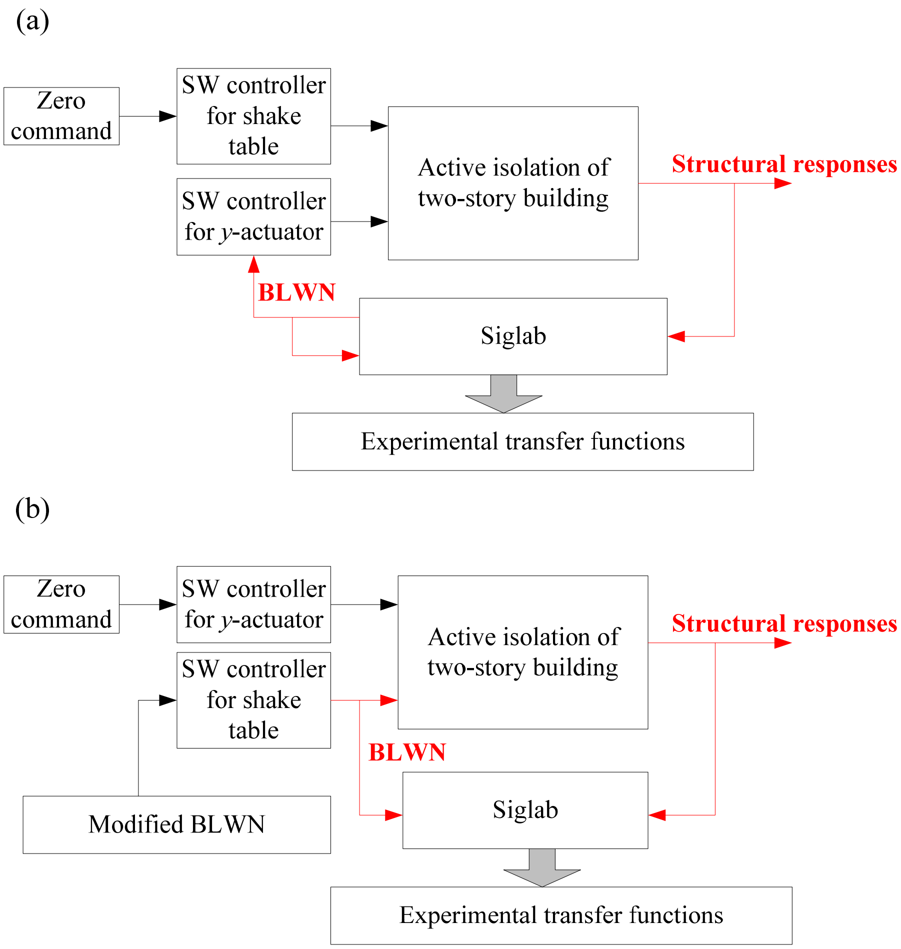

Figure 5.1. Experimental transfer functions for the active isolation system of the two-story building from (a) the *y*-actuator input commands and (b) the *y*-ground accelerations.

In the active isolation system of the six-story building, the procedure for experimental transfer functions is slightly different from that in the active isolation system of the two-story building. The major data collector in this structural system is the National Instrument (NI) data acquisition system (DAQ). Thus, the time-domain data are collected from the NI-DAQ and then processed into transfer functions in a personal computer. The BLWN commands for actuators are still generated from the Siglab, which can also produce the mutually independent BLWN commands for multiple channels concurrently. As for the experimental transfer functions from ground accelerations, the procedure is similar to that in the active isolation system of the two-story building, using the modified BLWN signals. The modified BLWN signals are generated from the low-pass filtered BLWN signals and then preloaded into the ShoreWestern digital controller for the shake table. All BLWN signals for this system have a band up to 50 Hz. Consequently, the transfer functions with respect to each input are experimentally obtained.

The procedure to obtain experimental transfer functions for the active isolation system of the six-story building is described first. Figure 5.2 sketches the flowchart of the procedure for this system along the *y*-direction. To obtain the experimental transfer functions from the *y*-actuator command input, the BLWN signals are generated from the Siglab and concurrently sent to the NI-DAQ. Meanwhile, the structural responses are also collected to the NI-DAQ in order to calculate the transfer functions (see Figure 5.2a). When determining the experimental transfer functions from the *y*-ground acceleration, the modified BLWN signals command the shake table and subsequently drive BLWN-type accelerations on the table. The NI-DAQ collects the BLWN-type ground accelerations and the structural responses to calculate the transfer functions. Finally, the transfer functions for identifying the system in the *y*-direction are determined.

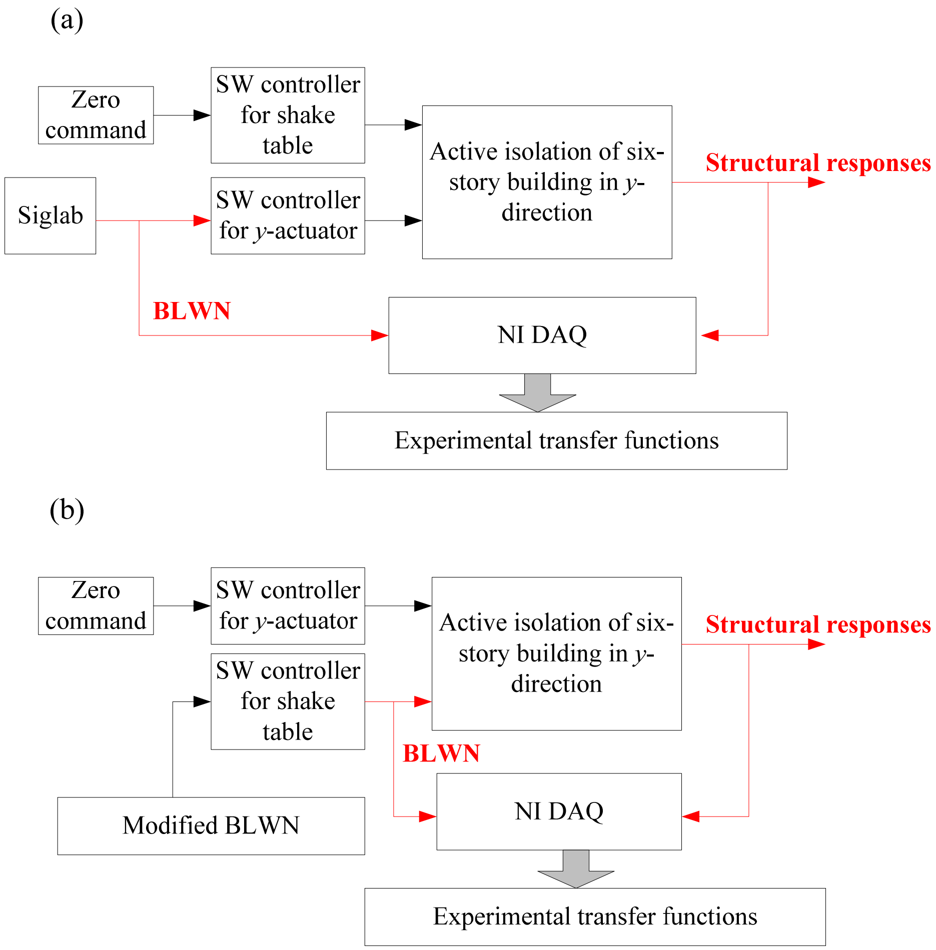

Figure 5.2. Experimental transfer functions for the active isolation system of the six-story building in the *y*-direction from (a) the *y*-actuator command input and (b) the *y*-ground acceleration.

As for the active isolation system of the six-story building in the *x*-direction, the procedure is adjusted in order to obtain more precise transfer functions of both *x*-actuators. Consider the transfer function matrix $\mathbf{G}_x$, given by

$$\mathbf{G}_x = \begin{bmatrix} G_{x_{b,x1}u_{x1}} & G_{x_{b,x1}u_{x2}} & G_{x_{b,x1}\ddot{x}_{g,x}} \\ G_{\ddot{x}^a_{b,x1}u_{x1}} & G_{\ddot{x}^a_{b,x1}u_{x2}} & G_{\ddot{x}^a_{b,x1}\ddot{x}_{g,x}} \\ G_{\ddot{x}^a_{1,x1}u_{x1}} & G_{\ddot{x}^a_{1,x1}u_{x2}} & G_{\ddot{x}^a_{1,x1}\ddot{x}_{g,x}} \\ \vdots & \vdots & \vdots \\ G_{\ddot{x}^a_{6,x1}u_{x1}} & G_{\ddot{x}^a_{6,x1}u_{x2}} & G_{\ddot{x}^a_{6,x1}\ddot{x}_{g,x}} \\ G_{x_{b,x2}u_{x1}} & G_{x_{b,x2}u_{x2}} & G_{x_{b,x2}\ddot{x}_{g,x}} \\ G_{\ddot{x}^a_{b,x2}u_{x1}} & G_{\ddot{x}^a_{b,x2}u_{x2}} & G_{\ddot{x}^a_{b,x2}\ddot{x}_{g,x}} \\ G_{\ddot{x}^a_{1,x2}u_{x1}} & G_{\ddot{x}^a_{1,x2}u_{x2}} & G_{\ddot{x}^a_{1,x2}\ddot{x}_{g,x}} \\ \vdots & \vdots & \vdots \\ G_{\ddot{x}^a_{6,x2}u_{x1}} & G_{\ddot{x}^a_{6,x2}u_{x2}} & G_{\ddot{x}^a_{6,x2}\ddot{x}_{g,x}} \end{bmatrix} \tag{5.2}$$

where this equation presents the experimental transfer function of this system in the x-direction. Again, in this research, **H** or H denotes polynomial transfer function models, and **G** or G denotes experimental transfer functions. Because the LQR design for this system in the x-direction requires a more accurate model with respect to both x-actuators, the interaction between these two actuators (i.e., the damping contributed from the $x2$-actuator when exciting the $x1$-actuator) should be concurrently considered in the experimental transfer functions. Thus, the transfer functions in the first two columns of $\mathbf{G}_x$ should be determined by the responses in which both actuators are excited from BLWN signals. For example, when determining the first column in $\mathbf{G}_x$ for the responses from the $x1$-actuator, BWLN signals with larger amplitudes are sent to the $x1$-actuator and different BLWN signals with smaller amplitudes are concurrently sent to the $x2$-actuator. Similarly, two mutually independent BLWN signals with larger and smaller amplitudes are sent to the $x2$- and $x1$- actuators, respectively, in order to determine the transfer functions from the $x2$-actuator, e.g., the second column in $\mathbf{G}_x$. Thus, the Siglab generates two BLWN signals to these two actuators in two different ways. The NI-DAQ collects the BLWN inputs bypassed from the Siglab as well as the structural responses to determine the first and second columns of $\mathbf{G}_x$ independently, as shown in Figure 5.3 (a) and (b). For the third column of $\mathbf{G}_x$, the procedure to determine the experimental transfer functions from the *x*-ground acceleration is similar to that of this system along the *y*-direction (see Figure 5.3c). By employing this procedure, all experimental transfer functions for the active isolation system of the six-story building in the *x*-direction can be determined.

The damping in the experimental transfer functions from ground accelerations maybe overestimated when using the procedures as mentioned above. In Section 4.3, the effect of actuators' nonlinearity has been addressed. The damping would be larger if the active isolation systems are excited by the ground motion with zero commands for actuators (e.g., similar to the zeroed control). When the active isolation systems are excited by both actuators and ground motions, the damping of the systems will be decreased due to the friction. However, the control design in this research relies on the LQR design more than the Kalman estimator design in the H_2/LQG methods. Thus, the identified models from ground accelerations are less important than those from the actuators. Therefore, the procedure to obtain the experimental transfer functions from the ground motions is acceptable for the system identification in the later portion of this chapter.

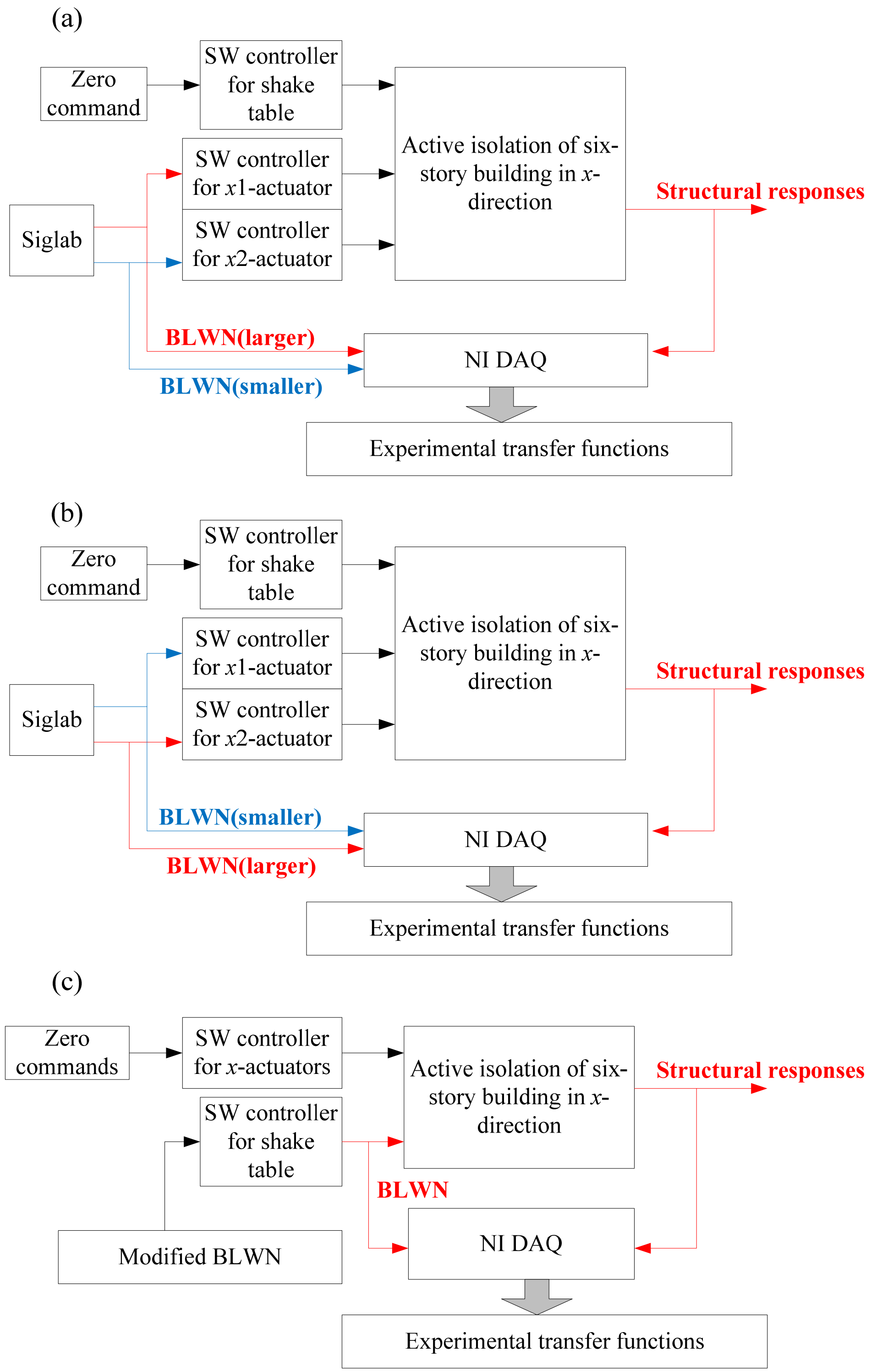

Figure 5.3. Experimental transfer functions for the active isolation system of the six-story building in the *x*-direction from (a) the *x*1-actuator command input, (b) the *x*2-actuator command input, and (c) the *x*-ground acceleration.

5.3 System identification

As mentioned before, the procedure to identify a system in this research contains two steps: (1) system identification for SIMO systems and (2) system combination for a minimal MIMO system. First, the SIMO system identification is employed to obtain the individual SIMO systems from an MIMO system. Once these SIMO systems are directly combined and then converted to a MIMO system, the duplicated eigenvalues will result in uncontrollable states or unobservable states. Through the proposed method in Section 5.3.3, the system combination can numerically eliminate these repeated eignevalues. Finally, a MIMO system model is identified using this two-step method.

5.3.1 SIMO system identification using MFDID

The system identification tool, MFDID (Kim et al. 2005), is introduced in this section. This tool can model a system as a rational polynomial transfer function in the continuous frequency domain. By assigning the transfer function obtained from the experiment, as in Eq. (5.1), this tool will give a model based on the predetermined numbers of poles and zeros. The main goal of this tool is to fit the experimental transfer function using the optimization algorithms for the rational polynomial form. This identification tool also provides different forms of weighting functions and different optimization methods that can be chosen in order to reduce the fitting errors. This highly nonlinear curve-fitting tool can consequently generate a model which can accurately describe the system behavior over the frequency of interest.

With this system identification tool, only the linear time-invariant dynamic systems can be identified as the rational polynomial transfer function models. For example, even if the system inherently contains some slight nonlinearity, this tool can also give a linearized result. Because the experimental transfer function is naturally discrete over a specific frequency range, this tool can only identify the poles lying within this frequency range. If the identified poles are located outside the range, the poles may be reflected from the phase of the transfer function or derived from the redundant numbers of poles. In most structural systems, the number of zeros is typically less than that of the poles. The inappropriate assignment of the numbers of poles and zeros would not give optimal results, though sometimes these results seem fine as compared to the experimental transfer function. Therefore, this system identification tool requires the prior information about the identified system.

This system identification tool contains four options for the optimization algorithms. First, the linear least-squares method is employed to obtain the initial solution of the rational polynomial transfer function. Because the curve-fitting problem processes the complex values, the linear least-squares method for this problem only gives an approximate result. Thus, three algorithms, the Steiglitz-Mcbride method, the Gauss-Newton method, and the Levenberg-Marquardt method, are used to obtain the closest estimate. Before employing these three methods, a rough result of the transfer function is required. For example, a model that can approximately describe the system can be optimized by these three methods to obtain an accurate result. Through this sequential procedure, the rational polynomial transfer function is accurately modeled with respect to the predetermined numbers of poles and zeros.

To demonstrate the operation of the MFDID tool, the details are addressed in this section. The MFDID tool is programmed in the graphic user interface (GUI) platform using MATLAB (2011). First, when opening this tool, the initial step is to click the upper right button, "*Data*", in order to enter the required data. The pop-up window shown in Figure 5.4 allows users to load the experimental transfer function (part *a*) with respect to the frequency vector (part *b*) to the tool in order to determine the number of inputs (part *c*) and outputs (part *d*) and assign the number of poles (part *e*) and zeros (part *f*). Note that the sequence of the transfer functions (e.g., the matrix of transfer functions for the MIMO cases) follows the output dimension first and then follows the input dimension, i.e., $h_{y_1u_1} \; \cdots \; h_{y_{ny}u_1} \;\; h_{y_1u_2} \; \cdots \; h_{y_{ny}u_2}$, where the system illustrated has two inputs and *ny* outputs. By completing this step, the program is ready to process the system identification based on these initial inputs.

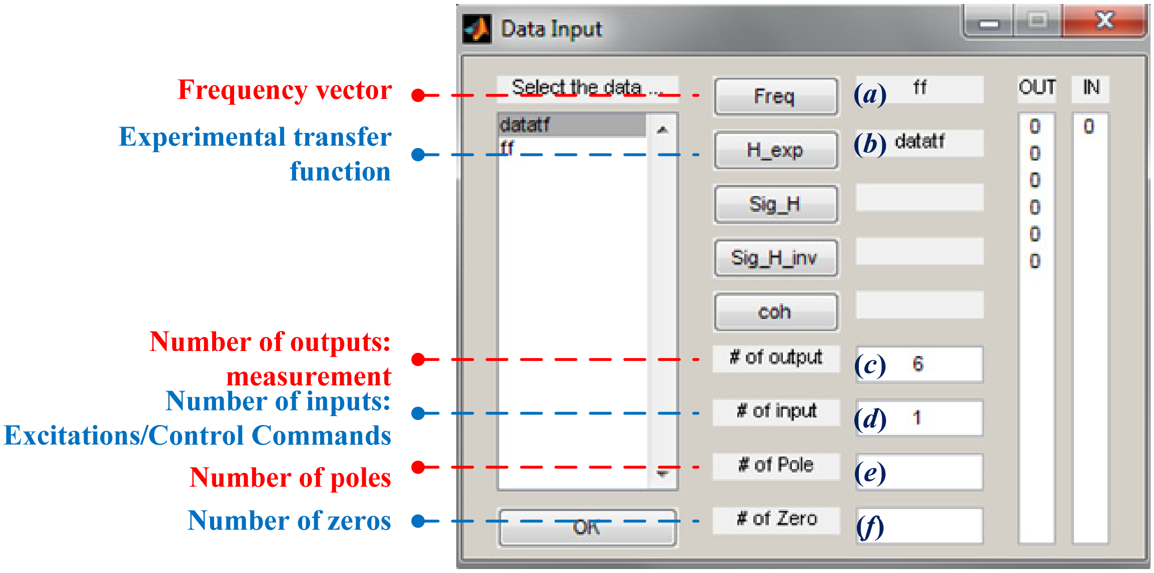

Frequency vector

Experimental transfer function

Number of outputs: measurement

Number of inputs: Excitations/Control Commands

Number of poles

Number of zeros

Select the data ...: datatf, ff

Freq (a) ff

H_exp (b) datatf

\# of output (c) 6

\# of input (d) 1

\# of Pole (e)

\# of Zero (f)

OUT: 0 0 0 0 0 0

IN: 0

Figure 5.4. Window for inputting data in MFDID.

After entering the required data, the procedure of the system identification is moved to the main program for the curve-fitting optimization as shown in Figure 5.5. First, the frequency range should be adjusted by "*FrA*" or "*FrD*" because this program would automatically change the original range to the 65% of the maximum frequency. The optimization algorithms can then be applied. If no transfer function model is preloaded to this program, the first step must be to employ the linear least-squares method, "*LLS*". Otherwise, any optimization algorithms can be selected to fit the experimental transfer functions and refine the original model repeatedly. The weighting functions provided at the bottom can be arbitrarily changed if necessary. Also, the number of poles and zeros can be adjusted for any single transfer function, while the calculated poles and zeros from the model can be manually added or deleted. According to the procedure, the rational polynomial transfer function model is accurately identified.

The optimization algorithms in the MFDID tool have different functions for the curve fitting. For example, the linear least-squares method only roughly sketches the system model in order to provide the initial values for the other algorithms. The Steiglitz-Mcbride method is employed to approach the accurate poles for the system model. When the final result cannot satisfy the desired accuracy and the problem is the identified poles, this method can be repeated to fit the experimental transfer function. The Gauss-Newton method mainly refines the zeros and slightly adjusts the poles. To obtain a more accurate system model from this program, these two steps can be used repeatedly. The Levenberg-Marquardt method can only adjust both poles and zeros very slightly. Using the instruction for the optimization algorithm, the identified system model will contain the poles and zeros comparable to the experimental system.

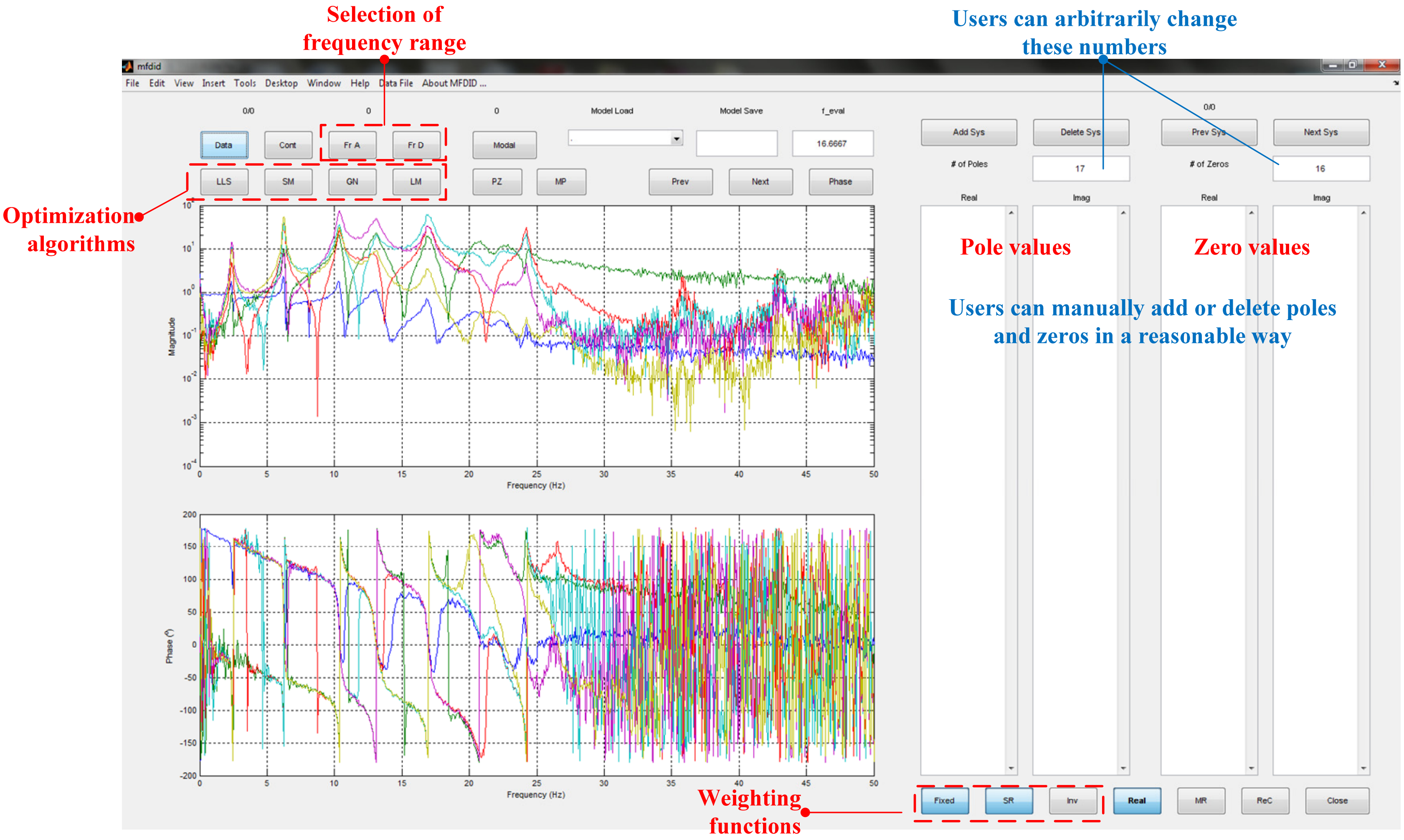

Selection of frequency range

Users can arbitrarily change these numbers

Optimization algorithms

Pole values

Zero values

Users can manually add or delete poles and zeros in a reasonable way

Weighting functions

Figure 5.5. Main program of MFDID.

The weighting functions are the key to accurately obtaining an identified transfer function. Initially, the program has no weighting functions incorporated. If the optimization algorithms have been repeated many times and the quality of the identified model is still unacceptable, the weighting functions should be initiated. The weighting functions, "*Fixed*" and "*SR*", are employed to increase the accuracy from the middle frequency range to the high frequencies, but the quality of the low frequency range is reduced. The other weighting function, "*Inv*", is used particularly for the low frequency range. For example, the "*Inv*" weighting function would work better if the outputs of the transfer function only contain the acceleration measurements in a structural system. The "*Fixed*" and "*SR*" are good options if the displacement measurements are the outputs of the transfer function. Hence, the weighting function should be used when seeking a highly accurate model.

5.3.2 SIMO system identification for discrete-time models

The SIMO system identification proposed in this section is developed for the discrete-frequency model because performing the identification in the discrete frequency domain usually results in stable solutions for poles and guarantees that the solution exists within the specific frequency range of interest. All the equations in the SIMO system identification are herein represented in the z domain (i.e., $z = e^{i\omega T}$, where i is the complex unit, ω is the frequency in rad/sec, and T is the sample period). All system models represented in the discrete time/frequency domain can be realized in the continuous time/frequency domain using linear system theory (Chen 1998).

The first task is to determine the SIMO model for each of the system inputs based on the measured data. The transfer functions in z-domain are parameterized as

$$H_m\left(z,\boldsymbol{\theta}\right) = \frac{B_m\left(z,\boldsymbol{\theta}\right)}{A\left(z,\boldsymbol{\theta}\right)} \tag{5.3}$$

where H_m is one of the transfer functions in **H** with respect to the m-th output; the roots of $B_m = 0$ are the zeros for the transfer function; the roots of $A = 0$ are the poles of the transfer function; $\boldsymbol{\theta}$ denotes the coefficients of the associated polynomial functions. Note that the order of the denominator polynomial indicates the order of the system. Least-squares (LS) minimization of the difference between Eq. (5.3) and the measured transfer functions is employed, i.e.,

$$\mathbf{L}(\boldsymbol{\theta}) = \arg\min_{\boldsymbol{\theta}} \sum_{m=1}^{ny} \sum_{l=1}^{nf} \left\| W_m(z_l)\left(B_m(z_l,\boldsymbol{\theta}) - A(z_l,\boldsymbol{\theta})G_m(z_l)\right)\right\|^2 \tag{5.4}$$

where ny and nf are the number of outputs and the fitting points, respectively; W_m is a weighting function designed to provide a better fit to the poles and zeros; G_m denotes the transfer functions directly obtained from the experiment. Eq. (5.4) can be expanded into a linear LS problem that can be solved without iterative calculation. After solving the linear LS problem based on Eq. (5.4), some errors may exist in the zeros of the identified SIMO system. Therefore, the next step for improving the identified system is to repeat the nonlinear LS algorithm in Eq. (5.4) iteratively, in order to further decrease the errors. This iterative process fixes the identified poles which is derived from the first step and refines the zeros in the transfer function output one by one. Through this method, the resulting SIMO systems can provide an excellent match for both the poles and zeros in the identified transfer functions.

5.3.3 System combination

Since the frequency-domain system identification technique usually duplicates the eigenvalues as realized to the state-space representation, the numerical approach for the minimal realization is employed to eliminate the additional eigenvalues, which can be interpreted as the additional poles or states. If a system model contains repeated eigenvalues, uncontrollable and unobservable conditions will occur and then result in the independent subsystems from one input to the others. Under this circumstance, the controller which is developed from this model may produce implicit instability in the physical system. Hence, the numerical minimal realization for the system combination becomes a part of the procedure in the system identification.

To realize a minimal state-space system, many previous studies introduced methods to approach the minimal model. For example, Dyke et al. (1994a and 1994b) adopted the balanced realization, which calculates the singular values from SIMO systems and reduces the number of states to realize a minimal system, to a controlled building system. In this approach, a weighting matrix is applied to the balanced realization in order to specify the relative importance in the model reduction. This approach would function well when the physical system for identification behaves relatively linearly and has low noise. Another example is the directly minimal realization algorithm, which eliminates uncontrollable or unobservable states from state-space models. In this algorithm, an orthogonal matrix is computed to transform the model into a minimal part with the other redundant part. Through elimination of the redundant part, a minimal state-space can be realized. Nevertheless, this algorithm requires the identified SIMO systems to have very close eigenvalues; otherwise, the result will be the same as the originally combined system which comes directly from the identified SIMO systems. Consequently, a modified minimal realization algorithm for a MIMO system from the perturbed SIMO systems is developed in this research.

Before introducing the modified minimal realization algorithm, the similarity transformation of state-space models is first described. Considering a state-space model such as Eq. (4.16), a nonsingular matrix, **T**, is used to transform into an arbitrary domain, given by

$$\begin{aligned}\dot{\bar{\mathbf{x}}} &= \mathbf{T}^{-1}\mathbf{A}\mathbf{T}\bar{\mathbf{x}} + \mathbf{T}^{-1}\mathbf{B}\mathbf{u} + \mathbf{T}^{-1}\mathbf{E}\ddot{\mathbf{x}}_g \\ \mathbf{y} &= \mathbf{C}\mathbf{T}\bar{\mathbf{x}}\end{aligned} \tag{5.5}$$

with

$$\mathbf{x} = \mathbf{T}\overline{\mathbf{x}}$$

where $\overline{\mathbf{x}}$ represents the transformed state from $\mathbf{x}$ and the noise is neglected. This equation can also interpret the state-space realization from the transfer function models. Equivalently, the form of the matrix **A** in Eq. (4.16) can be obtained from the identified model when this nonsingular matrix **T** exists. If the controllability matrix and the observability matrix are used to map the similarity transformation, the product of these two matrices before and after the similarity transformation is the same and is derived by

$$\tilde{\mathbf{O}}_o\tilde{\mathbf{C}}_o = \begin{bmatrix} \mathbf{CB} & \mathbf{CAB} & \cdots & \mathbf{CA}^{n-1}\mathbf{B} \\ \mathbf{CAB} & \mathbf{CA}^2\mathbf{B} & & \\ \vdots & & \ddots & \\ \mathbf{CA}^{n-1}\mathbf{B} & & & \mathbf{CA}^{2(n-1)}\mathbf{B} \end{bmatrix} = \tilde{\mathbf{O}}_s\tilde{\mathbf{C}}_s \tag{5.6}$$

where $\tilde{\mathbf{O}}_o$ and $\tilde{\mathbf{C}}_o$ denote the controllability matrix and the observability matrix before the similarity transformation; $\tilde{\mathbf{O}}_s$ and $\tilde{\mathbf{C}}_s$ denote the controllability matrix and the observability matrix after the similarity transformation; n is the number of states or the order of the system; the matrix **E** is neglected for simplicity in description. The product matrix in Eq. (5.6) is also known as the Markov parameter, which is invariant in any linear systems. Through the similarity transformation and the Markov invariant parameter, a state-space model can be arbitrarily transformed into the other form without changing the dynamic characteristics.

To represent a state-space model in a real-valued eigen domain, a modal canonical form can convert the system into several small state-space models. Again, considering Eq. (4.16) only with the control command inputs, the state-space model after the modal canonical realization is rewritten by

$$\begin{aligned} \dot{\overline{\mathbf{x}}} &= \overline{\mathbf{A}}\overline{\mathbf{x}} + \overline{\mathbf{B}}\mathbf{u} \\ \mathbf{y} &= \overline{\mathbf{C}}\overline{\mathbf{x}} \end{aligned} \tag{5.7}$$

with

$$\bar{\mathbf{A}} = \begin{bmatrix} 0 & 1 & & & & \ddots & & \\ -\omega_1^2 & -2\xi_1\omega_1 & & & & & \mathbf{0} & \\ & & 0 & 1 & & & & \ddots \\ & & -\omega_2^2 & -2\xi_2\omega_2 & & & & \\ & & & & \ddots & & & \\ \ddots & & & & & -\omega_j^2 & & \\ & \mathbf{0} & & & & & -\omega_{j+1}^2 & \\ & & \ddots & & & & & \ddots \end{bmatrix}$$

where ω_j and ξ_j denote the *j*-th natural frequency and the *j*-th damping in the system and the matrix $\bar{\mathbf{B}}$ and $\bar{\mathbf{C}}$ are accordingly derived from the similarity transformation. Note that the natural frequencies and the damping terms are calculated under consideration of the control-structure interaction, indicating that these values would be different from the building system itself. Because the matrix $\bar{\mathbf{A}}$ is a block diagonal form, the system can be divided into several small state-space models. After applying the modal canonical realization, the system can be reduced to several subsystems corresponding to each of the dynamic characteristics, e.g., the natural frequencies and damping.

After deriving the similarity transformation and the modal canonical realization for state-space modes, the system combination is introduced to construct the active isolation models from the identified SIMO system models. First, two state-space models are considered. One of the models is an SIMO system model which will be combined with the other MIMO (or SIMO) system model. Only one SIMO model can be combined to an existing SIMO or MIMO system model. These two models are defined by

$$\begin{aligned} \dot{\mathbf{x}}_1 &= \mathbf{A}_1\mathbf{x}_1 + \mathbf{B}_1\mathbf{u}_1 \\ \mathbf{y} &= \mathbf{C}_1\mathbf{x}_1 \end{aligned} \tag{5.8}$$

$$\begin{aligned}\dot{\mathbf{x}}_2 &= \mathbf{A}_2\mathbf{x}_2 + \mathbf{B}_2 u_2 \\ \mathbf{y} &= \mathbf{C}_2\mathbf{x}_2\end{aligned} \tag{5.9}$$

where Eq. (5.8) defines the MIMO system model 1 as the existing model and Eq. (5.9) indicates the SIMO system model 2 to be combined into model 1. Initially, both models are transformed into the modal canonical form. Thus, the matrices in both models are defined as

$$\begin{aligned}\mathbf{A}_1 &= diag\left(\mathbf{A}_{11} \quad \cdots \quad \mathbf{A}_{1nc} \quad \mathbf{A}_{1(nc+1)} \quad \cdots \quad \mathbf{A}_{1(nc+nr1)}\right) \\ \mathbf{B}_1 &= \left[\mathbf{B}_{11}^T \quad \cdots \quad \mathbf{B}_{1nc}^T \quad \mathbf{B}_{1(nc+1)}^T \quad \cdots \quad \mathbf{B}_{1(nc+nr1)}^T\right]^T \\ \mathbf{C}_1 &= \left[\mathbf{C}_{11} \quad \cdots \quad \mathbf{C}_{1nc} \quad \mathbf{C}_{1(nc+1)} \quad \cdots \quad \mathbf{C}_{1(nc+nr1)}\right]\end{aligned} \tag{5.10}$$

$$\begin{aligned}\mathbf{A}_2 &= diag\left(\mathbf{A}_{21} \quad \cdots \quad \mathbf{A}_{2nc} \quad \mathbf{A}_{2(nc+1)} \quad \cdots \quad \mathbf{A}_{2(nc+nr2)}\right) \\ \mathbf{B}_2 &= \left[\mathbf{B}_{21}^T \quad \cdots \quad \mathbf{B}_{2nc}^T \quad \mathbf{B}_{2(nc+1)}^T \quad \cdots \quad \mathbf{B}_{2(nc+nr2)}^T\right]^T \\ \mathbf{C}_2 &= \left[\mathbf{C}_{21} \quad \cdots \quad \mathbf{C}_{2nc} \quad \mathbf{C}_{2(nc+1)} \quad \cdots \quad \mathbf{C}_{2(nc+nr2)}\right]\end{aligned} \tag{5.11}$$

where $diag(\bullet)$ denotes the block diagonal matrix; $\mathbf{A}_{1k}$ indicates the *k*-th block matrix which represents the *k*-th mode and has a 2x2 or 1x1 dimension; $\mathbf{B}_{1k}^T$ and $\mathbf{C}_{1k}$ are accordingly formed with respect to $\mathbf{A}_{1k}$; *nc* denotes the number of states to be combined; *nr*1 and *nr*2 represent the uncontrollable states in model 2 and model 1, respectively; all parameters in model 2 follow the notations in model 1. According to the Markov invariant parameter, the combined system shares the product of the controllability matrix and the observability matrix from model 1 and model 2. Since both model 1 and model 2 also share the modal properties based on each block model (i.e., ($\mathbf{A}_{1k}$, $\mathbf{B}_{1k}$, $\mathbf{C}_{1k}$) and ($\mathbf{A}_{2k}$, $\mathbf{B}_{2k}$, $\mathbf{C}_{2k}$), where k is 1 ~ *nc*), the system combination is reduced to update the small block models one by one. For those uncontrollable states in model 1 and model 2, the block models are excluded in the process of the system combination. Thus, the Markov parameter for the *k*-th block models from both model 1 and model 2 is given by

$$\begin{aligned}&\begin{bmatrix}\mathbf{C}_{1k} & \mathbf{C}_{2k}\\ \mathbf{C}_{1k}\mathbf{A}_{1k} & \mathbf{C}_{2k}\mathbf{A}_{2k}\\ \vdots & \vdots\\ \mathbf{C}_{1k}\mathbf{A}_{1k}^{3} & \mathbf{C}_{2k}\mathbf{A}_{2k}^{3}\end{bmatrix}\begin{bmatrix}\mathbf{B}_{1k} & & \mathbf{A}_{1k}\mathbf{B}_{1k} & & \cdots & & \mathbf{A}_{1k}^{3}\mathbf{B}_{1k} & \\ & \mathbf{B}_{2k} & & \mathbf{A}_{2k}\mathbf{B}_{2k} & & \cdots & & \mathbf{A}_{2k}^{3}\mathbf{B}_{2k}\end{bmatrix}\\ &=\begin{bmatrix}\mathbf{U}_{\Sigma} & \mathbf{U}_{\varepsilon}\end{bmatrix}\begin{bmatrix}\mathbf{\Sigma} & \\ & \boldsymbol{\varepsilon}\end{bmatrix}\begin{bmatrix}\mathbf{V}_{\Sigma}\\ \mathbf{V}_{\varepsilon}\end{bmatrix}\end{aligned}\tag{5.12}$$

where $\mathbf{A}_{1k}$ and $\mathbf{A}_{2k}$ are assumed to be 2x2. If $\mathbf{A}_{1k}$ and $\mathbf{A}_{2k}$ have the 1x1 dimension, the dimension of the Markov parameter will be changed to half. The right-hand side of Eq. (5.12) is the singular value decomposition, in which the singular values are descended in the diagonal of the middle matrix. If both block models can be perfectly combined, the second half of the singular-valued matrix, $\boldsymbol{\varepsilon}$, is a zero matrix. However, both block models are derived from the identified models, which would contain the modeling errors. Hence, only the first half of the singular-valued matrix is retained, and then the system combination for the k-th block is given by

$$\begin{aligned}\mathbf{U}_{\Sigma}\mathbf{\Sigma}\mathbf{V}_{\Sigma}&=\left(\mathbf{U}_{\Sigma}\mathbf{\Sigma}^{1/2}\right)\left(\mathbf{\Sigma}^{1/2}\mathbf{V}_{\Sigma}\right)\\ &=\begin{bmatrix}\mathbf{C}_{comb,k}\\ \mathbf{C}_{comb,k}\mathbf{A}_{comb,k}\end{bmatrix}\begin{bmatrix}\mathbf{B}_{comb,k} & \mathbf{A}_{comb,k}\mathbf{B}_{comb,k}\end{bmatrix}\end{aligned}\tag{5.13}$$

where this equation is only suited for the 2x2 $\mathbf{A}_{1k}$ and $\mathbf{A}_{2k}$ in Eq. (5.12). For the 1x1 $\mathbf{A}_{1k}$ and $\mathbf{A}_{2k}$, the dimension is reduced by half. Using the least-squares method, the $\mathbf{A}_{comb,k}$, $\mathbf{B}_{comb,k}$, and $\mathbf{C}_{comb,k}$ can be determined. After repeating the same procedure to obtain the combined block model, the combined full model is written by

$$\begin{aligned}\dot{\mathbf{x}}_{comb}^{full}&=\mathbf{A}_{comb}^{full}\mathbf{x}_{comb}^{full}+\mathbf{B}_{comb}^{full}\begin{bmatrix}\mathbf{u}_1\\ u_2\end{bmatrix}\\ \mathbf{y}&=\mathbf{C}_{comb}^{full}\mathbf{x}_{comb}^{full}\end{aligned}\tag{5.14}$$

with

$$\mathbf{x}_{comb}^{full}=\begin{bmatrix}\mathbf{x}_{comb,1}^{T} & \cdots & \mathbf{x}_{comb,nc}^{T} & \mathbf{x}_{1(nc+1)}^{T} & \cdots & \mathbf{x}_{1(nc+nr1)}^{T} & \mathbf{x}_{2(nc+nr1)}^{T} & \cdots & \mathbf{x}_{2(nc+nr2)}^{T}\end{bmatrix}^{T}$$

$$\mathbf{A}_{comb}^{full} = diag\left(\mathbf{A}_{comb,1} \quad \cdots \quad \mathbf{A}_{comb,nc} \quad \mathbf{A}_{1(nc+1)} \quad \cdots \quad \mathbf{A}_{1(nc+nr1)} \quad \mathbf{A}_{2(nc+1)} \quad \cdots \quad \mathbf{A}_{2(nc+nr2)}\right)$$

$$\mathbf{B}_{comb}^{full} = \begin{bmatrix} \multicolumn{2}{c}{\mathbf{B}_{comb,1}} \\ \multicolumn{2}{c}{\vdots} \\ \multicolumn{2}{c}{\mathbf{B}_{comb,nc}} \\ \mathbf{B}_{1(nc+1)} & \mathbf{0} \\ \vdots & \vdots \\ \mathbf{B}_{1(nc+nr1)} & \mathbf{0} \\ \mathbf{0} & \mathbf{B}_{2(nc+1)} \\ \vdots & \vdots \\ \mathbf{0} & \mathbf{B}_{2(nc+nr2)} \end{bmatrix}$$

$$\mathbf{C}_{comb}^{full} = \left[\mathbf{C}_{comb,1} \quad \cdots \quad \mathbf{C}_{comb,nc} \quad \mathbf{C}_{1(nc+1)} \quad \cdots \quad \mathbf{C}_{1(nc+nr1)} \quad \mathbf{C}_{2(nc+1)} \quad \cdots \quad \mathbf{C}_{2(nc+nr2)}\right]$$

If the number of SIMO systems is greater than two, the MIMO system is obtained by repeating the procedure of Eqs. (5.8) – (5.14) to combine all SIMO systems.

5.4 Example: active isolation system of the two-story building

In this section, a system identification problem for the active isolation system of the two-story building is illustrated along the *y*-direction. This system has two inputs from one actuator command and one ground excitation as well as four outputs of the base displacement, the base acceleration, and the 1st floor and 2nd floor accelerations. As a result, the system can be viewed as a MIMO system which is a combination of two SIMO systems. The SIMO system identification uses the discrete-frequency method, introduced in Section 5.3.2, while this MIMO system is obtained from the system combination of the two SIMO systems. Finally, the transfer functions derived from the identified model are compared to the experimental transfer functions and then the differences are discussed.

Before applying the SIMO system identification, the numbers of poles and zeros should be determined. According to the shear-type building and the linearization of the bearings, the number of poles for the system without the actuator is 6. With consideration of the control-structure interaction, the number of poles becomes 7-9, depending on the orders for the actuator model. The number of zeros is determined by the numerical model, introduced in Section 4.4, because this number varies with the type of measurements and the complexity of the system (e.g., the pole-zero cancellation). The system identification technique usually requires the system parameters (e.g., the number of states or the numbers of poles and zeros) to be close to the behavior of the physical system; otherwise, the identified model will poorly perform the system behavior, especially in the control implementation. Therefore, the SIMO system models employ these values for the discrete-time frequency-domain identification (see Section 5.3.2).

Two SIMO systems in this active isolation system along the *y*-direction are identified using the discrete-time identification technique. For example, these two SIMO transfer function models in the whole system can be presented by

$$\mathbf{H} = \begin{bmatrix} H_{x_{b,y}u_y} & H_{x_{b,y}\ddot{x}_{g,y}} \\ H_{\ddot{x}^a_{b,y}u_y} & H_{\ddot{x}^a_{b,y}\ddot{x}_{g,y}} \\ H_{\ddot{x}^a_{1,y}u_y} & H_{\ddot{x}^a_{1,y}\ddot{x}_{g,y}} \\ H_{\ddot{x}^a_{2,y}u_y} & H_{\ddot{x}^a_{2,y}\ddot{x}_{g,y}} \end{bmatrix} \tag{5.15}$$

where "*a*" denotes the absolute response, i.e., $\ddot{x}^a$ is the absolute acceleration. In this equation, each column represents a SIMO system. For this system, the number of poles assigned is 9, which is equivalent to the 3rd-order actuator model for the control-structure interaction. To obtain fitting results, the frequency range is assigned to be 0-30 Hz, while the original experimental transfer functions contain frequencies up to 50 Hz. Figure 5.6 shows the results from the actuator command input (i.e., the first column in Eq. (5.15)), as compared to the experimental transfer functions. Figure 5.7 also shows the results from the ground acceleration (i.e., the second column in Eq. (5.15)), as compared to the experimental transfer functions. These two figures show the comparable results in the magnitudes and the phases of the experimental transfer functions. Typically, the results from the SIMO system identification should be highly comparable; otherwise, a poor MIMO system model will be produced from the system combination of the identified SIMO system models. According to these two figures, the SIMO system identification for the discrete-frequency models generates promisingly high-quality transfer function models similar to the previous example.

After identifying these two SIMO systems, an MIMO system model can be formed from the system combination introduced in Section 5.3.3. The corresponding eigenvalues, as known as the modes, between the two SIMO systems should be manually determined before using the system combination. Through the comparison of the natural frequencies between the SIMO system models and the numerical model, the modes for the actuators can be individually extracted. The extraction of the independent modes from the actuators may be different from those modes from the ground acceleration inputs due to the nonlinearity. Moreover, the results of the system model for the actuator command inputs should be highly comparable to the experimental transfer functions because the control design emphasizes this part of the system model more than the ground accelerations. Once these two steps are confirmed, the system combination can then be applied to these two SIMO system models.

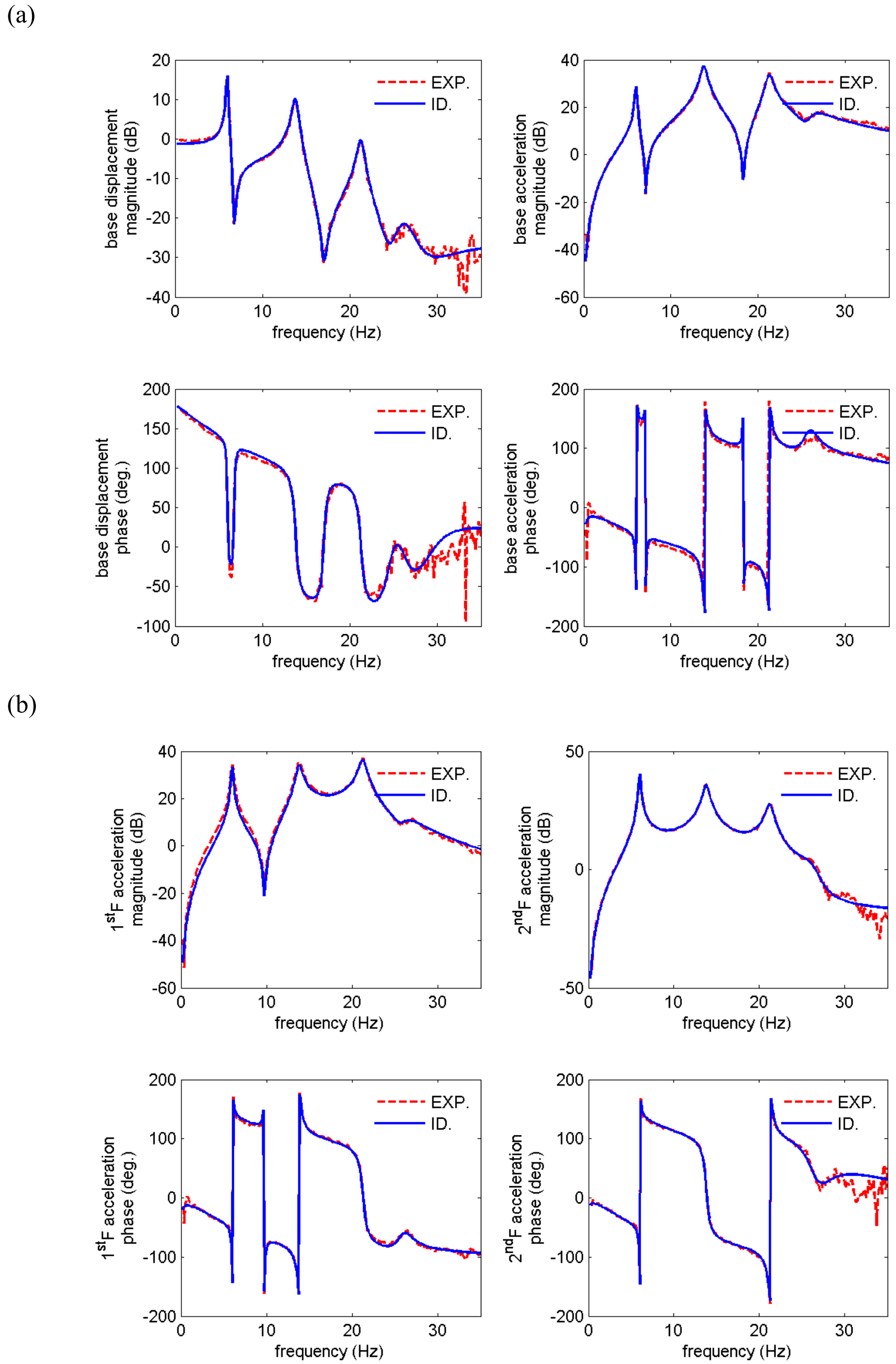

Figure 5.6. Transfer functions from the actuator command input using discrete-frequency SIMO system identification.

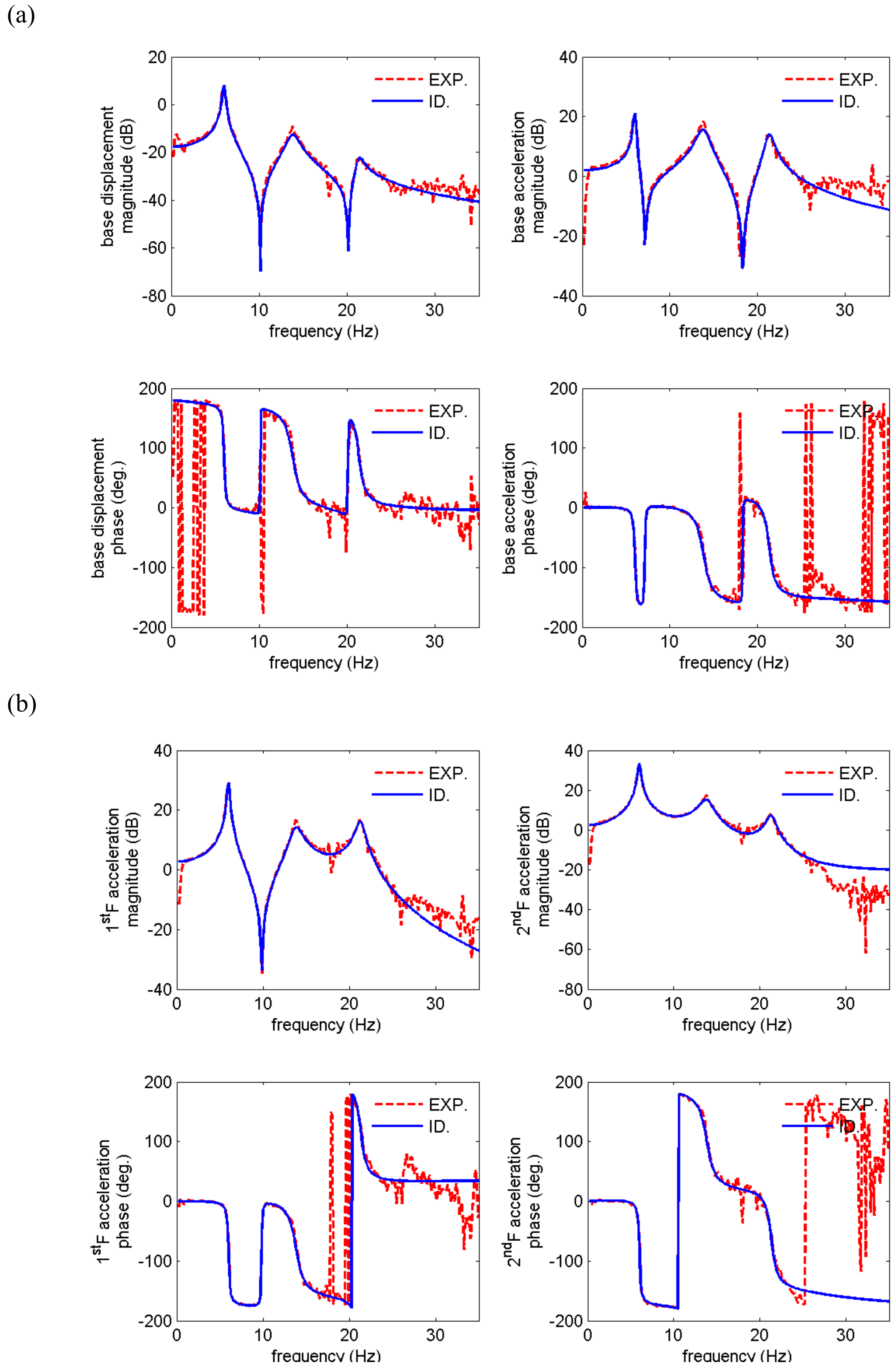

Figure 5.7. Transfer functions from ground acceleration using discrete-frequency SIMO system identification.

The results of the MIMO system model for the active isolation system of the two-story building is generated from the model using the system combination. This MIMO system contains the number of states equal to 11, indicating two redundant states from both the models from the actuator command input and the model from the ground acceleration (i.e., the number of total redundant states is 4 and the number of states in the combination is 7). Figures 5.8 (a) and (b) show the transfer functions from the *y*-actuator command input of the combined model, while Figures 5.8 (c) and (d) show the transfer functions from the ground acceleration in the *y*-direction. As mentioned in last paragraph, only less difference is allowed for the transfer functions from the actuator command input. The magnitudes in Figures 5.8 (a) and (b) have a very small difference, as compared to the experimental transfer functions, but the phases in the same figure have slight errors, particularly the ones near the 0 Hz. The errors may induce some problems for the active control implementation, which will be discussed in Chapter 6. When the results of the transfer functions from the ground acceleration are compared to the experimental transfer functions, smaller damping can be found in all transfer functions from the combined model. This type of result is necessary because the weighing least-squares method is applied to Eq. (5.13) in order to obtain a more precise model for the actuator command input. The same reason also affects the phases in Figures 5.8 (c) and (d). Although the system model derived from the system combination is slightly changed from the original SIMO systems, the overall behavior in the transfer functions still performs well, as compared to the experimental results.

To briefly sum up the system identification for this example, some remarks are highlighted. The number of poles and zeros should be able to represent the physical system. A certain range of frequency for the transfer functions should be specified when using the SIMO system identification. The values of poles or the eigenvalues of the system (e.g., the natural frequencies and damping) may be different among different inputs because of the nonlinearity. The MIMO system model, after using the system combination, should accurately represent the dynamic behavior for the actuator input; otherwise, the errors between the model and the physical system might induce the instability problem during the experimental implementation. Through these considerations for the system identification, the identified MIMO system model will accurately represent this active isolation system.

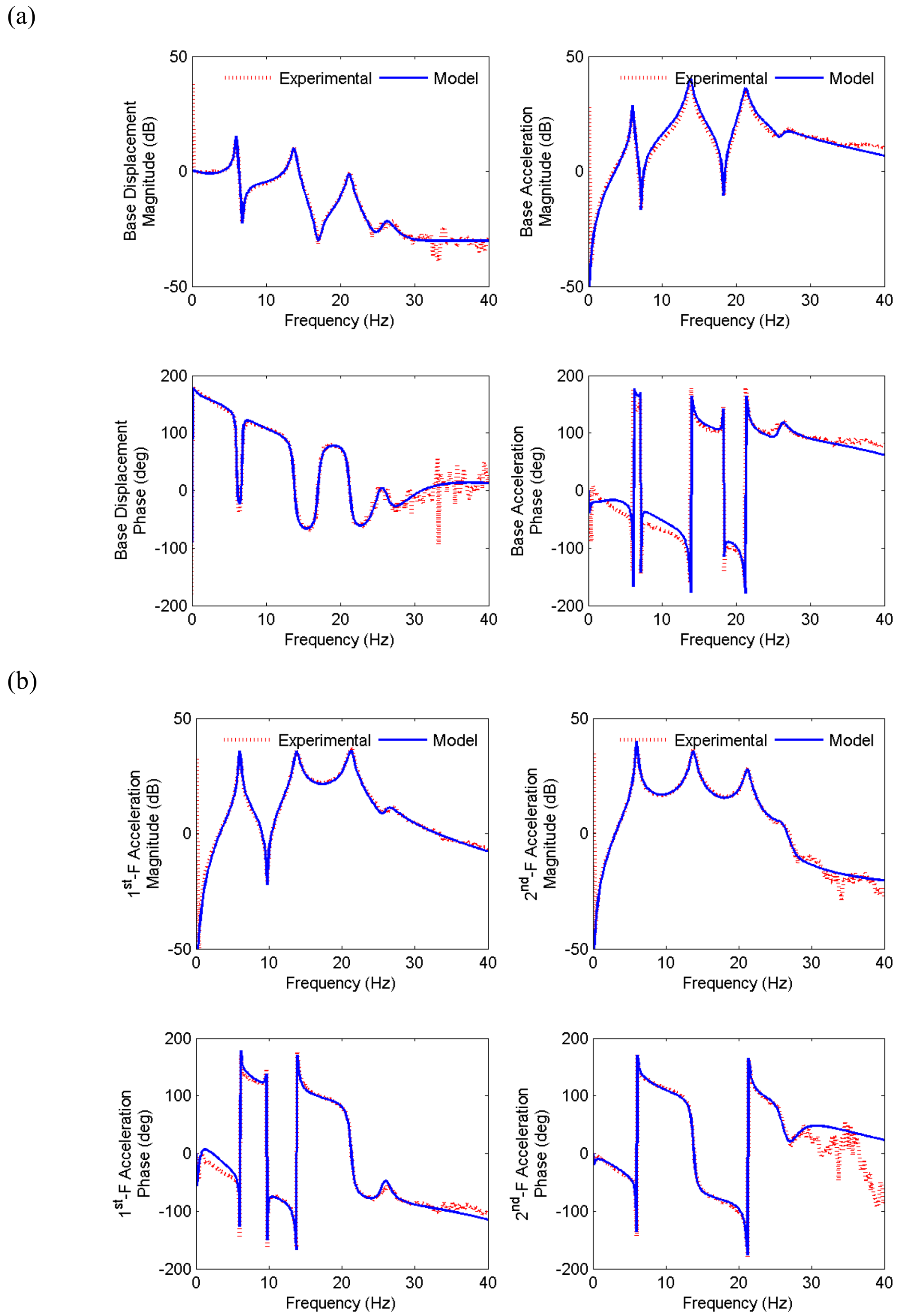

Figure 5.8. Transfer functions from the identified MIMO system using system combination: (a) and (b) from actuator input and (c) and (d) from ground acceleration.

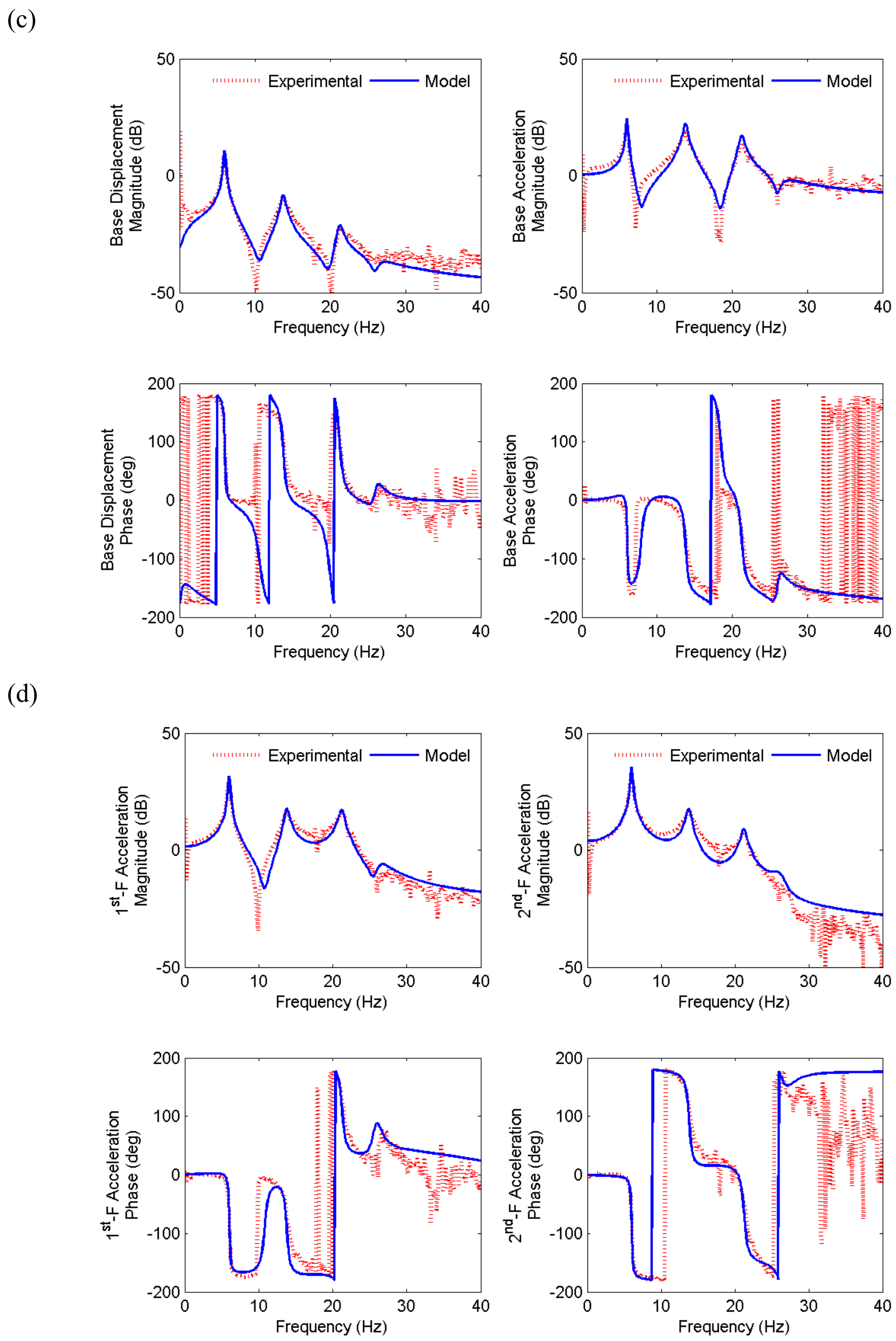

Figure 5.8. cont.

5.5 Example: active isolation system of the six-story building

This section presents the system identification for the active isolation system of the six-story building in both the *x*- and *y*- directions. This system identification problem is more complex than the previous example in Section 5.4 because the number of states has increased, and some of natural frequencies might be outside the frequency of interest. Moreover, the system in the *x*-direction has torsional modes which are mostly induced from the different behaviors of both *x*-actuators. Hence, the numerical model developed in Chapter 4 becomes an important part of this problem because the identified model should behave similarly to this numerical model, i.e., the values of poles in the transfer functions.

This complex active isolation system contains five inputs and multiple outputs in accordance with the setup of sensors, as shown in Figure 5.9. Again, because of the actuators' locations, the system can be interpreted with two models: (1) the model along the *y*-direction and (2) the model along the *x*-direction. Due to the separation, the transfer function models for both systems can be represented by

$$\mathbf{H}_y = \begin{bmatrix} H_{x_{b,y}u_y} & H_{x_{b,y}\ddot{x}_{g,y}} \\ H_{\ddot{x}^a_{b,y}u_y} & H_{\ddot{x}^a_{b,y}\ddot{x}_{g,y}} \\ H_{\ddot{x}^a_{1,y}u_y} & H_{\ddot{x}^a_{1,y}\ddot{x}_{g,y}} \\ \vdots & \vdots \\ H_{\ddot{x}^a_{6,y}u_y} & H_{\ddot{x}^a_{6,y}\ddot{x}_{g,y}} \end{bmatrix}, \quad \mathbf{H}_x = \begin{bmatrix} H_{x_{b,x1}u_{x1}} & H_{x_{b,x1}u_{x2}} & H_{x_{b,x1}\ddot{x}_{g,x}} \\ H_{\ddot{x}^a_{b,x1}u_{x1}} & H_{\ddot{x}^a_{b,x1}u_{x2}} & H_{\ddot{x}^a_{b,x1}\ddot{x}_{g,x}} \\ H_{\ddot{x}^a_{1,x1}u_{x1}} & H_{\ddot{x}^a_{1,x1}u_{x2}} & H_{\ddot{x}^a_{1,x1}\ddot{x}_{g,x}} \\ \vdots & \vdots & \vdots \\ H_{\ddot{x}^a_{6,x1}u_{x1}} & H_{\ddot{x}^a_{6,x1}u_{x2}} & H_{\ddot{x}^a_{6,x1}\ddot{x}_{g,x}} \\ H_{x_{b,x2}u_{x1}} & H_{x_{b,x2}u_{x2}} & H_{x_{b,x2}\ddot{x}_{g,x}} \\ H_{\ddot{x}^a_{b,x2}u_{x1}} & H_{\ddot{x}^a_{b,x2}u_{x2}} & H_{\ddot{x}^a_{b,x2}\ddot{x}_{g,x}} \\ H_{\ddot{x}^a_{1,x2}u_{x1}} & H_{\ddot{x}^a_{1,x2}u_{x2}} & H_{\ddot{x}^a_{1,x2}\ddot{x}_{g,x}} \\ \vdots & \vdots & \vdots \\ H_{\ddot{x}^a_{6,x2}u_{x1}} & H_{\ddot{x}^a_{6,x2}u_{x2}} & H_{\ddot{x}^a_{6,x2}\ddot{x}_{g,x}} \end{bmatrix} \tag{5.16}$$

where "a" denotes the absolute responses, i.e., $\ddot{x}^a$ indicates the absolute acceleration. To form the models in these two directions, the system in the y-direction contains two SIMO systems, while the system in the x-direction contains three SIMO systems.

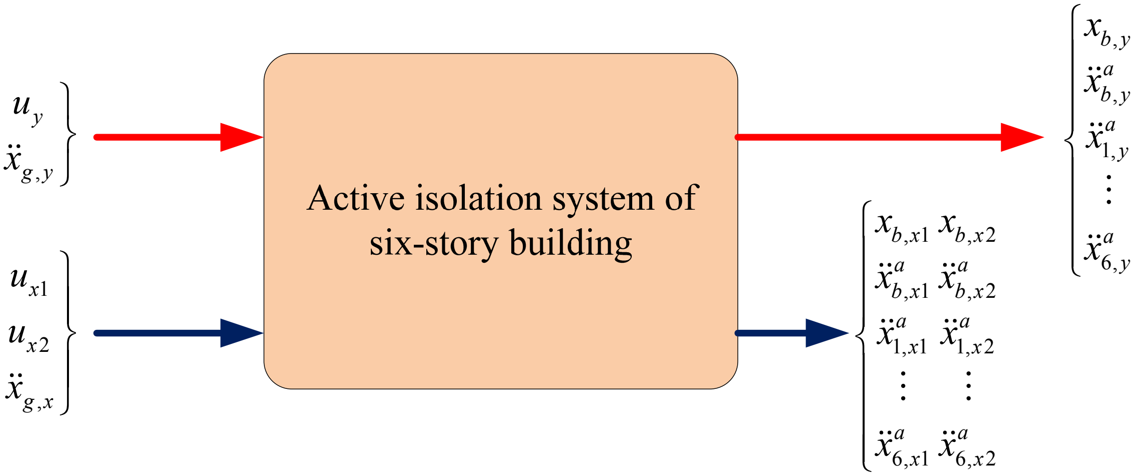

Figure 5.9. Schematic of the MIMO system for the active isolation of the six-story building.

According to the procedure of the system identification, the SIMO systems are first identified. The identified SIMO system models in the y-direction have 14 poles for the isolated building and 2-3 poles for the actuator, resulting in a total of 16-17 poles. The SIMO system models in the x-direction are more complex than those in the y-direction. For example, the number of poles for the isolated building in these SIMO system models in the x-direction is 14 for the translational degrees of freedom and 14 for the torsional degrees of freedom. The number of poles for the actuator in these models is 4-6 depending on the orders of the actuator models. Thus, the total number of poles for the SIMO systems in the x-direction is 32-34. Moreover, the identified SIMO system models in the x-direction may have a smaller number of poles than the predetermined number because some higher modes or some torsional modes are not visible in the experimental transfer functions. Therefore, the SIMO system identification for this problem should be carefully conducted and compared to the numerical model at the same time, in order to ensure the identified poles are compatible with those in the numerical model.

In this problem, all SIMO system models are obtained from the MFDID. First, the SIMO system identification of the *y*-direction models is addressed. The frequency ranges for the actuator command input and the ground excitation are 0-35 Hz. Although the setup of sensors includes the acceleration measurements using the wireless sensors at the 1st and 3rd floors, only the acceleration responses using the wired accelerometers are used for the system identification. The number of poles for the SIMO system from the actuator command input, e.g., the first column in $\mathbf{H}_y$ in Eq. (5.16), is 17, while the number of poles for the system from the ground acceleration, e.g., the second column in $\mathbf{H}_y$ in Eq. (5.16), is 15. The smaller number of the system from the ground acceleration is due to fact that the mode at the highest frequency is vague. As for the SIMO system identification of the *x*-direction models, a detailed discussion follows. The frequency of interest for the actuator command inputs and the ground excitation is 0-35 Hz and 0-25 Hz, respectively. Because the noisy phases reach above 25 Hz in the experimental transfer functions, the frequency of interest for the ground excitation is cut off at this frequency. The number of poles for the SIMO system from the *x*-actuator command inputs, e.g., the first and second columns in $\mathbf{H}_x$ in Eq. (5.16), is 29 for both, while the number of poles for the SIMO system from the ground excitation, e.g., the third column in $\mathbf{H}_x$ in Eq. (5.16), is 19. These numbers are less than the predetermined number (e.g., 32-34); however, the natural frequencies of the system, which are calculated from the poles, are comparable to the first few poles of the numerical model. Thus, the neglected poles at high frequencies are acceptable in this system identification. Therefore, all SIMO systems for this active isolation system are reasonably identified and are successfully comparable to the experimental transfer functions.

After identifying the SIMO systems successfully, the results of the MIMO system model in the *y*-direction using the system combination technique are presented first. Figure 5.10 shows the transfer functions from the *y*-actuator command input. Again, the identified transfer functions agree with the experimental results, mostly the zeros and poles at low frequencies. Those poorly identified poles or zeros at high frequencies should be carefully considered when the model is used in the control design. Moreover, most phases in the acceleration transfer functions of the model start at zero degrees, which is identical to the numerical model. As for the model from the ground excitation, Figure 5.11 shows the transfer functions, as compared to the experimental results. Most magnitudes and phases in the transfer functions accurately match the experimental results, although some phases have slight differences from the experimental results. Additionally, the magnitudes of the acceleration transfer functions typically start at 0 dB, which corresponds with the relationship of the dynamics of regular structural systems. Furthermore, the number of states in this model is increased to 18 because one mode at the high frequency cannot be matched in both SIMO systems. In order to obtain the highly accurate model, this mode is then viewed as the redundant mode. According to these results, the overall quality of this model is as good as expected.

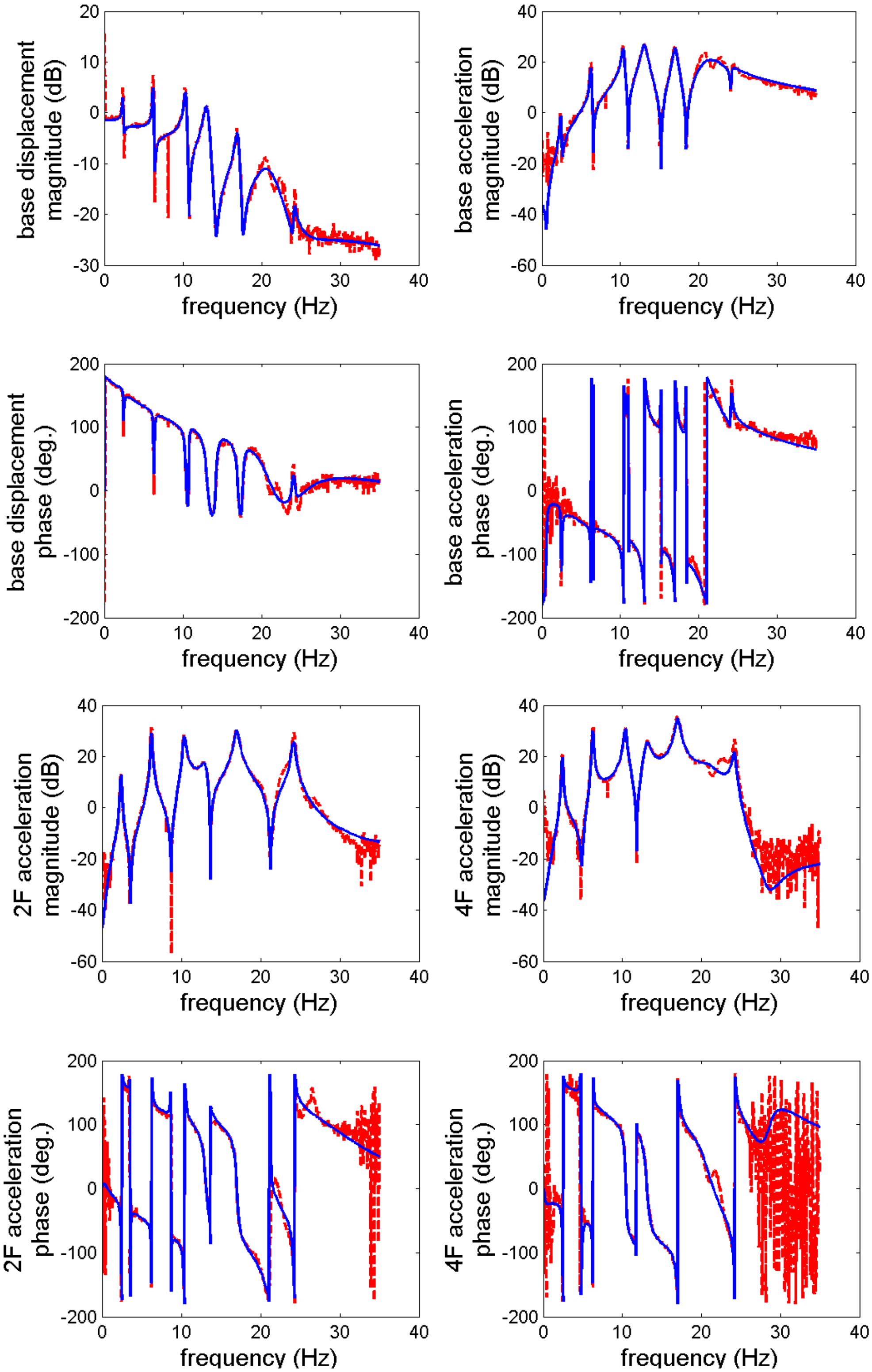

Figure 5.10. Transfer functions of the MIMO system model from the *y*-actuator input.

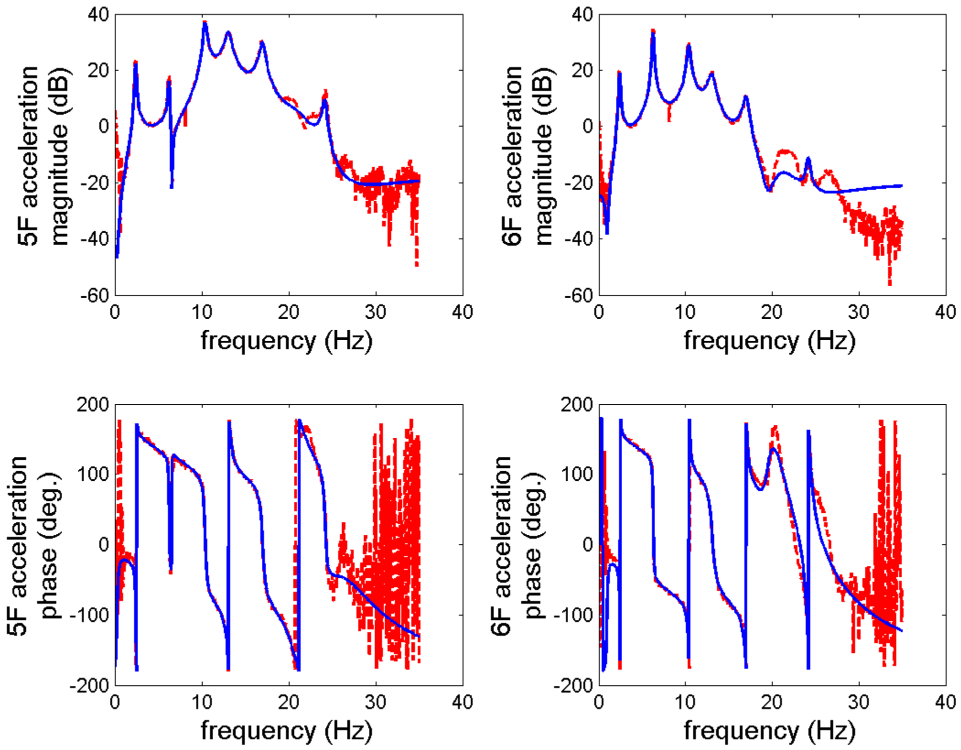

Figure 5.10. cont.

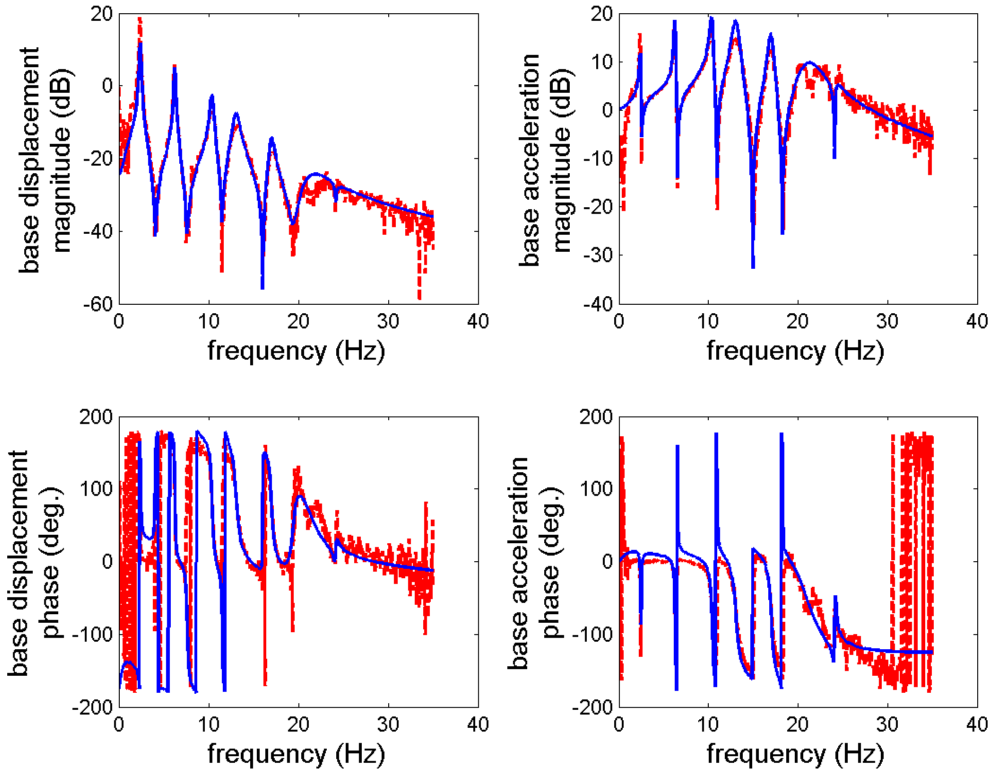

Figure 5.11. Transfer functions of the MIMO system model from the *y*-ground acceleration.

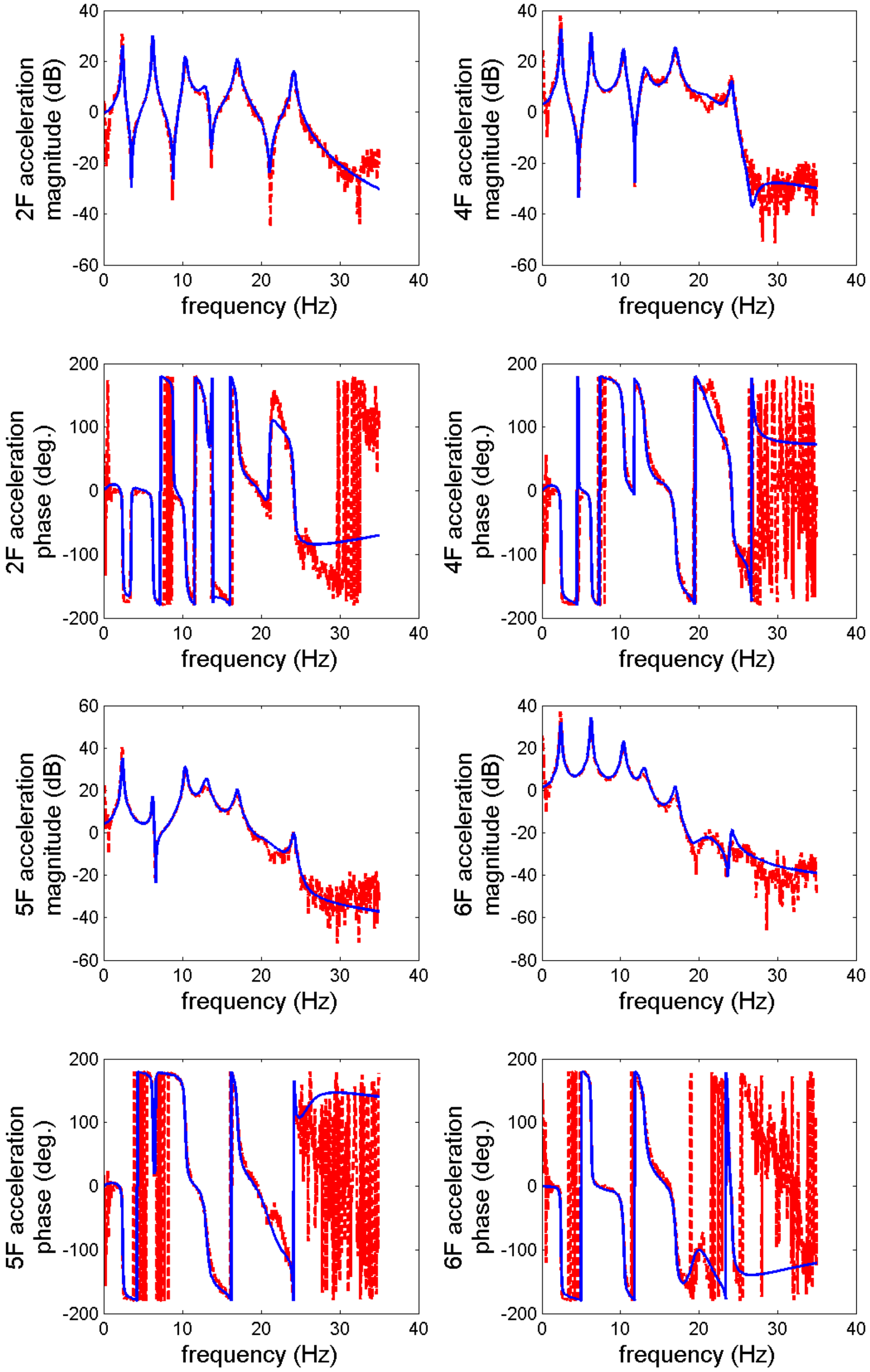

Figure 5.11. cont.

The system model along the *x*-direction is even more complex than that along the *y*-direction when applying the system combination technique. This system has three inputs of which two are the actuator input commands. Due to the symmetry of the building and bearings themselves, the torsion responses are mostly induced by these two actuators. The challenging part of the system combination of these SIMO system models is that some poles at high frequencies have very low magnitudes, resulting in the difficulty for the system combination. Thus, the difficulty leads some poles or modes to be uncontrollable to other inputs as the redundant modes, which cannot be combined. For example, the results shown in Figure 5.12 present the transfer functions from the *x*1-actuator in the responses along the *x*1-direction. The MIMO system model with the three inputs has 39 poles, while the SIMO system model for this *x*1-acutator command input originally has 29 poles. Before obtaining the complete MIMO system model with three inputs, the procedure of the system combination should be repeated two times. The first step of the system combination for this MIMO system model is to combine the SIMO system models for the two *x*-actuator command inputs, and then this combined system model is combined with the SIMO system model of the ground excitation. In the first step, total number of combined poles is 26 for the combined MIMO system model of two *x*-actuator command inputs, while the original SIMO system models for these two actuators have 29 each. After combining the SIMO system of the ground excitation to the combined *x*-actuator model, the total number of poles (or modes) is increased to 39. Because high noise perturbs the poles in the SIMO system of the ground excitation and these noised poles are not identified in the SIMO system, the number of poles after the second system combination is moderately increased. In addition, Figure 5.13 shows the results of the transfer functions from the *x*2-actuator in the responses along the *x*2-direction. Moreover, Figure 5.14 shows the results of the transfer function from the ground acceleration in the response along the $x1$-direction. According to Figures 5.9-5.11, the combined model represents this system well up to 30 Hz for the actuators and up to 20 Hz for the ground acceleration. The quality of the combined system model is acceptable because this model interprets the low-frequency behavior as well as the original SIMO system models. Although the number of poles after system combination has increased slightly, the final results show good agreement in the transfer functions, indicating this model can be applied in the control design.

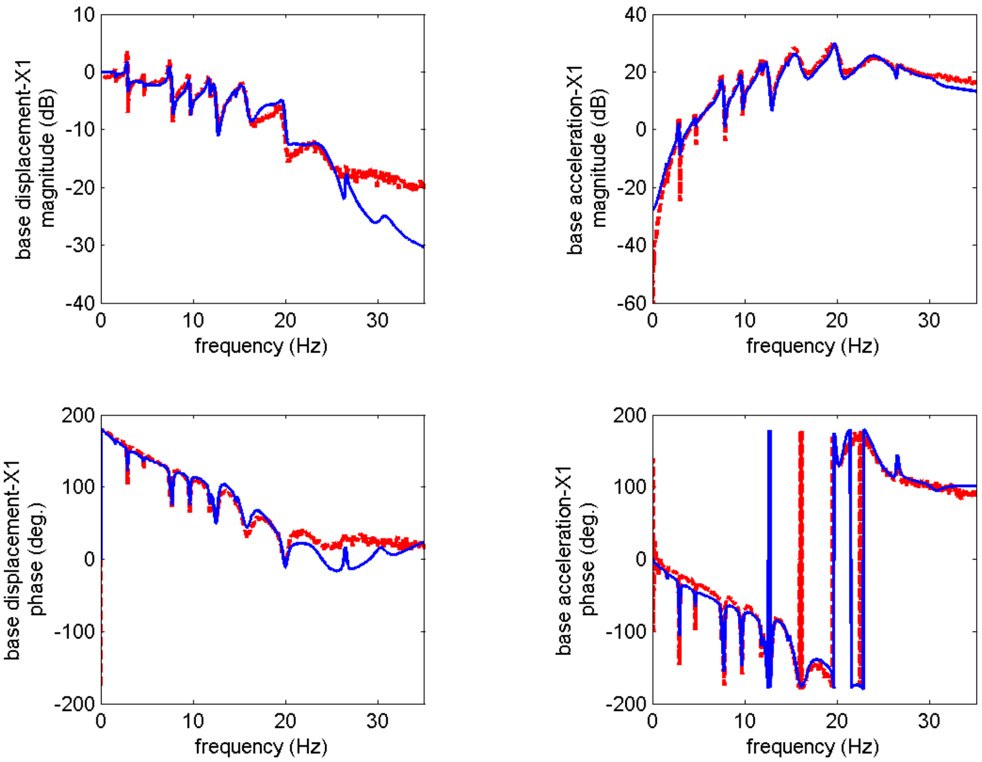

Figure 5.12. Transfer functions of the MIMO system model from the *x*1-actuator.

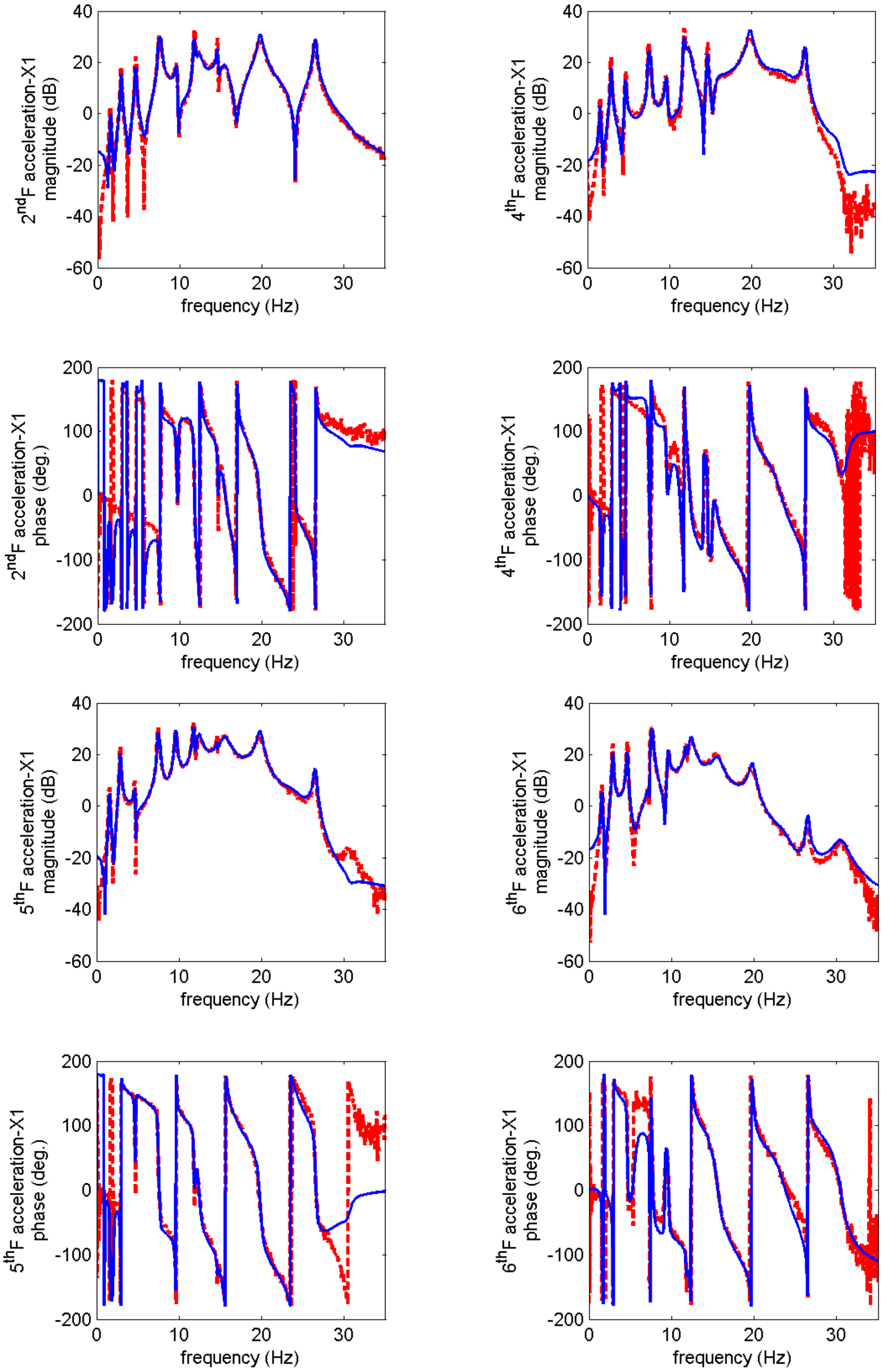

Figure 5.12. cont.

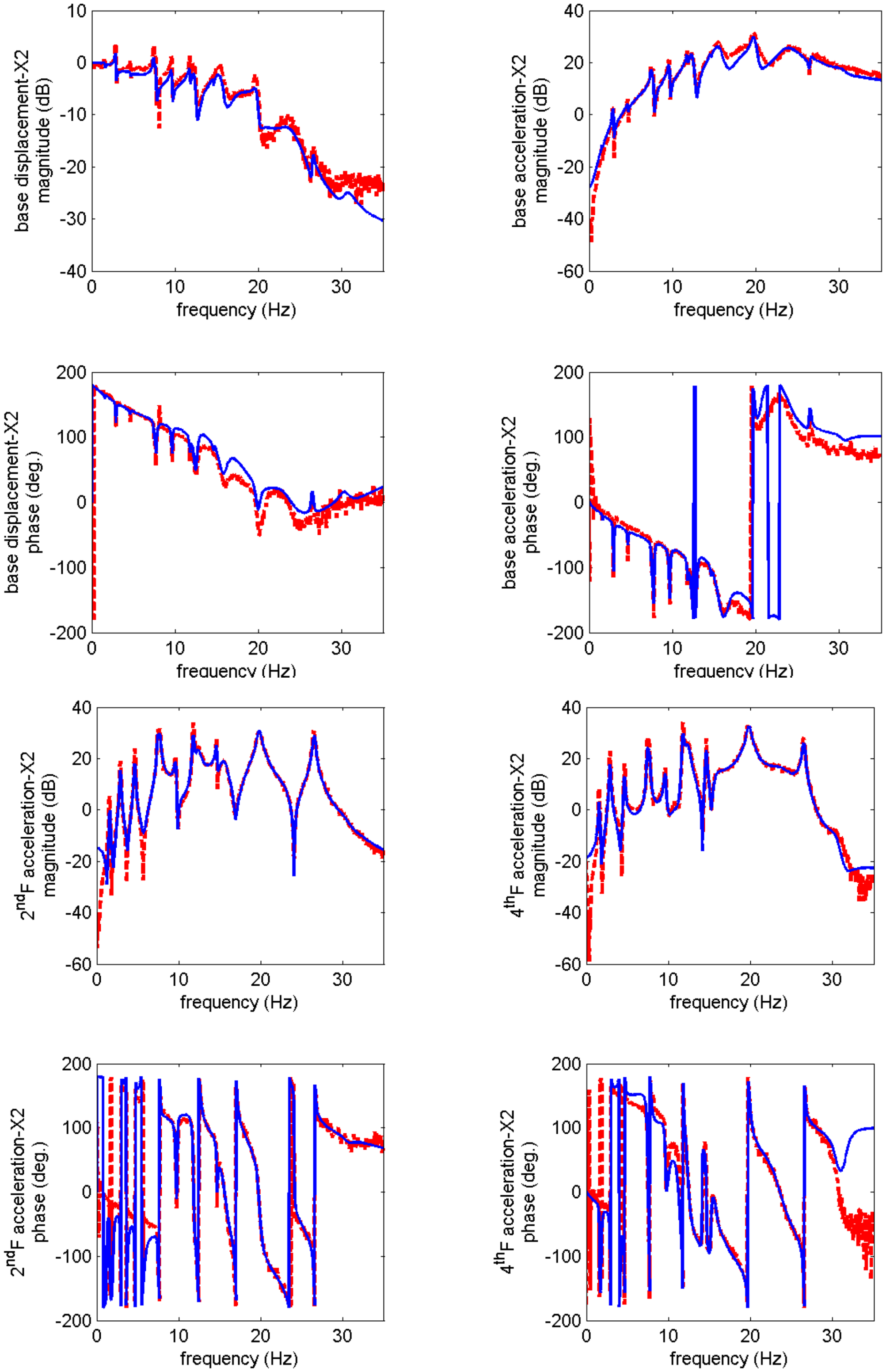

Figure 5.13. Transfer functions of the MIMO system model from the *x*2-actuator.

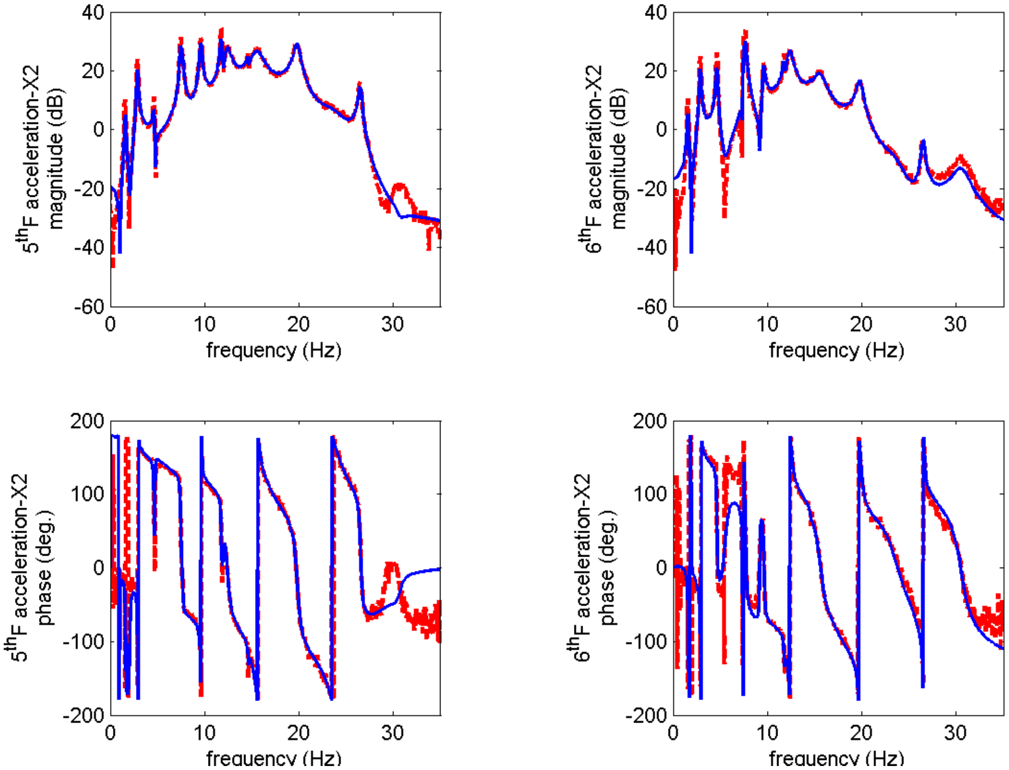

Figure 5.13. cont.

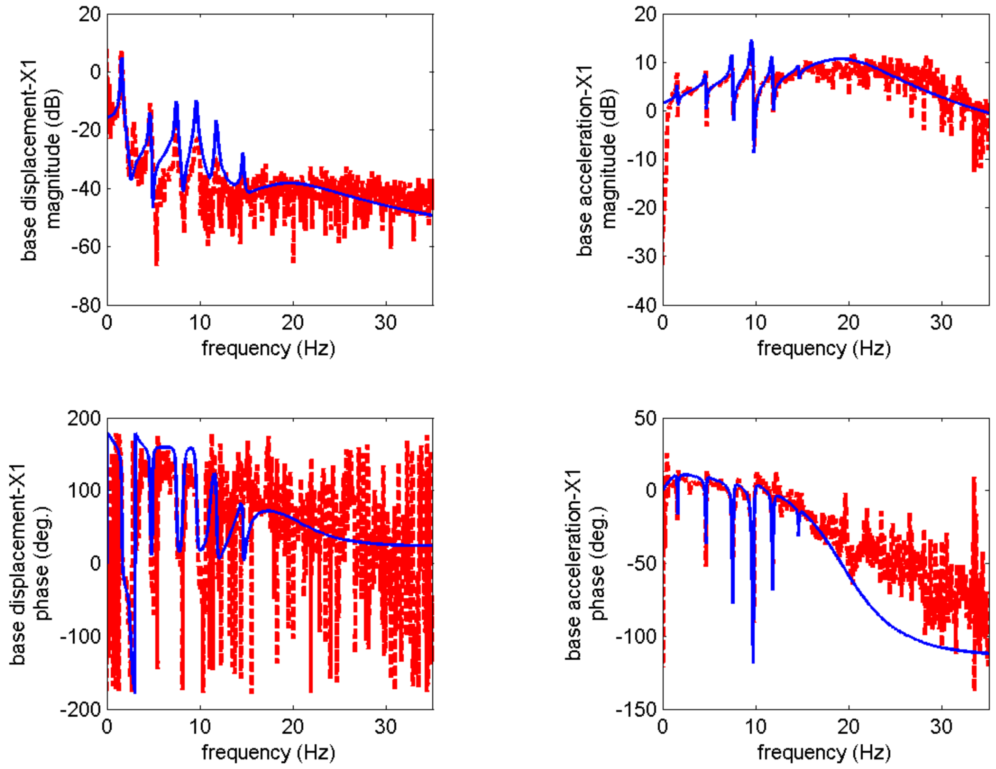

Figure 5.14. Transfer functions of the MIMO system model from the *x*-ground acceleration.

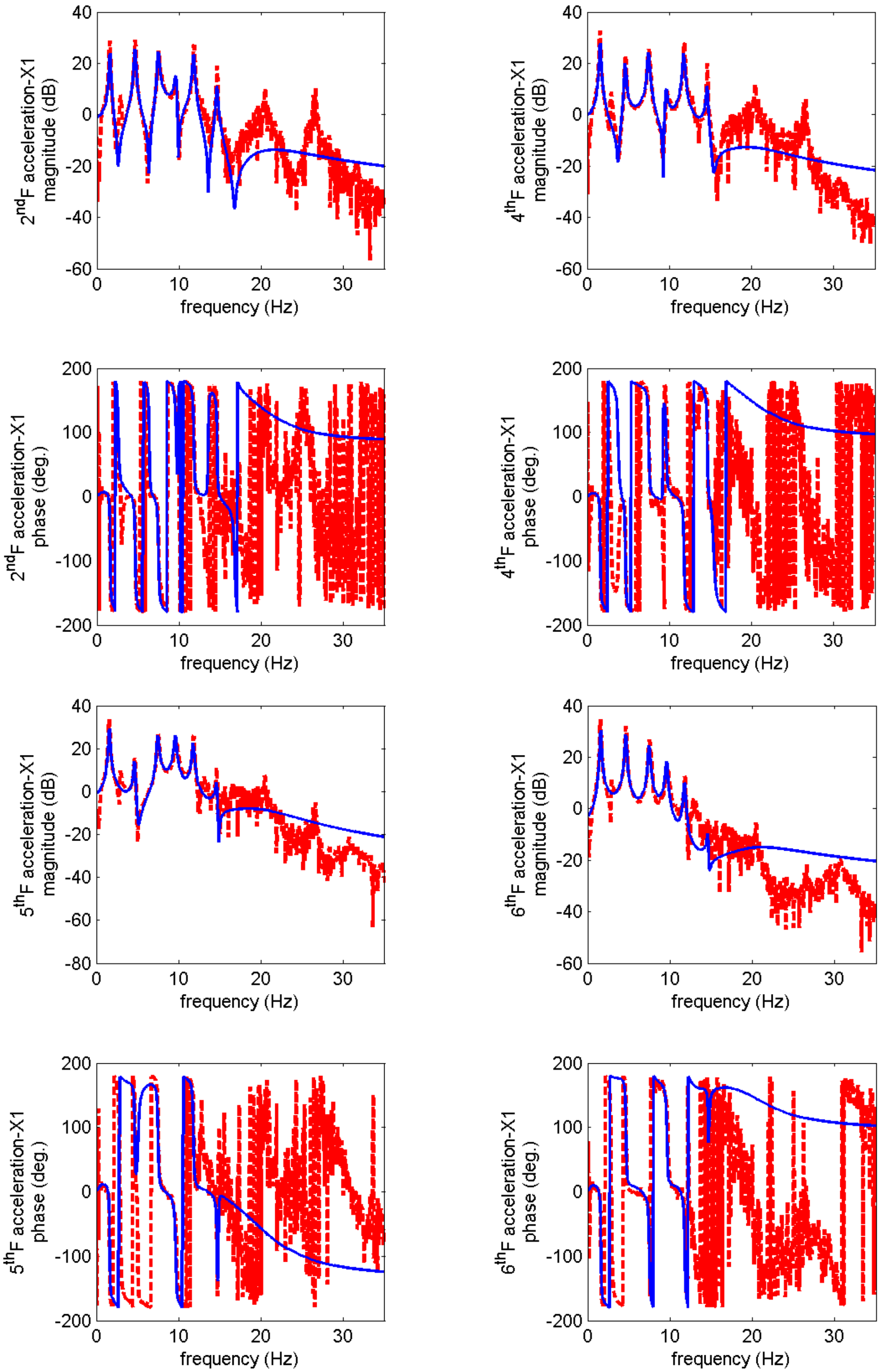

Figure 5.14. cont.

5.6 Summary

This section presented the identification procedure for building the system model for use in the control design. This procedure included the SIMO system identification and the system combination. The SIMO system identification is employed to obtain the system models with respect to the inputs, such as the actuator command inputs and the ground excitations. The system combination is used to derive an MIMO system which represents the physical behavior of the system, e.g., the controllable and observable states with respect to all inputs. Moreover, two techniques, which have different advantages for the SIMO system identification, were provided in this chapter. The system combination technique contained the options to weigh the SIMO/MIMO system model which has more relevance than the other system model. In addition to the system identification procedure, two examples based on the active isolation systems of the two-story and six-story buildings were given. The identified models in these two examples will be used for the control design in Chapter 6. In Sections 5.4 and 5.5, the results presented have shown the comparable transfer functions from the identified models, and the system identification procedure was validated through these examples. Using this system identification procedure, the resulting model will not only capture the dynamic characteristics (e.g., the natural frequencies and damping) of the system but also promise the controllability of the control devices (e.g., the actuators) over low frequencies.

CHAPTER 6 CONTROL DESIGN

A control problem always shows a trade-off option between high performance and robust stability. A highly authoritative controller usually results in better performance, while uncertainties in the system model or the control implementation may decrease performance and even produce instabilities. Spencer et al. (1994) have shown that H_2/LQG control methods not only effectively reduce the contribution from these uncertainties to the system but also guarantee high control performance against earthquakes. In this research, the control design still depends on this H_2/LQG control algorithm to design the controllers for the control implementation of active isolation systems. To further consider the seismic effect in the controller, the control design is adequately modified with incorporation of the Kanai-Tajimi filter (Ramallo et al. 2002 and Yoshioka et al. 2002). Therefore, this section begins by reviewing the H_2/LQG control algorithm with and without the Kanai-Tajimi filter in control design. Thus, different control strategies are designed based on different control objectives and different measurements for feedback control in seeking high performance. Due to the trade-off problem, a design procedure for considerations with uncertainties and control performance is also introduced in this section. Finally, two examples using the active isolation system of the two-story and six-story buildings are employed to illustrate the control design for the control implementation in Chapters 7 and 8.

6.1 Review of H_2/LQG control algorithm

Consider the block diagram shown in Figure 6.1 for a general seismic control problem using the feedback control. Similar to Eq. (4.16), $\ddot{\mathbf{x}}_g$ represents the vector of the ground excitations, $\mathbf{y}$ is the measured output vector of structural responses, and $\mathbf{u}$ is the control input vector from the designed controller. The regulated output vector **z** may be comprised of any linear combination of the states of the system and components of the control input vector **u**, thus allowing a broad range of control design objectives to be formulated through appropriate choice of elements of **z**. Generally speaking, the vector **z** could be directly selected from the output vector **y**. If further considerations are given to design, the vector **z** could be modified from the output vector **y**, i.e., using a weighting function in the time or frequency domain. Because the control-oriented problem derives the model from system identification, the vector **z** using a function of the system states does not exist. Hence, the concept using the vectors, **y** and **z**, realizes the H_2/LQG control methods to develop the controller.

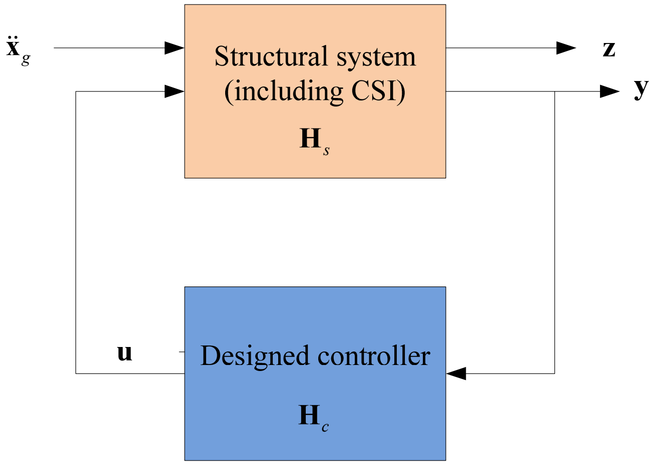

Figure 6.1. Block diagram for a general feedback control problem.

To illustrate the control problem for control design, consider a structural system under seismic excitations $\ddot{\mathbf{x}}_g$ and control input commands **u**. The linear time-invariant state-space representation of this input-output structural system with the control-structure interaction is presented as

$$\begin{aligned}\dot{\mathbf{x}} &= \mathbf{A}\mathbf{x} + \mathbf{B}\mathbf{u} + \mathbf{E}\ddot{\mathbf{x}}_g \\ \mathbf{y} &= \mathbf{C}\mathbf{x} + \mathbf{D}\mathbf{u} + \mathbf{F}\ddot{\mathbf{x}}_g + \mathbf{v} \\ \mathbf{z} &= \mathbf{C}_\mathbf{z}\mathbf{x} + \mathbf{D}_\mathbf{z}\mathrm{u}\end{aligned} \tag{6.1}$$

where **x** is the state vector, which may not represent the structural displacements and velocities as Eq. (4.16) due to the identified model (see Chapter 5); the measured output vector **y** depends on the sensors installed in the structural system; **z** is the vector to be regulated without considering the measurement noise. Note that the matrices, **D**, **F**, and $\mathbf{D_z}$, are zero for the active isolation systems due to the control-structure interaction. In Eq. (6.1), the structural system can be represented by the inputs $\ddot{\mathbf{x}}_g$ and **u** and the output **y**; however, this equation can be also interpreted as a system plant for control design. Equivalently, the system plant can be modified appropriately for control design if the modification still stabilizes the structural system. For the control design, the H_2/LQG control methods used in this research generate the controller based on Eq. (6.1) with adequate modification, such as weighting by the Kanai-Tajimi filter.

Before deriving the controller using the H_2/LQG control methods, a modified system plant is introduced. The H_2/LQG control methods are developed to regulate the system responses over a wide-band excitation (e.g., a wide-band $\ddot{\mathbf{x}}_g$ in Eq. (6.1)). However, this controller, derived from this definition, may reduce performance if the system vibrates under an excitation in a specific band, such as earthquakes. To incorporate the effect of earthquakes for a seismic control problem, a shaping filter for the excitation inputs of a system is employed to reasonably adjust the system plant. For example, consider a generalized filter in the state-space representation for the inputs, given by

$$\begin{aligned}\dot{\mathbf{x}}_{in} &= \mathbf{A}_{in}\mathbf{x}_{in} + \mathbf{B}_{in}\mathbf{w} \\ \ddot{\mathbf{x}}_g &= \mathbf{C}_{in}\mathbf{x}_{in}\end{aligned} \tag{6.2}$$

where $\mathbf{A}_{in}$, $\mathbf{B}_{in}$, and $\mathbf{C}_{in}$ are the matrices which satisfy the definition of the state-space representation without inducing instability, and **w** is the wide-band white noise. In addition to the shaping filter for excitation inputs, a shaping filter for the regulated outputs can be introduced in the system plant for control design. As mentioned before, the diagram for a general control problem in Figure 6.1 that illustrates the regulated output **z** is a part of the measured output **y**. In most control problems, the output noise may contribute to the high frequency components. The modification of the regulated output **z** could be, for instance, a low-pass filter to lower the noise contributions. The shaping filter for the regulated outputs is based on this assumption and then given by

$$\begin{aligned} \dot{\mathbf{x}}_{out} &= \mathbf{A}\mathbf{x}_{out} + \mathbf{B}_{out}\mathbf{z} \\ \mathbf{z}_m &= \mathbf{C}_{out}\mathbf{x}_{out} + \mathbf{D}_{out}\mathbf{z} \end{aligned} \tag{6.3}$$

where $\mathbf{A}_{out}$, $\mathbf{B}_{out}$, $\mathbf{C}_{out}$ and $\mathbf{D}_{out}$ are, again, the matrices which satisfy the definition of the state-space representation without inducing instability, and $\mathbf{z}_m$ is the modified vector from the regulated outputs. Note that the dimension of the vector $\mathbf{z}_m$ may be different from that of the vector **z** in this equation. To merge these two types of shaping filters into the system plant, the augmented system is adjusted from Eq. (6.1) and then written by

$$\begin{aligned} \dot{\bar{\mathbf{x}}} &= \bar{\mathbf{A}}\bar{\mathbf{x}} + \bar{\mathbf{B}}\mathbf{u} + \bar{\mathbf{E}}\mathbf{w} \\ \bar{\mathbf{y}} &= \bar{\mathbf{C}}\bar{\mathbf{x}} + \bar{\mathbf{D}}\mathbf{u} + \mathbf{v} \\ \bar{\mathbf{z}} &= \bar{\mathbf{C}}_{\mathbf{z}}\bar{\mathbf{x}} + \bar{\mathbf{D}}_{\mathbf{z}}\mathbf{u} \end{aligned} \tag{6.4}$$

with

$$\bar{\mathbf{A}} = \begin{bmatrix} \mathbf{A} & \mathbf{E}\mathbf{C}_{in} & \mathbf{0} \\ \mathbf{0} & \mathbf{A}_{in} & \mathbf{0} \\ \mathbf{B}_{out}\mathbf{C}_{\mathbf{z}} & \mathbf{0} & \mathbf{A}_{out} \end{bmatrix},\ \bar{\mathbf{B}} = \begin{bmatrix} \mathbf{B} \\ \mathbf{0} \\ \mathbf{B}_{out}\mathbf{D}_{\mathbf{z}} \end{bmatrix},\ \bar{\mathbf{E}} = \begin{bmatrix} \mathbf{0} \\ \mathbf{B}_{in} \\ \mathbf{0} \end{bmatrix},\ \bar{\mathbf{y}} = \begin{bmatrix} \mathbf{y} \\ \ddot{\mathbf{x}}_g \end{bmatrix},\ \bar{\mathbf{z}} = \begin{bmatrix} \mathbf{z} \\ \mathbf{z}_m \end{bmatrix}$$

$$\bar{\mathbf{x}} = \begin{bmatrix} \mathbf{x} \\ \mathbf{x}_{in} \\ \mathbf{x}_{out} \end{bmatrix}, \ \bar{\mathbf{C}} = \begin{bmatrix} \mathbf{C} & \mathbf{FC}_{in} & \mathbf{0} \\ \mathbf{0} & \mathbf{C}_{in} & \mathbf{0} \end{bmatrix}, \ \bar{\mathbf{D}} = \begin{bmatrix} \mathbf{D} \\ \mathbf{0} \end{bmatrix}, \ \bar{\mathbf{C}}_{\mathbf{z}} = \begin{bmatrix} \mathbf{C}_{\mathbf{z}} & \mathbf{0} & \mathbf{0} \\ \mathbf{D}_{out}\mathbf{C}_{\mathbf{z}} & \mathbf{0} & \mathbf{C}_{out} \end{bmatrix}, \ \bar{\mathbf{D}}_{\mathbf{z}} = \begin{bmatrix} \mathbf{D}_{\mathbf{z}} \\ \mathbf{D}_{out}\mathbf{D}_{\mathbf{z}} \end{bmatrix}$$

where the measured output vector $\bar{\mathbf{y}}$ is augmented to include the excitation inputs, and the regulated output vector $\bar{\mathbf{z}}$ considers the original regulated outputs and the filtered ones. Figure 6.2 also illustrates the augmented system plant in order to compare it with the original one as shown in Figure 6.1. According to the augmented system plant in Eq. (6.4), a controller used to regulate the system can be robustly developed using the H_2/LQG control methods.

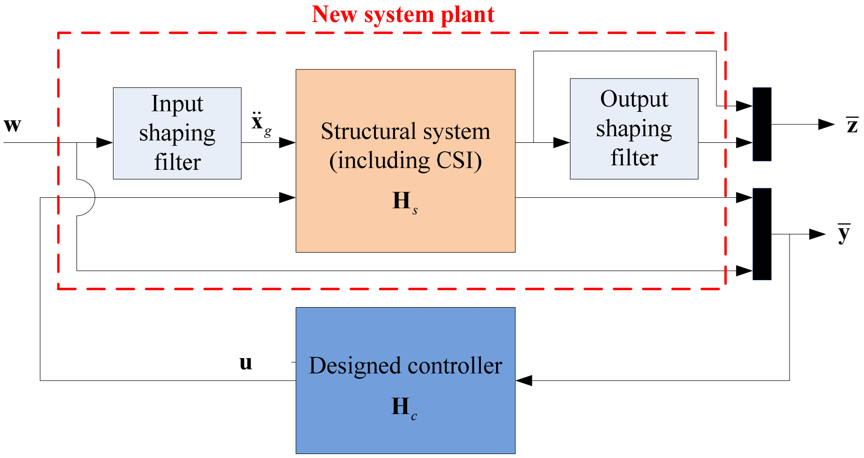

Figure 6.2. A new system plant for control design.

The H_2/LQG control methods are a two-step design procedure which includes the linear quadratic regulation (LQG) and the Kalman estimator. First, the LQR results in an optimal control gain, which is derived from a specific objective function, J, given by

$$J = \lim_{T \to \infty} \frac{1}{T} E\left[\int_0^T \left(\bar{\mathbf{z}}^T(t)\mathbf{Q}_{\mathbf{z}}\bar{\mathbf{z}}(t) + \mathbf{u}^T(t)\mathbf{R}_{\mathbf{u}}\mathbf{u}(t) \right) dt \right] \tag{6.5}$$

where $\mathbf{Q}_{\mathbf{z}}$ is the semi-definite matrix of a weighting function for the new regulated output vector $\bar{\mathbf{z}}$, $\mathbf{R}_{\mathbf{u}}$ is the positive-definite matrix of a weighting function for the control input commands, and

$E[\bullet]$ denotes the expected value. Solving the Riccati equation for Eq. (6.5), the optimal control gain can be obtained by

$$\mathbf{u}(t) = -\mathbf{K}\bar{\mathbf{x}}(t) = -\left(\mathbf{R_u} + \bar{\mathbf{D}}_\mathbf{z}^T\mathbf{Q_z}\bar{\mathbf{D}}_\mathbf{z}\right)^{-1}\left(\bar{\mathbf{B}}^T\mathbf{P} + \bar{\mathbf{D}}_\mathbf{z}^T\mathbf{Q_z}\bar{\mathbf{C}}_\mathbf{z}\right)\bar{\mathbf{x}}(t) \tag{6.6}$$

where

$$\mathbf{P}\bar{\mathbf{A}} + \bar{\mathbf{A}}^T\mathbf{P} - \left(\mathbf{P}\bar{\mathbf{B}} + \bar{\mathbf{C}}_\mathbf{z}^T\mathbf{Q_z}\bar{\mathbf{D}}_\mathbf{z}\right)\left(\mathbf{R_u} + \bar{\mathbf{D}}_\mathbf{z}^T\mathbf{Q_z}\bar{\mathbf{D}}_\mathbf{z}\right)^{-1}\left(\mathbf{P}\bar{\mathbf{B}} + \bar{\mathbf{C}}_\mathbf{z}^T\mathbf{Q_z}\bar{\mathbf{D}}_\mathbf{z}\right) + \mathbf{Q_z} = \mathbf{0} \tag{6.7}$$

The optimal control gain is the matrix, **K**, with respect to the states of the augmented system plant. Eq. (6.7) presents the Riccati equation of which the solution, **P**, is a symmetric and positive-definite matrix. By specifying the appropriate matrix weighting functions, $\mathbf{Q_z}$ and $\mathbf{R_u}$, the optimal control commands, **u**, can be designed to regulate the objective vector, $\bar{\mathbf{z}}$, using the solution of Eq. (6.7).

After obtaining the optimal control gain from the objective function in Eq. (6.5), the Kalman estimator is then designed to realize the H_2/LQG control. Typically, the states are barely available in control problems, especially the states in the identified models. Since the states are obtained with difficulty from a system plant, the alternative option is an observer, which can convert the measurements to approach the states of the system plant, such that

$$\dot{\hat{\mathbf{x}}} = \bar{\mathbf{A}}\hat{\mathbf{x}} + \bar{\mathbf{B}}\mathbf{u} + \mathbf{L}\left(\bar{\mathbf{y}} - \left(\bar{\mathbf{C}}\hat{\mathbf{x}} + \bar{\mathbf{D}}\mathbf{u}\right)\right) \tag{6.8}$$

where $\bar{\mathbf{y}}$ is the measured output directly from the readings of sensors, and **L** is the observer gain. The observer gain can be obtained through several methods, e.g., the pole placement; however, the observer can be optimally designed using the Kalman estimator theory. Similarly to the LQR algorithm, the derivation of the Kalman estimator solves the other form of the Riccati equation, given by

$$\mathbf{L} = \mathbf{M}\bar{\mathbf{C}}^T\mathbf{R}_\mathbf{v}^{-1} \tag{6.9}$$

where

$$\mathbf{M}\bar{\mathbf{A}}^T + \bar{\mathbf{A}}\mathbf{M} - \mathbf{M}\bar{\mathbf{C}}^T\mathbf{R}_\mathbf{v}^{-1}\bar{\mathbf{C}}\mathbf{M} + \mathbf{Q}_\mathbf{w} = \mathbf{0} \tag{6.10}$$

$$E\left[\mathbf{w}\mathbf{w}^T\right] = \mathbf{Q}_\mathbf{w},\ E\left[\mathbf{v}\mathbf{v}^T\right] = \mathbf{R}_\mathbf{v},\ E\left[\mathbf{w}\mathbf{v}^T\right] = \mathbf{0}$$

In both Eqs. (6.9) and (6.10), $\mathbf{Q}_\mathbf{w}$ is the semi-definite matrix of a weighting function for the wide-band excitation input vector, $\mathbf{w}$; $\mathbf{R}_\mathbf{v}$ is the positive-definite matrix of a weighting function for the measurement noise vector, $\mathbf{v}$; and $\mathbf{M}$ is a symmetric and positive-definite matrix solution of the Riccati equation for the optimal observer. The Kalman estimator, after assigning $\mathbf{Q}_\mathbf{w}$ and $\mathbf{R}_\mathbf{v}$, can be determined and then results in an optimal observer for estimating the states of the new system plant as shown in Figure 6.2.

Through this two-step design procedure, an optimal feedback controller, which is combined from Eqs. (6.6) and (6.8), is derived to regulate the structural system responses, given by

$$\mathbf{H}_c(s): \begin{cases} \dot{\hat{\mathbf{x}}} = \left(\bar{\mathbf{A}} - \bar{\mathbf{B}}\mathbf{K} - \mathbf{L}\bar{\mathbf{C}} + \mathbf{L}\bar{\mathbf{D}}\mathbf{K}\right)\hat{\mathbf{x}} + \mathbf{L}\bar{\mathbf{y}} \\ \mathbf{u} = -\mathbf{K}\hat{\mathbf{x}} \end{cases} \tag{6.11}$$

or

$$\mathbf{H}_c(s): \begin{cases} \dot{\hat{\mathbf{x}}} = \mathbf{A}_c\hat{\mathbf{x}} + \mathbf{L}_1\mathbf{y} + \mathbf{L}_2\ddot{\mathbf{x}}_g \\ \mathbf{u} = -\mathbf{K}\hat{\mathbf{x}} \end{cases} \tag{6.12}$$

where

$$\mathbf{L}\bar{\mathbf{C}} = \begin{bmatrix}\mathbf{L}_1\mathbf{C} & \mathbf{L}_1\mathbf{F}\mathbf{C}_{in} + \mathbf{L}_2\mathbf{C}_{in} & \mathbf{0}\end{bmatrix},\ \mathbf{L}\bar{\mathbf{y}} = \begin{bmatrix}\mathbf{L}_1 & \mathbf{L}_2\end{bmatrix}\begin{bmatrix}\mathbf{y} \\ \ddot{\mathbf{x}}_g\end{bmatrix},\ \mathbf{L}\bar{\mathbf{D}}\mathbf{K} = \mathbf{L}_1\mathbf{D}\mathbf{K}$$

This equation expresses a differential controller in a state-space representation, while this controller can be also represented using the transfer function model as $\mathbf{H}_c(s)$. If a closed-loop control system, as shown in Figure 6.1, is considered, the structural system in Eq. (6.1) after applying the feedback control is written by

$$\begin{aligned}
\begin{bmatrix} \dot{\mathbf{x}} \\ \dot{\hat{\mathbf{x}}} \end{bmatrix} &= \begin{bmatrix} \mathbf{A} & -\mathbf{BK} \\ \mathbf{L}_1\mathbf{C} & \mathbf{A}_c - \mathbf{L}_1\mathbf{DK} \end{bmatrix} \begin{bmatrix} \mathbf{x} \\ \hat{\mathbf{x}} \end{bmatrix} + \begin{bmatrix} \mathbf{E} \\ \mathbf{L}_1\mathbf{F} + \mathbf{L}_2 \end{bmatrix} \ddot{\mathbf{x}}_g \\
\mathbf{y} &= \begin{bmatrix} \mathbf{C} & \mathbf{DK} \end{bmatrix} \begin{bmatrix} \mathbf{x} \\ \hat{\mathbf{x}} \end{bmatrix} + \mathbf{F}\ddot{\mathbf{x}}_g + \mathbf{v} \qquad (6.13) \\
\mathbf{z} &= \begin{bmatrix} \mathbf{C}_\mathbf{z} & \mathbf{D}_\mathbf{z}\mathbf{K} \end{bmatrix} \begin{bmatrix} \mathbf{x} \\ \hat{\mathbf{x}} \end{bmatrix}
\end{aligned}$$

or

$$\begin{aligned}
\mathbf{H}_{\mathbf{y}\ddot{\mathbf{x}}_g}^{CL} &= \left(\mathbf{I} - \mathbf{H}_{\mathbf{yu}}\mathbf{H}_{\mathbf{uy}}\right)^{-1} \left(\mathbf{H}_{\mathbf{y}\ddot{\mathbf{x}}_g} + \mathbf{H}_{\mathbf{yu}}\mathbf{H}_{\mathbf{u}\ddot{\mathbf{x}}_g}\right) \\
\mathbf{H}_{\mathbf{z}\ddot{\mathbf{x}}_g}^{CL} &= \left(\mathbf{I} - \mathbf{H}_{\mathbf{zu}}\mathbf{H}_{\mathbf{uy}}\mathbf{T}_{\mathbf{yz}}\right)^{-1} \left(\mathbf{H}_{\mathbf{z}\ddot{\mathbf{x}}_g} + \mathbf{H}_{\mathbf{zu}}\mathbf{H}_{\mathbf{u}\ddot{\mathbf{x}}_g}\right)
\end{aligned} \qquad (6.14)$$

with

$$\mathbf{H}_c(s) = \begin{bmatrix} \mathbf{H}_{\mathbf{uy}} & \mathbf{H}_{\mathbf{u}\ddot{\mathbf{x}}_g} \end{bmatrix}, \ \mathbf{y} = \mathbf{T}_{\mathbf{yz}}\mathbf{z}$$

$$\mathbf{H}_s(s) = \begin{bmatrix} \mathbf{H}_{\mathbf{yu}} & \mathbf{H}_{\mathbf{y}\ddot{\mathbf{x}}_g} \\ \mathbf{H}_{\mathbf{zu}} & \mathbf{H}_{\mathbf{z}\ddot{\mathbf{x}}_g} \end{bmatrix}$$

where $\mathbf{H}_{\mathbf{y}\ddot{\mathbf{x}}_g}^{CL}$ and $\mathbf{H}_{\mathbf{z}\ddot{\mathbf{x}}_g}^{CL}$ denote the closed-loop transfer functions from the excitation input $\ddot{\mathbf{x}}_g$ to the measured output **y** and the regulated output **z**, respectively. As a result of Eq. (6.13) or (6.14), the structural system with the H_2/LQG controller stabilizes the closed-loop system and promises to regulate the structural responses.

To further extend the H_2/LQG control methods for structural control applications, some discussions are drawn as follows. First, Eq. (6.5) does not consider the coupled term between the modified regulated output vector $\bar{\mathbf{z}}$ and the control input commands **u**. Additional criteria should be considered, e.g., the modified $\mathbf{Q_z}$ and $\mathbf{R_u}$, due to the coupled term. Similarly, the Riccati equation in Eq. (6.10) can include the effect from the coupled **w** and **v**, such as $E\left[\mathbf{w}\mathbf{v}^T\right] \neq \mathbf{0}$, if necessary. Again, the corresponding criteria for the modified $\mathbf{Q}_\mathbf{w}$ and $\mathbf{R}_\mathbf{v}$ should be considered. Moreover, the augmented system plant in Eq. (6.4) contains two inherent conditions. The first one is that the wide-band excitation input **w** is only controllable to the original states **x** and the states of the input shaping filter $\mathbf{x}_{in}$, such that

$$\left(\begin{bmatrix} \mathbf{A} & \mathbf{E}\mathbf{C}_{in} \\ \mathbf{0} & \mathbf{A}_{in} \end{bmatrix}, \begin{bmatrix} \mathbf{0} \\ \mathbf{B}_{in} \end{bmatrix}\right) \text{ is controllable.}$$

The second condition is that the control input commands **u** is only controllable to the original states **x** and the states of the output shaping filter $\mathbf{x}_{out}$, such that

$$\left(\begin{bmatrix} \mathbf{A} & \mathbf{0} \\ \mathbf{B}_{out}\mathbf{C}_\mathbf{z} & \mathbf{A}_{out} \end{bmatrix}, \begin{bmatrix} \mathbf{B} \\ \mathbf{B}_{out}\mathbf{D}_\mathbf{z} \end{bmatrix}\right) \text{ is controllable.}$$

These two conditions satisfy the “separation principle”, which says that the H_2/LQG control algorithm can design the control gain from the LQR algorithm and the observer using the Kalman estimator separately. Thus, the separation principle also implies that the eigenvalues of the closed-loop system are equal to two subsystems in accordance to the LQR design and the Kalman estimator design, such that

$$eig\left(\begin{bmatrix} \mathbf{A} & -\overline{\mathbf{B}}\mathbf{K} \\ \mathbf{L}_1\overline{\mathbf{C}} & \mathbf{A}_c - \mathbf{L}_1\overline{\mathbf{D}}\mathbf{K} \end{bmatrix}\right) \text{ are equal to } eig\left(\begin{bmatrix} \mathbf{A} & \mathbf{0} \\ \mathbf{B}_{out}\mathbf{C}_\mathbf{z} & \mathbf{A}_{out} \end{bmatrix} - \begin{bmatrix} \mathbf{B} \\ \mathbf{B}_{out}\mathbf{D}_\mathbf{z} \end{bmatrix} \begin{bmatrix} \mathbf{K}_1 & \mathbf{K}_3 \end{bmatrix}\right) \text{ and}$$

$$eig\left(\begin{bmatrix} \mathbf{A} & \mathbf{E}\mathbf{C}_{in} \\ \mathbf{0} & \mathbf{A}_{in} \end{bmatrix} - \begin{bmatrix} \mathbf{L}_{11} & \mathbf{L}_{21} \\ \mathbf{L}_{12} & \mathbf{L}_{22} \end{bmatrix} \begin{bmatrix} \mathbf{C} & \mathbf{F}\mathbf{C}_{in} \\ \mathbf{0} & \mathbf{C}_{in} \end{bmatrix}\right)$$

where

$$\overline{\mathbf{B}}\mathbf{K} = \begin{bmatrix} \mathbf{B} \\ \mathbf{0} \\ \mathbf{B}_{out}\mathbf{D}_z \end{bmatrix} \begin{bmatrix} \mathbf{K}_1 & \mathbf{K}_2 & \mathbf{K}_3 \end{bmatrix},\ \mathbf{L}\overline{\mathbf{C}} = \begin{bmatrix} \mathbf{L}_1 & \mathbf{L}_2 \end{bmatrix}\overline{\mathbf{C}} = \begin{bmatrix} \mathbf{L}_{11} & \mathbf{L}_{21} \\ \mathbf{L}_{12} & \mathbf{L}_{22} \\ \mathbf{L}_{13} & \mathbf{L}_{23} \end{bmatrix} \begin{bmatrix} \mathbf{C} & \mathbf{F}\mathbf{C}_{in} & \mathbf{0} \\ \mathbf{0} & \mathbf{C}_{in} & \mathbf{0} \end{bmatrix}$$

$eig(\bullet)$ denotes the eigenvalues of a square matrix. All the eigenvalues described above satisfy the criteria for stability (i.e., eigenvalues of uncontrollable states lie in the left-half complex plane) as well as the stabilizing issue (i.e., eigenvalues of controllable states still lie in the left-half complex plane in the closed-loop system). Consequently, the H_2/LQG control methods with the input and output shaping filters stabilize the original structural system of Eq. (6.1) and contain much flexibility to advance the performance for control.

6.2 Design consideration and procedure

Before implementing a designed controller for structural systems, the stability and robustness of the closed-loop systems are still unknown. Moreover, a controller design based on Eq. (6.11) or (6.12) does guarantee the control performance, but the achieved performance after implementing the closed-loop system is also unknown. In this section, a procedure to determine the performance and check the stability of closed-loop control systems is introduced.

In Figure 6.1, this block diagram is introduced not only for a closed-loop system of control implementations but also for a system plant. A structural system including the control-structure interaction is basically obtained from the identified model for a control-oriented problem. After designing the controller using the H_2/LQG control methods, the closed-loop system in this figure can be numerically implemented. However, this research is aimed at the seismic protection using structural control techniques. The H_2/LQG control methods are developed for a control problem which focuses on reducing structural system responses over wide-band excitations. The main objective of these control methods may result in poor performance due to relatively narrow-band earthquakes at low frequencies. As mentioned in Section 6.1, an input shaping filter can represent the characteristics of the excitations. In this section, the input shaping filter adopts the Kanai-Tajimi filter (Ramallo et al. 2002 and Yoshioka et al. 2002) to examine performance, which is formed as a second-order dynamic system to represent seismic excitations, given by

$$\begin{aligned} \mathbf{H}_{\ddot{\mathbf{x}}_g \mathbf{w}}(s) &= \begin{bmatrix} F_1(s) & & \\ & \ddots & \\ & & F_{nw}(s) \end{bmatrix} \mathbf{w} \\ F_i(s) &= \frac{2\zeta_{g,i}\omega_{g,i}s + \omega_{g,i}^2}{s^2 + 2\zeta_{g,i}\omega_{g,i}s + \omega_{g,i}^2} \end{aligned} \tag{6.15}$$

where this equation represents a transfer function matrix from *nw* wide-band excitations to *nw* seismic excitations, $F_i(s)$ denotes a single transfer function from the *i*-th wide-band excitation to the *i*-th seismic excitation, and $\omega_{g,i}$ and $\zeta_{g,i}$ are the effective natural frequency and damping of the seismic characteristics in $F_i(s)$, respectively. Note that the input shaping filter in Section 6.1 could be different from the Kanai-Tajimi filter. Moreover, the root-mean-square (RMS) responses in a state-space model over white noise excitations have a deterministic solution by solving the Lyapunov equation. For example, a closed-loop control system, after incorporating with the Kanai-Tajimi filter, is written by

$$\begin{aligned} \dot{\mathbf{x}}_{CL} &= \mathbf{A}_{CL}\mathbf{x}_{CL} + \mathbf{E}_{CL}\mathbf{w} \\ \mathbf{y} &= \mathbf{C}_{CL}\mathbf{x}_{CL} \end{aligned} \tag{6.16}$$

where $\ddot{\mathbf{x}}_g$ is substituted by the wide-band excitations $\mathbf{w}$, and $\mathbf{y}$ is the outputs for evaluation of which these outputs could be the regulated outputs or the measured outputs as defined previously. Thus, the mean square responses of the output vector $\mathbf{y}$ is calculated by

$$\left\|\mathbf{y}\right\|_{RMS}^2 = diag\left(\mathbf{C}_{CL}\mathbf{Q}\mathbf{C}_{CL}^T\right) \tag{6.17}$$

where

$$\mathbf{A}_{CL}\mathbf{Q} + \mathbf{Q}\mathbf{A}_{CL}^T + \mathbf{E}_{CL}\mathbf{W}\mathbf{E}_{CL}^T = \mathbf{0} \tag{6.18}$$

$$E\left[\mathbf{w}(t)\mathbf{w}^T(\tau)\right] = \mathbf{W}\delta(t-\tau),\ \|\mathbf{y}\|_{RMS}^2 = \left[\|y_1\|_{RMS}^2 \quad \|y_2\|_{RMS}^2 \quad \cdots \quad \|y_{ny}\|_{RMS}^2\right]^T$$

$diag(\bullet)$ denotes the diagonal terms in a square matrix, $E[\bullet]$ denotes the expected value or matrix, and $\mathbf{W}$ is the power matrix of the wide-band excitations which only contains the diagonal terms. In Eq. (6.17), the term, $\mathbf{C}_{CL}\mathbf{Q}\mathbf{C}_{CL}^T$, indicates the covariance matrix of the output vector $\mathbf{y}$ and implies the variances of each components in the vector $\mathbf{y}$ in the diagonal. The matrix, $\mathbf{Q}$, in Eq. (6.18) is the solution of the Lyapunov equation which represents the covariance matrix of the state vector $\mathbf{x}_{CL}$. Using Eq. (6.17), the RMS responses of the output vector $\mathbf{y}$ can be obtained. Therefore, the first step in the design procedure includes employing the Kanai-Tajimi filter to simulate the seismic excitations and then calculating the RMS responses for determining performance for a closed-loop system.

Section 6.1 has introduced the flexibility of the H_2/LQG control methods in the design. For example, different selections on the regulated outputs $\mathbf{z}$ or the modified $\bar{\mathbf{z}}$ can generate different performance with respect to the specific weighting functions of $\mathbf{Q_z}$ and $\mathbf{R_u}$ in Eq. (6.5). Similarly, different selections on the measured outputs $\mathbf{y}$ or the modified $\bar{\mathbf{y}}$ can result in a different performance with respect to the specific weighting functions of $\mathbf{Q_w}$ and $\mathbf{R_v}$ in Eqs. (6.8)-(6.10). Each specific design for a controller as Eq. (6.11) or (6.12) will differently characterize the system, such as the different eigenvalues or the different eigenvectors. However, the resulting eignevalues will only exist within a certain margin. Instead of calculating the theoretic margin for the H_2/LQG controllers, developing multiple controllers based on different weighting functions or different selections on the regulated outputs or the measured outputs is the alternative solution to observe the performance margin. The controllers for examination can then be selected based on the desired performance using the RMS responses over a certain power of wide-band excitations. As a result, the margin of the eigenvalues' locations can be substituted by examining the performance using a number of controllers.

After determining a certain amount of designed controllers, the stability check of these controllers should be evaluated prior to the control implementation. First, reconsider the structural system only with the inputs from control devices as shown in Figure 6.3. In this block diagram, the open loop (followed by the blue solid line) is defined when the calculated control commands are not sent back to the structural system; otherwise, the system (followed by the red dash line) is a closed loop. According to these definitions, the transfer function from the input, $\mathbf{u}_i$, to the output, $\mathbf{y}$, in the closed-loop system can be written by

$$\mathbf{H}_{\mathbf{yu}_i}^{CL} = \mathbf{H}_{\mathbf{yu}}\left(\mathbf{I} - \mathbf{H}_{\mathbf{uy}}\mathbf{H}_{\mathbf{yu}}\right)^{-1} \tag{6.19}$$

where

$$\mathbf{L}(s) = \mathbf{H}_{\mathbf{uy}}\mathbf{H}_{\mathbf{yu}} \tag{6.20}$$

$$\mathbf{S}(s) = \mathbf{I} - \mathbf{H}_{\mathbf{uy}}\mathbf{H}_{\mathbf{yu}} \tag{6.21}$$

As illustrated in Figure 6.3, $\mathbf{H}_{\mathbf{yu}}$ is the transfer function matrix of the structural system from the control input commands to the structural responses, and $\mathbf{H}_{\mathbf{uy}}$ is the transfer function matrix of the controller from the structural responses to the control commands. In order to separate the two types of control commands, $\mathbf{u}_i$ denotes the arbitrary input signals to the control devices, while $\mathbf{u}_o$ denotes the output calculated from the designed controller. Moreover, $\mathbf{L}(s)$ in Eq. (6.20), called an input loop gain transfer function, is defined as the relationship between the input commands and the output control commands and is obtained from the open loop. Similarly, $\mathbf{S}(s)$ in Eq. (6.21), called an input sensitivity transfer function, directly influences the control performance and performs in an open loop as well. Due to the definition of $\mathbf{L}(s)$, this transfer function is exactly identical to the open-loop transfer function in Figure 6.3, such that

$$\mathbf{H}_{\mathbf{u}_o\mathbf{u}_i} = \mathbf{H}_{\mathbf{uy}}\mathbf{H}_{\mathbf{yu}}$$

Therefore, this transfer function $\mathbf{L}(s)$ is accessible for the experimental testing, i.e., the transfer function can be obtained from the measurement $\mathbf{u}_o$ when applying the white noise to the input $\mathbf{u}_i$. Thus, the sensitivity $\mathbf{S}(s)$ is then calculated. Through both $\mathbf{L}(s)$ and $\mathbf{S}(s)$, the control stability and the control performance can be examined before control implementation.

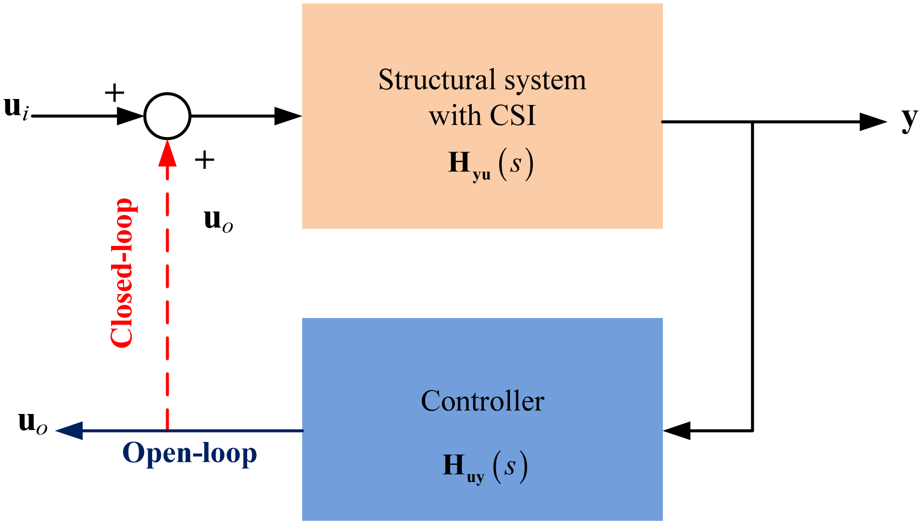

Figure 6.3. Illustration of the loop gain transfer function.

To address the assessment of the control stability and the control performance, the following provides the procedure. A control device can typically generate high performance in low frequencies, indicating that a high authoritative controller should be used in this region. Thus, the input loop gain transfer function, $\mathbf{L}(s)$, should produce large magnitudes in low frequencies, and the sensitivity transfer function, $\mathbf{S}(s)$, should exhibit the same behavior in this region. If this phenomenon is interpreted in a closed-loop transfer function from excitation inputs to structural responses (e.g. the measured output vector **y** or the regulated output vector **z**), an equation, which is transformed from Eq. (6.14), can be given by

$$\begin{aligned}\mathbf{H}_{\mathbf{y}\ddot{\mathbf{x}}_g}^{CL} &= \left(\mathbf{I}+\mathbf{H}_{\mathbf{yu}}\left(\mathbf{I}-\mathbf{H}_{\mathbf{uy}}\mathbf{H}_{\mathbf{yu}}\right)^{-1}\mathbf{H}_{\mathbf{uy}}\right)\left(\mathbf{H}_{\mathbf{y}\ddot{\mathbf{x}}_g}+\mathbf{H}_{\mathbf{yu}}\mathbf{H}_{\mathbf{u}\ddot{\mathbf{x}}_g}\right)\\ \mathbf{H}_{\mathbf{z}\ddot{\mathbf{x}}_g}^{CL} &= \left(\mathbf{I}+\mathbf{H}_{\mathbf{zu}}\left(\mathbf{I}-\mathbf{H}_{\mathbf{uy}}\mathbf{H}_{\mathbf{yu}}\right)^{-1}\mathbf{H}_{\mathbf{uy}}\mathbf{T}_{\mathbf{yz}}\right)\left(\mathbf{H}_{\mathbf{z}\ddot{\mathbf{x}}_g}+\mathbf{H}_{\mathbf{zu}}\mathbf{H}_{\mathbf{u}\ddot{\mathbf{x}}_g}\right)\end{aligned} \tag{6.22}$$

This equation also stratified the criteria of high performance when **L**(s) and **S**(s) have large magnitudes in low frequencies. Note that large magnitudes in **L**(s) do not always guarantee large magnitudes in **S**(s) due to the phases. As for the stability issue, **L**(s) should generate the magnitudes as low as possible in the region of uncertainties, e.g., typically in high frequencies. These uncertainties include the region where the model poorly represents the system behavior and where the system behaves highly nonlinearly. Moreover, lower magnitudes in **L**(s) indicate high noise rejection for sensors because sensors typically have higher noise in high frequencies. Thus, **S**(s) in the region of uncertainties should result in the magnitude close to one in the case of a single control command input. In case of multiple control command inputs, the maximum singular matrix of the transfer function matrix **S**(s) at a specific frequency should be close to one, indicating less control power is applied to this region of uncertainties. These criteria for control performance and stability, given for **L**(s) and **S**(s), promise high reductions in structural system responses as well as robustness of designed controllers.

When introducing a feed-forward gain in the controller (e.g, $\mathbf{H}_{\mathbf{u}\ddot{\mathbf{x}}_g}$ in Eq. (6.14)), additional rules for control design should be considered. Because the feed-forward gain is derived from the modified version of measured outputs, Eq. (6.4) has shown that an input shaping filter is uncontrollable through the control input commands. Thus, an input shaping filter only affects the Kalman estimator design, i.e., changing the entries in $\mathbf{R}_\mathbf{v}$ of Eq. (6.10) with respect to the excitation inputs will significantly influence the control performance. Typically, these entries should be relatively close to specific entries of $\mathbf{Q_w}$ correspondingly; otherwise, placing too small values in these entries of $\mathbf{R_v}$ may decrease the robustness to the system in high frequencies. For example, the Kanai-Tajimi filter is adopted to form an input shaping filter. When increasing the entries of $\mathbf{R_v}$, the contribution from the resulting feed-forward gain to the control performance will be approaching zero. Contrary to this, the magnitudes of $\mathbf{H}_{\mathbf{u}\ddot{\mathbf{x}}_g}$ will be increased in high frequencies when these entries are significantly decreased. Hence, the transfer function, $\mathbf{H_{yu}}\mathbf{H}_{\mathbf{u}\ddot{\mathbf{x}}_g}$ as a term shown in Eq. (6.22), should be numerically checked before control implementation. This transfer function should exhibit high performance in low frequencies, while low magnitudes should be found in high frequencies in order to avoid inducing the system instability.

To briefly summarize the considerations after designing controllers using the H_2/LQG control methods, the design procedure is described as follows. A number of designed controllers based on different weighting functions and different types of measured outputs and regulated outputs are first examined in order to determine the desired performance. For seismic control problems, the Kanai-Tajimi filter can be employed to evaluate these designed controllers numerically, and then the RMS responses of the measured outputs and the regulated outputs can be calculated. Once the controllers for testing have been selected by the pervious criteria, an input loop gain transfer function and a sensitivity transfer function should be numerically checked. If these two numerical transfer functions pass the rule as previously addressed, the experimental testing for the two transfer functions can then proceeds to prove their suitability. By following this procedure, the closed-loop structural system can confirm high performance and stability prior to control implementation.

6.3 Example: active isolation system of the two-story building

This section presents an example of the control design performance and the design procedure for the active isolation system of the two-story building in the *y*-direction. The example employs a H_2/LQG controller with the acceleration feedback to illustrate the design. Different predetermined weighting functions are used to design a number of controllers and then to examine control performance, while both the input loop gain transfer function and the sensitivity transfer function are provided to ensure the implementable controllers. Although the design procedure also requires the check of these two transfer functions experimentally, the detailed introduction will be described in Chapter 7. In addition to the example of the acceleration feedback control, several controllers based on different measurements for feedback control are examined in this research. These controllers, which will be described in this section, are also developed in the same procedures. The example of the acceleration feedback control shows the design procedure and illustrates the idea for development of other H_2/LQG controllers.

In Section 6.1, the H_2/LQG control methods allow the design to arbitrarily select measured outputs and regulated outputs in accordance with the sensor setup. To fully enhance the LQR control design, all available measurements (see Eq. (5.14)) are selected to be the regulated outputs. Since the example in this section only focuses on the acceleration feedback control, only the accelerations at the base, the 1st floor, and the 2nd floor are the measured outputs. Thus, three groups of controllers, which are listed in Table 6.1, are illustrated and the associated settings for each group are addressed as follows:

- Group A: only the conventional H_2/LQG control design is considered. The measured outputs and the regulated outputs are the same as the previous definition, indicating that no input or output shaping filter is incorporated.

- Group B: this group considers an input shaping filter using the Kanai-Tajimi form. The effective natural frequency and damping are 6 Hz (e.g., the same as the first natural frequency of this active isolation system) and 60%, respectively. Although the regulated outputs can be augmented with the excitation input, this group does not consider this term, which implies that no feed-forward gain, $\mathbf{H}_{\mathbf{y}\ddot{\mathbf{x}}_g}$ in Eq. (6.14), participates in the closed-loop structural system.
- Group C: this group considers both input and output shaping filters. The filter form and the associated parameters of the input shaping filter are the same as those in the group B. The excitation input is still exclusive in the regulated outputs. The output shaping filter adopts a 3rd-order Butterworth low-pass filter for the base displacements, resulting in five measured outputs in the LQR design. The objective of this output shaping filter is to reduce the base displacements. Also, the cutoff frequency in this low-pass filter is selected to be 30 Hz.

In each group, eight controllers are examined for the design procedure. The weighting functions, $\mathbf{Q}_\mathbf{z}$ in the LQR design and $\mathbf{R}_\mathbf{v}$ in the Kalman estimator design, are also described in Table 6.1. By changing the $\mathbf{R}_\mathbf{u}$ in the LQR design and $\mathbf{Q}_\mathbf{w}$ in the Kalman estimator design, different controllers are generated with respect to the specific $\mathbf{Q}_\mathbf{z}$ and $\mathbf{R}_\mathbf{v}$. The selected controllers for control implementation are those which can significantly reduce the floor accelerations without increasing the base displacements as compared to the zeroed control. The zeroed control is defined as control input commands that are always equal to zeros (i.e., $\mathbf{H}_{\mathbf{uy}}$ and $\mathbf{H}_{\mathbf{u}\ddot{\mathbf{x}}_g}$ are equal to zero in Eq. (6.14)). Since this example is only aimed at the active isolation along the *y*-direction, the control input commands for the *x*-actuators are always zero.

Table 6.1. Examining controllers for an example of acceleration feedback control.

Case name	**LQR design weighing on Q_y**				**Kalman estimator design weighing on Q_v**	
	all floor accelerations	base displacement	top floor acceleration	base responses	all floor accelerations	base acceleration
A/B/C-1	X				X	
A/B/C-2	X					X
A/B/C-3		X			X	
A/B/C-4		X				X
A/B/C-5			X		X	
A/B/C-6			X			X
A/B/C-7				X	X	
A/B/C-8				X		X

The first step in the design procedure is to examine the performance on structural RMS response over a wide-band excitation when using the acceleration feedback control. As previously mentioned, the Kanai-Tajimi filter is employed to simulate earthquakes using $\omega_g = 25$ rad/sec and $\zeta_g = 30$ %. Note that this Kanai-Tajimi filter has a different meaning from the input shaping filter. Through the comparison of the RMS responses of base displacements and all floor accelerations, the qualified controllers can be selected. The results of the group-A controllers shown in Figure 6.4 are discussed as follows:

- LQR design: the weighting on top floor accelerations produces better performance in all floor accelerations, while the weighting on base displacements results in significant reductions in base displacements.
- Kalman estimator design: the Kalman estimator is ineffective at improving the performance of this acceleration feedback control.
- Qualified controllers: the controllers in the cases A1-2 and A5-8 are selected where the RMS accelerations are around 4.5, 7, and 10 at the base, the 1st floor, and the 2nd floor,

respectively. The cases A3-4 produce fewer reductions in the 2nd floor accelerations; consequently, the controllers in these cases are not selected.

For the group-B controllers, Figure 6.5 shows the results, and the associated discussions are drawn as follows:

- Input shaping filter: the control performance of all controllers is slightly improved as compared to the group A. The input shaping filter significantly influences the controllers in the cases B5-6 as compared to the cases A5-6.
- LQR design: the trend of the LQR design shows behavior similar to group A.
- Kalman estimator design: this design shows minor variances between cases, e.g., between the cases B1 and B2.
- Qualified controllers: the controllers in the cases B1-2 and B5-8 are selected where the RMS accelerations are around 4.3, 6, and 8 at the base, the 1st floor, and the 2nd floor, respectively. The cases B3-4 are still unqualified because the controllers in these cases cannot explore the specific performance at top floor accelerations.

Using both input and output shaping filters in control design, the results of the group-C controllers are shown in Figure 6.6. The discussions among these controllers are addressed as follows:

- Output shaping filter: the output shaping filter significantly changes the performance patterns for most controllers such as cases C3-8, because the main objective of the output shaping filter is to place the weightings on the base displacements and then to reduce the base displacements.
- Qualified controllers: in this case, only the controllers in the cases C1-2 are qualified. The selected ones have RMS accelerations around 4.3, 6, and 8 at the base, the 1st floor, and

the 2nd floor, respectively. Although the controllers in the other cases effectively reduce the base displacements, the specific levels at the top floor accelerations are not reached. According to this analysis, only a few controllers are qualified to proceed in the second step of the design procedure. The results among all controllers in Figures 6.4-6.6 not only illustrate the design based on the RMS responses but also demonstrate the flexibility of the H_2/LQG control methods.

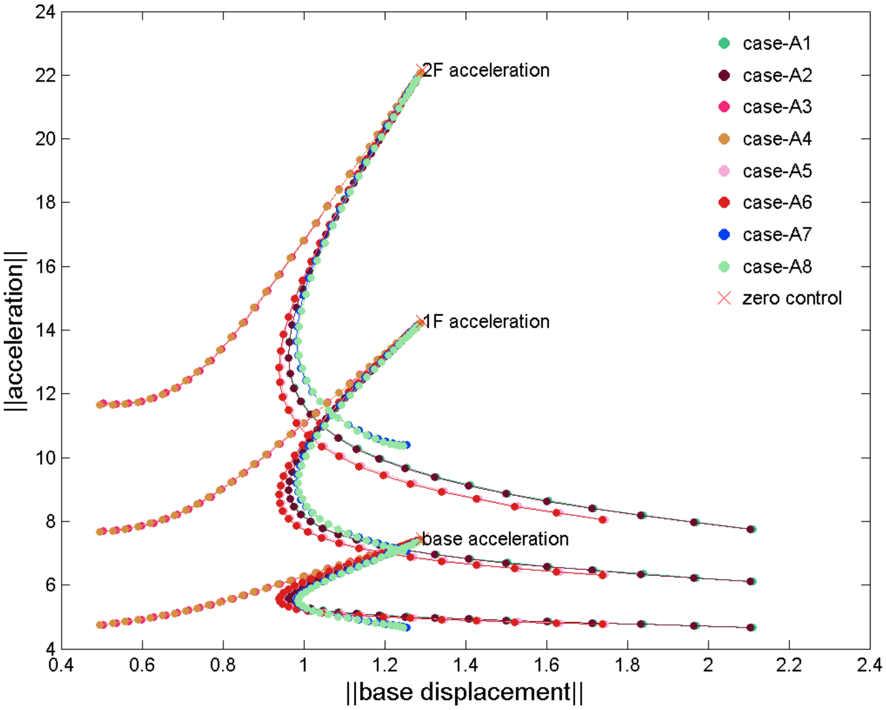

Figure 6.4. Control performance examination using control strategies in group A.

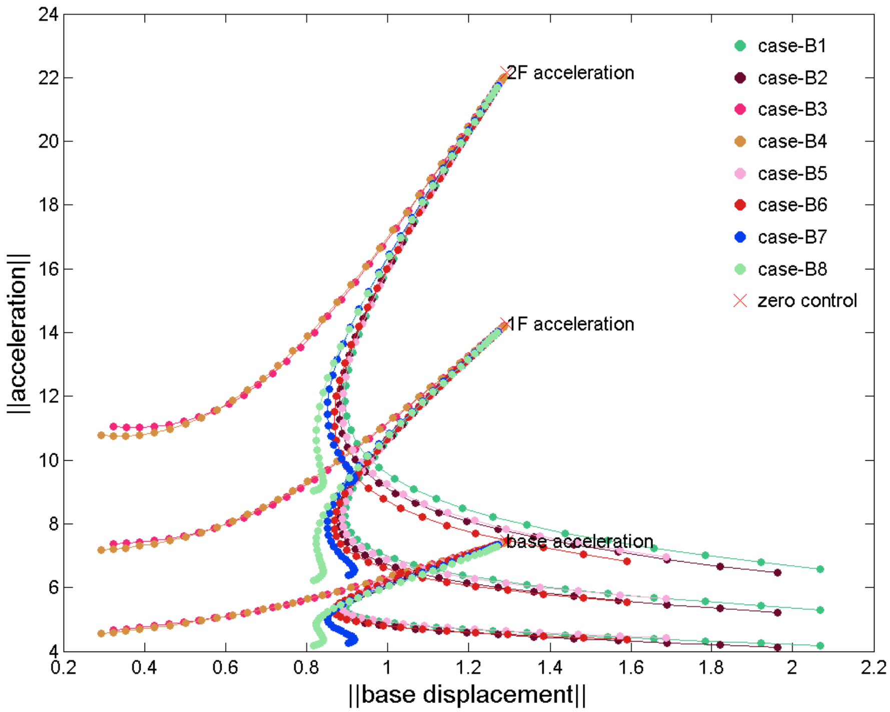

Figure 6.5. Control performance examination using control strategies in group B.

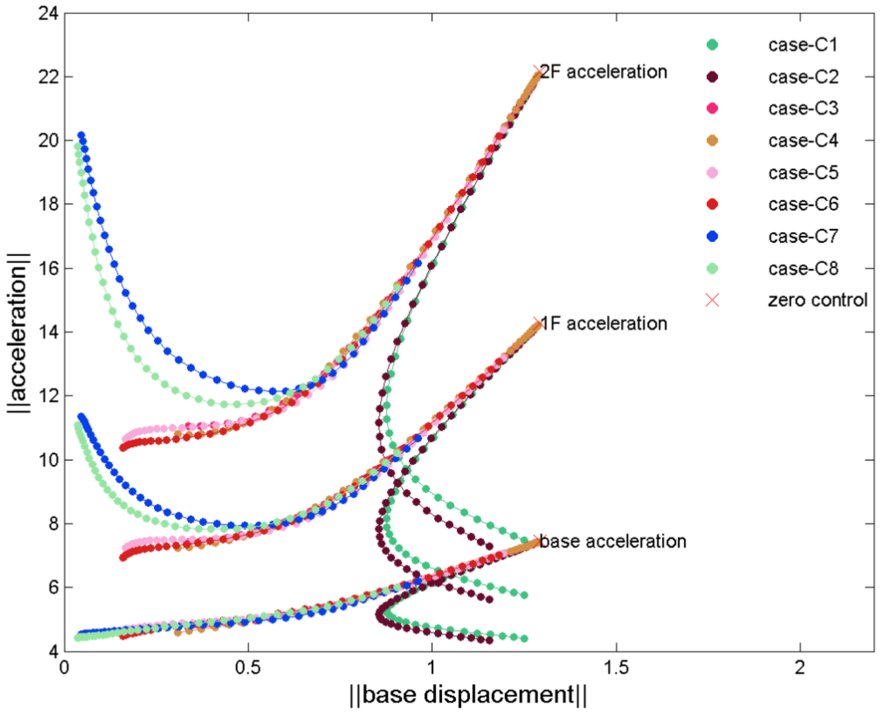

Figure 6.6. Control performance examination using control strategies in group C.

The second step employs the input loop gain transfer function and the sensitivity transfer function to further check the performance and the robustness of control strategies. In this step, both transfer functions are only performed numerically, while the experimental ones will be introduced in Chapter 8. The results of the input loop gain transfer functions should show high magnitudes in low frequencies (e.g., below 30Hz), while those of the sensitivity transfer functions should have magnitudes close to one (e.g., 0 dB) above 30 Hz. Note that only those qualified controllers from the results of figures should be considered, although the controllers of all cases in each group are shown. Additionally, the qualified controllers in each group have the same weightings on the $\mathbf{R_u}$ in the LQR design and $\mathbf{Q_w}$ in the Kalman estimator design. The results for the second step in the design procedure, when using the specific controllers in the cases A1-2 and A5-8, are shown in Figure 6.7. The discussions of these results are listed as follows:

- Input loop gain: all controllers in this group A pass the rules where there are large magnitudes below 30 Hz.
- Sensitivity: most controllers pass the rules of the sensitivity transfer function, but the controller in case A8 has an unexpected pole at 27 Hz, which may result in an instability problem.
- Qualified controllers: the controllers in cases A1-2 and A5-7.

The results for the second step in the design procedure, using the specific controllers in cases B1-2 and B5-8, are shown in Figure 6.7. The associated discussions are addressed as follows:

- Input loop gain: all controllers in this group B also pass the basic rules. The magnitudes at first poles are slightly increased as compared to those in the group A.

- Sensitivity: the controllers in the cases B5 and B7-8 pass the rules of the sensitivity transfer function, while the controllers in the cases B1-2 and B6 fail because the magnitudes above 30 Hz are much higher or less than one (0 dB). In these results, the controller in the case B8 is improved because of the input shaping filter as compared to the one in case A8.
- Qualified controllers: the controllers in cases B1-2 and B6.

When using the specific controllers in cases C1-2, Figure 6.8 shows the results from both types of transfer functions. The discussions for these two controllers are as follows:

- Input loop gain: the behavior of both controllers adheres to the rules. The magnitudes of these controllers are slightly decreased as compared to the group B.
- Sensitivity: these two controllers still pass the rules of the sensitivity transfer function. Additionally, these two controllers converge into one very quickly.
- Qualified controllers: both controllers in cases C1-2 are qualified.

As seen in the results of the example, one control strategy (e.g., the acceleration feedback control) can generate a variety of controllers from the H_2/LQG control methods. In a brief conclusion of these results, the conventional H_2/LQG control methods (i.e, the control design does not include an input or output shaping filter) often guarantee the control performance, while the robustness in high frequencies may not always be promising. For example, the input loop gain transfer functions roll off the magnitudes in Figure 6.7 slower than those in Figures 6.8 and 6.9. The advanced H_2/LQG control methods using an input shaping filter often produce a higher performance and better robustness. When using input and output shaping filters in the H_2/LQG control methods, the robustness is enhanced as compared to the methods only using an input shaping filter. Based on the results, most controllers, which developed from the conventional

H_2/LQG control methods or the methods with an input shaping filter, are acceptable for control implementation, if the controllers also obey the criteria of input loop gain and sensitivity transfer functions. The advanced H_2/LQG control methods using an output shaping filter are not as effective as expected. The research for the active isolation system of the two-story building will eliminate this type of controller.

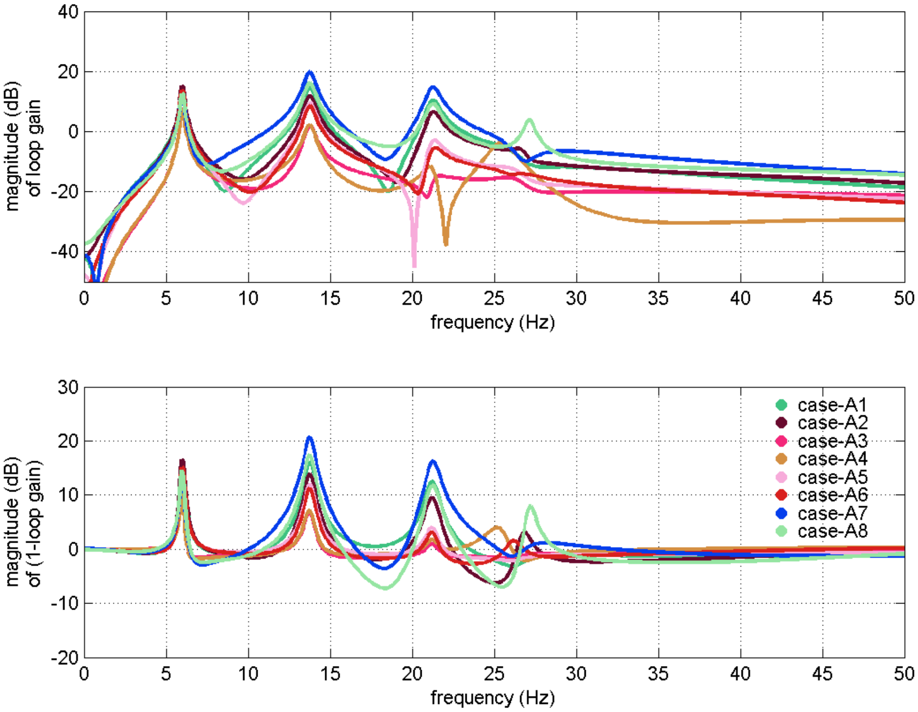

Figure 6.7. Numerical loop gains and sensitivities of the control strategies in group A.

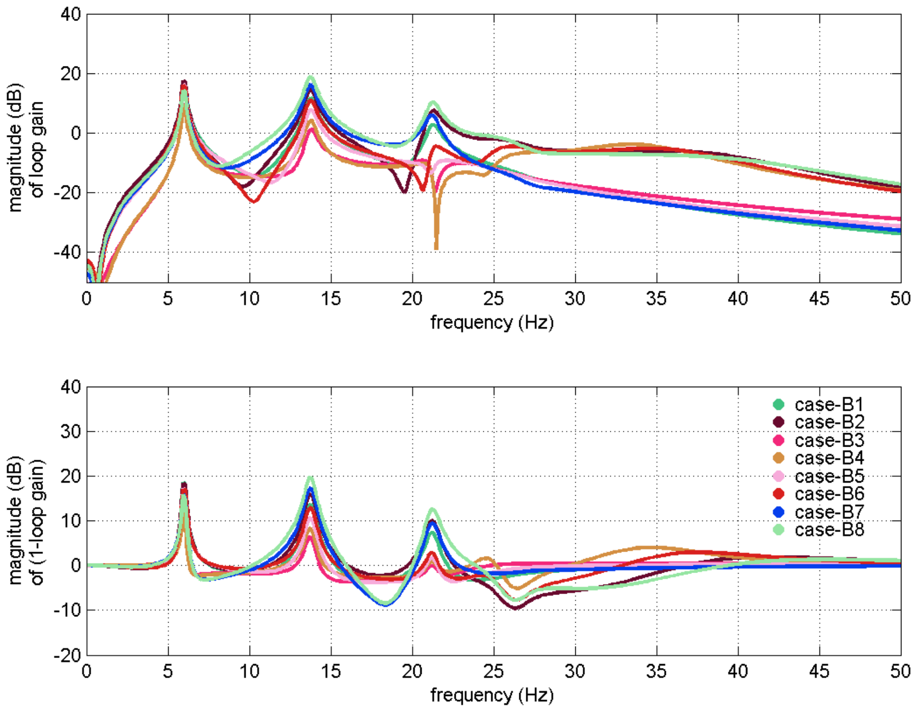

Figure 6.8. Numerical loop gains and sensitivities of the control strategies in group B.

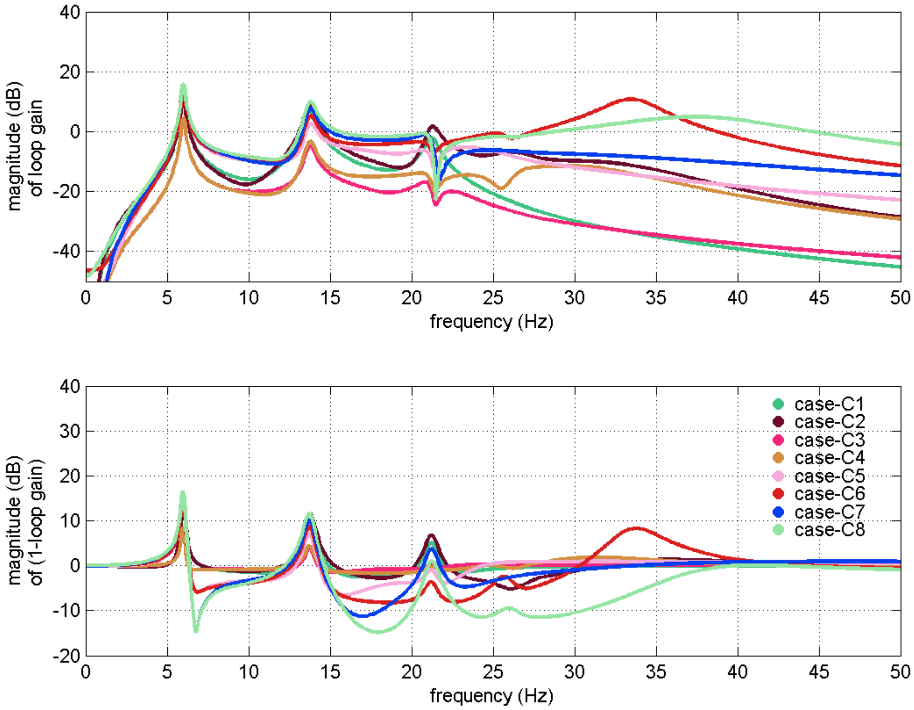

Figure 6.9. Numerical loop gains and sensitivities of the control strategies in group C.

After performing the control design for acceleration feedback controllers, the controllers based on different measurements for feedback control can be developed using the same procedure. One of the objectives in this research is the examination of controllers using different numbers of sensors to complete the feedback control. Therefore, four types of controllers are employed in this research. The first type use the measurements from all sensors (e.g., base displacements and all floor accelerations), while the second type use all floor accelerations for feedback control, as given in this section. Both the third and fourth types employ base displacements with top floor accelerations and base accelerations for feedback control, respectively. All controllers described here share the purpose of reducing base displacements and floor accelerations, as compared to the passive isolation control (i.e., the structural system has no actuators attached to the base) and the zeroed control (i.e., the actuator receives zero commands all the time as previously defined). In the control implementation, a number of candidate controllers will be evaluated after they have been designed through the procedure in this chapter.

6.4 Example: active isolation system of the six-story building

This section illustrates the process of control design for the active isolation system of the six-story building in the both *x*- and *y*- directions. As described in Section 5.4, this active isolation system can be divided into two systems, a system along the *x*-direction and a system along the *y*-direction. In control design, the controllers for the *x*-actuators and the *y*-actuator are also separately designed. Thus, the controllers in the *x*-direction only employ the *x*-directional measurements for feedback control, while the *y*-direction measurements are only used for the *y*-directional controllers. After examining many candidate controllers numerically, this section only demonstrates those controllers which will be used in control implementation. Similarly to the example in Section 6.3, the two steps in the design procedure are employed to evaluate performance and robustness. Finally, the selected controllers, which perform well in accordance with the design criteria, can be implemented using shake table testing.

Three types of control strategies using the H_2/LQG control methods are examined for the both *x*- and *y*- actuators in this active isolation system. These control strategies basically employ different measurements for feedback control. All of these control strategies also adopt an input shaping filter in their design in order to include the dynamic characteristics in the controllers. The details of the development for these control strategies are listed as follows:

- Controller F: the measurements for feedback control are taken for base displacements, base accelerations, 2nd floor acceleration, 4th floor acceleration, and 6th floor acceleration in the *y*-, *x*1-, and *x*2- directions. The controller for the *y*-direction includes a feed-forward gain, while the *x*-directional controller only adopts an input shaping filter without introducing any feed-forward gains.
- Controller FA: the measurements for feedback control are base accelerations, 2nd floor acceleration, 4th floor acceleration, and 6th floor acceleration in the *y*-, *x*1-, and *x*2- directions. The both *x*- and *y*- directional controllers consider input shaping filters in design and include feed-forward gains.
- Controller BA: the measurements for feedback control are taken for base displacements and 6th floor accelerations in the *y*-, *x*1-, and *x*2- directions. The *y*-directional controller employs an input shaping filter without having a feed-forward gain, while the *x*-directional controller has a feed-forward gain derived from the input shaping filter.

According to this list, all controllers are designed with input shaping filters taking into account the robustness in high frequencies. The feed-forward gain is defined as when the modified measured outputs from the excitation inputs are incorporated in a controller, e.g., the *y*-ground acceleration for the *y*-directional controller F. Therefore, this example illustrates the control design for all controllers in the list using the proposed design procedure.

6.4.1 Controllers in the *y*-direction

The first step in the design procedure is to determine the performance. The example in this section has predetermined the weighting functions, $\mathbf{Q_z}$ in the LQR design and $\mathbf{R_v}$ in the Kalman estimator design. Thus, the results in this step of the design procedure are focused on the variances of performance when changing the weighting function $\mathbf{R_u}$ in the LQR design and $\mathbf{Q_w}$ in the Kalman estimator design. As mentioned before, all controllers adopt input shaping filters in the design where the effective natural frequency and damping are 2.6 Hz and 60 % based on the form of the Kanai-Tajimi filter. To effectively evaluate the performance in simulation, the Kanai-Tajimi filter, which has 10 rad/sec and 30% damping for the effective natural frequency and damping, is used. Note that the Kanai-Tajimi filter for performance evaluation does not participate in the H_2/LQG control methods. Hence, the controllers based on these settings are developed and then evaluated by the performance in RMS responses.

The main objective of the control performance for controllers in this direction is to reduce the floor accelerations without inducing much base displacement response. Figure 6.10 shows the results of the performance evaluation for controllers in the *y*-direction. The discussions on each controller are given as follows:

- Controller F: when increasing the weighting functions, $\mathbf{Q_z}$ and $\mathbf{R_v}$, the floor accelerations are significantly reduced. However, the base displacements have a difficult time reducing when the controllers perform well in floor accelerations. Therefore, the controller, which is selected based on the performance evaluation, is the moderate one with the RMS base displacement equal to 8.5.

- Controller FA: the controllers in this category slightly increase the RMS responses as compared to the category of the controller F. The overall behavior is also very similar to the category of the controller F. The controller with the RMS base displacement equal to 8.6 is selected.
- Controller BA: the controllers in this category have little higher performance among these three categories. Theses controllers still have a difficult time reducing the base displacements when seeking high performance on floor accelerations. The controller with the RMS base displacement equal to 5.5 is selected.

All three of these categories have very similar performance, though the controllers are derived from different weighting functions and different measurements for feedback and/or feed-forward control. The moderate controllers are selected, taking robustness into consideration. To effectively reduce the floor accelerations, the base displacements are amplified in all controllers.

To further check the performance and the robustness of the selected controller from the first step, the input loop gain and sensitivity transfer functions are employed. In Section 5.4, the results of system identification have showed that the identified model poorly represents the system above 30 Hz. Thus, the frequency, 30 Hz, is divided to distinguish the input loop gain and the sensitivity for the performance (e.g., below 30 Hz) and the robustness (e.g., above 30 Hz), respectively. Figure 6.11 shows the results of these two transfer functions for which the associated discussions are listed as follows:

- Input loop gain: all controllers show the input loop gain transfer functions with high magnitudes below 30 Hz. These transfer functions particularly roll off the magnitudes at least to -20 dB at 30 Hz. Through checking these types of transfer functions, the performance of these three controllers is numerically validated once again.

- Sensitivity: all controllers have the magnitudes of sensitivity transfer functions close to one above 30 Hz. Even though the controller F has some variances around one in magnitudes of this transfer function above 30 Hz, the overall behavior is acceptable as is the behavior of the other two.

According to the check on these two transfer functions, three controllers can produce the performance as expected and give the robust behavior as well. Although the RMS responses in Figure 6.10 illustrate very similar performance among these three controllers, the input loop gain and sensitivity transfer functions have different patterns.

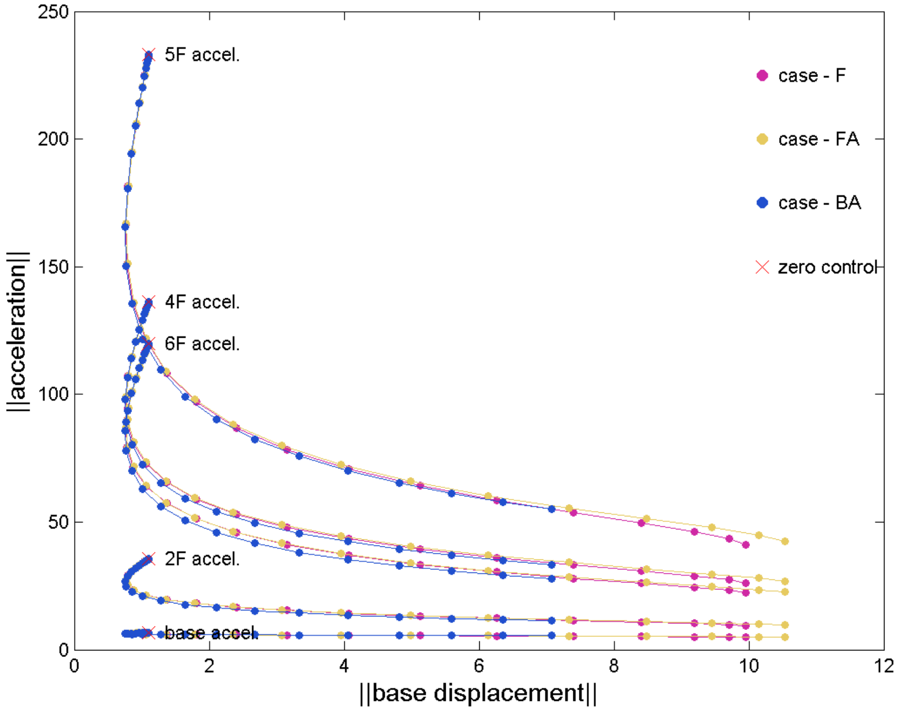

Figure 6.10. Performance of the RMS responses in control design for the *y*-direction.

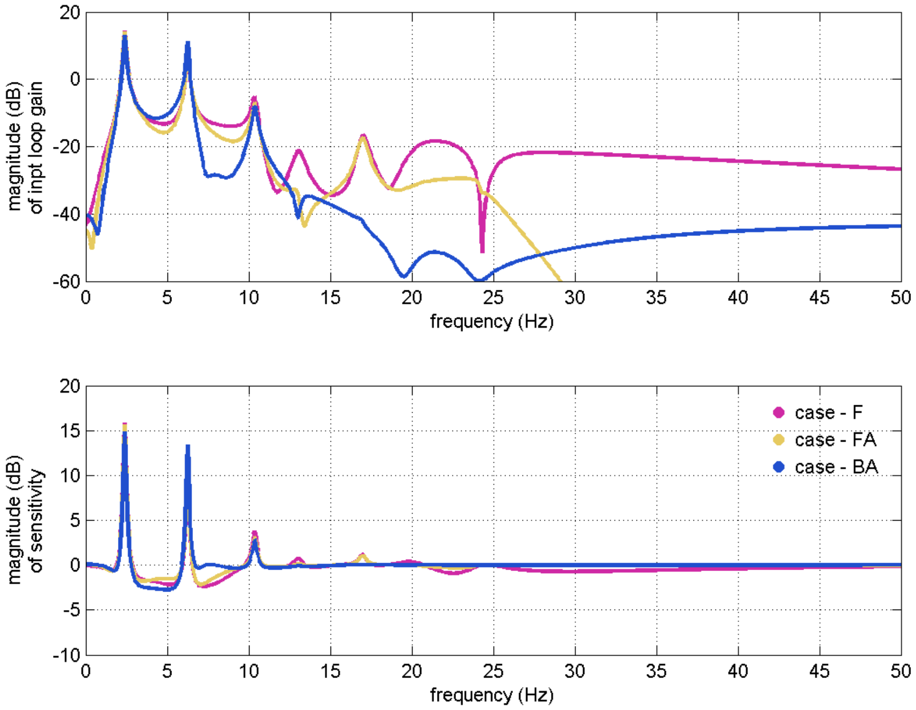

Figure 6.11. Input loop gain and sensitivity transfer functions for three controllers in the *y*-direction.

6.4.2 Controllers in the *x*-direction

Similarly to Section 6.4.1, these controllers in the *x*-direction are first checked for their performance of the RMS responses. Again, the example in this section has predetermined the weighting functions, $\mathbf{Q_z}$ in the LQR design and $\mathbf{R_v}$ in the Kalman estimator design. Thus, the results in this step of the design procedure are focused on the variances of performance when changing the weighting function $\mathbf{R_u}$ in the LQR design and $\mathbf{Q_w}$ in the Kalman estimator design. Due to two actuators in this direction, $\mathbf{R_u}$ is determined by an arbitrary constant multiplied with an identity matrix. Moreover, the input shaping filters for the *x*-directional controllers employ the same Kanai-Tajimi filter with an effective natural frequency of 1.5 Hz, and an effective damping at 60%. Additionally, the Kanai-Tajimi filter, which has 10 rad/sec and 30% damping for the effective natural frequency and damping, is used to perform the seismic excitations in order to effectively represent the responses of the system. Through these settings, the performance of controllers can be evaluated.

An additional control objective for controllers in the *x*-direction is to reduce the floor accelerations without increasing the base displacements too much. Figure 6.12 shows the results of the performance evaluation for controllers in the *x*-direction. The controllers in these three categories have very similar performance. The floor accelerations can be significantly reduced, particular accelerations at the top floors, while the base displacements are barely reduced. Thus, the controllers F, FA, and BA are selected because they achieved RMS base displacement responses at 95, 75, and 78, respectively. Hence, the resulting performance is still acceptable when referring to the control objective.

The second step in the design procedure is to check both the input loop gain and sensitivity transfer functions. Due to two actuators in the *x*-direction, the transfer functions are 2x2 matrices, which poorly represent the performance and the robustness. Thus, the singular values of transfer function matrices over frequencies are adopted to evaluate the input loop gain and the sensitivity. Moreover, the identified model in Section 5.4 poorly represents the system above 30 Hz, which becomes the divide to distinguish the performance and the robustness. As a result, Figure 6.13 shows the singular values of the input loop gain and sensitivity transfer function matrices from the selected controllers. The associated discussions are listed as follows:

- Input loop gain: when using the singular values to check an input loop gain transfer function matrix, the transfer function with the largest singular values indicates the performance of the specific controller. For these three controllers, the magnitudes of this transfer function below 30 Hz are sufficiently large. Therefore, the performance of all three controllers is acceptable.

- Sensitivity: the sensitivity transfer function with the largest singular values indicates the robustness in high frequencies. In Figure 6.13, the magnitudes of this transfer function are always close to one among three controllers above 30 Hz. These three controllers are all qualified after checking the robustness.

After checking the performance and the robustness, these three controllers are recognized as acceptable for control implementation. Due to the complexity of the system along the *x*-direction, the robustness of controllers is more important than the performance. Therefore, the design procedure for the system in the *x*-direction is more focused on the robustness, although the performance is rarely compromised in design.

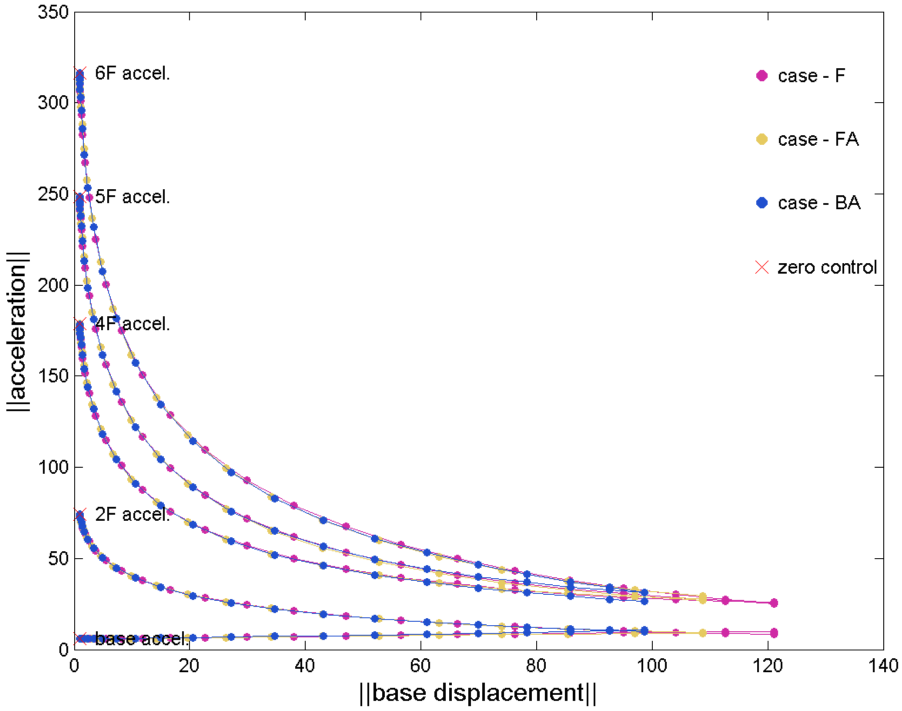

Figure 6.12. Performance of the RMS responses in control design for the *x*-direction.

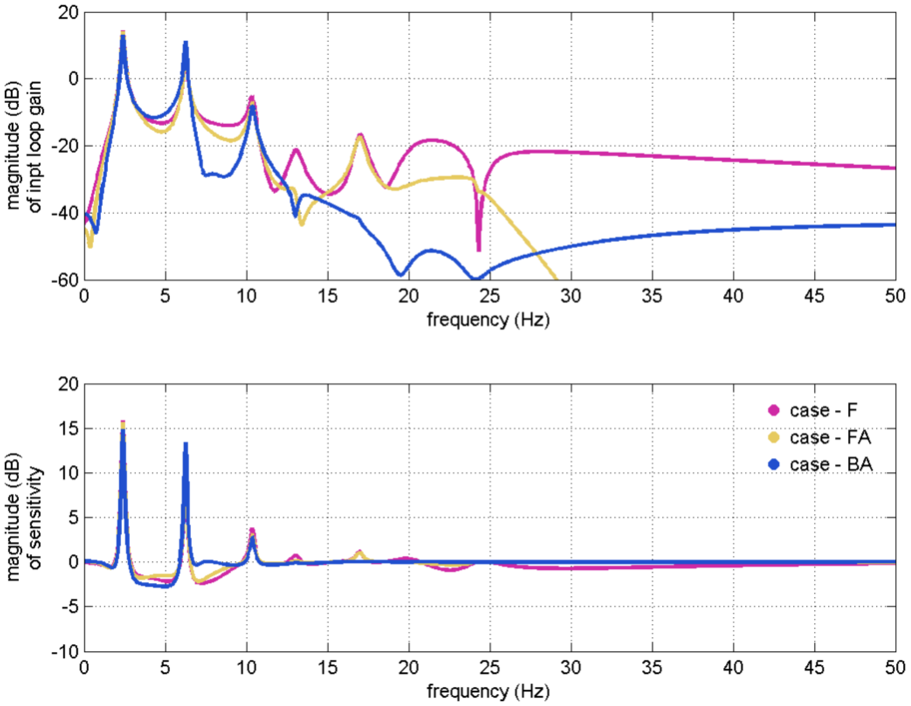

Figure 6.13. Input loop gain and sensitivity transfer functions for three controllers in the *x*-direction.

6.5 Summary

This section presented the control algorithm and the design procedure for the development of controllers. The control algorithms were advanced from the conventional H_2/LQG control methods with consideration of input and output shaping filters. The design procedure was developed to determine the qualified controllers by two steps: first, to choose the controllers that achieved the performance in accordance with the control objectives, and second, to further check the performance using the input loop gain transfer functions and the robustness using the sensitivity transfer functions. Two examples were illustrated for the controllers that will be used in control implementations for the active isolation systems of the two-story and six-story buildings, respectively. Through the advanced H_2/LQG control methods and the proposed design procedure, the controllers are both effective and robust for the active isolation systems in this research.

CHAPTER 7 ACTIVE ISOLATION IMPLEMENTATION FOR A TWO-STORY BUILDING

The first experimental verification of active isolation for seismically excited buildings in this research is the active isolation system of the two-story building, which is only focused on the movement along the *y*-direction. This structural system is implemented under unidirectional excitations using shake table testing. The control objective of this system is to exhibit a reduction in the floor accelerations and base displacements as compared to the zeroed control (i.e., all actuators are always received with zero commands) and the passive control (i.e., no actuators are attached to the structure). Thus, this section briefly describes this active isolation system again and then explains the experimental procedure. The analysis of the results in comparison with the zeroed and passive control is subsequently demonstrated in the frequency and time domain. The control implementation for the active isolation system of the two-story building is successfully verified through shake table testing.

7.1 Brief introduction

The active isolation system of the two-story building still consists of three actuators that are attached to the building at the base. The control objective for this setup is to develop an effective controller for the *y*-actuator, while both *x*-actuators are commanded with zeros. To evaluate control performance, all floor accelerations in the *y*-direction are sensed, and the base displacements in this direction are measured. In comparison with this active isolation system, two control strategies, the zeroed control and the passive control, are also employed through the shake table testing. Finally, the results are illustrated and analyzed in the following sections in this chapter.

As described in Section 6.3, in this research, different active control strategies are developed to examine this active isolation system. The three main categories involved with these active control strategies are:

- Different weighting schemes for the H_2/LQG control design: This category is mainly focused on those weighting functions in the LQR design in Eq. (6.5) and the Kalman estimator design in (6.10). Dyke et al. (1994a and 1994b) stated that weighting on floor accelerations for the H_2/LQG control algorithm, particularly in the LQR design, can achieve high performance for reductions of both floor accelerations and displacements. In this research, this idea is also incorporated in the examination of active controllers, but other weighting strategies are also employed, i.e., weighing more on base displacements in the LQR design. In the design of the Kalman estimator, appropriate weighting function can allow the high-frequency noise of sensors to be rolled off and estimate the system state for low-frequency components with respect to the seismic characteristics. Moreover, the Kalman estimator design can also create the possibility to employ different grouped measurements for feedback control (i.e., only using some of the existing sensors to implement feedback control). Hence, the controllers developed by appropriate and efficient weighting schemes for the H_2/LQG control design are investigated using shake table testing for this active isolation.
- Different grouped measurements for feedback control: In the Kalman estimator design, the selection for measurements in feedback control is arbitrary in accordance with the control environment. For example, more sensors in the feedback controllers may induce

the computation loading for the digital controller. Additionally, the sensors which are far away from control devices may be ineffective in the Kalman estimator design. Therefore, this research explores different measurements to implement feedback control for the active isolation of the two-story building in the *y*-direction.

- Incorporation of an input shaping filter: As mentioned in Section 6.3, an input shaping filter cannot only roll off structural responses components in high frequencies but can also incorporate an additional feed-forward gain in control design. In this research, the effectiveness of the control design with an input shaping filter is studied in control implementations.

Active controllers, which are developed through the previously mentioned categories, should also pass the design criteria as illustrated in Section 6.3. Subsequently, the qualified controllers are implemented and verified under a variety of excitations on the shake table.

Looking for high performance in this active isolation system, 16 candidate controllers are examined through shake table testing. Table 7.1 lists all controllers, varied with different control objectives, different feedback setups, and considerations with or without the seismic characteristics. Note that all testing tasks are adequate for both buildings with different stories and the definitions for the measurement feedbacks are listed as follows:

- Full measurements (F) – base displacements and all floor accelerations in the two-story building; base displacements, base accelerations, and accelerations of odd-number floors in the six-story building.
- Full accelerations (FA) – all floor accelerations in the two-story building; base accelerations and accelerations of odd-number floors in the six-story building.
- Base measurements (B) – base displacements and base accelerations in both buildings.

- Base displacements and roof accelerations (BA) – base displacements and top floor accelerations in both buildings.

To demonstrate the control performance of the active base isolation systems systematically, the criteria are provided for evaluation of the control designs as compared to the passive base isolation control and the zeroed control. As mentioned in Chapter 2, one of goals in this research is to test the active base isolation systems against a wide range of excitations. Hence, the frequency-domain analysis and the time-domain analysis are studied in this active isolation system.

- Frequency-domain analysis: Every designed controller for the active base isolation systems will be evaluated on the shake table under the band-limit white noise (BLWN) excitations. All measured responses, such as the base displacement and the absolute floor accelerations, can be transformed into the transfer functions with respect to the ground accelerations. Moreover, this sort of test focuses on the variations in the transfer functions, indicating the reductions in the total energy and the modal magnitudes. Hence, in addition to exploring the variations by comparing the transfer functions directly, the pole reductions in the first few modes and the area reductions over the limited band are also investigated. These reductions indirectly indicate the control performance of the active base isolation systems against seismic excitations.
- Time-domain analysis: To evaluate the control performance in the time domain, every controller will be tested on the shake table under various seismic excitations. For the seismic excitations, this proposed research will select some near-fault earthquake records because the previous studies showed the sort of excitations potentially able to damage the isolated buildings. The responses considered in the time-domain analysis include base

displacements, absolute floor accelerations, and base shears. According to the benchmark control problem mentioned in Section 2.3.4, the control performance for evaluation must achieve the lower base displacements as well as the acceptable absolute floor accelerations, as compared to the passive base isolation. Likewise in the frequency-domain analysis, the peak response reductions in the time histories are investigated in this research, while the root-mean-squared (RMS) responses, which indicate the total energy, are also observed. These response reductions provide the evidences for the verification of the implementation of the active base isolation systems.

In this chapter, the results of this active isolation system are demonstrated through the proposed evaluation procedure. The associated discussions (e.g., the dynamic characteristics of the passive control, the modal analysis, and the ground excitations, etc.) are also addressed in the following sections. The verification of the active isolation system for the two-story building is eventually given in the analysis.

Table 7.1. List of controllers.

Controller Names	Objectives	Feedback	Input Shaping Filter
Passive control	Comparison	Not applied	Not applied
Zeroed control	Comparison	Not applied	Not applied
Active control (F1)	Base responses	F	No
Active control (F2)	Floor accelerations	F	No
Active control (F3)	Base responses	F	Yes
Active control (F4)	Floor accelerations	F	Yes
Active control (FA1)	Base responses	FA	No
Active control (FA2)	Floor accelerations	FA	No
Active control (FA3)	Base responses	FA	Yes
Active control (FA4)	Floor accelerations	FA	Yes
Active control (B1)	Base responses	B	No
Active control (B2)	Floor accelerations	B	No
Active control (B3)	Base responses	B	Yes
Active control (B4)	Floor accelerations	B	Yes
Active control (BA1)	Base responses	BA	No
Active control (BA2)	Floor accelerations	BA	No
Active control (BA3)	Base responses	BA	Yes
Active control (BA4)	Floor accelerations	BA	Yes

7.2 Experimental input loop gain and sensitivity transfer functions

As described in Section 6.2, both input loop gain and sensitivity transfer functions are not only used in control design but also validated through experiments. Although the control performance can be implicitly indicated from these two transfer functions, the more important aspect is the recognition of robustness from the developed controllers to the active isolation systems. First, both magnitudes and phases from the experimental input loop gain transfer functions should be comparable to those from the models, particularly in low frequencies. The experimental sensitivity transfer functions, which are calculated from the input loop gain transfer functions using Eq. (6.21), should be close to one in high frequencies. In the case of multiple actuator inputs, the comparison of phases is evaluated for the original experimental transfer functions and the singular values in the input loop gains. Additionally, the sensitivities from the original experimental transfer functions and the singular values should be close to one. After confirming these transfer functions, the controllers are applicable to the control implementations. In this section, only the procedure for the input loop gain transfer functions is introduced, while the sensitivity transfer functions can be directly calculated from these experimental loop gains.

First, the input loop gain transfer functions from experiments are introduced. For example, the active isolation in the y-direction only requires one input loop gain transfer function owing to the one actuator in this direction. Figure 7.1 illustrates the procedure to determine this input loop gain transfer function. BLWN signals are sent from the Siglab to the y-actuator, while the dSpace calculates the commands from structural responses based on the designed controller. For some controllers, a feed-forward gain is included. The contribution from this feed-forward gain is also inherently included during the testing because of the structure-table interaction. Nevertheless, this contribution should be very small because of the rigidity of the shake table. Meanwhile, the feed-forward gain is relatively small as mentioned in Section 6.2. Thus, the contribution from the feed-forward gain is negligible during the input loop gain testing. Hence, the performance and robustness of a controller can be quickly examined through the experimental loop gain testing, and the assessment of the sensitivity transfer function is then conducted using this testing result.

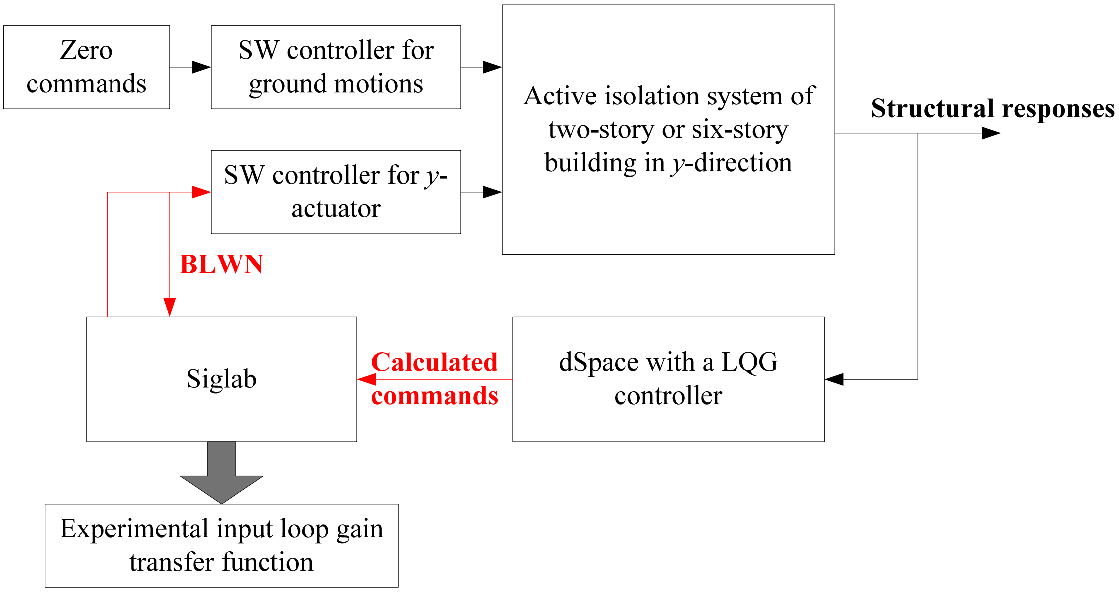

Figure 7.1. Procedure for an input loop gain transfer function from the *y*-actuator.

7.3 Control implementation procedure

This section presents the procedure to implement the active isolation systems. To analyze the performance of the active isolation systems, the first step is the frequency-domain evaluation, i.e., using BLWN ground accelerations to evaluate performance in transfer functions. Because this research also focuses on active isolation for seismic protection, the time-domain analysis is the second step which employs earthquake records to excite the structural system. In order to effectively demonstrate the active isolation systems, the passive control (e.g., isolated buildings without hydraulic actuators) and the zeroed control (e.g., zero commands sent to actuators all the time) are used to compare the performance in both the time and frequency domains. In this section, the procedure for the two-domain analysis is described, and the associated components (e.g., controllers in the dSpace and input commands for reproducing earthquake records) are addressed.

All control implementations are tested on the shake table with specific excitations, e.g., BLWN ground accelerations or earthquake records. When examining structural systems for the frequency-domain responses, the modified BLWN signals, which are identical to the signals used in the experimental system identification, are preloaded in the ShoreWestern digital controller and then drive the BLWN accelerations on the shake table. As for the time-domain analysis, this research uses several earthquake records to test structural systems. Because the shake table is intrinsically nonlinear, a method to convert an earthquake excitation into input commands for the shake table is employed. The method, called the transfer function iteration (Spencer and Yang 1998), calculates the required commands for a shake table based on the relationship between commands and table accelerations. The iteration process needs to initially interact with the actual accelerations from the shake table. In this research, the iteration process is conducted offline on a personal computer that gives results with comparable ground accelerations. Additionally, if precise BLWN ground accelerations are required, this transfer function iteration method can be used. This research mainly analyzes all structural systems by these two types of excitations.

A set of earthquake records is considered for evaluation purposes in control implementations. For the active isolation system of the two-story building, two earthquake records are employed to evaluate the time-domain performance along the y-direction. They are:

- El Centro: North-South component of the 1940 El Centro earthquake record at Imperial Valley, California.
- Kobe: North-South component of the 1995 Kobe earthquake record at Hyogo-ken, Nanbu, Japan.

These earthquake records are linearly adjusted to a specific peak ground acceleration (PGA) in control implementation. Moreover, each earthquake record utilizes the transfer function iteration to calculate the commands for the ShoreWestern digital controller in the shake table. Finally, all control strategies can be evaluated under seismic excitations through the shake table testing.

Control implementations for the passive control and the zeroed control are introduced. The passive control essentially employs the conventional shake table testing as the procedure is shown in Figure 7.2(a). The structural responses are measured when the structural system is excited by a specific type of acceleration (e.g., BLWN for frequency-domain analysis or earthquake records for time-domain analysis). Similarly, the zeroed control is implemented by the same procedure, in which all actuators are always received with zero commands as shown in Figure 7.2(b). These two control strategies are essentially examined for comparison with the developed control strategies for the active isolation systems, in order to demonstrate active isolation performance. Note that the wireless sensors and the Krypton system are only available in the active isolation system of the six-story building discussed in Chapter 8.

When implementing the active isolation systems, a closed-loop control enables the designed controller through the dSpace. Similar to the zeroed control, the overall active isolation systems are excited by the shake table, while a designed controller is concurrently implemented in the dSpace, as shown in Figure 7.3(a). The dSpace receives input signals from the structural responses and then sends the required commands for actuators based on the designed controller. This process requires three steps to complete the calculation in the dSpace, as shown in Figure 7.3(b). The first step is to remove the DC offsets in the input signals in order to avoid initial jumps occurring in the actuators. Then, the dSpace calculates the actuator commands from a state-space controller. To ensure the actuators remain within a certain range of movement, the calculated commands are constrained by a saturation function, which limits the minimum and maximum commands to the specified levels. Consequently, the active isolation systems are implemented on the shake table under BLWN or seismic excitations. Note that the wireless sensors are only used on the active isolation system of the six-story building in Chapter 8.

(a) passive control

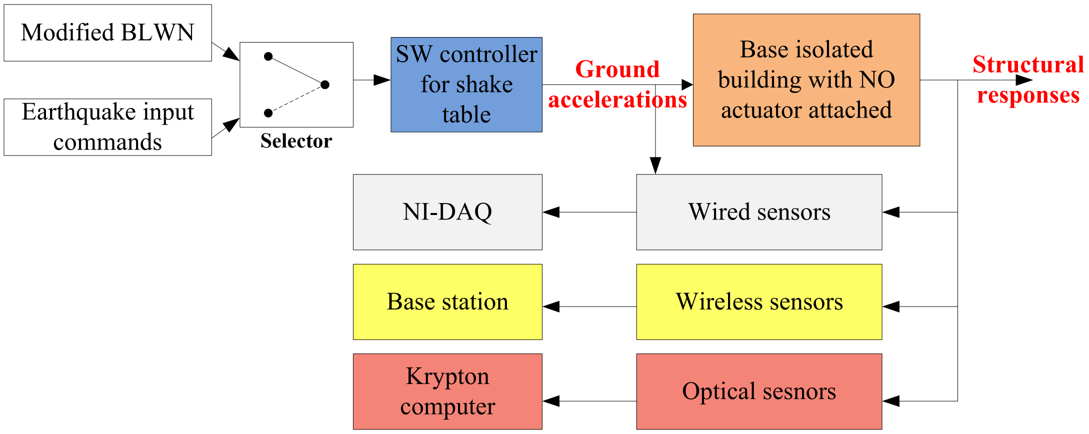

(b) zeroed control

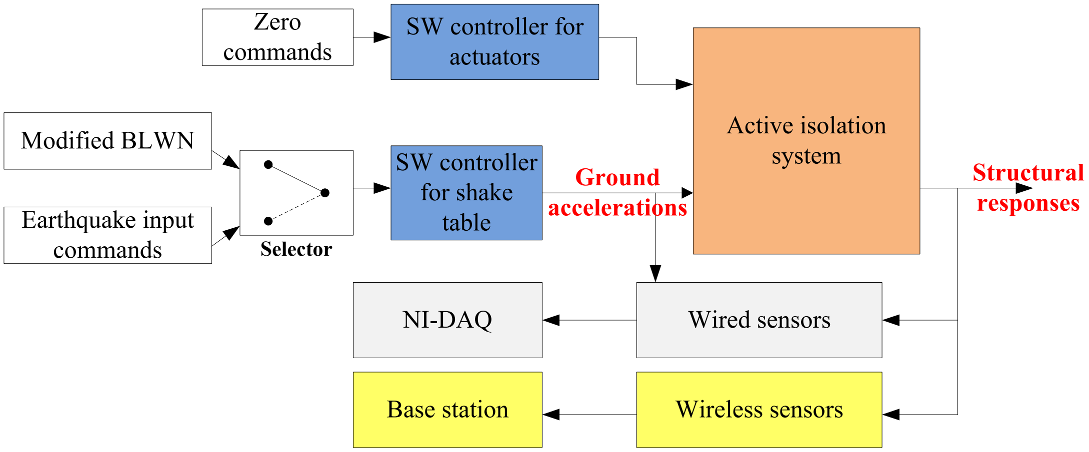

Figure 7.2. Control implementation for (a) passive control and (b) zeroed control.

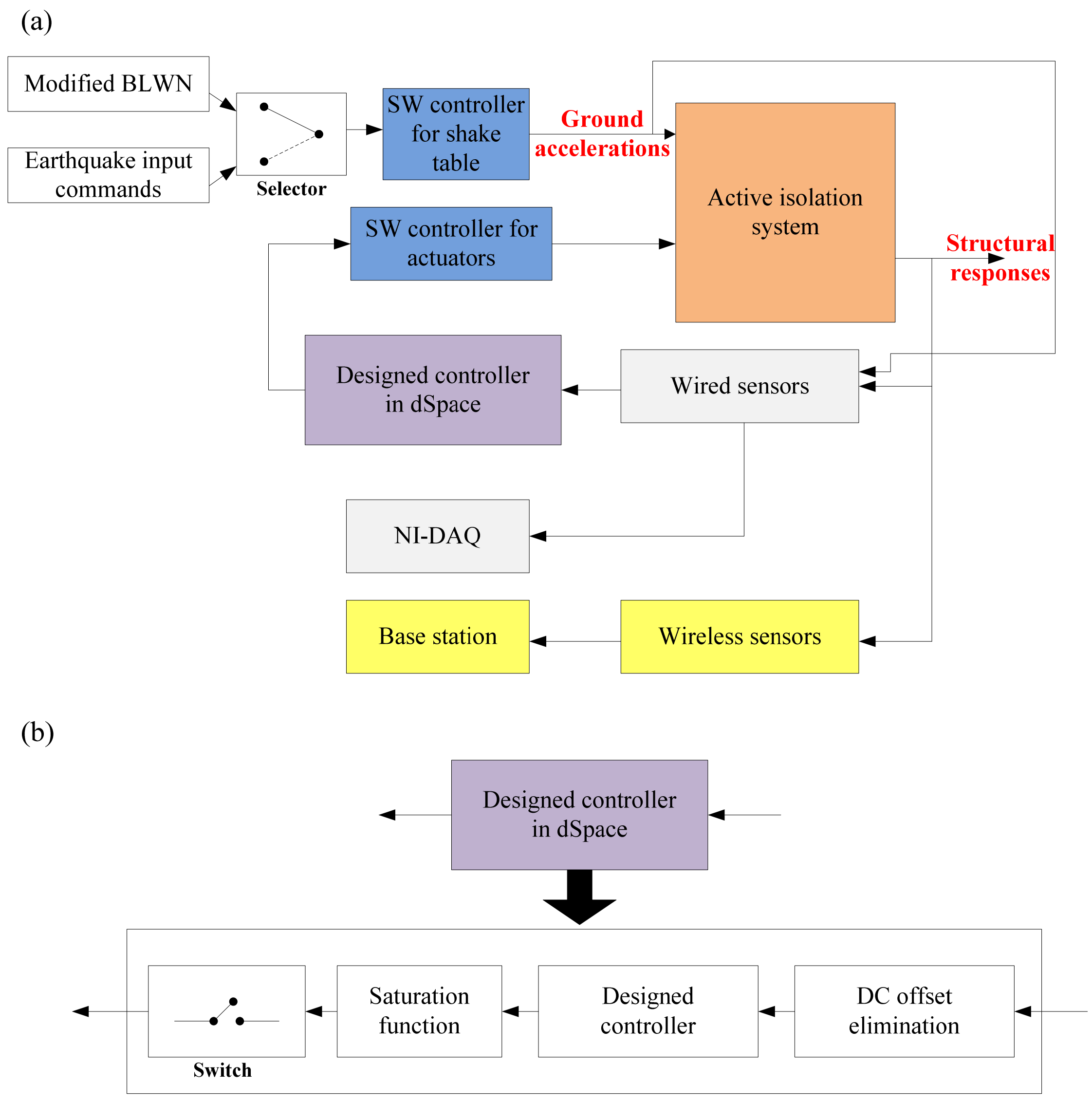

Figure 7.3. Control implementation for (a) active isolation systems and (b) designed active controllers in dSpace.

7.4 Experimental results

This section shows all results of the control implementation based on the active isolation system of the two-story building, including the passive control and the zeroed control. The control implementation follows the procedure which will be described in this section. All active controllers are developed using the H_2/LQG control methods which has been reviewed in Section

6.1. These diverse controllers are designed with different control schemes (e.g., control objectives, grouped measurements for feedback control, and incorporation with or without a feed-forward gain with respect to ground excitations), as described in Section 7.1. Because the inherent instability of this active isolation system may occur in control implementations, the input loop gain and sensitivity transfer functions are examined in advance as described in Section 7.2. Thus, the active controllers which pass the criteria of the input loop gain and sensitivity are implemented on the shake table. Moreover, the experimental procedure will be back to the system identification if too many controllers fail in the control implementation (i.e., becoming unstable). Therefore, this section first describes the tuning process of actuators. Then, the ground excitations are illustrated in order to ensure the workability of the transfer function iteration method (Spencer and Yang 1998). The dynamic characteristics of the passive control are subsequently addressed in order to understand the slight nonlinearity of these isolation bearings. The modal analysis of the natural frequencies is also given for the passive control and the zeroed control. Before the control implementation, both the input loop gain and sensitivity transfer functions are evaluated. These two transfer functions from one of the candidate active controllers are then demonstrated. Finally, all active controllers listed in Table 7.1 are implemented and verified under BLWN and seismic excitations. The frequency-domain and time-domain analyses are given group by group (i.e., the first group indicates the active controllers F1-F4), as compared to the passive control and the zeroed control. These results will verify the control implementations on this active isolation of the two-story building against seismic excitations.

7.4.1 Actuators

As mentioned in Sections 4.3.3 and 4.3.5, each actuator requires appropriate gains for the PID controller of the servo-valve before its use. Typically, only the proportional gain in the PID controller is tuned by a step function. In the tuning process, the displacement of the actuator's rod should achieve the command without introducing too much overshooting. Once the displacement response oscillates around the target of the step function, a derivative gain may be used to damp out the oscillations. After the tuning process, an actuator can be fully implemented for a real-time dynamic problem.

The tuning process for an actuator is conducted before attaching to the structure. The tuning process is basically aimed at the assignment of the proportional gain by a step function, but the tests using a sinusoid function and a band-limit white noise (BLWN) for transfer functions are also needed for checking the dynamic characteristics, e.g., the friction and the stability. Figure 7.4 lays out the testing flowchart for all steps in the tuning process. For example, the Siglab box is employed to generate the step, sinusoid, or BLWN functions for different purposes. The first step in the tuning process is to examine the different values of the proportional gain through a step function, which typically has a 5-10 % of the actuator stroke with a low resonant frequency (e.g., less than 1 Hz). The proportional gains for the actuators are assigned in the ShoreWestern digital controller in this research. Once the assigned proportional gain satisfies the overshooting criteria, the actuator is examined by a sinusoid function in order to check the dynamic behavior, i.e., the actuator should correctly behave at the peaks of the sinusoid function. If the actuator cannot perform as well as the sinusoid input, a physical inspection (e.g., the leaking problem, damaged servo valves, etc.) is required. Then, a BLWN function from the Siglab is used to test the transfer function of this actuator from the input command to the displacement output. If the PID controller with the assigned proportional gain induces unstable vibrations, the proportional gain should be determined again. In this research, the three actuators are independently examined through this procedure in order to ensure the applicability for the active isolation systems.

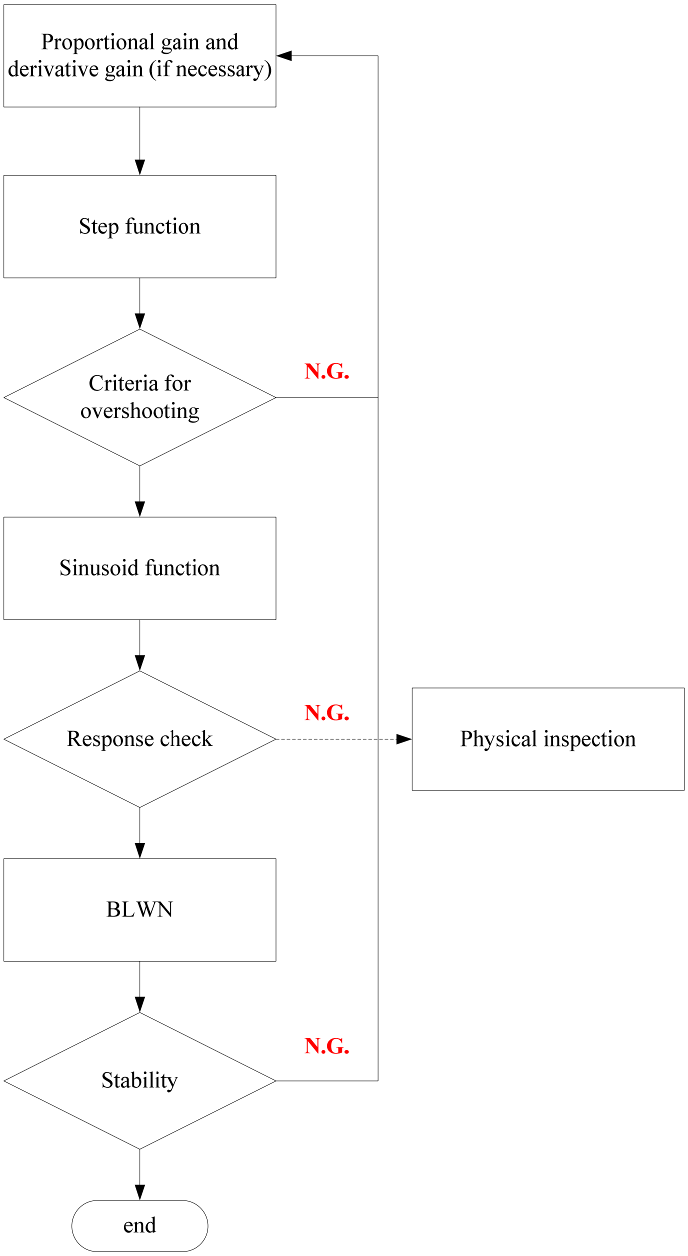

Figure 7.4. Flowchart for the actuator tuning process.

After tuning the three actuators, Figure 7.5 shows the results from the tests of the step, sinusoid, and BLWN functions. The command for the actuators in Figure 7.5(a) is a 0.2-Hz step function with 0.03-volt amplitude. All actuators achieve the command of this step function quickly without inducing too much overshoot. The sinusoid testing in Figure 7.5(b) generates the commands with different resonant frequency and different amplitudes. Typically, a sluggish step or sinusoid function will result in poor actuator responses (e.g., a 0.1-Hz step or sinusoid function). Moreover, when using the Siglab to generate a step or sinusoid function, the anti-aliasing filter should be switched off in order to ensure correct wave forms. Figure 7.5(c) illustrates the transfer functions of three actuators from the BLWN testing, indicating very similar behaviors amongst them. After completing the procedure shown in the flowchart in Figure 7.4, the actuators can be attached to the structures.

The dynamics of the actuators should be recognized again after attaching them to the structure. The displacement responses of the actuators will be slower and degraded as compared to the responses of the bare actuators. Thus, the proportional gains may need to be changed, e.g., increasing the proportional gains. However, increasing the proportional gains too much may implicitly cause an instability problem as mentioned in Section 4.3.3. In this research, the changes in the actuator dynamics are insignificant when all actuators are attached at the base layer for the two active isolation systems. If the proportional gain should be reassigned, further examinations, such as a step function or BLWN test, must be accomplished before control implementation.

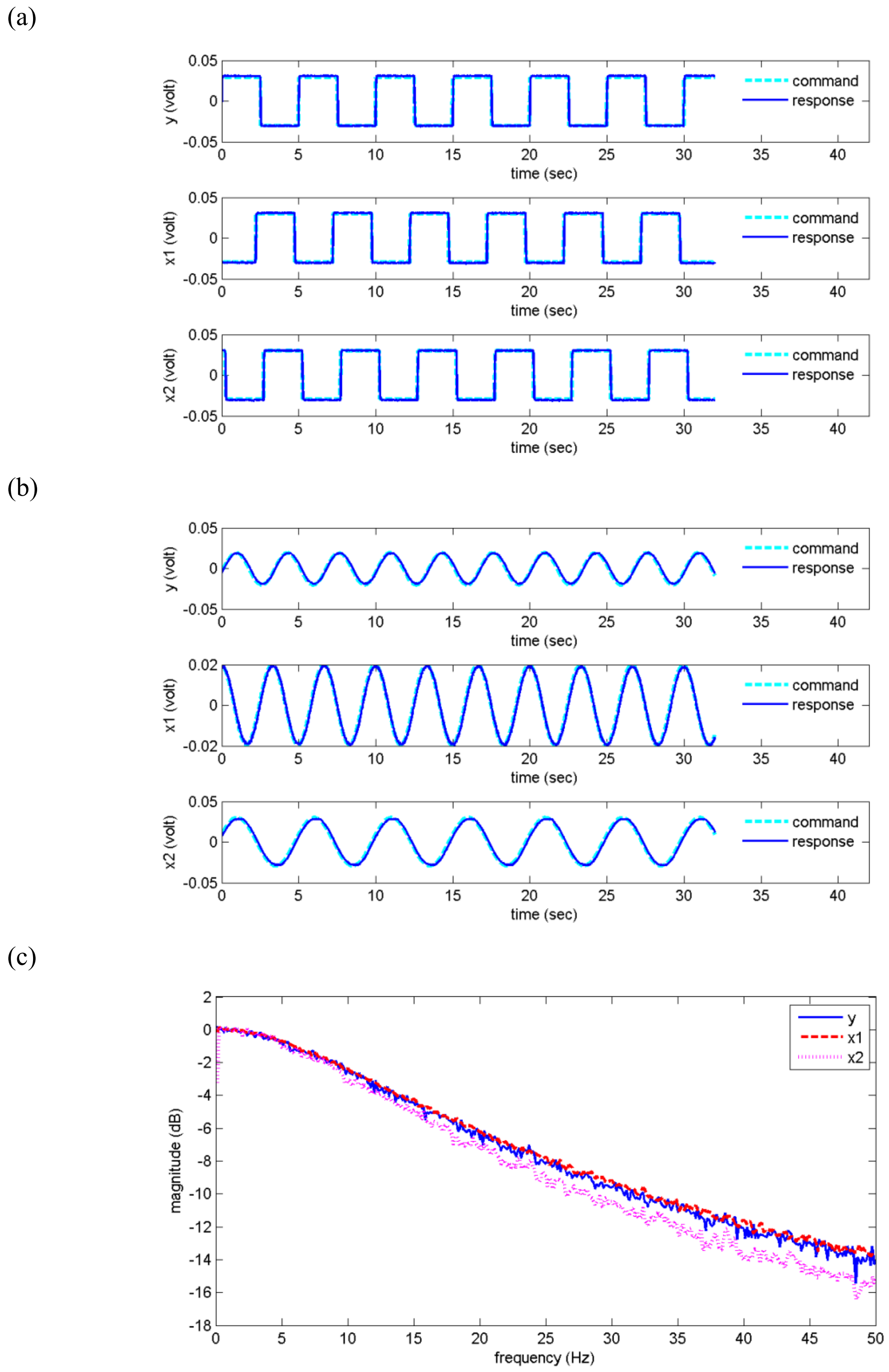

Figure 7.5. Results of the tuning process: (a) step function testing, (b) sinusoid testing, and (c) BLWN testing.

7.4.2 Verification of seismic excitations

One of goals in this research is to verify the active base isolation systems against seismic excitations. In the frequency-domain analysis, BLWN excitations are employed to test all control strategies. The method to generate BLWN excitations for the shake table has been described in Section 7.3. This type of excitation only requires approximate conversion from the BLWN ground acceleration to displacement input commands for the shake table, namely the modified BLWN commands in this research. As for duplications of historical earthquake records, more precise accelerations should be achieved in order to correctly represent the structural responses with respect to the specific seismic excitations. The transfer function iteration process aids the conversion of the ground accelerations into the displacement input commands for the shake table. Figure 7.6 demonstrates the comparison of the displacements and the accelerations of the shake table in the y-direction, indicating the target response can always be achieved with the shake table. Note that the displacement input commands must be regenerated if the structural system has been changed (i.e., different displacement input commands for the active isolation systems of the two-story and six-story buildings if the same historical earthquake record is employed).

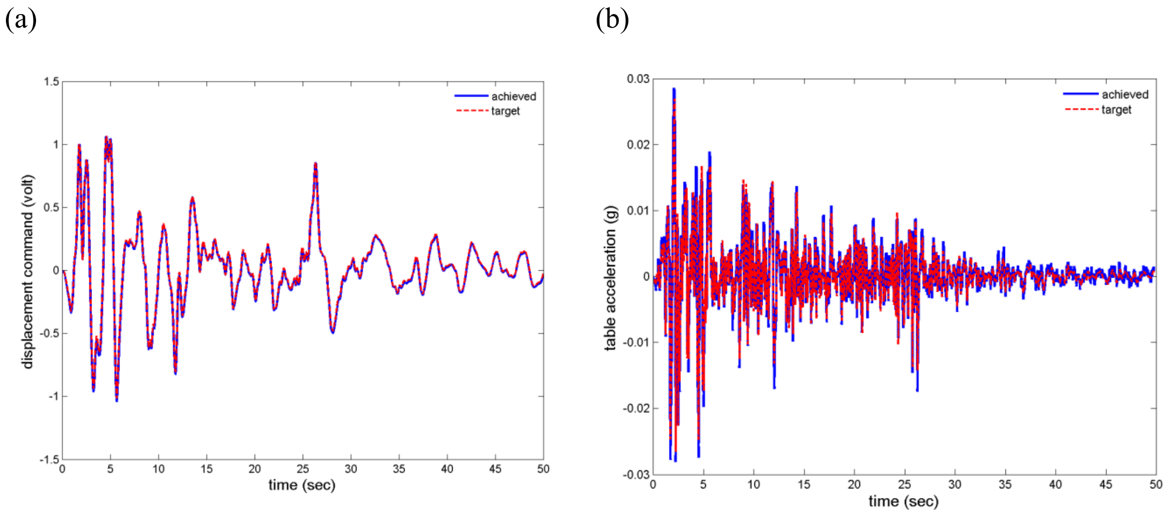

Figure 7.6. Illustration of the shake table: (a) displacement commands and (b) ground accelerations, using the El Centro record.

7.4.3 Characteristics of isolation bearings

The passive control is first examined to understand the behavior of the isolation bearings. BLWN shake table tests were employed. The natural frequencies and damping of the passive isolation system are determined and presented in Figure 7.7 under different levels of excitations to investigate system nonlinearity. Note that the passive isolation system herein is based on the two-story building. The amplitude index in the figure corresponds to the levels of the input voltages of the BLWN, which are proportional to the peak ground accelerations applied to the shake table. Because of the ball-n-cone isolation bearings, the effective stiffness decreases with amplitudes in the conical area, as shown in this figure. The results also show a significant amplitude-dependence in the isolator damping. Control designs must be robust to such system nonlinearities.

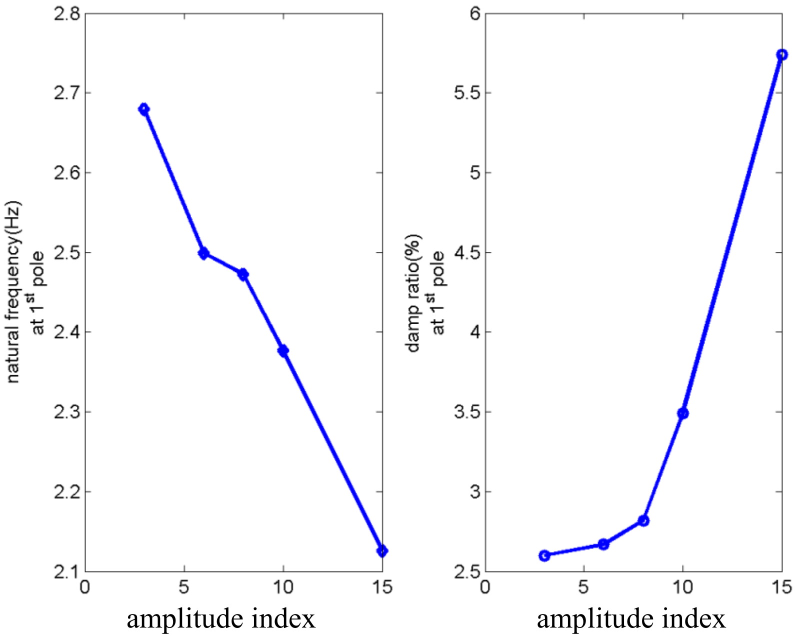

Figure 7.7. Natural frequencies and damping ratios under different amplitudes of BLWN excitations for the passive base isolation system.

The natural frequencies of the systems with the passive and zeroed control methods are respectively investigated and shown in Table 7.2. The first three natural frequencies listed in this table are directly obtained from the peak-picking method using the transfer functions from the shake table tests. As expected, the first natural frequency in the passive control is lower than that in the zeroed control. Moreover, the systems using these two control methods still behave nonlinearly. Hence, the natural frequencies and damping may vary with the amplitudes of excitations.

Table 7.2. Natural frequencies in the passive and zeroed control method.

Mode	Passive control (Hz)	Zeroed control (Hz)
1	2.6	6.0
2	10.5	13.8
3	20.5	21.3

7.4.4 Check of experimental input loop gain and sensitivity

Before control implementations, the designed controllers for the active isolation system should first be examined with the input loop gain and sensitivity transfer functions. This procedure, based on an open-loop system (see Figure 7.1), can double check the control performance and the robustness in advance. Figure 7.8 illustrates the input loop gain and sensitivity transfer functions of the active control-F1 (see Table 7.1). The magnitudes and phases of this input loop gain match well with the simulation results, particularly at low frequencies. This agreement indicates that the active control-F1 can achieve predetermined control performance. When observing the sensitivity, the magnitudes perform close to one (0 dB), indicating good robustness at high frequencies. According to the check on both transfer functions, this control can be implemented using shake table testing. All other active controllers listed in Table 7.1 are also tested by the same procedure. Once any of these controllers pass the criteria, the controller can be implemented on the shake table.

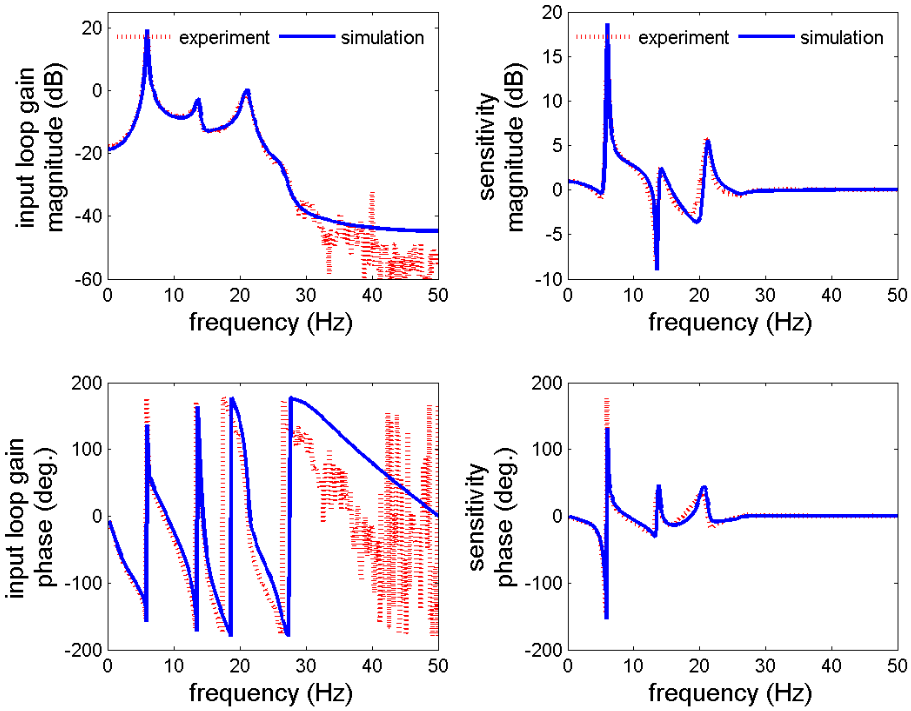

Figure 7.8. Illustration of the input loop gain and sensitivity transfer functions.

7.4.5 Results of active isolation implementations

All active controllers listed in Table 7.1 are implemented on the shake table under unidirectional excitations. The active controllers from this table are divided into four groups in accordance with the measurement feedbacks (i.e., the different colored sets in this table). Each group will be discussed for both frequency-domain analysis and time-domain analysis.

First group

The first group in this active isolation system includes three active controllers. Note that the active control-F4 is missing because the active control-F3 has achieved the same control performance as the original active control-F4 in the reductions of the base responses and the floor accelerations, although the control objectives in the designs are different. The experimental results for the base displacement and accelerations using these active controllers are provided in Table 8.3; all the response ratios are derived from the comparison to the zeroed control case.

In this group, the disturbance shaping filter is the 2nd –order Kanai-Tajimi filter with a 60% damping ratio and a 6-Hz natural frequency. For the frequency-domain analysis, the active control-F1 achieves good performance in reducing the base displacements, while the floor accelerations are still reduced as compared to the zeroed control in Table 7.3. Figure 7.9 demonstrates the control performance of this controller as compared to the passive control and the zeroed control. Note that the passive control system results provided in this section do not include the Krypton system, which can measure the base displacement in the passive isolation system. In Figure 7.9, the first natural frequency shifts to the left, indicating that applying this controller to the system increases the stiffness. Hence, this active control-F1 exhibits the capability of reducing the base displacements, which corresponds to the designed control objective.

The time-domain control performance in this group is also evaluated. Figure 7.10 shows the time-domain responses using the active control-F1 under the Kobe earthquake excitations. This controller is able to reduce the RMS floor accelerations to at least 50% of the passive control, while the peak reductions of the floor accelerations also achieve at least a 20% reduction. By looking at the time histories, the base displacement is significantly reduced using this controller, indicating the matched behavior in the frequency-domain analysis as shown in Figure 7.9. After comparing with other active controllers in Table 7.3, the active control-F1 exhibits the ability to reduce the base displacements as well as floor accelerations.

Table 7.3. Control performance in controller group 1.

Frequency domain					
Active controller	Base displacement	Base acceleration	1st Floor acceleration	2nd Floor acceleration	
(a) ratios in responses at 1st natural frequency (pole) to responses of zeroed control					
F1	0.01	0.04	0.08	0.12	
F2	0.01	0.03	0.07	0.09	
F3	0.03	0.06	0.08	0.11	
(b) ratios in RMS responses to responses of zeroed control					
F1	0.76	0.98	0.92	0.87	
F2	0.81	0.96	0.88	0.85	
F3	0.76	0.93	0.87	0.83	
Time domain					
Active controller	Base displacement	Base acceleration	1st Floor acceleration	2nd Floor acceleration	Base shear
(a) ratios in peak responses to responses of zeroed control for El Centro earthquake					
F1	0.56	0.61	0.75	0.76	0.76
F2	0.62	0.53	0.64	0.69	0.68
F3	0.58	0.66	0.77	0.77	0.79
(b) ratios in RMS responses to responses of zeroed control for El Centro earthquake					
F1	0.63	0.78	0.84	0.92	0.85
F2	0.73	0.76	0.78	0.84	0.78
F3	0.64	0.79	0.81	0.86	0.82
(c) ratios in peak responses to responses of zeroed control for Kobe earthquake					
F1	0.47	0.67	0.52	0.52	0.51
F2	0.64	0.75	0.44	0.47	0.47
F3	0.48	0.77	0.53	0.50	0.53
(d) ratios in RMS responses to responses of zeroed control for Kobe earthquake					
F1	0.39	0.54	0.39	0.36	0.39
F2	0.49	0.53	0.37	0.34	0.37
F3	0.40	0.56	0.41	0.38	0.41

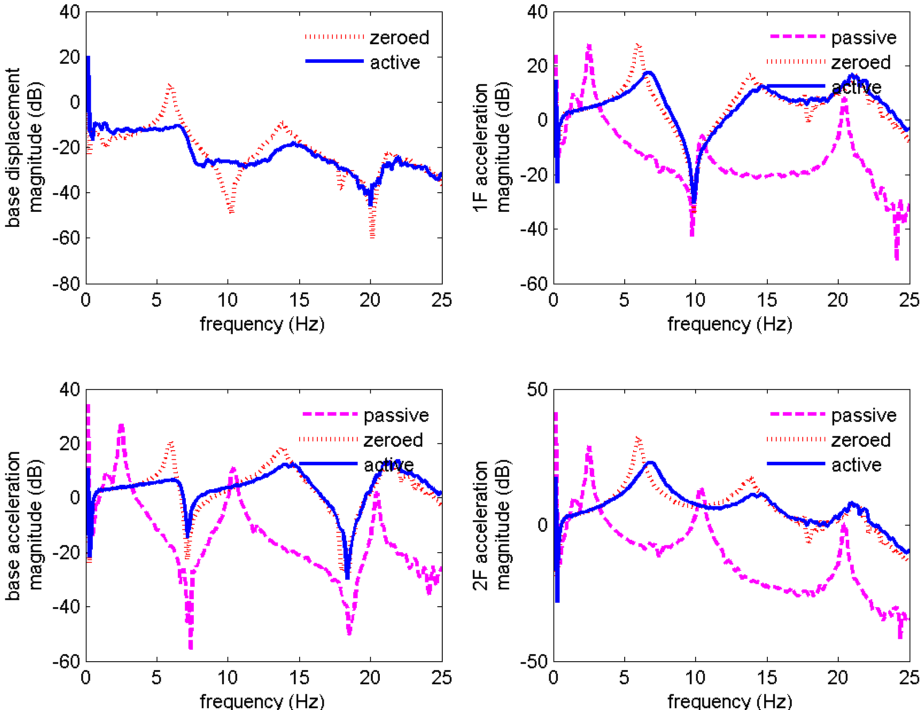

Figure 7.9. Comparison of frequency-domain responses using active control-F1.

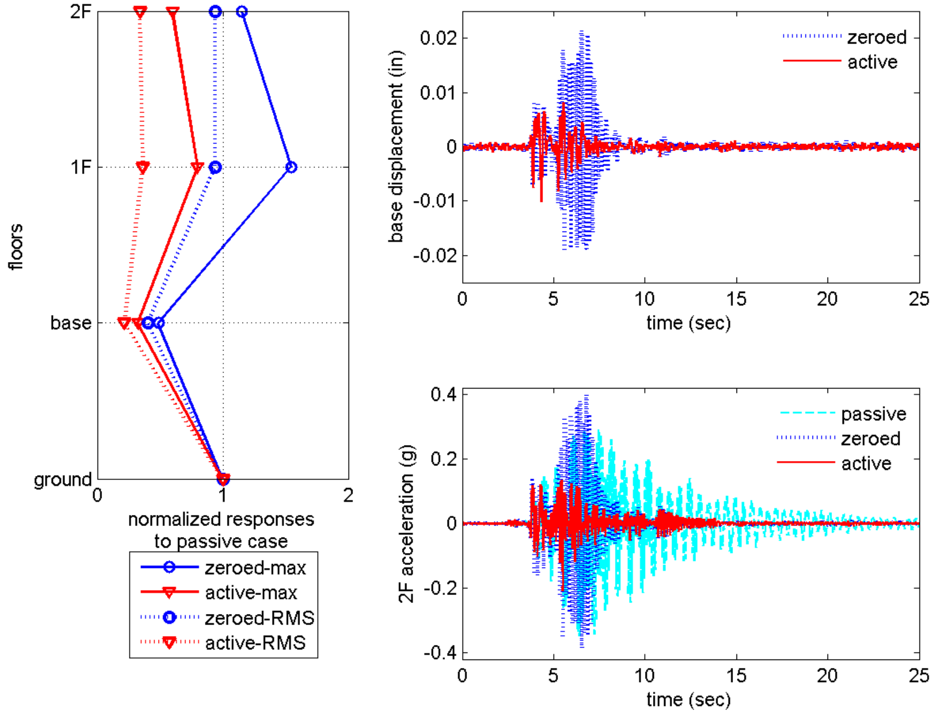

Figure 7.10. Comparison of time-domain responses using active control-F1.

Second group

This group employs only the floor accelerations to complete the closed-loop feedback control. Four active controllers are included in this group in order to compare their control performance. All control results are shown in Table 7.4, which follows the same analysis approach as Table 7.3. Both the frequency-domain analysis and the time-domain analysis are discussed in the following.

First, the controllers using acceleration feedback exhibit significant response reductions in the frequency-domain. The active control-FA4 is focused on the reductions of the floor accelerations, which is visible in the corresponding results in Table 7.4 and the transfer-function responses in Figure 7.11. The high damping from this controller results in the direct reduction of all accelerations of the 1st-mode response. This figure also demonstrates reductions in the floor accelerations of the first two modes, which indicates the flexibility of the control designs using the H_2/LQG control methods with an input shaping filter.

All active controllers in this group are also examined on the shake table against the three seismic excitations. Figure 7.12 illustrates the time-domain control performance using the active control-FA4 design under the Kobe earthquake excitation. In this figure, this controller significantly reduces the roof acceleration as is reflected in either the RMS response or in the peak response. Again, the behavior shown in this figure matches that in the frequency domain; for example, the 98% and 27% reductions in the transfer-function magnitude at the first natural frequency and the RMS response in Table 7.4, respectively. Again, the control designs based on the H_2/LQG control methods with an input shaping filter exhibits the ability to significantly reduce the floor accelerations, while also decreasing the base displacement.

Table 7.4. Control performance in controller group 2.

Frequency domain					
Active controller	Base displacement	Base acceleration	1st Floor acceleration	2nd Floor acceleration	
(a) reductions in responses at 1st natural frequency (pole) to responses of zeroed control					
FA1	0.03	0.04	0.04	0.05	
FA2	0.03	0.04	0.03	0.04	
FA3	0.00	0.16	0.69	0.98	
FA4	0.06	0.03	0.01	0.02	
(b) reductions in RMS responses to responses of zeroed control					
FA1	0.83	0.94	0.85	0.80	
FA2	0.86	0.93	0.83	0.79	
FA3	0.75	1.09	1.00	1.00	
FA4	1.01	0.91	0.79	0.73	
Time domain					
Active controller	Base displacement	Base acceleration	1st Floor acceleration	2nd Floor acceleration	Base shear
(a) ratios in peak responses to responses of zeroed control for El Centro earthquake					
FA1	0.75	0.62	0.67	0.65	0.71
FA2	0.86	0.65	0.65	0.63	0.71
FA3	0.43	0.60	0.89	1.02	0.94
FA4	1.17	0.67	0.49	0.52	0.59
(b) ratios in RMS responses to responses of zeroed control for El Centro earthquake					
FA1	0.78	0.76	0.70	0.73	0.71
FA2	0.88	0.76	0.68	0.70	0.69
FA3	0.55	0.87	1.25	1.46	1.28
FA4	1.27	0.76	0.59	0.55	0.58
(c) ratios in peak responses to responses of zeroed control for Kobe earthquake					
FA1	0.64	0.80	0.47	0.44	0.47
FA2	0.66	0.74	0.43	0.43	0.44
FA3	0.57	0.67	0.54	0.53	0.56
FA4	0.94	0.80	0.40	0.33	0.43
(d) ratios in RMS responses to responses of zeroed control for Kobe earthquake					
FA1	0.51	0.55	0.39	0.35	0.38
FA2	0.54	0.55	0.38	0.34	0.38
FA3	0.41	0.53	0.41	0.39	0.40
FA4	0.77	0.57	0.36	0.30	0.35

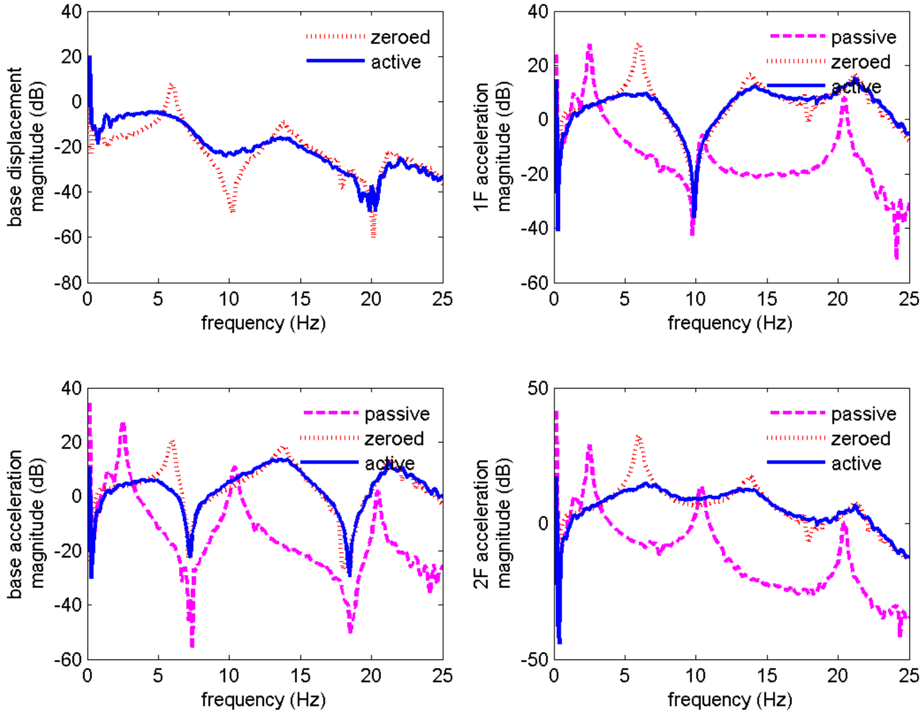

Figure 7.11. Comparison of frequency-domain responses using active control-FA4.

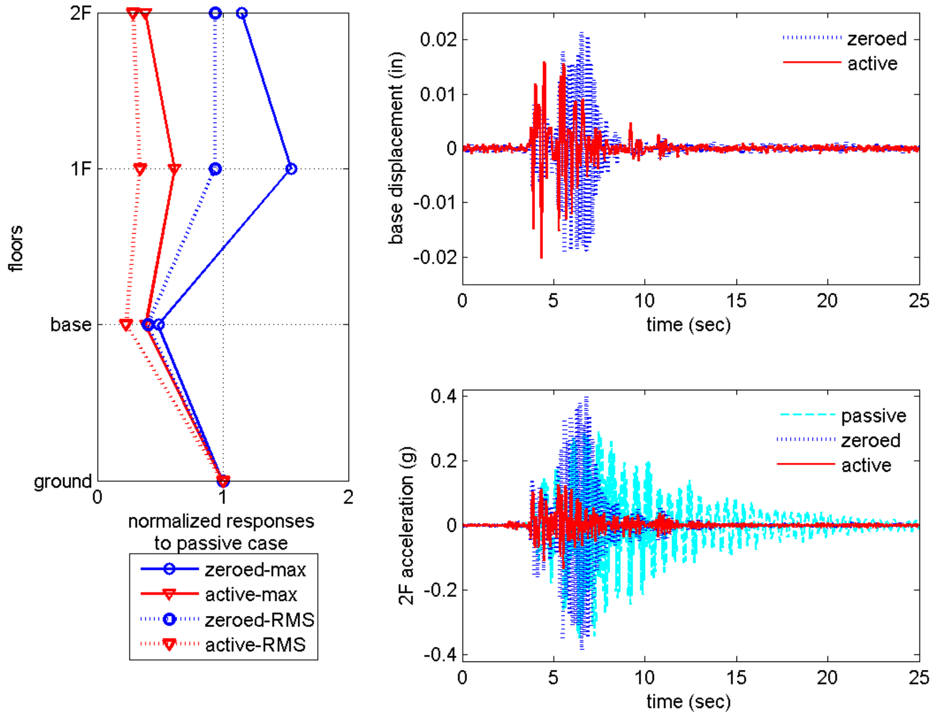

Figure 7.12. Comparison of time-domain responses using active control-FA4.

Third group

The controllers in the third group seek to control the isolated building using less information; only the base displacement and the base acceleration measurements are used for feedback control. Although the base responses are selected as the feedback measurements, the control objectives can still be focused on the floor accelerations as is the case in active control-B2 and -B3. In this group, all the results are shown in Table 7.5, which is organized the same way as the previous two groups. Based on the results, the active control-B3 design is selected for discussion of both the frequency-domain and time-domain analysis in this section.

Figure 7.13 shows the frequency-domain results using the active control-B3. As compared to the results in Table 7.5, the control objective of the base displacement in this controller exhibits reductions in three modes of the transfer-function response of this measurement. For example, the reduction in the magnitude of the transfer function at the first natural frequency achieves around 96%. The significant reduction in the base displacements illustrates the concept of the active base isolation approach in which both the base displacements and floor accelerations are reduced. Hence, this control strategy also proves the feasibility of an active isolation system.

A time-domain analysis is also conducted in this group. Figure 7.14 shows the peak/RMS floor acceleration reductions as compared to the passive control and the zeroed control as well as the time histories of the base displacement and the roof acceleration. This figure illustrates that the controller exhibits high control performance in the RMS response of the base displacement as well as the base displacement itself, which corresponds to the control objective. These results, evident in all four controllers, especially the active control-B3, verify the idea of designing the controllers to use the base responses as the feedback measurements.

Table 7.5. Control performance in controller group 3.

Frequency domain					
Active controller	Base displacement	Base acceleration	1st Floor acceleration	2nd Floor acceleration	
	(a) reductions in responses at 1st natural frequency (pole) to responses of zeroed control				
B1	0.13	0.16	0.20	0.21	
B2	0.12	0.17	0.17	0.19	
B3	0.04	0.08	0.11	0.13	
B4	0.24	0.09	0.03	0.02	
	(b) reductions in RMS responses to responses of zeroed control				
B1	0.87	0.99	0.93	0.87	
B2	0.88	1.00	0.93	0.87	
B3	0.78	0.92	0.85	0.81	
B4	1.27	1.01	0.88	0.77	
Time domain					
Active controller	Base displacement	Base acceleration	1st Floor acceleration	2nd Floor acceleration	Base shear
	(a) ratios in peak responses to responses of zeroed control for El Centro earthquake				
B1	0.78	0.83	0.87	0.83	0.86
B2	0.83	0.86	0.90	0.84	0.88
B3	0.78	0.74	0.82	0.75	0.81
B4	1.46	1.07	0.77	0.74	0.73
	(b) ratios in RMS responses to responses of zeroed control for El Centro earthquake				
B1	0.82	0.86	0.83	0.84	0.83
B2	0.82	0.86	0.83	0.84	0.83
B3	0.74	0.82	0.82	0.85	0.82
B4	1.73	1.01	0.73	0.64	0.67
	(c) ratios in peak responses to responses of zeroed control for Kobe earthquake				
B1	0.58	0.73	0.62	0.63	0.61
B2	0.57	0.79	0.64	0.63	0.62
B3	0.52	0.79	0.54	0.49	0.51
B4	1.33	1.07	0.61	0.48	0.58
	(d) ratios in RMS responses to responses of zeroed control for Kobe earthquake				
B1	0.50	0.67	0.51	0.47	0.49
B2	0.51	0.67	0.51	0.47	0.50
B3	0.42	0.57	0.42	0.39	0.42
B4	1.06	0.82	0.48	0.39	0.43

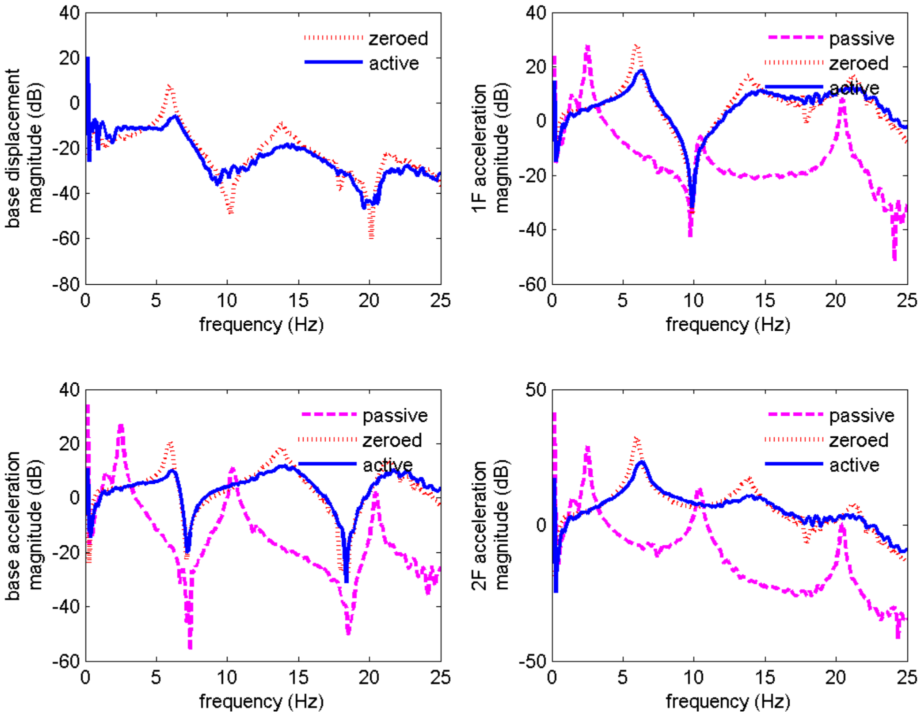

Figure 7.13. Comparison of frequency-domain responses using active control-B3.

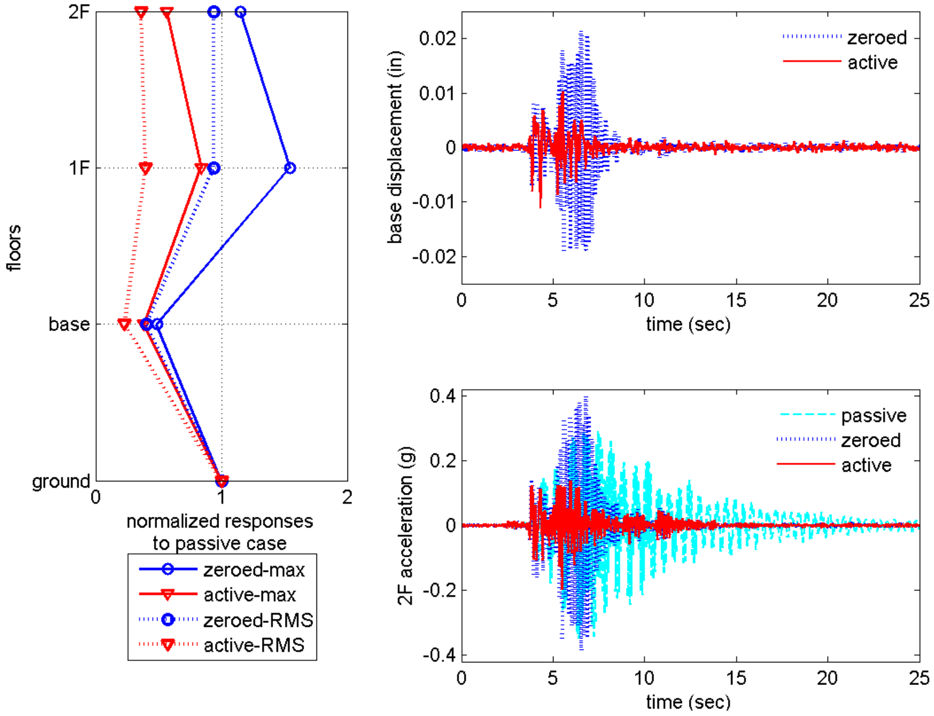

Figure 7.14. Comparison of time-domain responses using active control-B3.

Fourth group

In this control group, the design of the controllers is based on the base displacement and the roof acceleration as the feedback measurements in the closed-loop control. The control results for all tests under the three different excitations are presented in Table 7.6. In this table, the active control-BA2 significantly reduces the floor accelerations. Although the active base isolation system cannot always guarantee a reduction in the base displacement and the roof acceleration at the same time, a control design based on these two measurements for feedback still achieves the desired levels of control performance as shown in this table. Hence, this controller demonstrates the design flexibility of the H_2/LQG control methods as well. Further analysis of this controller is provided in the following discussions.

The frequency-domain analysis of the active control-BA2 is provided in Figure 7.15 and illustrates the high damping at the 1st mode due to this controller design. Most active base isolation systems can reduce the structural responses if the control design focuses on the 1st-mode reductions (Riley et al. 1998). As a result, this controller reduces the RMS responses of the base displacement and the roof acceleration in the frequency-domain analysis to 16% and 10%, respectively.

The considerable reductions of the base displacement and the roof acceleration due to active control-BA2 are visible in the time-domain as well, which is given in Figure 7.16. The results show the control performance of floor accelerations achieving at least 50% off the RMS responses of the passive control, while the reductions in the peak responses of all the accelerations are at least 20% off the passive control. The results verify the control objective of this active control-BA2 (i.e., the active base isolation is barely able to reduce the base displacement and the roof acceleration at the same time). Therefore, the active base isolation system based on this control strategy is a feasible alternative to mitigate the structural responses.

Table 7.6. Control performance in controller group 4.

Frequency domain				
Active controller	Base displacement	Base acceleration	1st Floor acceleration	2nd Floor acceleration
(a) reductions in responses at 1st natural frequency (pole) to responses of zeroed control				
BA1	0.03	0.05	0.05	0.05
BA2	0.04	0.05	0.05	0.05
BA3	0.16	0.09	0.04	0.03
BA4	0.15	0.08	0.03	0.02
(b) reductions in RMS responses to responses of zeroed control				
BA1	0.83	0.95	0.83	0.81
BA2	0.84	0.96	0.83	0.80
BA3	1.05	0.92	0.80	0.75
BA4	1.07	0.92	0.81	0.76

Time domain					
Active controller	Base displacement	Base acceleration	1st Floor acceleration	2nd Floor acceleration	Base shear
(a) ratios in peak responses to responses of zeroed control for El Centro earthquake					
BA1	0.76	0.76	0.72	0.68	0.79
BA2	0.90	0.80	0.76	0.69	0.80
BA3	1.70	0.92	0.87	0.77	0.87
BA4	1.54	0.91	0.81	0.79	0.81
(b) ratios in RMS responses to responses of zeroed control for El Centro earthquake					
BA1	0.76	0.79	0.73	0.75	0.74
BA2	0.87	0.80	0.72	0.74	0.73
BA3	1.67	0.97	0.74	0.67	0.71
BA4	1.60	0.95	0.73	0.66	0.71
(c) ratios in peak responses to responses of zeroed control for Kobe earthquake					
BA1	0.53	0.79	0.50	0.49	0.48
BA2	0.56	0.77	0.48	0.48	0.49
BA3	0.99	0.83	0.49	0.46	0.50
BA4	0.95	0.76	0.50	0.49	0.51
(d) ratios in RMS responses to responses of zeroed control for Kobe earthquake					
BA1	0.46	0.58	0.40	0.36	0.39
BA2	0.50	0.58	0.41	0.36	0.40
BA3	0.91	0.68	0.44	0.37	0.43
BA4	0.90	0.69	0.45	0.38	0.43

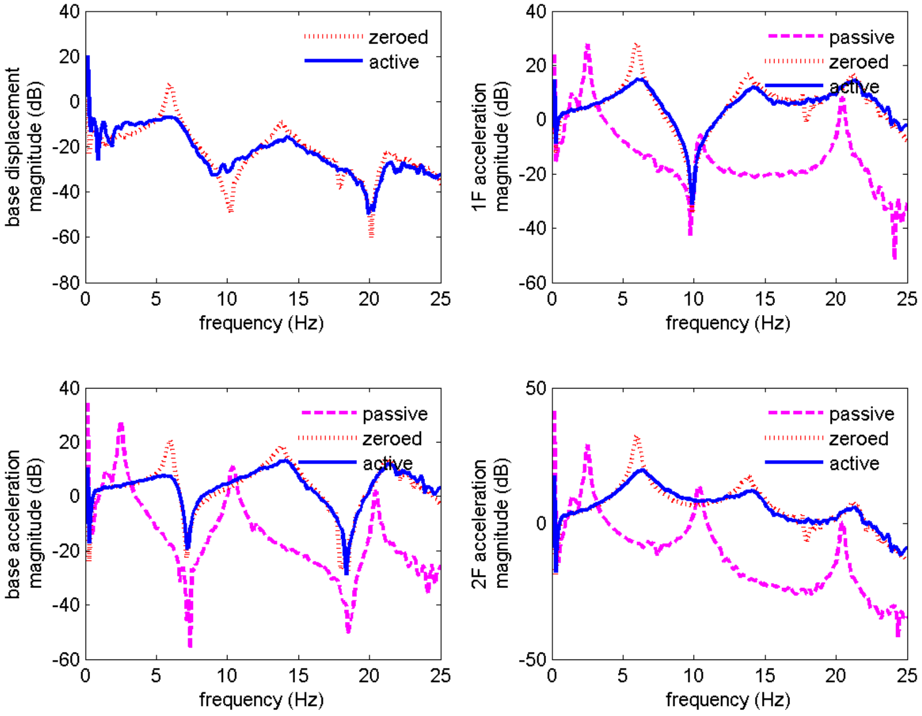

Figure 7.15. Comparison of frequency-domain responses using active control-BA2.

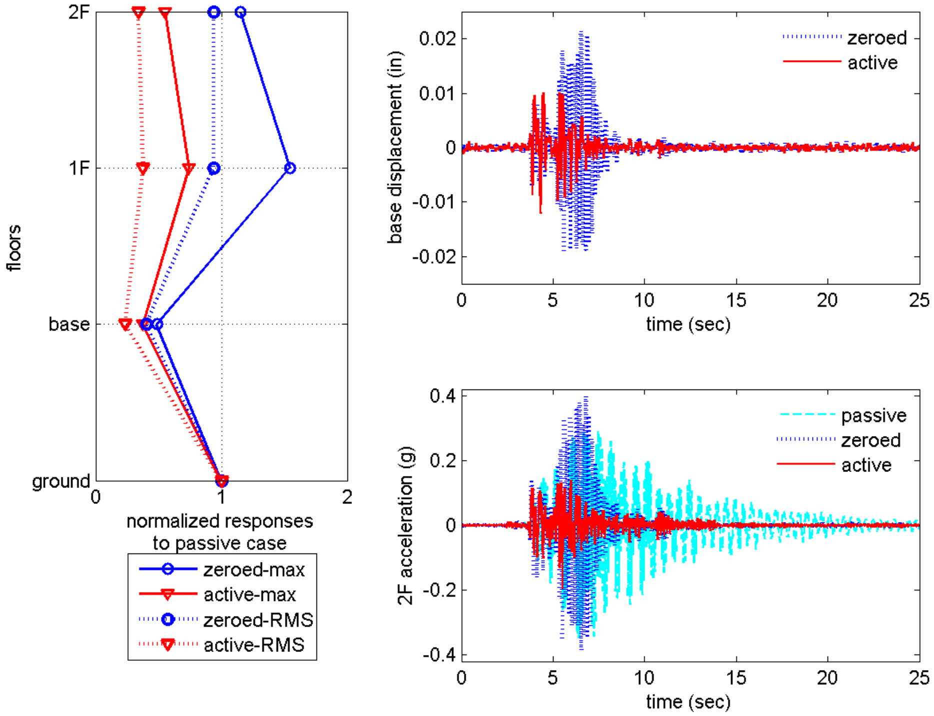

Figure 7.16. Comparison of time-domain responses using active control-BA2.

7.5 Summary

This section presented the results of control implementations for the active isolation system of the two-story building. First, the setup of this active isolation system was briefly introduced again. All control strategies such as the passive, zeroed, and active control methods were also introduced. The detailed control objectives of the examined active controllers were addressed in order to ensure the workable active control strategies for this system. Before control implementations, the dynamics of the isolation bearings were characterized by the passive control under different levels of BLWN excitations. The input loop gain and sensitivity transfer functions were then illustrated to confirm the performance and robustness of an active controller. This active isolation system was eventually implemented and verified on the shake table under unidirectional excitations.

In summary of implementation results, various control strategies for the active isolation system were designed and verified using the shake table tests under unidirectional excitations. All control strategies demonstrated the control performance corresponding to the control objectives, i.e., the concurrent reductions in base displacements and floor accelerations. The results also indicated the applicability of the H_2/LQG control methods to active base isolation systems. Similar performance was found among all control groups, although the grouped measurements for feedback control were selected differently. The successful control implementations for this active isolation system of the two-story building in the *y*-direction proved the effectiveness of the H_2/LQG controllers and gave the possibility of control implementations for the active isolation system of the six-story building under bi-directional excitations, which will be presented in next chapter.

CHAPTER 8 ACTIVE ISOLATION OF A SIX-STORY BUILDING UNDER BI-DIRECTIONAL EXCITATION

An active isolation system of a six-story building is implemented under bi-directional excitations using the shake table testing. The six-story steel-frame building, which is isolated by the ball-n-cone bearings, is actively controlled by three hydraulic actuators against seismic excitations. These three actuators are distributed along the horizontal plane, where one of them is installed on the strong axis and the other two are placed evenly and symmetrically to the weak axis (e.g., the axis through the center of gravity of the structural system). The control objective of this active isolation system is to significantly reduce the base displacements of this building while slightly inducing floor accelerations, as compared to the passively isolated building in the planar motions (e.g., two horizontally translational motions and one torsion motion with respect to the vertical axis). Three control strategies based on the H_2/LQG control design employ differently grouped measurements to realize the feedback control in order to verify the applicability of this control method and to demonstrate high performance based on this design. In this chapter, a brief introduction of this active isolation system is provided. This introduction contains all control strategies used in the control implementation, the control objectives and setups of three active control strategies, and the procedure to analyze results of the control implementation. Before control implementation, the input loop gain and sensitivity transfer functions are tested in order to ensure the performance and robustness of the active controllers. Finally, this active isolation of the six-story building is verified through the shake table testing against a wide range of seismic excitation.

8.1 Brief introduction of the active isolation system

This active isolation of the six-story building is developed to implement structural control along the horizontal plane. One hydraulic actuator which is located in the *y*-direction (strong axis as shown in Figure 3.1(b)) basically controls the *y*- translational motions. The other two actuators, which are respectively located in the *x*1- and *x*2- directions, control the *x*- translation and torsional motions. Although the entire system is symmetric with respect to the center of gravity of this structure, the torsion responses may still occur due to the different dynamics of the two *x*-actuators. Three sets of five wired accelerometers are placed at the base, 2nd floor, 4th floor, 5th floor, and 6th floor in the *y*-, *x*1-, and *x*2- directions, respectively. Two wireless sensors embedded with tiny tri-axial accelerometers are located at the center of gravity in the 1st and 3rd floors. Three LVDTs along with the actuators are employed to measure the base displacements. For control purposes, only partial sensors should be incorporated in the control implementations, but measurements from all sensors are used to evaluate the control performance. After designing the active controllers, this active isolation system can be implemented on the shake table against bi-directional seismic excitations.

In a control-oriented problem, the model of this active isolation system is obtained through the system identification technique as described in Chapter 5. Using the system identification procedure mentioned in Section 5.3, a time-invariant continuous-time model is identified based on the measurements of all wired accelerometers and three LVDTs. Due to the geometrical symmetry, the dynamics of this active isolation system are divided into two models with respect to both *x*- and *y*- directions. Through assembly of these two models, a full model can describe the horizontally planar motions of this active isolation system. The results of the identified model have been shown in Section 5.5, in which the comparable transfer functions from the identified model are validated with the experimental transfer functions. This precisely identified model is subsequently employed to develop controllers for the three actuators.

As discussed in Section 6.4, the advanced H_2/LQG control method is employed to generate active controllers for this active isolation system. This advanced method contains an input shaping filter for the controllers in both *x*- and *y*- directions. Note that the system is divided into two models due to the geometrical symmetry, so controllers for each direction are designed independently. Moreover, an input shaping filter in the H_2/LQG control design not only gives the excitation inputs to be additional measurements in the Kalman estimator design but also provides the choice to include a feed-forward gain in a control design. This input shaping filter can consider the dominate frequency components of excitations in structural responses as well as roll off uncertain components in high frequencies. Three controllers, which are developed based on the H_2/LQG control method, are categorized in accordance with the grouped measurements for feedback control as:

- Controller F: this control design employs wired measurements to realize the feedback control, e.g., the base displacement and the base, 2nd floor, 4th floor, and 6th floor accelerations in the *y*-direction for the *y*-actuator and in the *x*1- and *x*2- directions for both *x*-actuators. Only the *y*-controller contains a feed-forward gain in this case.
- Controller FA: this control design utilizes acceleration measurements for the feedback control, such as the base, 2nd floor, 4th floor, and 6th floor accelerations along the *y*-direction for the *y*-actuator and along the *x*1- and *x*2- directions for both *x*-actuators. Both controllers in these two directions contain feed-forward gain, respectively.
- Controller BA: this control design uses few measurements for the feedback control, such as the base displacement and top floor acceleration along the *y*-direction for the *y*-

actuator and along the *x*1- and *x*2- directions for both *x*-actuators. Only the *x*-controller has a feed-forward gain.

The main control objective among these three control strategies is focused on base displacement reductions without increasing floor accelerations too much. Thus, following the design procedure in Section 6.2, these controllers are developed with consideration of high performance and control robustness. An example for the controller-FA has been illustrated in Section 6.4, and subsequently the other two controllers are generated based on the same procedure.

To evaluate the performance of this active isolation system, two additional control strategies are also tested in order to compare effectiveness of the developed active controllers. The first one, named the zeroed control, always sends zero commands to three actuators, in which the inherent PID controller for the servo-valve seeks to minimize the displacements at the base at the actuator's locations. The other control strategy, named the passive control, uses the purely isolated building without any actuators attached. In an ideal performance, the active isolation system should significantly reduce base displacements and perform comparable floor accelerations as compared to the passive control. When referring to the zeroed control, the active isolation system should effectively lower floor accelerations and slightly induce base displacements as well. Hence, this active isolation system can achieve the ideal performance if the three controllers have been adequately designed corresponding with the predetermined control objectives.

As mentioned in Section 7.2, the input loop gain and sensitivity transfer functions are experimentally examined before control implementation. Again, these two transfer functions can check an active controller for quality (e.g., the agreement of magnitudes and phases), performance (e.g., singular values at low frequencies), and robustness (e.g., singular values at high frequencies). The numerical input loop gains should have identical magnitudes and phases in low frequencies, while the singular values of the transfer functions should be potentially high in the input loop gains and very close to one in the sensitivities. In this control problem, the *y*-controller (e.g., the controller only for the *y*-actuator) only contains one transfer function for the input loop gain, indicating that the singular values of the transfer function are identical to the magnitudes of this transfer function.

As for the *x*-controller (e.g., the controller for both *x*-actuators), the singular values of the input loop gain and sensitivity transfer functions are calculated by the singular value decomposition after these 2x2 transfer functions are experimentally determined. Using these transfer functions, the control performance of the designed controller is foreseeable, and the robustness of this controller can be recognized. The detailed procedure is also described in Section 8.2.

In control implementation, the active controllers are performed with the digital controller of the dSpace. Figure 7.3(b) clearly illustrates the steps to implement an active controller. However, this flowchart contains an important key, the sampling rate (or the sampling frequency). The sampling rate is usually chosen to be as high as possible; otherwise, the aliasing effect will occur in the system, particularly in the feedback loop. The potential aliasing effect also gives a reason to examine the input loop gain and sensitivity transfer function experimentally. In the control implementation of this active isolation system, the sampling rate is tuned to 2000 Hz. The designed active controllers are correspondingly converted into a discrete-time, state-space form, although the controllers are originally designed based on a continuous-time identified model. Thus, all components for the implementation in the dSpace are in discrete-time. According to the procedure in Figure 7.3(b) with this high sampling rate, an active controller can be successfully implemented for this active isolation system.

To completely analyze the control implementations, the results are presented in both time and frequency domain. The three-minute BLWN signals are employed to obtain the transfer functions for the frequency-domain analysis, while five earthquake records given in the following are used to test all controller strategies performance in the time domain.

- El Centro: two horizontal components of the 1940 El Centro record at El Centro, California.
- Jiji: two horizontal components of the 1999 Jiji earthquake record at the TCU-068 station, Taichung, Taiwan.
- Kobe: two horizontal components of the 1995 Kobe earthquake record at Hyogo-ken, Nanbu, Japan.
- Newhall: two horizontal components of the 1994 Northridge earthquake record at Newhall County, California.
- Sylmar: two horizontal components of the 1994 Northridge earthquake record at Sylmar, California.

The frequency-domain analysis contains the direct comparison of transfer functions as well as the RMS responses and the magnitude reductions at the first natural frequencies. The time-domain analysis compares the maximum and RMS responses of measurements and the differences of the responses under the five earthquake records. A detailed analysis will be given in the following section.

Through a series of procedures, the active isolation of the six-story building can be verified and implemented against seismic excitations using shake table testing. The results of the control implementation will demonstrate the advantages of active isolation. These results will also indicate the verification of an active isolation system under bi-directional excitations.

8.2 Experimental input loop gain and sensitivity for the *x*-actuators

When the system has two actuator inputs as it does with the active isolation system in the *x*-direction, the procedure to determine the experimental input loop gain transfer function is slightly altered. Similarly to the experimental system identification procedure for this system, the input loop gains employ two steps to obtain the transfer functions with respect to each actuator input. The experimental input loop gain transfer function matrix, **L**, can be defined as

$$\mathbf{L}(s)=\begin{bmatrix} G_{u_{x1}u_{x1}} & G_{u_{x1}u_{x2}} \\ G_{u_{x2}u_{x1}} & G_{u_{x2}u_{x2}} \end{bmatrix} \tag{7.1}$$

The first step in the procedure is to obtain the first column in Eq. (8.1). Thus, BLWN signals with larger amplitudes are sent to the *x*1-actuator, while smaller BLWN signals are sent to the *x*2-actuator. The input loop gain transfer functions for the *x*1-actuator are subsequently determined. Similarly, BLWN signals with larger and smaller amplitudes are sent to the *x*2- and *x*1- actuators, and the input loop gain transfer functions for the *x*2-actuator are then determined. Thus, Figure 8.1 (a) and (b) illustrate these two steps for the input loop gain transfer functions for the *x*1- and *x*2- actuators, respectively. Again, if a controller for this system has a feed-forward gain, the contribution for this gain can be neglected during the testing. Therefore, a controller for the active isolation system of the six-story building in the *x*-direction can be confirmed by the performance and the robustness.

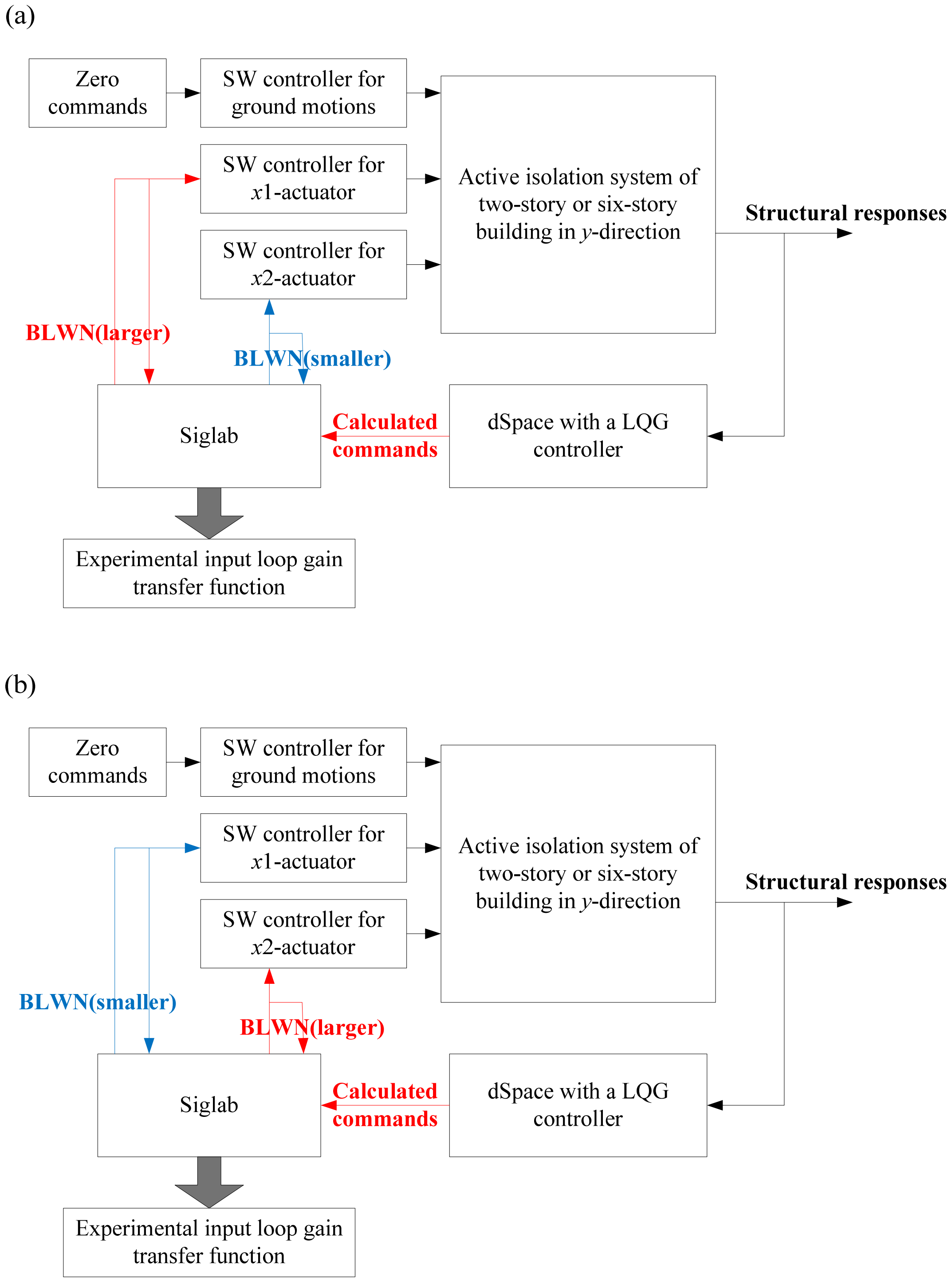

Figure 8.1. Procedure for the input loop gain transfer functions from (a) the *x*1-actuator and (b) the *x*2-actuator.

8.3 Results of the control implementation

This section presents all results from the control implementation of the active isolation of the six-story building under various bi-directional excitations. First, the actuators are calibrated and tuned in accordance with the results in Section 7.1. The earthquake records used in this active isolation system are subsequently introduced. The identified model for the development of all active controllers has been introduced in Section 5.5. Thus, the control design also employs the identification results to generate active controllers. Before control implementation, the input loop gain and sensitivity transfer functions should be checked. These two types of transfer functions are then illustrated using one of three active controllers for the three actuators. The active isolation system is consequently implemented on the shake table under BLWN or seismic excitations. Meanwhile, the passive control and the zeroed control are performed using the shake table testing as well. The results in accordance with the BLWN excitations and the historical earthquakes are individually demonstrated. These results will indicate the successful implementation of an active isolation system against the bi-directional seismic excitations.

8.3.1 Excitations

Two types of excitations are used to examine this active isolation system. The first type is the BLWN signals for accelerations on the shake table. As mentioned in Section 7.3, the input commands for the shake table is a function of displacements. The modified BLWN signals are applied to these input commands in order to correctly generate the BLWN accelerations on the shake table. Also, five earthquake records are selected to test this active isolation system in the time-domain performance. Both types of excitations can provide complete verification of the active isolation implementation.

These five earthquake records are normalized to different levels of peak ground accelerations (PGA). Different levels of PGAs can test the nonlinearity of the active isolation system. Thus, the PGAs are ranged in 0.05g, 0.1g, 0.15g, and 0.2g. Figure 8.2 shows all records at 0.2-g PGA as compared to the achieved accelerations when using the active control-FA. Note that the achieved accelerations are slightly different from the exact 0.2g because of the nonlinearity of the shake table. The input commands for these earthquake records to the shake table are generated based on the transfer function iteration method as mentioned in Section 7.3. According to the results in Figure 8.2, the accelerations achieved on the shake table are acceptable for both directions.

To effectively analyze the control performance in the frequency domain, a Kanai-Tajimi filter is fitted based on these five earthquake records. This filter is employed to represent the seismic characteristics, particularly in low frequencies. In the frequency-domain analysis, the transfer functions of this active isolation systems resulting from the BLWN excitations do not include the seismic effect. Thus, the transfer functions multiplied by this filter can effectively represent the frequency-domain behavior. After using the least-squares curve fitting method on all of the earthquake records, the result forms the filter with a 10-rad/sec effective frequency and a 30% damping, as shown in Figure 8.3. Hence, this filter will be used in the post-process analysis for the frequency-domain responses.

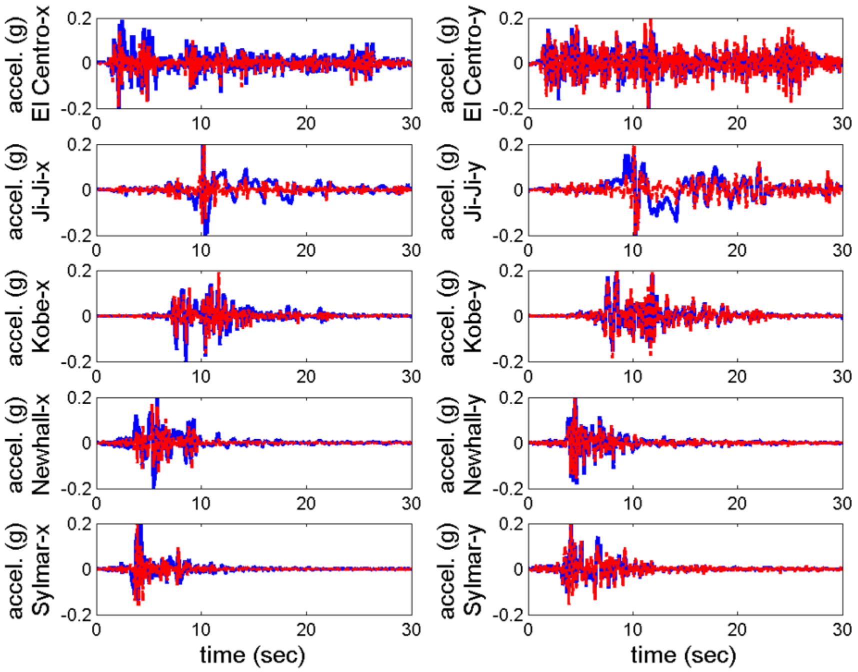

Figure 8.2. Comparison of ground accelerations between the earthquake records (solid blue lines) and the achieved responses (dash red lines) from the shake table.

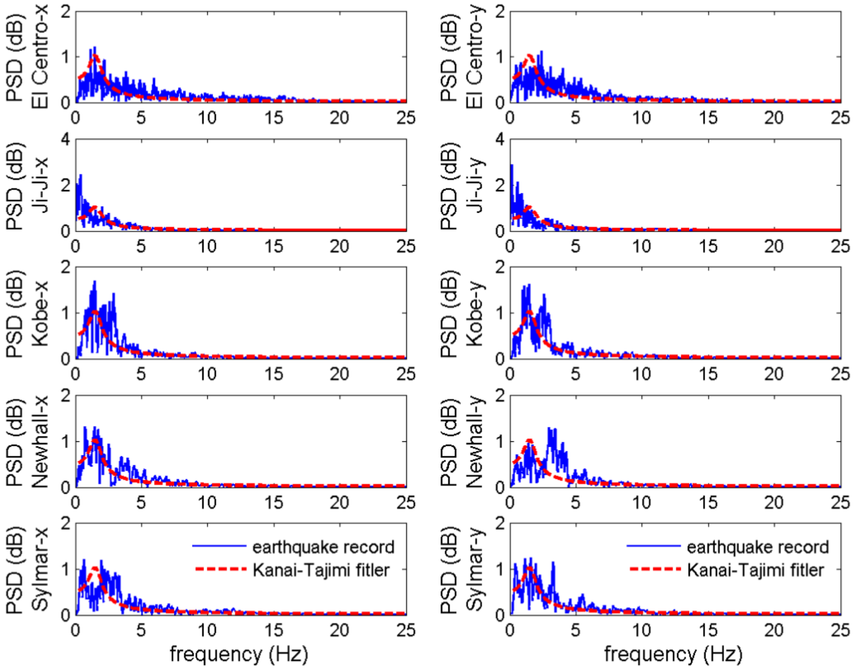

Figure 8.3. Power density functions from the earthquake records and a Kanai-Tajimi filter.

8.3.2 Experimental input loop gain and sensitivity

To check control performance and robustness before control implementation, the input loop gain and sensitivity transfer functions are performed. In a designed active controller, two state-space dynamic feedback controls are used to command the *y*-actuator and the *x*-actuators, respectively. Thus, the input loop gain and sensitivity for the *y*-actuator can only be evaluated with the original transfer functions. The transfer functions of these two indices for the *x*-actuators should be checked with the original ones and be converted to the singular values. The original transfer functions contain the phase information, while the singular values only exhibit the magnitudes. Through the check of these two transfer functions, the active controllers can be implemented on this active isolation system.

Figure 8.4 displays the results of the input loop gain and sensitivity for the *y*-actuator using the active control-FA. The magnitudes of the input loop gain are much larger than 1 (0 dB) within 15 Hz, while the phases of this transfer function are matched with the experimental one up to 25 Hz. This 25-Hz threshold is also very close to the one used in the system identification (i.e., the identified model has excellent agreement with the experimental transfer functions below the threshold). As for the sensitivity transfer function, the magnitudes are flat along 1 (0 dB) above 30 Hz, while the phases also remain around 0 degrees in this frequency range. According to the results, the control-FA for the *y*-actuator passes the criteria of the input loop gain and sensitivity. This controller can be then implemented for this active isolation system along the *y*-direction.

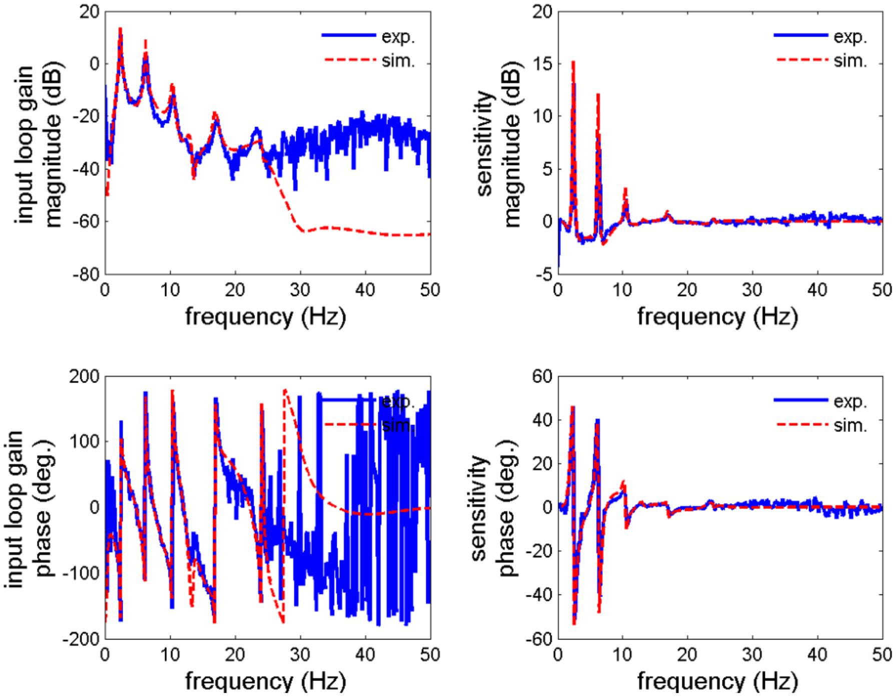

Figure 8.4. Input loop gain and sensitivity transfer functions for the *y*-actuator.

The input loop gain and sensitivity transfer functions for the *x*-actuators are shown in Figure 8.5 using the same active control-FA. Because the controller for these two actuators generates a 2x2 transfer function matrix of the input loop gain (see Eq. (8.1)), Figure 8.5(a) demonstrates the diagonal terms of the transfer function matrix. These diagonal terms should match with the experimental ones on magnitudes and phases. Thus, the results illustrate similar magnitudes and phases up to 20 Hz, of which this frequency is also the threshold for the system identification for the *x*-direction. In addition to the original transfer functions, the singular values of these two types of transfer functions are exhibited in Figure 8.5(b). The larger singular values of both transfer functions are sufficiently below 7 Hz, indicating high performance in this frequency range. The larger singular values in the sensitivity always remain at 1 (0 dB) above 20 Hz, indicating robustness of this controller. The small singular values in the input loop gain are located at different levels because of the sensor noise. Meanwhile, the small singular values in the sensitivity are always close to one, resulting in a validating robustness of this controller. According to a series of analyses, this controller for the *x*-actuators is proved to be implementable on this active isolation system.

The other two active controllers also follow the same procedure to confirm performance and robustness. If the designed controllers fail to pass the criteria of this procedure, the controller should be redesigned. If all designed controllers fail in this procedure, the model for control design should be identified again in order to obtain a more precise model. If both transfer functions pass the necessary checks, they can guarantee a certain level of performance and promise robustness through system uncertainties in particular.

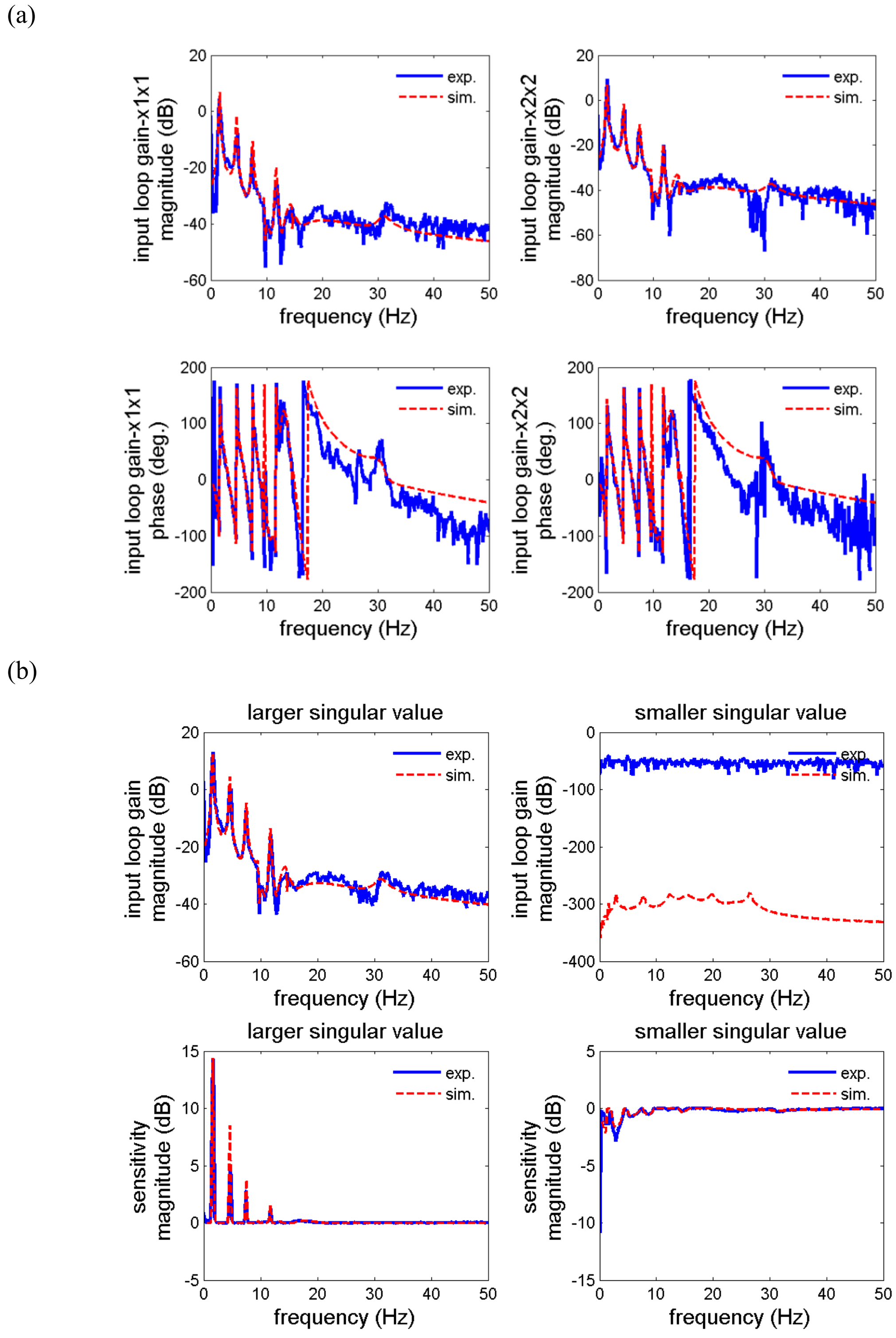

Figure 8.5. Input loop gain and sensitivity transfer functions for the *x*-actuator: (a) diagonal terms and (b) singular values of the original transfer functions.

8.3.3 Passive control

The control implementation for the passive isolation system employs the Krypton system to obtain the base displacements in two horizontal directions. The Krypton system requires a number of LEDs on measuring targets with a high-resolution camera at a fixed location. Because the Krypton system only acquires absolute displacements with respect to the camera, those LEDs are placed at the base plate as well as on the shake table. The base displacements are then calculated by the difference of the responses between these two layers. Moreover, the sampling rate in the Krypton system also depends on the number of LEDs. In this research, the total number of LEDs for this Krypton system is nine which gives a 163-Hz sampling rate when the backlight function is off. The resulting resolution reaches only 0.5% error in maximum displacements when using a 128-Hz sampling rate in the control implementation. Hence, this Krypton system is applicable to shake table testing and is adequate for comparison of the performance of displacements to the active isolation system.

8.3.4 Zeroed control

Since wireless sensors with embedded accelerometers are employed to measure the 1^{st} and 3^{rd} floor accelerations in both directions, phase delays may occur between the data acquisition system of wired sensors and these two wireless sensor units. However, the phase delays in the frequency domain can still be corrected through the method in Nagayama and Spencer (2007). Figure 8.6 demonstrates the results of the acceleration transfer functions at the first floor in the both directions before/after correction, as compared to the neighboring wired accelerometers. A constant slope in the phases exists in the original transfer functions, while this slope has vanished and is compatible with the transfer functions at the neighboring floors after correction. This correction contributes to the further modal analysis. For the results of the active isolation implementation, the same procedure is also applied in order to obtain the correct transfer functions.

Vertical accelerations are found during the zeroed control, although the shake table only excites the horizontal directions. Figure 8.7 exhibits the transfer functions of vertical accelerations at the base in the both directions as compared to the horizontal ones. The significantly vertical responses share the first few natural frequencies of the horizontal responses in the *y*-direction, while the vertical responses are relatively small in the *x*-direction. Thus, the zeroed control is only implemented under 0.05g seismic excitations in order to avoid the potential rocking effect. This effect may damage the bearing itself as well as induce instability in the system. Note that the active isolation implementations induce very small vertical responses. Therefore, the restriction in the control implementations only applies to the zeroed control under seismic excitations.

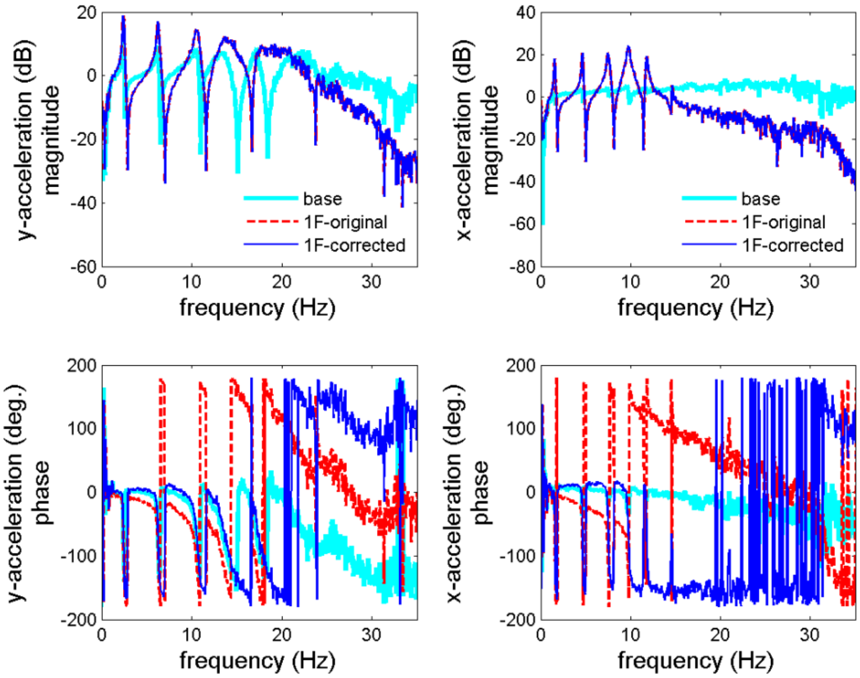

Figure 8.6. Phase delay correction in zeroed control.

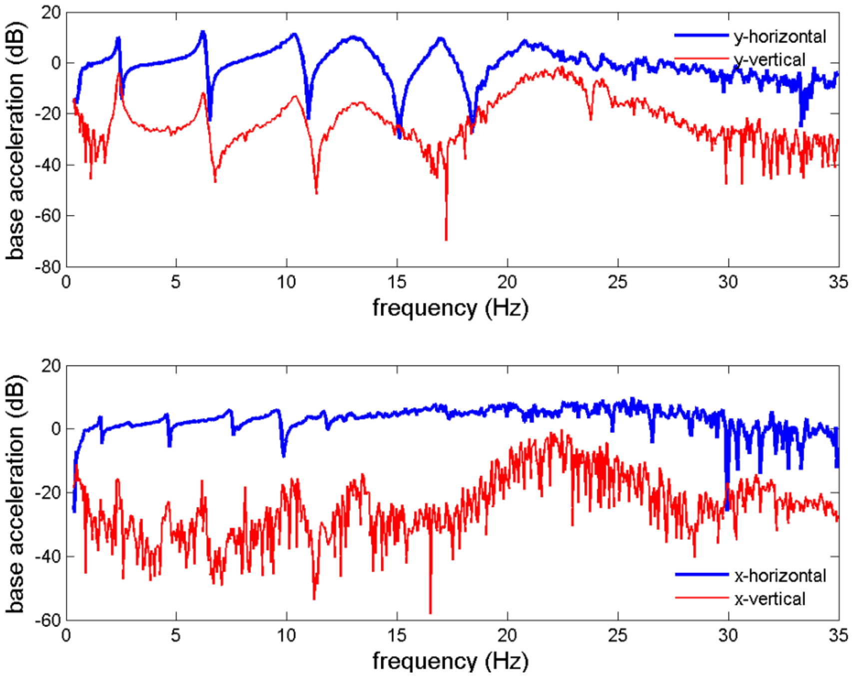

Figure 8.7. Vertical accelerations in both directions.

8.3.5 Active control

This section presents the results of the active isolation implementation using three developed active controllers (see Section 8.1). The two additional control strategies, the passive control and the zeroed control, are employed to evaluate the performance of the active isolation implementation. Both frequency-domain and time-domain analyses are individually provided to compare the control effectiveness. Thus, this section addresses the results sequentially by the domains.

Frequency-domain analysis

The transfer functions of the active isolation implementation are first presented as compared to the passive and zeroed controls. Figure 8.8 illustrates the results using the active control-FA. In this figure, the results only demonstrate responses along the $x1$- and y-directions. The active control-FA performs better in reducing the y-directional accelerations at the top floors in low frequencies, while this control slightly amplifies the *y*-directional base displacements in the same frequency range, as compared to the zeroed control. This active control exhibits significant reductions in the *y*-directional base displacements as well as effectively decreases the *y*-directional accelerations at the lower floors in low frequencies, when compared to the passive isolation. In addition to responses in the *y* direction, the active control-FA shows reductions in *x*2-directional accelerations around the first natural frequency, while the base displacements are increased in low frequencies in this direction, as compared to the zeroed control. Meanwhile, this active control demonstrates average reductions in *x*2-directional base displacements but significant reductions in *x*2-directional accelerations at the lower floors, as compared to the passive isolation. As for comparison of the active control-FA of two directional responses, the results in the *y* direction present better performance in base displacements but medium performance in floor accelerations, as compared to those in the *x* direction. According to this investigation, the active isolation system will give much smaller base displacements with comparable floor accelerations under seismic excitations to the passive isolation, while this active system will generate significant reductions in floor accelerations with similar performance in base displacements to the zeroed control.

Table 8.1 also lists the RMS responses and the magnitude reductions at the fist natural frequency as normalized to the passive or zeroed control. The RMS responses are calculated by the area under the magnitude curves, while the magnitude reductions at the first natural frequency are obtained from the maximum magnitudes at the lowest natural frequency between the active control and the passive or zeroed control. By introducing the seismic characteristics into performance evaluation, a Kanai-Tajimi filter is also considered in the RMS responses. This filter has a 10-rad/sec (1.6 Hz) natural frequency and 30% damping. As a result, Table 8.1 shows that the active control-FA exhibits large reductions in the *y*-directional RMS accelerations at the 2nd-5th floors, as compared to both the passive and zeroed controls. This active control also effectively mitigates the *y*-directional magnitudes of transfer functions over all of the measurements at the first natural frequency, as compared to the passive and zeroed controls. In comparison of the *x*-directional responses, lower performance from the active control-FA can be found in all RMS responses when referring to the passive control, while this active control performs better at reducing RMS floor accelerations with respect to the zeroed control. As for the magnitudes of transfer functions at the first natural frequency in the *x* direction, the active control-FA still shows high capability of reducing floor accelerations, as compared to the passive and zeroed controls. When the comparison is made amongst three active control strategies, the results demonstrate very similar performances to each other. Moreover, a trade-off effect is also demonstrated among these active control strategies in Table 8.1. For example, the active control-BA exhibits better performance in RMS base displacements with respect to the zeroed control, while the active control-F is better at reducing accelerations at the top floors. This effect, in reference to the control design, can also be seen in Figure 6.12, which clearly presents the relationship between the base displacements and the floor accelerations. To sum up, the developed active control strategies not only achieve the control objective of this research but also meet the performance levels determined in Section 6.4.

The transfer functions of the active isolation implementation are also compared to the numerical ones using the identified model. Figure 8.9 displays the comparison of the active control-FA for (a) the *y*-directional responses and (b) the *x*2-directional responses. The experimental transfer functions in the *y*-direction provide slightly larger damping than the numerical ones. The similar results between the experimental and numerical transfer functions in the $x1$-direction are found in the first few modes, although in the second mode the experimental transfer functions do not match well with the numerical one. This unmatched mode is the first torsion mode; however, the active isolation introduces less torsion to the whole building. Thus, the unmatched mode is negligible. According to the results, the accuracy of the identified model is proven again.

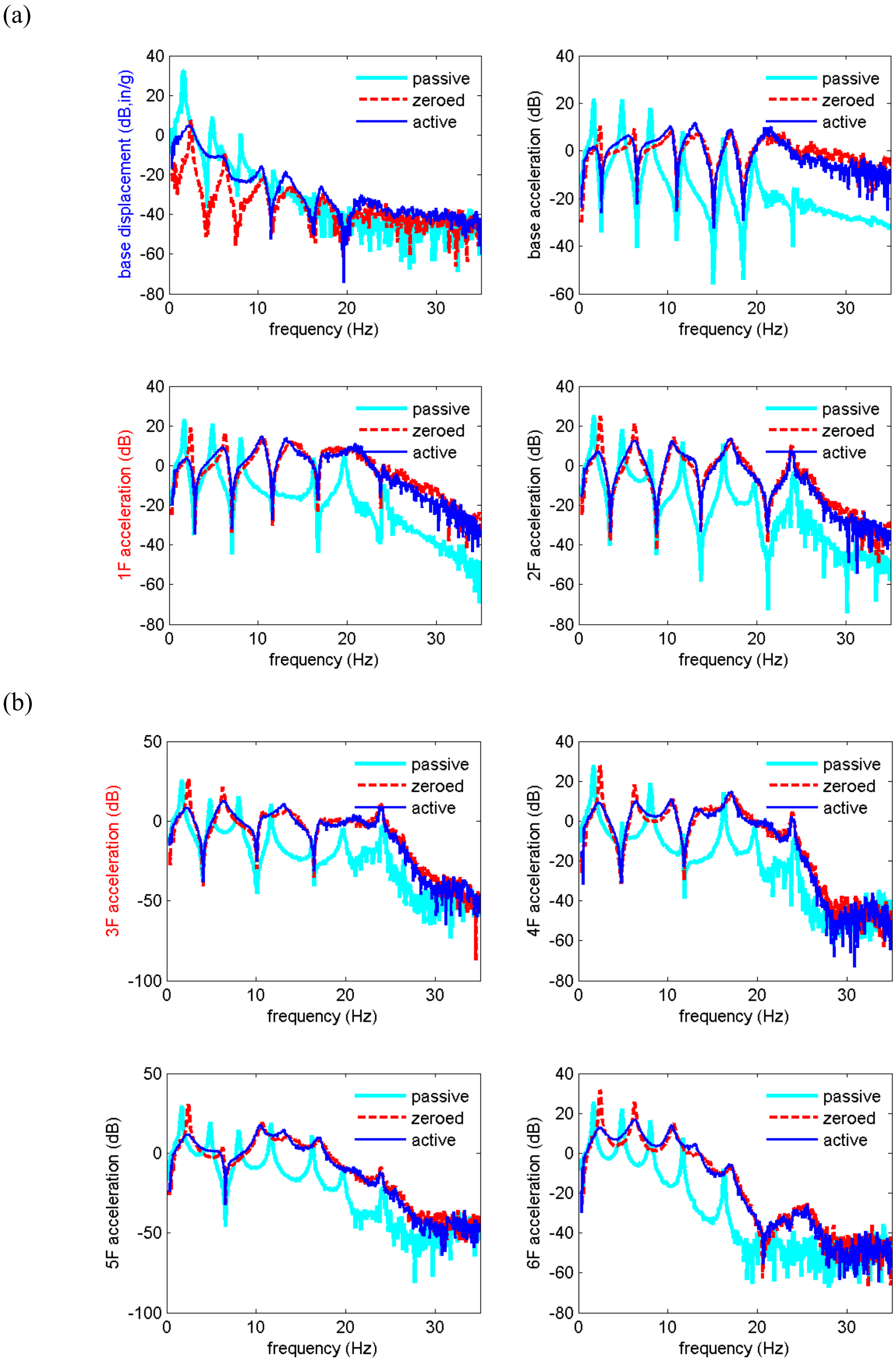

Figure 8.8. Transfer functions of all control strategies from ground acceleration to the structural responses: (a) and (b) are in the *y*-direction and (c) and (d) are in the *x*-direction.

(c)

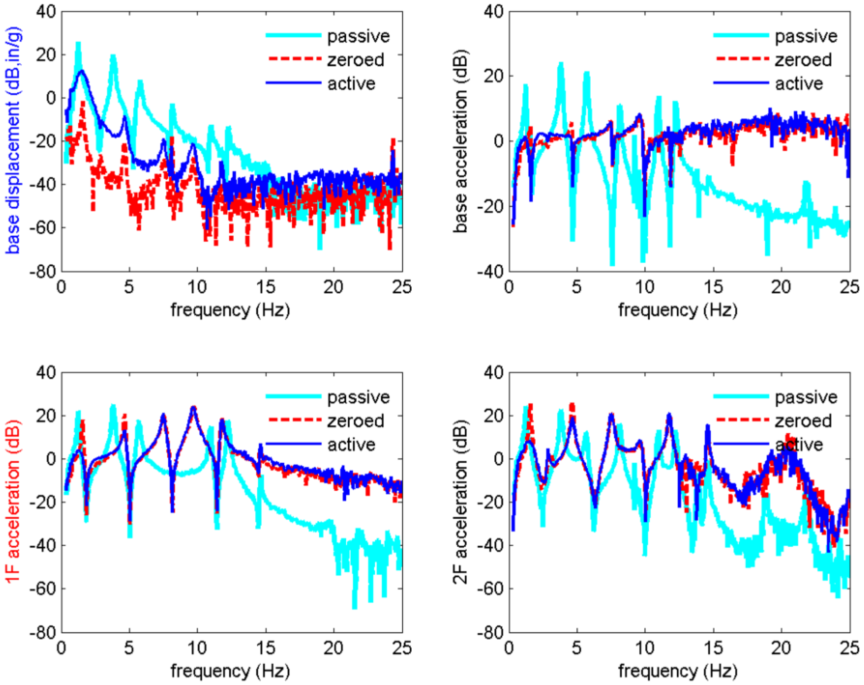

(d)

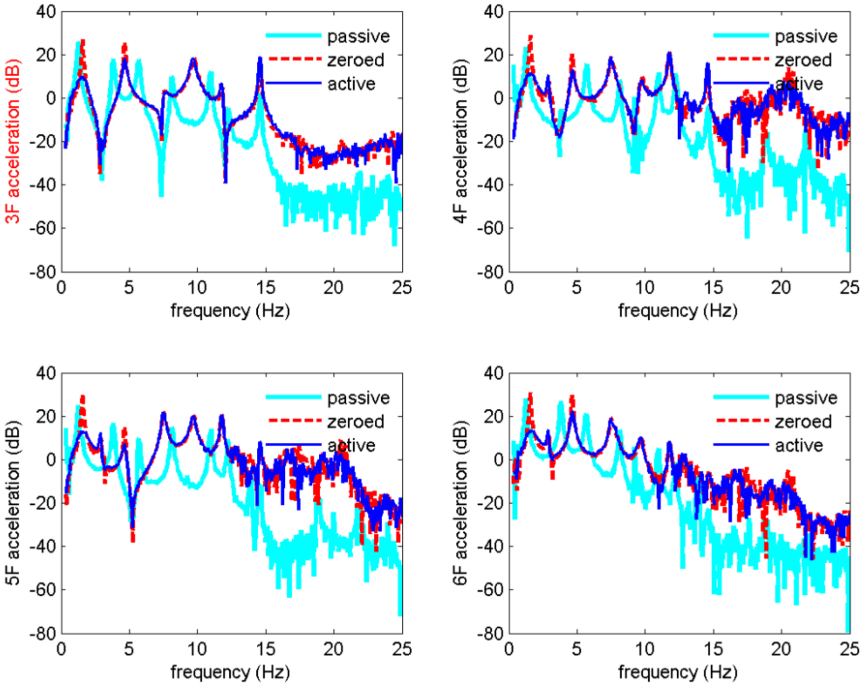

Figure 8.8. cont.

Table 8.1. Responses of the active isolation control strategies as compared to the passive control and zeroed control in frequency domain.

active control	base displacement	base	1F	2F	3F	4F	5F	6F
		acceleration						
Ratios of RMS responses from active isolation to passive isolation in the *y*-direction								
F	0.15	0.72	0.71	0.66	0.64	0.51	0.51	0.89
FA	0.15	0.71	0.71	0.67	0.64	0.51	0.52	0.90
BA	0.13	0.72	0.71	0.66	0.65	0.53	0.55	0.92
Ratios of Max. responses from active isolation to passive isolation in the *y*-direction								
F	0.04	0.10	0.10	0.12	0.13	0.11	0.12	0.22
FA	0.04	0.10	0.10	0.12	0.13	0.11	0.12	0.23
BA	0.04	0.11	0.12	0.14	0.15	0.13	0.14	0.26
Ratios of RMS responses from active isolation to zeroed control in the *y*-direction								
F	3.95	1.06	0.91	0.76	0.72	0.70	0.69	0.70
FA	3.87	1.05	0.90	0.77	0.73	0.71	0.70	0.70
BA	3.56	1.07	0.90	0.76	0.73	0.73	0.74	0.72
Ratios of Max. responses from active isolation to zeroed control in the *y*-direction								
F	0.69	0.37	0.16	0.12	0.12	0.11	0.11	0.11
FA	0.73	0.37	0.17	0.13	0.12	0.12	0.11	0.11
BA	0.76	0.40	0.20	0.15	0.14	0.13	0.13	0.13
Ratios of RMS responses from active isolation to passive isolation in the *x*1-direction								
F	0.85	0.79	0.80	0.66	0.67	0.70	0.72	0.67
FA	0.71	0.79	0.81	0.72	0.74	0.77	0.78	0.74
BA	0.77	0.86	0.81	0.69	0.71	0.74	0.76	0.71
Ratios of Max. responses from active isolation to passive isolation in the *x*1-direction								
F	0.24	0.10	0.12	0.11	0.13	0.12	0.12	0.13
FA	0.21	0.11	0.13	0.12	0.16	0.15	0.16	0.16
BA	0.20	0.11	0.13	0.12	0.13	0.12	0.13	0.14

Table 8.1. cont.

active	base	base	1F	2F	3F	4F	5F	6F
control	displacement	acceleration						
Ratios of RMS responses from active isolation to zeroed control in the x1-direction								
F	15.59	1.00	0.82	0.62	0.57	0.57	0.59	0.57
FA	13.11	0.99	0.83	0.67	0.62	0.63	0.64	0.63
BA	14.07	1.09	0.83	0.65	0.60	0.61	0.62	0.61
Ratios of Max. responses from active isolation to zeroed control in the x1-direction								
F	5.00	0.83	0.19	0.13	0.11	0.11	0.11	0.10
FA	4.43	0.88	0.20	0.14	0.14	0.13	0.13	0.13
BA	4.12	0.86	0.20	0.13	0.12	0.11	0.11	0.11
Ratios of RMS responses from active isolation to passive isolation in the x2-direction								
F	0.84	0.84	0.80	0.74	0.67	0.94	0.94	0.70
FA	0.70	0.84	0.81	0.80	0.74	1.02	1.02	0.76
BA	0.78	0.87	0.81	0.79	0.71	1.01	1.02	0.75
Ratios of Max. responses from active isolation to passive isolation in the x2-direction								
F	0.24	0.14	0.12	0.14	0.13	0.20	0.20	0.14
FA	0.22	0.16	0.13	0.16	0.16	0.25	0.25	0.18
BA	0.21	0.15	0.13	0.15	0.13	0.21	0.22	0.17
Ratios of RMS responses from active isolation to zeroed control in the x2-direction								
F	15.09	1.02	0.82	0.62	0.57	0.59	0.59	0.59
FA	12.59	1.02	0.83	0.67	0.62	0.64	0.64	0.65
BA	13.97	1.05	0.83	0.65	0.60	0.63	0.64	0.63
Ratios of Max. responses from active isolation to zeroed control in the x2-direction								
F	5.54	0.64	0.19	0.12	0.11	0.11	0.11	0.10
FA	5.05	0.70	0.20	0.14	0.14	0.14	0.13	0.13
BA	4.78	0.66	0.20	0.13	0.12	0.12	0.12	0.12

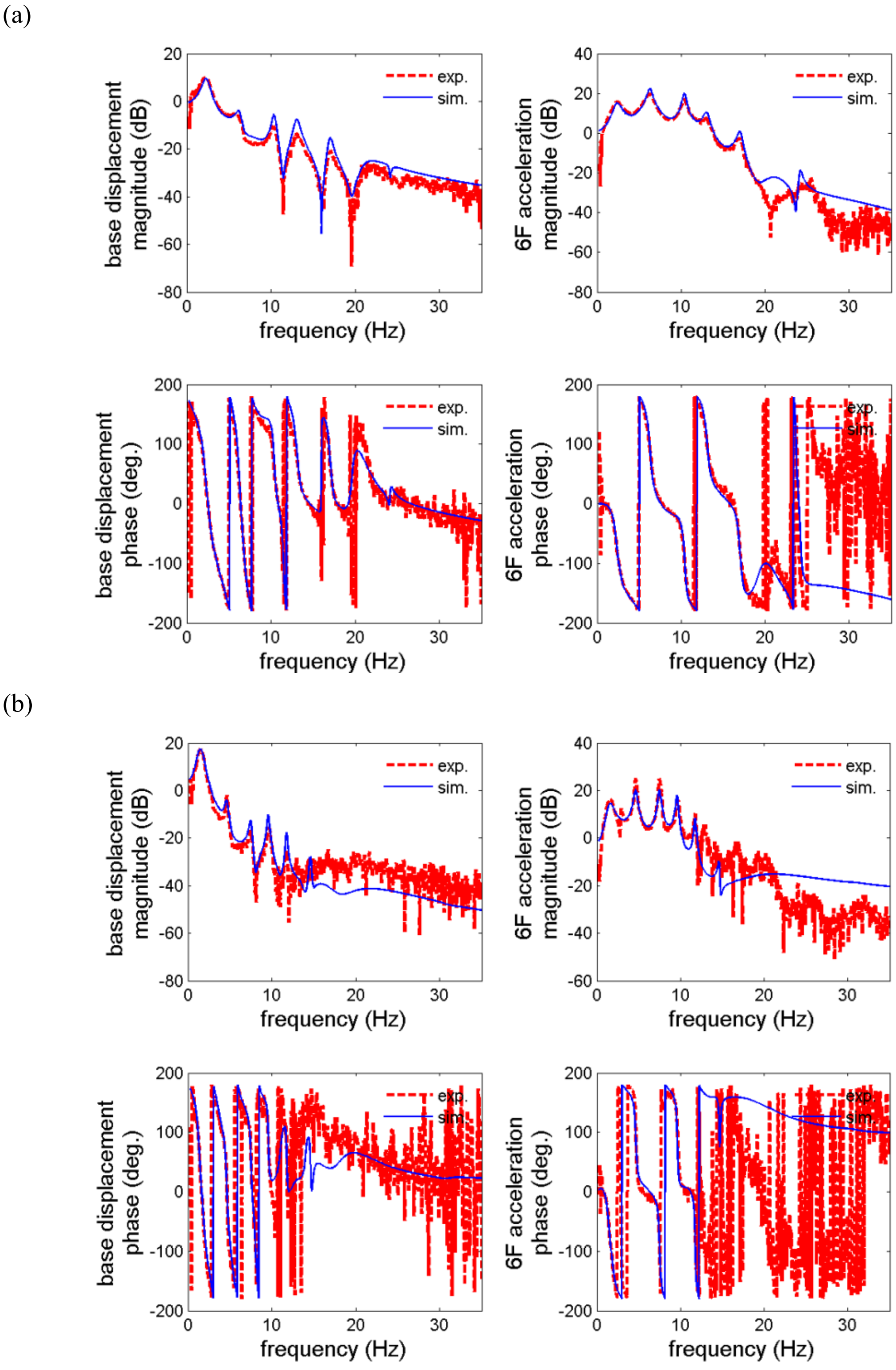

Figure 8.9. Comparison of the transfer functions of active control-FA between the experimental results and the identified model.

The mode shapes among three types of control strategies are also investigated in the frequency-domain analysis. All mode shapes are computed from the identified models, which are derived from the MFDID (see Section 5.3) by experimental transfer functions. The active control-FA is representative for the active control category because the performance among three active control strategies is very similar. Figure 8.10 presents the mode shapes of these three types of control strategies in the first six modes. For all mode shapes in the *y*-direction, the passive isolation induces significant base displacements in the first three modes as well as very small interstory drifts at the first mode. The zeroed control presents clear shear-type interstory drifts over all of the floors and produces very small base displacements as well. The active control-FA generates average base displacements between the passive and zeroed controls in the first three modes, while the interstory drifts at the lower floors using the active isolation are comparable to the passive control. As for the mode shapes in the *x*-direction, very large base displacements are found in the first three modes in the passive control, while this control also produces relatively small interstory drifts among three types of control strategies. The zeroed control causes significant interstory drifts at the lower floors in the first three modes and produces very small base displacements. The active control-FA exhibits similar mode shapes to the passive control in the lower floors in the first mode, while the other mode shapes in this control strategy are close to the zeroed control. Although the control implementation does not measure displacement on the building, these mode shapes still adequately describe the displacement responses in different types of control strategies.

(a) **passive control in the *y*-direction**

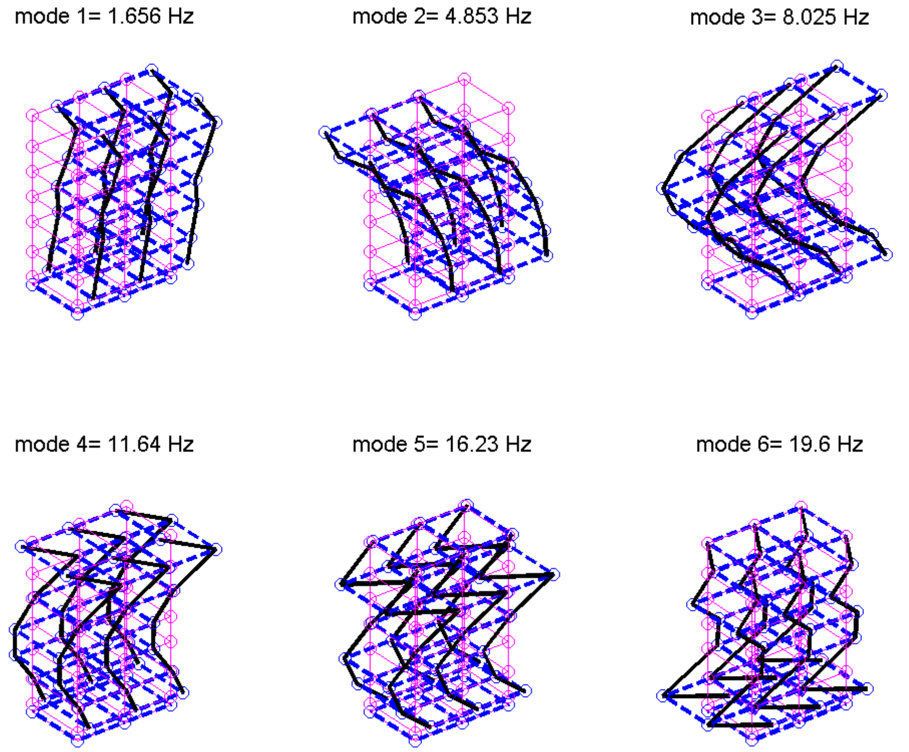

(b) **passive isolation in the *x*-direction**

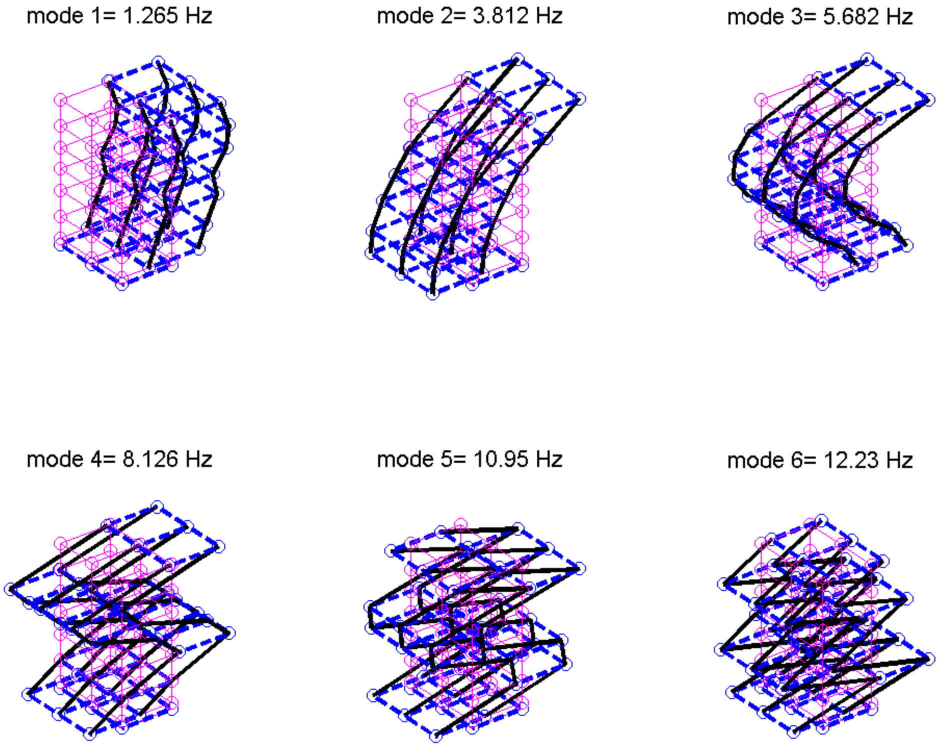

Figure 8.10. Mode shapes of the (a) and (b) passive control, the (c) and (d) zeroed control, and the (e) and (f) active control-FA.

(c) **zeroed control in the *y*-direction**

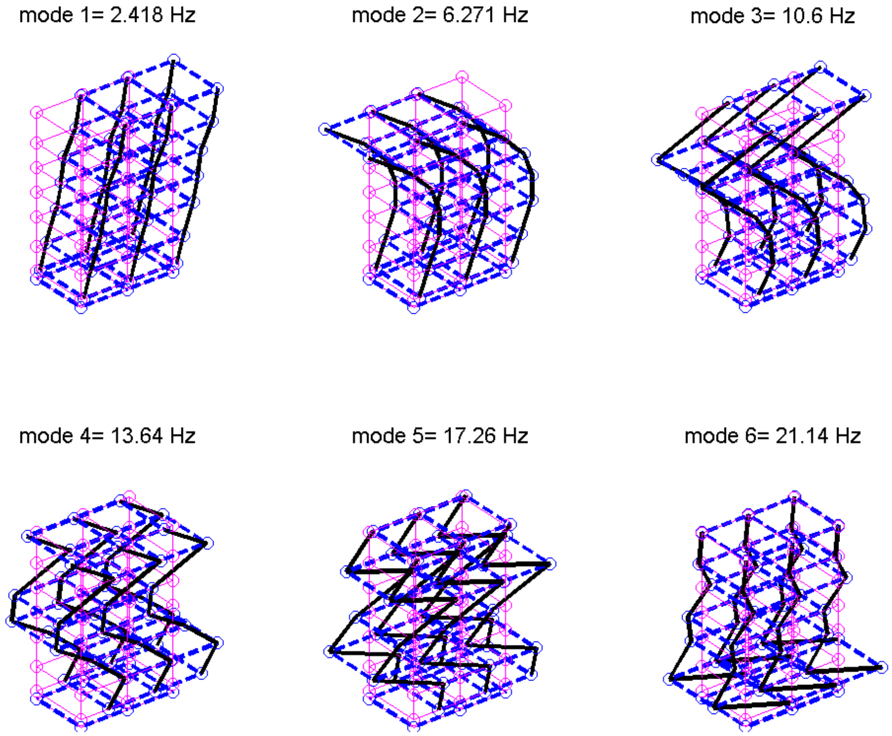

(d) **zeroed control in the *x*-direction**

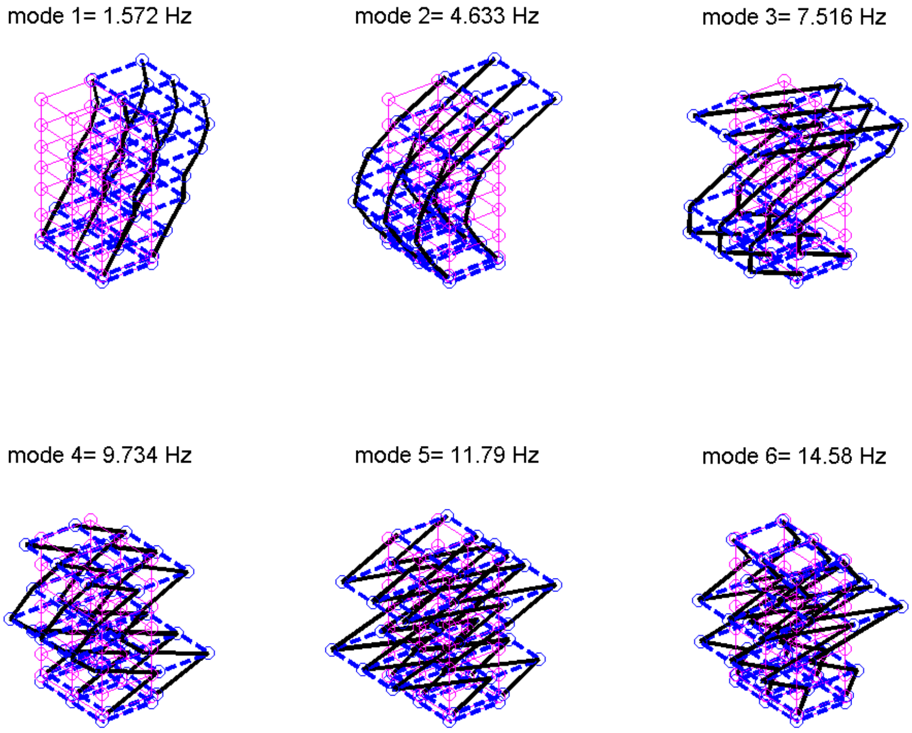

Figure 8.10. cont.

(e) **active control-FA in the *y*-direction**

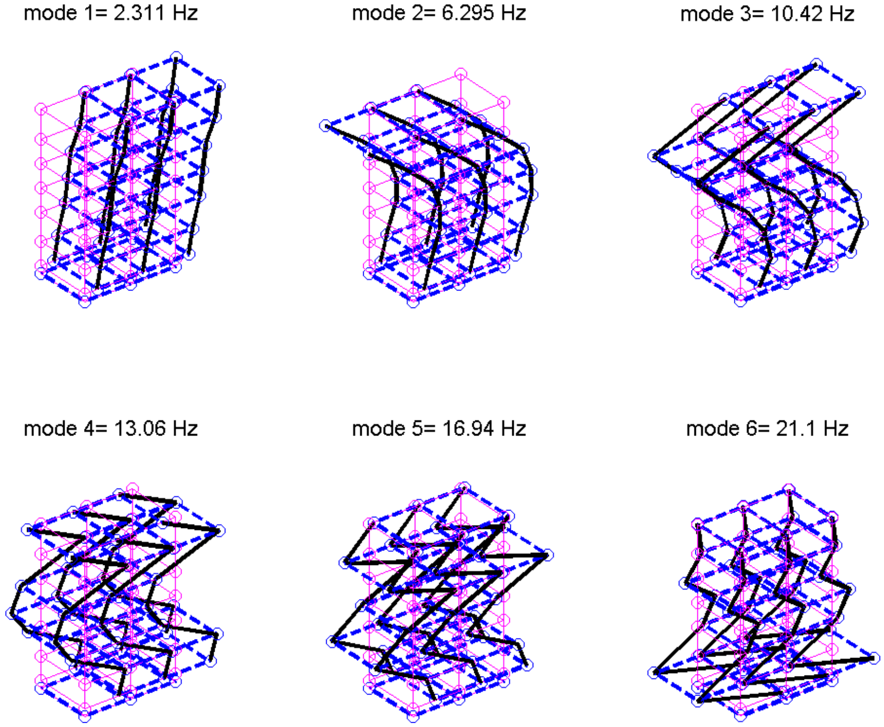
mode 1= 2.311 Hz

mode 2= 6.295 Hz

mode 3= 10.42 Hz

mode 4= 13.06 Hz

mode 5= 16.94 Hz

mode 6= 21.1 Hz

(f) **active control-FA in the *x*-direction**

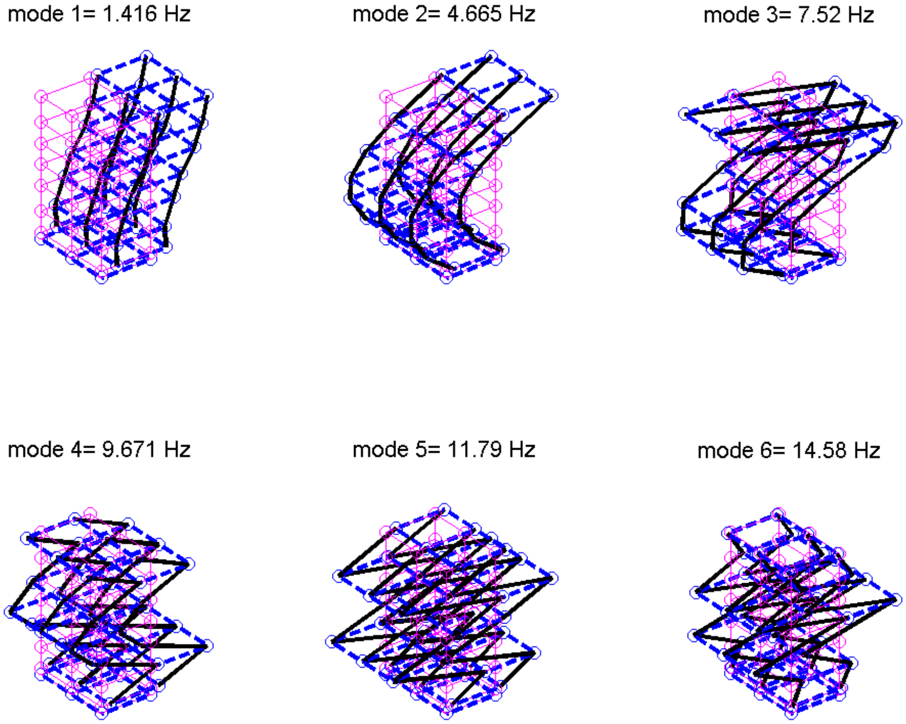
mode 1= 1.416 Hz

mode 2= 4.665 Hz

mode 3= 7.52 Hz

mode 4= 9.671 Hz

mode 5= 11.79 Hz

mode 6= 14.58 Hz

Figure 8.10. cont.

Time-domain analysis

This section presents the time-domain results the focus of which is the comparison between the active isolation and the passive isolation. As a potential rocking effect may be dangerous to the active isolation using the zeroed control under large excitations, the results of the zeroed control will not be included in the time-domain performance evaluation. To effectively compare these control strategies, four different evaluation perspectives are included in this section. The time histories, which are obtained from the horizontally bi-directional excitations of the El Centro and Kobe earthquake records with 0.2-g peak ground accelerations (PGAs), are presented first. To avoid confusion with the responses along the $x1$- and $x2$- directions, this section only provides the averaged responses for the x-direction. The maximum and RMS responses from these two types of excitations are then examined in figures in order to understand their behavior within the different systems. Moreover, these two types of responses are also investigated over a number of PGA levels to observe the linear or nonlinear behaviors within the different systems. These responses from the five earthquake records at 0.2-g PGA are also listed in a table for evaluation on performance. In addition to comparisons amongst the control strategies, the identified model of this active isolation is validated by the time histories using the active control-FA. Through this analysis procedure, the experimental verification of this active isolation will be clearly exhibited as compared to the passive isolation.

The time histories of the active isolation are presented first. Figure 8.11 shows the y-directional responses from the 0.2-g El Centro earthquake record. In this case, the base displacements of the active control-FA are significantly decreased as expected, while the base accelerations are comparable to the passive isolation. Meanwhile, the active control slightly increases the accelerations at higher floors. As for the x-directional responses from the same earthquake record, Figure 8.12 presents almost a 50% reduction in the base displacements of the active control-FA as compared to the passive isolation. This active control exhibits comparable performance in floor accelerations to the passive isolation as well. When considering the *y*-directional responses from the 0.2-g Kobe earthquake record, the base displacements of the active control-FA still performs well, as shown in Figure 8.13. In the same figure, the performance level of the active isolation decreases when the number of floors is increased. If the analysis is conducted in the *x*-direction for the same earthquake record, Figure 8.14 presents a similar performance of the responses at the base, as seen in Figure 8.12. The accelerations at the higher floors are still amplified as compared to the passive isolation. Hence, the active isolation effectively reduces the base displacements and the accelerations at the lower floors but slightly increases the accelerations at the higher floors, as compared to the passive isolation. The results correspondingly reflect the main control objective as well.

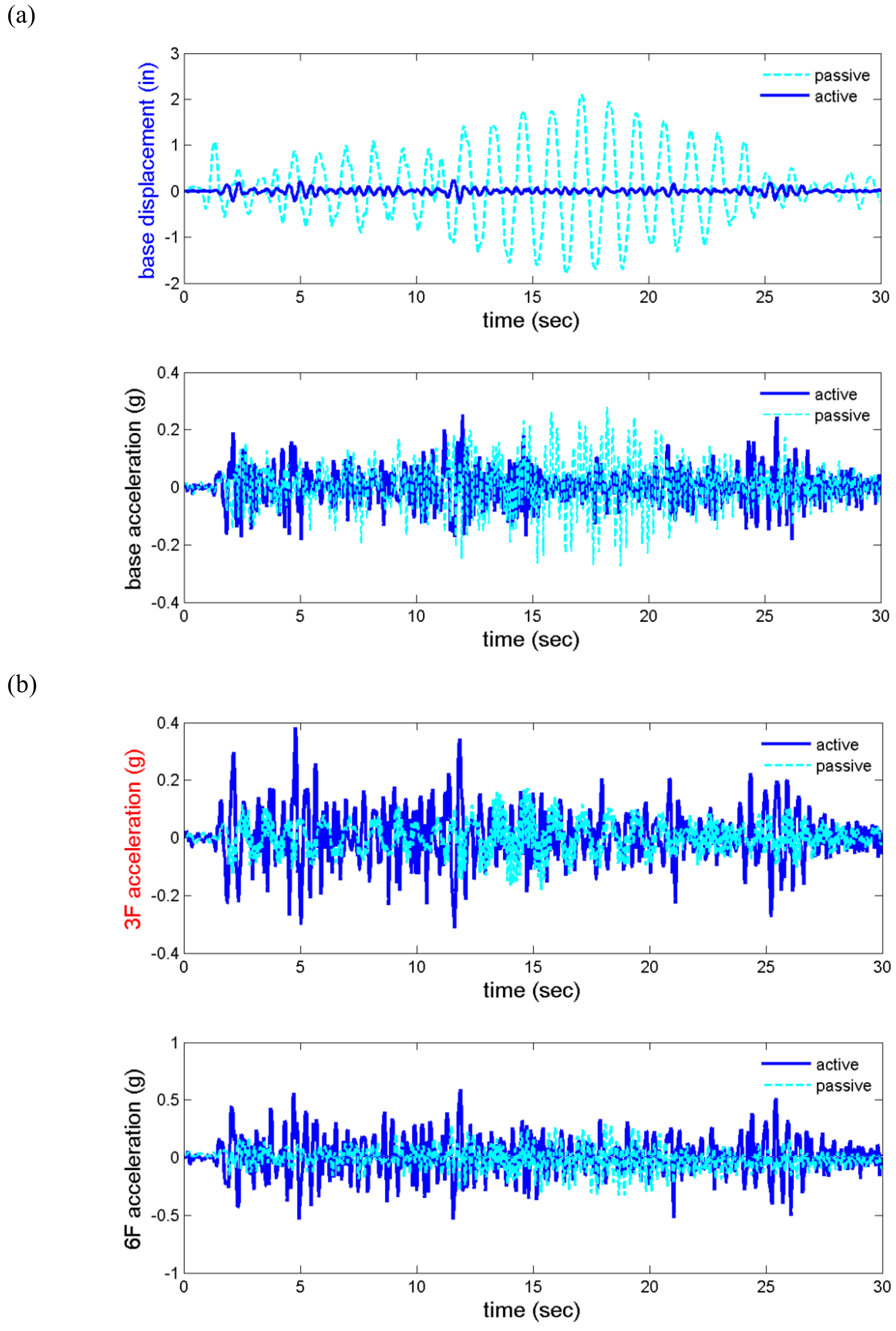

Figure 8.11. Time histories in the *y*-direction under the 0.2-g El Centro earthquake: (a) the base displacement and acceleration and (b) the 3F and 6F accelerations.

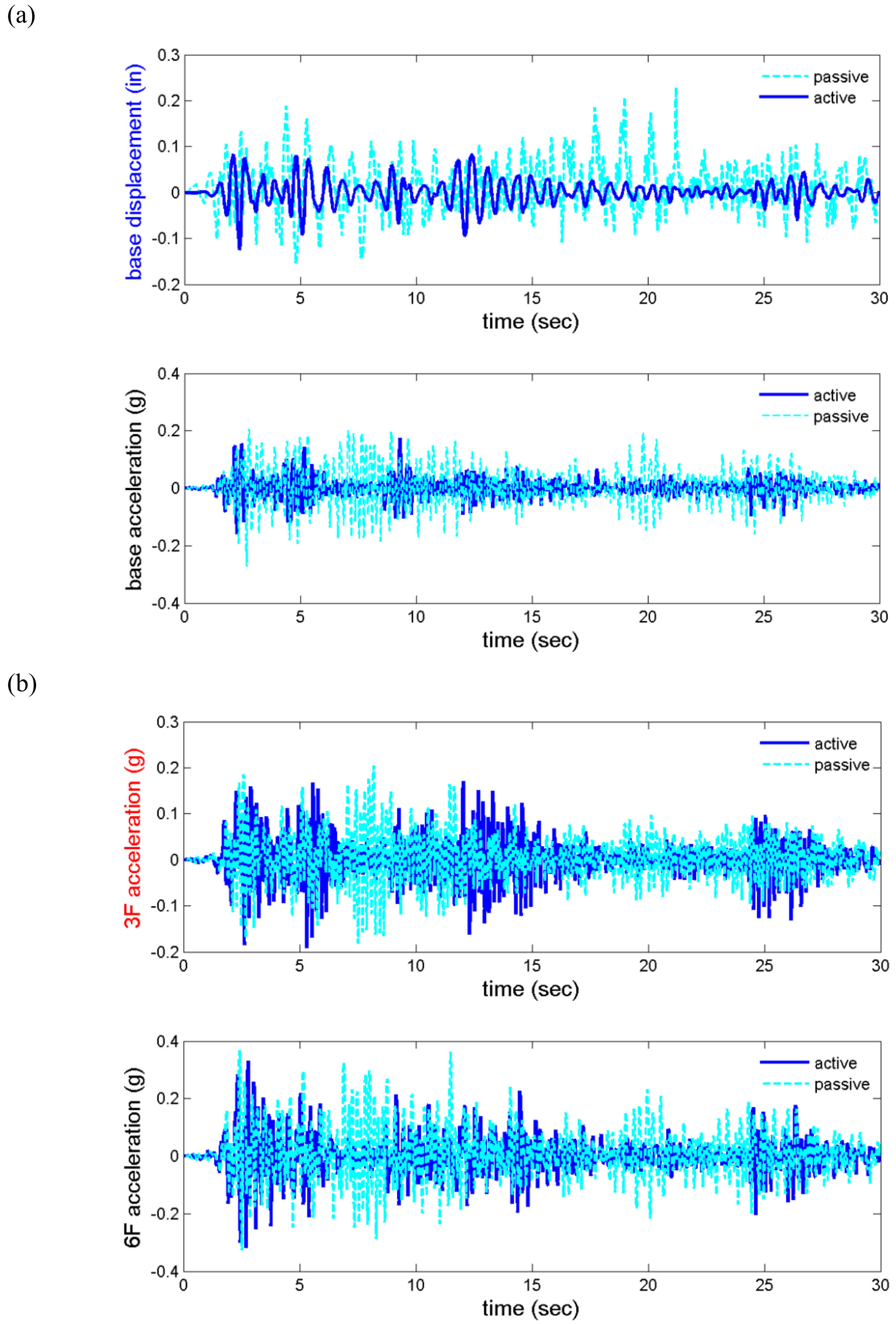

Figure 8.12. Time histories in the *x*-direction under the 0.2-g El Centro earthquake: (a) the base displacement and acceleration and (b) the 3F and 6F accelerations.

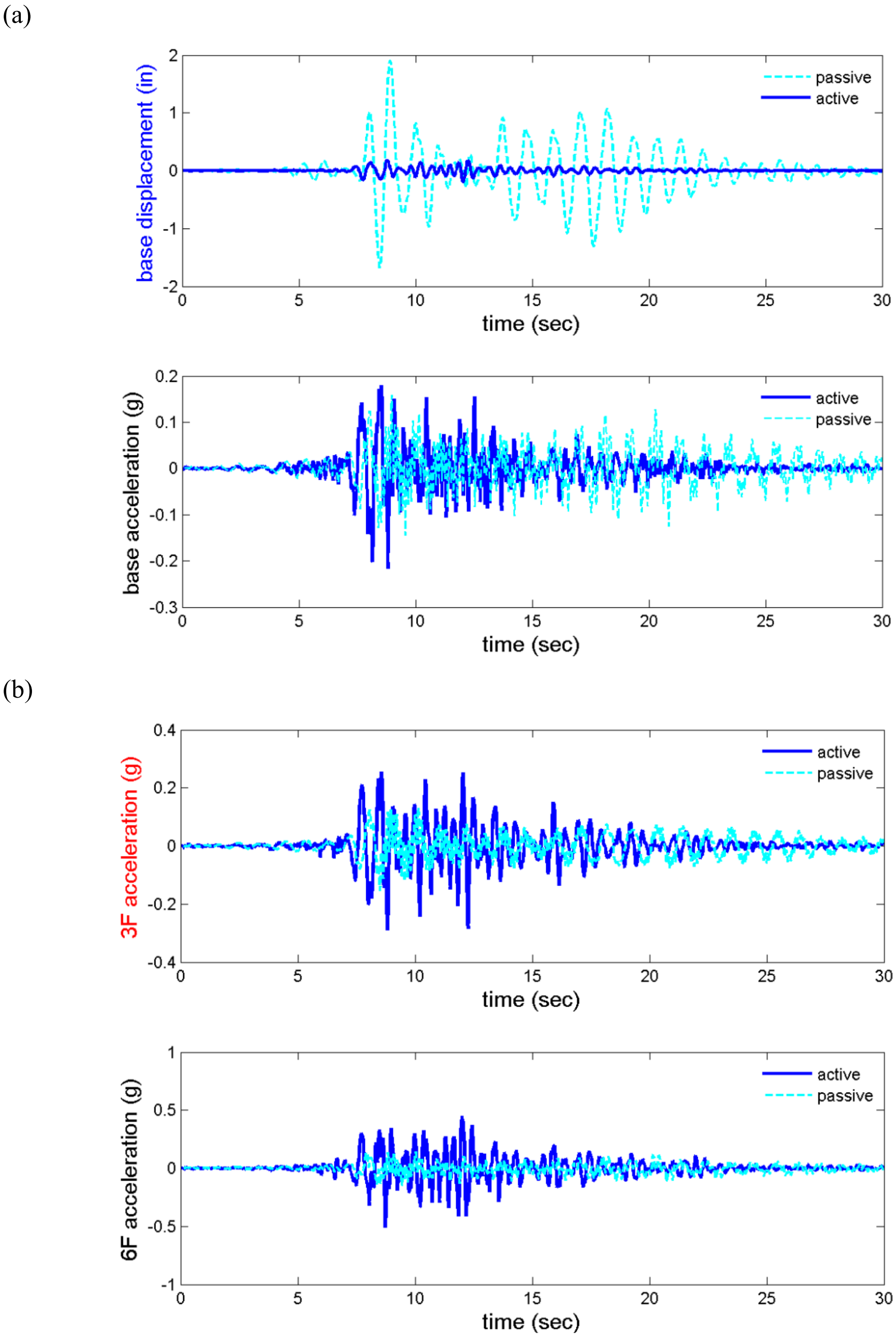

Figure 8.13. Time histories in the *y*-direction under the 0.2-g Kobe earthquake: (a) the base displacement and acceleration and (b) the 3F and 6F accelerations.

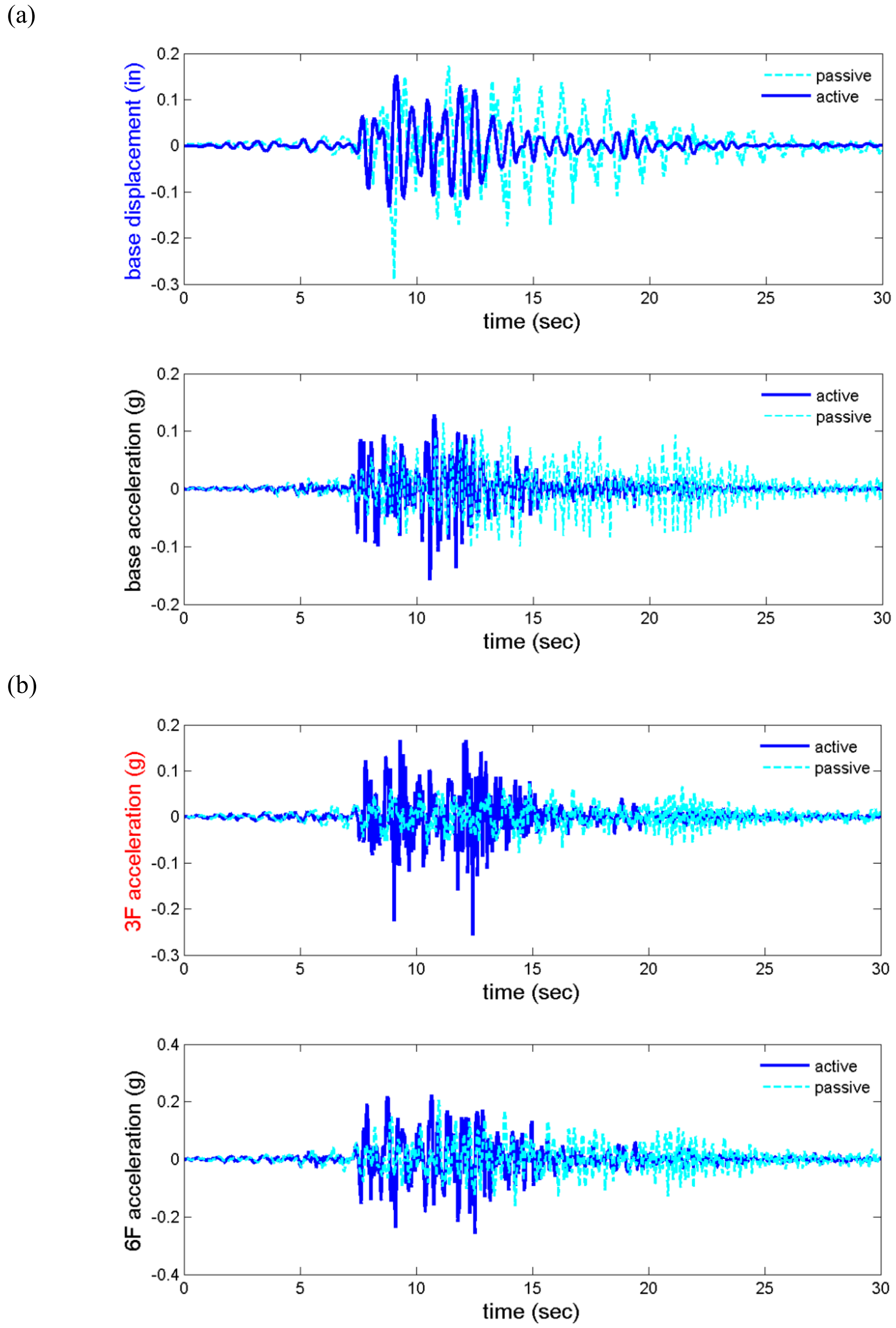

Figure 8.14. Time histories in the *x*-direction under the 0.2-g El Centro station record of the Northridge earthquake: (a) the base displacement and acceleration and (b) the 3F and 6F accelerations.

The maximum and RMS responses are also investigated with the active isolation. Figure 8.15 presents these two types of responses under the 0.2-g El Centro earthquake. In this figure, the maximum floor accelerations of the active isolation perform closely to the passive isolation in the *x*-direction, while the maximum base displacements of the active isolation are reduced to about 75% of those in the passive isolation along the same direction. For the *x*-directional RMS responses, the active isolation has better performance at the 2nd-4th floors and the base, while the base displacements of the active isolation are mitigated to 50% of those in the passive isolation. Although the active isolation amplified the maximum floor accelerations with comparison to the passive isolation in the *y*-direction, the base displacements in the active isolation remain very small in this direction. For the *y*-directional RMS responses, the floor accelerations are slightly amplified using the active isolation, while a high performance level of the base displacements is still found in the active isolation. In addition to the El Centro earthquake, Figure 8.16 demonstrates the responses under the Kobe earthquake. The passive isolation always performs well concerning the maximum floor accelerations, while the active isolation still reduces the base displacements effectively in both directions. These two control strategies also produce similar performance in the RMS floor acceleration along two directions, but the base displacements of the active isolation still remain in the lower RMS values. Again, the results in the maximum and RMS responses show the performance of the active isolation as it corresponds to the control objective and verify the effectiveness of the active isolation, as compared to the passive isolation.

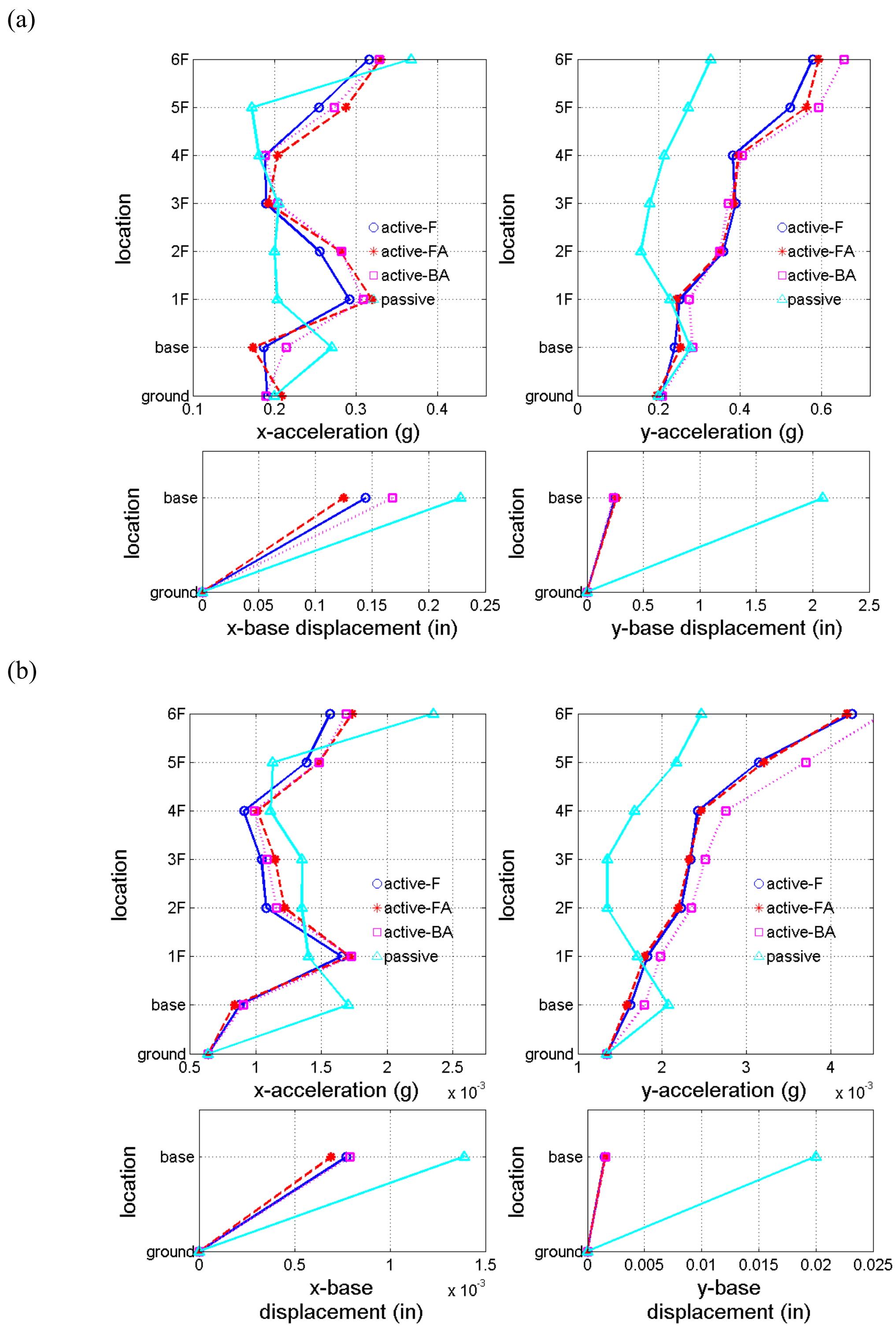

Figure 8.15. Comparison of the responses between the active isolation and passive isolation under the 0.2-g El Centro earthquake: (a) the maximum responses and (b) the RMS responses.

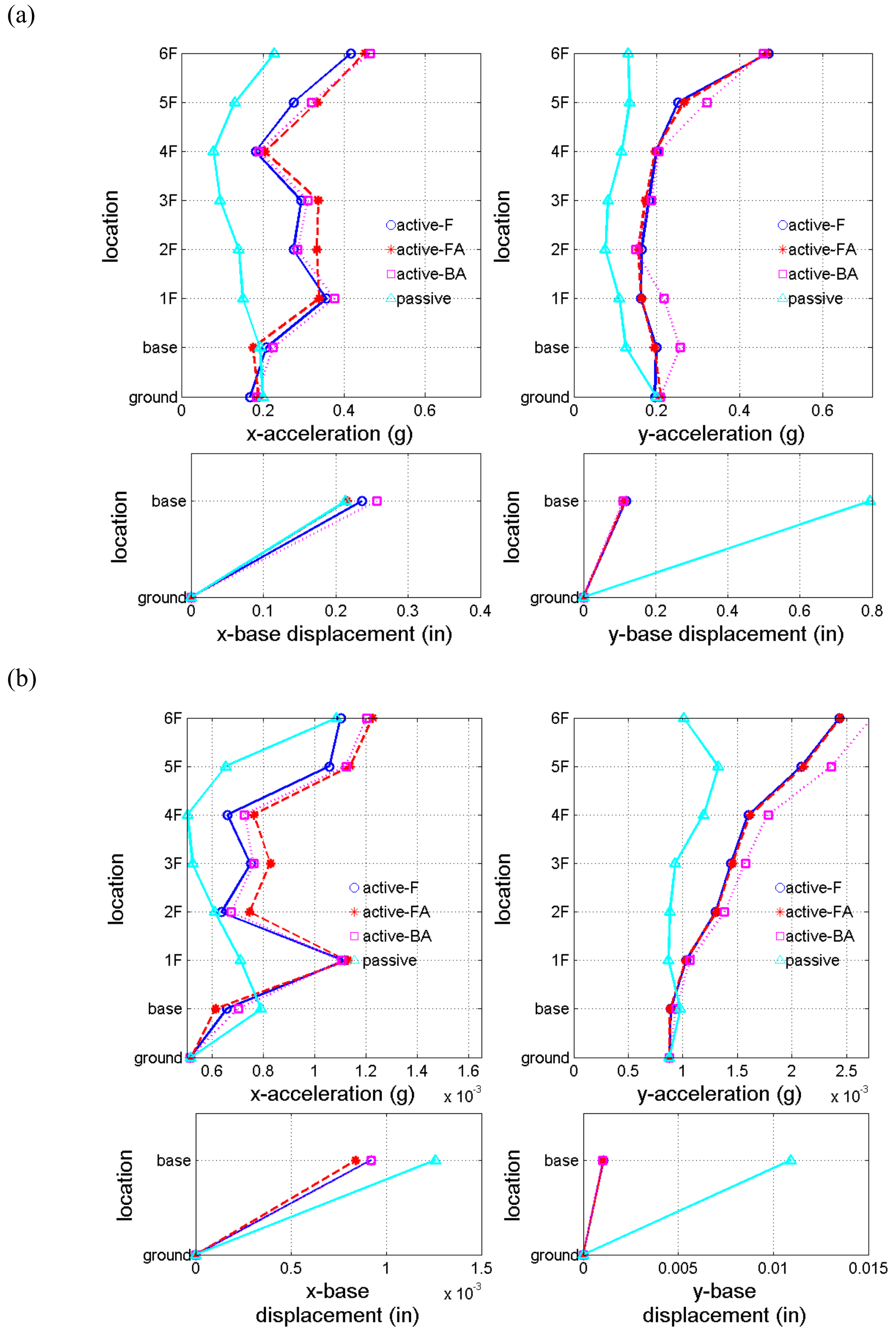

Figure 8.16. Comparison of the responses between the active isolation and passive isolation under the 0.2-g Kobe earthquake: (a) the maximum responses and (b) the RMS responses.

This research also investigates the maximum and RMS responses over different levels of peak ground accelerations for the active isolation. Figure 8.17 illustrates these two types of responses in the active control-FA under the five earthquake records, in which the PGAs are 0.05 g, 0.1 g, and 0.2g. Both types of responses from the displacement-acceleration curves almost behave linearly. These results indicate that the active isolation can stay in a linear manner if the excitation is under 0.2 g. Similarly, Figure 8.18 shows the two types of responses in the passive isolation. Most displacement-acceleration curves are irregular either in the maximum responses or in the RMS responses. Thus, the high nonlinearity of the isolation bearings is implied in the passive isolation when the excitation is increased. Hence, the active isolation in this research is designed with the H_2/LQG control method, which is only adequate for the linear model. Because the results indicate the linearity of the active isolation under all excitations, the performance would still follow the designed objective.

The identified model can also predict the responses of the active isolation in the time domain. For example, Figure 8.19 illustrates the time histories of the active control-FA under the 0.05- and 0.2- g El Centro earthquake. The time histories from the simulation are obtained from the identified model with the designed controller. The results in this figure show a good agreement between the simulation and the experiment, indicating the linearity of the active isolation and the quality of the identified model. The identified model is also validated again through the time-domain analysis.

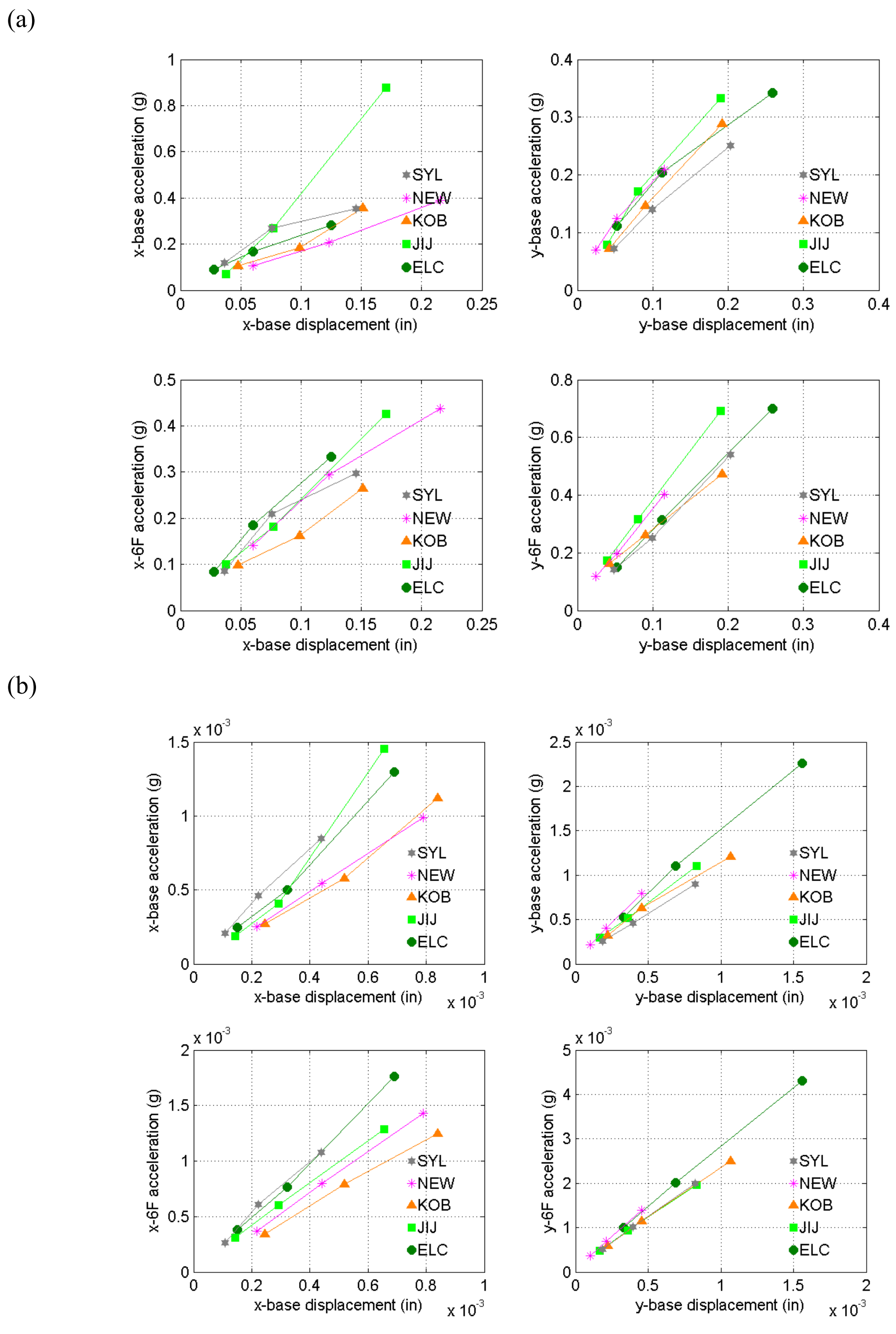

Figure 8.17. Responses of the active control-FA at three PGA levels over five seismic excitations: (a) the maximum responses and (b) the RMS responses.

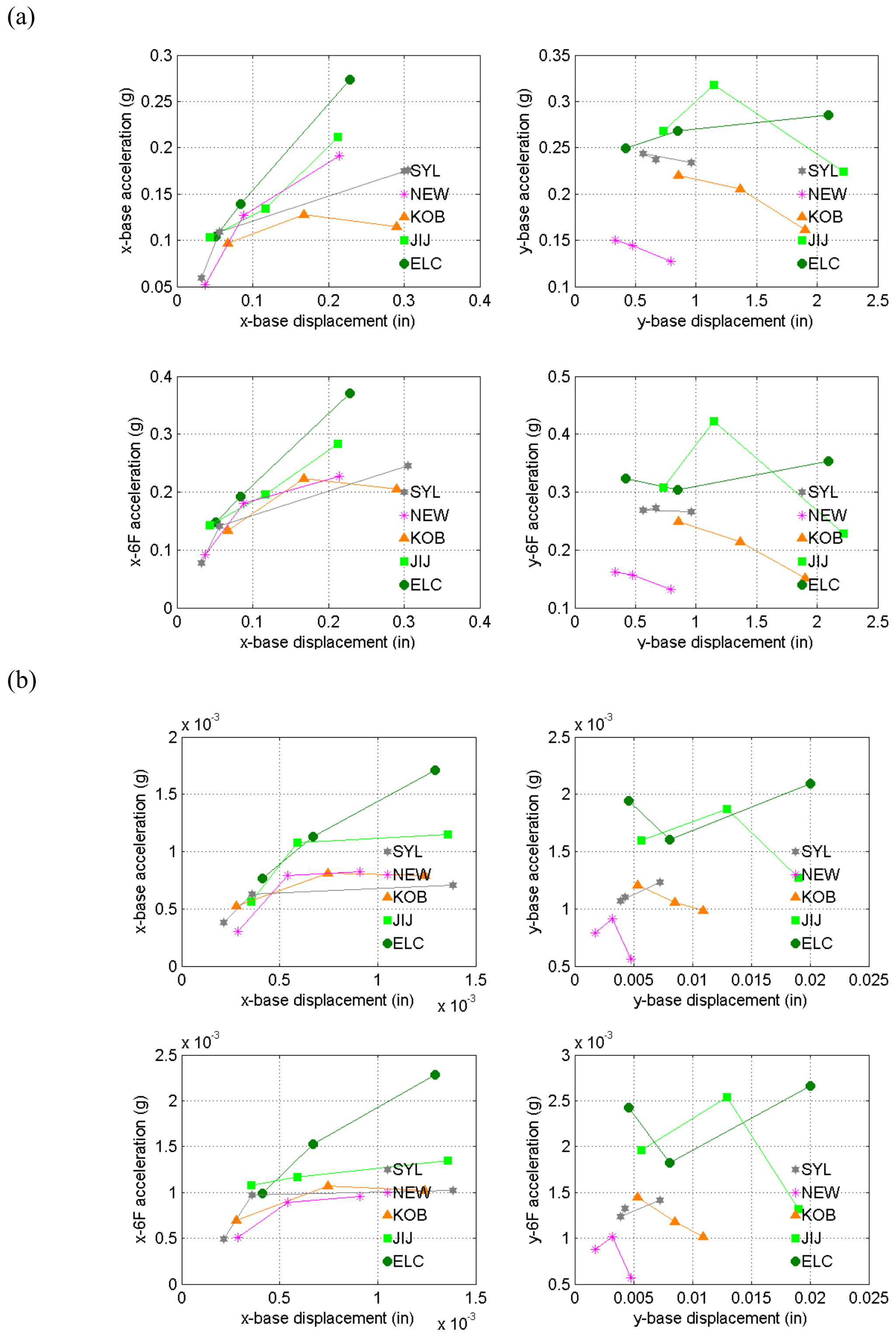

Figure 8.18. Responses of the passive isolation at three PGA levels over five seismic excitations: (a) the maximum responses and (b) the RMS responses.

(a) **0.05g**

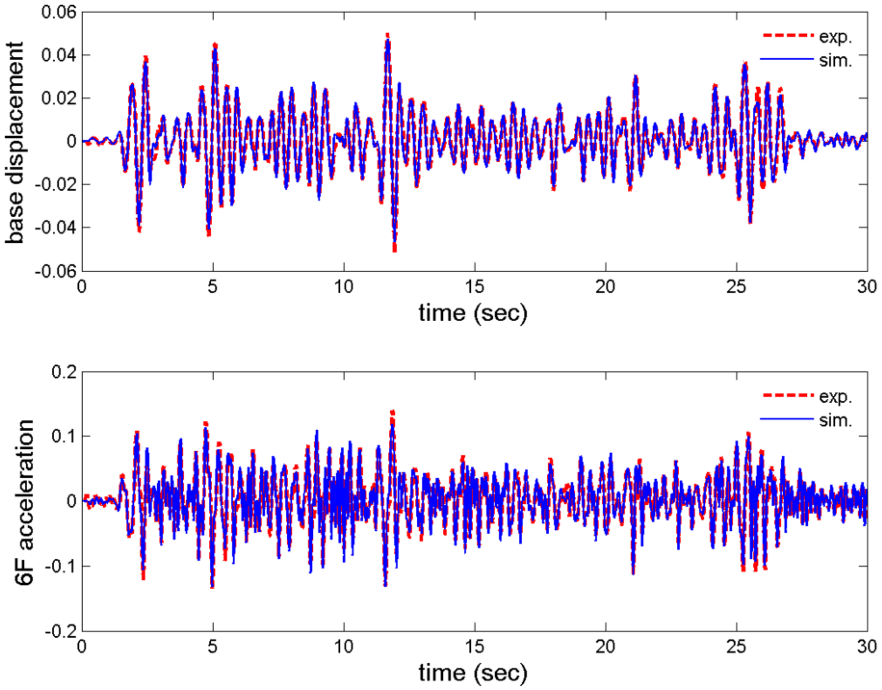

(b) **0.2g**

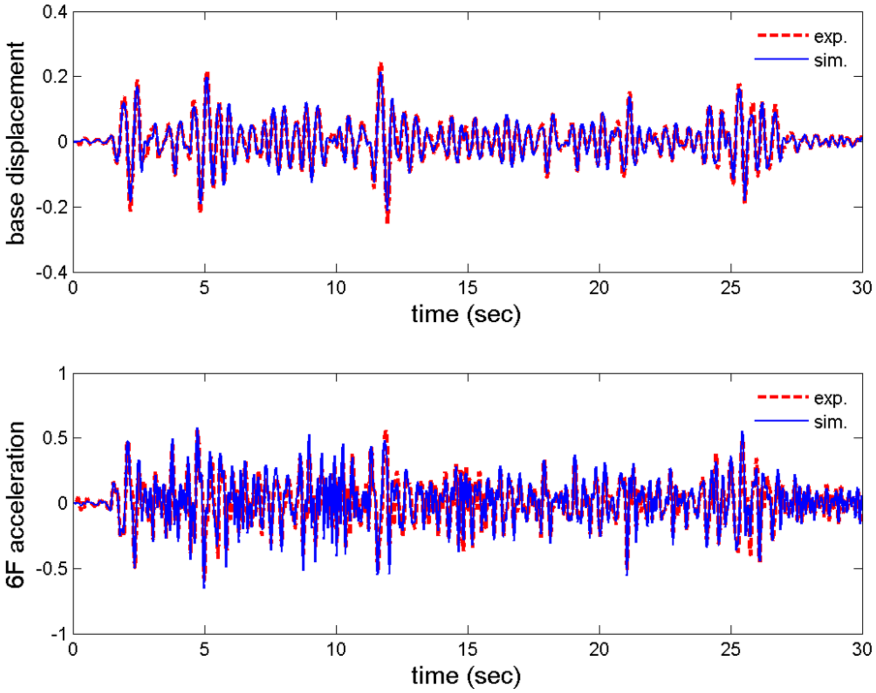

Figure 8.19. Comparison of the base displacements and 6F accelerations between the simulations and experiments under the (a) and (b) El Centro earthquake and the (c) and (d) Kobe earthquake.

(c) **0.05g**

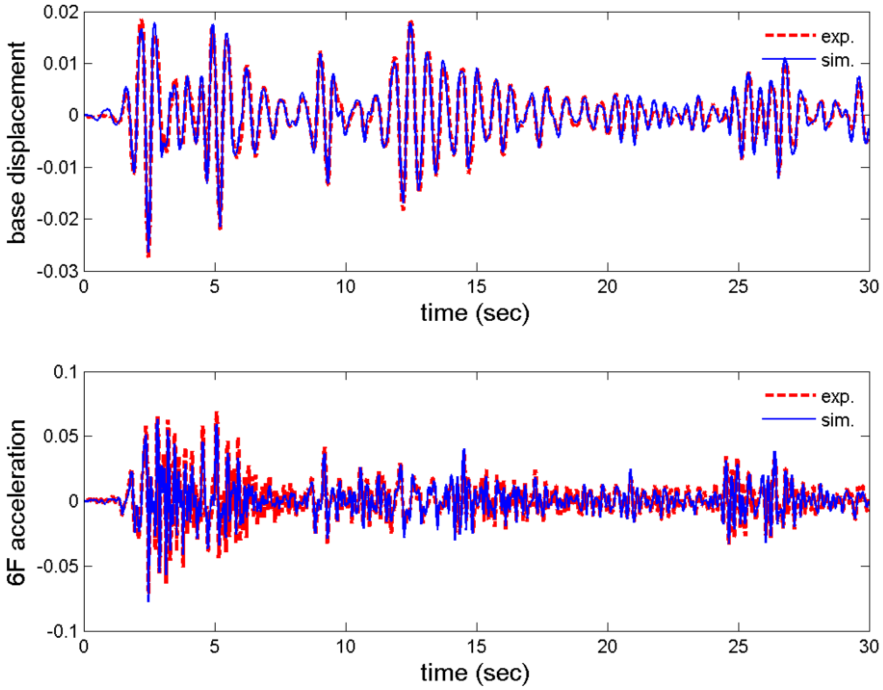

(d) **0.2g**

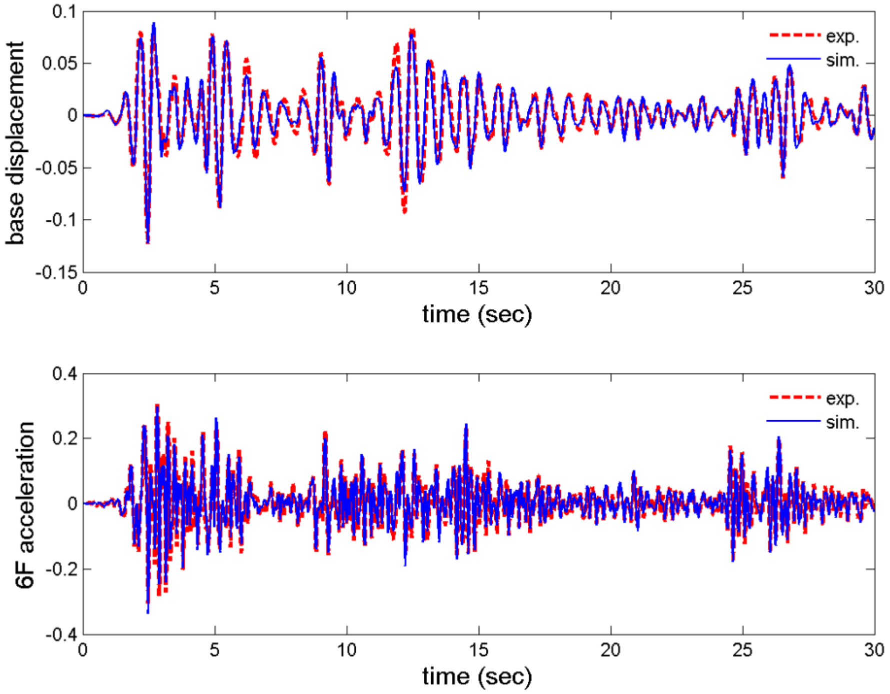

Figure 8.19. cont.

The overall performance of this active isolation is finally presented in Tables 8.2-5. First, Table 8.2 lists the y-directional maximum responses of the passive isolation and three active control strategies under 0.2-g seismic excitations. Typically, the passive isolation produces much larger base displacements than all the active isolation strategies. The performance of the floor accelerations in the active isolation strategies achieves similar levels to the passive isolation at the base and 1st floor. In the higher floors, the performance of the accelerations is decreased using the active isolation as compared to the passive isolation. In addition, the active control-FA gives slightly higher control effectiveness over the other two, while the active control-BA still works well for this active isolation. Therefore, the active isolation in this direction effectively reduces the base displacements but slightly induces the floor accelerations, particularly in the higher floors.

Table 8.3 presents the x-directional maximum responses of the passive isolation and three active control strategies under 0.2-g seismic excitations. The overall performance of floor accelerations of three active isolation strategies in this direction is very similar to that of the y-directional results. However, the reductions in base displacements using the active isolation are less, as compared to the y-direction. Again, the active control-FA performs better among the three active control strategies, while the other two strategies still have a performance that corresponds with the control objective. After evaluating the maximum responses in these two directions, the expected control effectiveness is achieved using these three active isolation control strategies. The active control-FA, which employs floor accelerations for the feedback control, always guarantees the higher performance among the three active isolation strategies.

Table 8.2. Maximum responses of the passive and active isolation control strategies in the *y*-direction under 0.2-g seismic excitations.

active or passive isolation in *y*-direction under 0.2-g excitations									
earthquake	control strategy	base displacement (in)	base	1F	2F	3F	4F	5F	6F
			acceleration (g)						
El Centro	passive	2.09	0.28	0.23	0.16	0.18	0.21	0.27	0.33
	active-F	0.25	0.24	0.25	0.36	0.39	0.38	0.52	0.58
	active-FA	0.26	0.25	0.24	0.35	0.38	0.40	0.56	0.59
	active-BA	0.24	0.28	0.28	0.35	0.37	0.40	0.59	0.66
Ji-Ji	passive	2.22	0.22	0.19	0.14	0.16	0.20	0.20	0.23
	active-F	0.18	0.27	0.25	0.37	0.41	0.38	0.33	0.63
	active-FA	0.19	0.28	0.25	0.36	0.39	0.39	0.33	0.61
	active-BA	0.21	0.34	0.31	0.34	0.38	0.37	0.39	0.70
Kobe	passive	1.90	0.16	0.13	0.15	0.15	0.17	0.19	0.15
	active-F	0.20	0.21	0.27	0.31	0.29	0.33	0.39	0.53
	active-FA	0.19	0.22	0.27	0.30	0.29	0.31	0.39	0.51
	active-BA	0.18	0.21	0.23	0.28	0.31	0.36	0.46	0.56
Northridge at Newhall station	passive	0.79	0.13	0.11	0.08	0.08	0.12	0.13	0.13
	active-F	0.12	0.20	0.16	0.16	0.18	0.20	0.25	0.47
	active-FA	0.11	0.20	0.16	0.16	0.17	0.20	0.27	0.47
	active-BA	0.11	0.26	0.22	0.15	0.19	0.21	0.32	0.46
Northridge at Sylmar station	passive	0.96	0.24	0.17	0.15	0.14	0.19	0.26	0.27
	active-F	0.20	0.21	0.23	0.33	0.37	0.39	0.40	0.52
	active-FA	0.20	0.20	0.22	0.33	0.36	0.39	0.39	0.53
	active-BA	0.21	0.22	0.24	0.33	0.36	0.38	0.46	0.65

Table 8.3. Maximum responses of the passive and active isolation control strategies in the x-direction under 0.2-g seismic excitations.

active or passive isolation in x-direction under 0.2-g excitations									
earthquake	control strategy	base displacement (in)	base	1F	2F	3F	4F	5F	6F
			acceleration (g)						
El Centro	passive	0.23	0.27	0.20	0.20	0.21	0.18	0.17	0.37
	active-F	0.14	0.19	0.29	0.26	0.19	0.19	0.25	0.32
	active-FA	0.12	0.17	0.32	0.28	0.19	0.20	0.29	0.33
	active-BA	0.17	0.21	0.31	0.28	0.20	0.19	0.27	0.33
Ji-Ji	passive	0.21	0.21	0.16	0.13	0.12	0.10	0.14	0.28
	active-F	0.23	0.24	0.26	0.23	0.18	0.18	0.23	0.41
	active-FA	0.17	0.23	0.22	0.24	0.20	0.20	0.25	0.41
	active-BA	0.24	0.25	0.27	0.23	0.22	0.20	0.26	0.43
Kobe	passive	0.29	0.11	0.10	0.09	0.08	0.08	0.11	0.21
	active-F	0.17	0.17	0.29	0.16	0.23	0.15	0.23	0.22
	active-FA	0.15	0.16	0.27	0.18	0.26	0.15	0.27	0.26
	active-BA	0.17	0.17	0.22	0.16	0.22	0.15	0.23	0.21
Northridge at Newhall station	passive	0.21	0.19	0.15	0.14	0.09	0.08	0.13	0.23
	active-F	0.24	0.21	0.36	0.27	0.29	0.18	0.28	0.42
	active-FA	0.22	0.18	0.34	0.33	0.34	0.20	0.33	0.45
	active-BA	0.26	0.22	0.38	0.29	0.31	0.19	0.32	0.46
Northridge at Sylmar station	passive	0.31	0.17	0.16	0.10	0.12	0.09	0.14	0.25
	active-F	0.18	0.25	0.37	0.22	0.15	0.22	0.31	0.32
	active-FA	0.15	0.23	0.39	0.24	0.16	0.23	0.33	0.31
	active-BA	0.21	0.27	0.44	0.26	0.18	0.23	0.35	0.32

In addition to the maximum responses, Tables 8.4 and 8.5 investigate the RMS responses of the passive isolation and three active isolation control strategies under 0.2-g seismic excitations in the *y*- and *x*- directions, respectively. In Table 8.4, the RMS base displacements of the passive isolation are still much higher than those of the active isolation. The active isolation demonstrates the comparable performance in floor accelerations to the passive isolation, particularly at the lower floors. For the *y*-directional RMS responses among three active isolation strategies, the active control-FA shows the best control ability where the reduction in accelerations is always better than the other two. The active control-F can mitigate the RMS base displacements more effectively than the others, while the active control-BA has an average performance amongst the three. According to the results, the active isolation in the *y*-direction can significantly reduce the base displacements with a slight increase in accelerations at the higher floors.

Tale 8.5 lists the RMS responses along the *x*-direction. In contrast with the *y*-directional results, the active isolation performs better than the passive isolation in some excitations, such as with the El Centro and Ji-Ji earthquakes. In these two cases, the floor accelerations of the active isolation are relatively comparable and are less than those of the passive isolation, while the base displacements in the active isolation are always lower than those in the passive isolation. In the other cases, the floor accelerations of the active isolation are still acceptable. Similarly to the performance in the *y*-direction, the active control-FA can still mitigate the structural RMS responses better than the other two. To sum up the RMS responses in both directions, the active isolation always generates a better performance in this type of responses due to the H_2/LQG control algorithm. The active control-FA has still been evaluated as the best choice amongst the three active control strategies.

Table 8.4. RMS responses of the passive and active isolation control strategies in the *y*-direction under 0.2-g seismic excitations.

active or passive isolation in *y*-direction under 0.2-g excitations									
earthquake	control strategy	base displacement (10^{-3} × in)	base	1F	2F	3F	4F	5F	6F
			acceleration (10^{-3} × g)						
El Centro	passive	20.02	2.07	1.71	1.35	1.35	1.68	2.17	2.47
	active-F	1.52	1.63	1.82	2.23	2.33	2.42	3.14	4.26
	active-FA	1.56	1.58	1.79	2.19	2.32	2.46	3.21	4.19
	active-BA	1.59	1.79	1.98	2.34	2.51	2.75	3.70	4.63
Ji-Ji	passive	19.03	1.25	1.14	1.08	1.08	1.36	1.61	1.29
	active-F	0.81	0.88	0.94	1.10	1.17	1.24	1.57	1.89
	active-FA	0.83	0.88	0.95	1.12	1.19	1.27	1.62	1.90
	active-BA	0.77	0.93	0.99	1.16	1.26	1.38	1.80	2.08
Kobe	passive	10.94	0.98	0.87	0.88	0.93	1.19	1.33	1.01
	active-F	1.04	0.89	1.03	1.30	1.44	1.60	2.09	2.44
	active-FA	1.06	0.88	1.03	1.31	1.46	1.62	2.11	2.44
	active-BA	1.02	0.94	1.06	1.38	1.57	1.78	2.36	2.73
Northridge at Newhall station	passive	4.76	0.56	0.51	0.50	0.50	0.64	0.79	0.57
	active-F	0.46	0.60	0.57	0.61	0.65	0.72	1.02	1.38
	active-FA	0.46	0.59	0.55	0.59	0.64	0.72	1.03	1.36
	active-BA	0.44	0.68	0.61	0.62	0.68	0.80	1.18	1.53
Northridge at Sylmar station	passive	7.26	1.22	0.90	0.80	0.82	1.04	1.28	1.38
	active-F	0.79	0.75	0.87	1.08	1.16	1.22	1.57	1.95
	active-FA	0.82	0.76	0.88	1.09	1.17	1.26	1.64	1.96
	active-BA	0.80	0.81	0.90	1.13	1.24	1.35	1.77	2.12

Table 8.5. RMS responses of the passive and active isolation control strategies in the *x*-direction under 0.2-g seismic excitations

active or passive isolation in *x*-direction under 0.2-g excitations									
earthquake	control strategy	base displacement (10^{-3} × in)	base	1F	2F	3F	4F	5F	6F
			acceleration (10^{-3} × g)						
El Centro	passive	1.39	1.71	1.40	1.35	1.35	1.12	1.13	2.35
	active-F	0.77	0.88	1.65	1.08	1.05	0.91	1.38	1.57
	active-FA	0.69	0.84	1.72	1.22	1.15	1.01	1.48	1.74
	active-BA	0.79	0.90	1.73	1.16	1.08	0.99	1.48	1.69
Ji-Ji	passive	1.40	1.15	0.95	0.83	0.70	0.68	0.91	1.53
	active-F	0.74	0.62	0.92	0.67	0.64	0.61	0.85	1.11
	active-FA	0.66	0.59	0.93	0.80	0.74	0.71	0.91	1.26
	active-BA	0.75	0.68	1.03	0.72	0.71	0.69	0.95	1.22
Kobe	passive	1.26	0.79	0.71	0.61	0.52	0.50	0.65	1.09
	active-F	0.92	0.66	1.12	0.64	0.75	0.66	1.06	1.10
	active-FA	0.84	0.61	1.13	0.75	0.83	0.76	1.14	1.23
	active-BA	0.92	0.70	1.11	0.67	0.76	0.72	1.12	1.20
Northridge at Newhall station	passive	0.89	0.82	0.76	0.67	0.51	0.46	0.66	1.11
	active-F	0.85	0.60	1.29	0.77	0.84	0.72	1.09	1.20
	active-FA	0.79	0.57	1.30	0.95	0.92	0.88	1.20	1.41
	active-BA	0.85	0.63	1.34	0.86	0.89	0.81	1.19	1.33
Northridge at Sylmar station	passive	1.47	0.70	0.73	0.41	0.56	0.48	0.57	1.12
	active-F	0.52	0.60	1.12	0.62	0.57	0.63	0.94	0.97
	active-FA	0.44	0.56	1.12	0.73	0.57	0.74	1.01	1.07
	active-BA	0.58	0.65	1.23	0.80	0.59	0.80	1.12	1.15

8.4 Summary

This chapter provided all the experimental evidences toward the successful control implementation and verification of active isolation under bi-directional excitations using shake table tests. Five control strategies, which include the passive isolation, the zeroed control, and three active control strategies using different measurements for the feedback control, were investigated. To fully examine the active isolation system as well as understand the behavior, the BLWN signals and five earthquake records were employed to excite the passive and active isolation systems. As a result of the control implementation, the active isolation effectively mitigated the base displacements as well as the floor accelerations along two directions in the frequency-domain analysis, as compared to the passive isolation. Moreover, the active isolation also lowered the floor accelerations successfully, as compared to the zeroed control. The result was also compatible with the control objective which has been addressed in Section 6.4. In addition to the frequency-domain analysis, the performance of the active isolation was also evaluated through seismic excitations on the shake table. The active isolation among the three active control strategies significantly mitigated the base displacements, while the floor accelerations were slightly increased as compared to the passive isolation. In conclusion, the developed active isolation employed the H_2/LQG control method to implement the feedback control in accordance with the structural responses. The active isolation employing the acceleration feedback control not only effectively decreased the catastrophic base displacements of the passive isolation but also promised floor accelerations within the acceptable range. The active isolation, with few measurements for the feedback control, i.e., the active control-BA, still exhibited similar performance to the active isolation using the acceleration feedback. This successful control implementation has also validated the control effectiveness of the active isolation against bi-directional seismic excitations.

CHAPTER 9 CONCULSIONS AND RECOMMENDATIONS

9.1 Conclusions

In this dissertation, active isolation has been implemented and experimentally verified for seismically excited buildings under multi-directional earthquake excitations. Active isolation consists of a base isolation system combined with controllable actuators. The efficiency offered by the base isolation system in reducing interstory drifts and floor accelerations has been combined with the adaptive nature of the active system to provide improved performance against a wide range of earthquakes. Thus, the protection of structures employing active isolation increases a building's survival chances without introducing large base displacements that can occur with passive isolation systems. Previous experimental studies of active isolation only investigated in-plane structural motions under the unidirectional seismic excitations; this research verified active isolation for both in-plane and out-of-plane motions under the bi-directional excitations. By employing the state-of-the-art system identification and control design, the developed control strategies in the active isolation system have demonstrated significant reductions in the base displacements and acceptable performance of the floor accelerations as compared the conventional seismic isolation. The successful implementation of the active isolation demonstrated it to be a good option for seismic protection of building structures.

First, two model buildings with different heights were designed to match the dynamic and control characteristics of a representative full-scale structures. The six-story model building was designed to be dynamically similar to a seismically deficient structure in the San Francisco Bay area, while the two-story model building was established for the preliminary study on the active isolation implementation. The isolation bearings used in this research had strongly vertical stiffness and small levels of friction, which allowed the building to move stably and smoothly in the horizontal direction. The active control devices, i.e., the hydraulic actuators, were custom manufactured to have capabilities proportional to the building weight. To implement the feedback control for the active isolation system, a number of digital controllers were also carefully synthesized. Moreover, several types of sensors were installed on the building for evaluating the performance and implementing the active isolation systems. This experimental setup was employed to perform all active isolation experiments.

To understand the dynamics of the active isolation systems, a simplified model was derived based on a lumped-mass system. An isolated building model was developed for the bi-directional horizontal vibration plus torsion. Control-structure interaction was incorporated, and higher-order actuator models were developed to correctly represent the behavior of the hydraulic actuators in this research. For active isolation of the two-story building in the *y*-direction, a 2nd-order model of the actuator works well, whereas for the six-story building, a 3rd-order model for the three actuators was required to correctly represent the system behavior of both actuators. The actuator models were then incorporated into the simplified model to fully portray the active isolation systems. The model was then used to determine the number of poles and zeros in the associated polynomial transfer functions; this information was then used in a more accurate frequency-domain system identification procedure.

The system model for the control design in this research was obtained from a two-step frequency-domain system identification procedure. First, the system models were identified using either the MFDID tool or the developed discrete-time, frequency-domain approach. This approach gave a single-input and multi-output (SIMO) system model by forming the polynomial transfer functions. However, the active isolation system is physically a single multi-input and multi-output (MIMO) system. Thus, a system combination approach was proposed to integrate all SIMO systems into a minimum realization of the MIMO system. This system identification procedure provided a high-quality model, which matched well with the experimental transfer functions.

The control design in this research employed the H_2/LQG control method to implement the active isolation. Typically, the conventional H_2/LQG control method generates a controller assuming a white noise excitation to the system. To further consider the seismic effects and the structural characteristics, this research incorporated input and/or output shaping filters. Without employing these additional shaping filters in the control design, the desired performance of the active isolation system was not achievable.

This research also developed a control design procedure for the active isolation. First, all shaping filters used in the control design are characterized in advance. A number of controllers are then developed from the advanced H_2/LQG control method by frequency-domain shaping of the control commands. Comparing the trade-offs in performance between the base displacements and the floor accelerations, a suitable controller for this problem was subsequently picked. Before implementing the designed controller in the active isolation, the analytical loop-gain transfer function, which is defined by breaking the feedback loop at the input, is determined. This transfer function was used to avoid the potential instability to the system (e.g., high magnitude in regions of substantial model uncertainty). Moreover, this loop gain transfer function is examined experimentally and compared with the analytical one to ensure the developed models appropriately represent the physical system. Using this complete control design procedure, a high-performance and robust controller can be developed.

The active isolation of the two-story building was tested along the *y*-direction first. Several active control strategies were applied based on different feedback measurements, different control objectives, and with/without an input shaping filter in control design. The performance of this active isolation system was compared with two control strategies: (i) the passive isolation which has no actuators attached to the base of the building, and (ii) the zeroed control which always commands zeros for the actuators. The proposed active isolation system was able to concurrently reduce the base displacements and floor accelerations, as compared to both the zeroed control and the passive isolation. This successful control implementation verified the applicability of active isolation using the H_2/LQG control algorithm. Using the Kanai-Tajimi input shaping filter showed higher performance in the results as well. Hence, this active isolation of the two-story building proved the ability of the response mitigation against unidirectional seismic excitations, and gave a guideline for the active isolation implementation of the six-story building under bi-directional excitations.

The performance of the active isolation of the six-story building was experimentally verified under the bi-directional excitations using the six degree-of-freedom shake table in the Smart Structures Technology Laboratory. The active isolation system employed active control strategies which were developed using the H_2/LQG control synthesis approach developed herein. Likewise, the passive isolation and the zeroed control were included in the control comparison. To further explore the performance among all control strategies, the Krypton system was used to measure the base displacements for the passive isolation case. Additionally, two wireless sensors were incorporated with all control assessment to provide additional measurements of the structural responses. A band-limited white noise (BLWN) signal with a 50 Hz bandwidth was selected to test the frequency-domain performance of this active isolation system, while five earthquake records were chosen for the performance evaluation in the time domain. The frequency-domain investigation showed that the active isolation system was able to reduce the base displacements in both directions, as compared to the passive isolation system, while maintaining acceptable floor acceleration levels. As compared to the zeroed control, the active isolation performed better in reductions in the floor accelerations.

The time-domain analysis demonstrated the potential of the active isolation system for protecting buildings against seismic excitations. The results showed the ability of the active isolation in reducing of the base displacements as compared to the passive isolation, while the floor accelerations still remained at a moderate level. Moreover, the active isolation always produced comparable accelerations to the passive isolation at the lower floors, although the accelerations at the top floors were slightly amplified. Through a series of shake table tests, the active isolation has shown promising performance with consistent behavior in a wide range of excitations. Hence, the successful implementation of this active isolation under bi-directional excitations verified the feasibility and functionality of the control strategy proposed in this research.

The experimental results reported indicate that high-performance can be achieved with the active isolation system using the given control design procedure. This successful experimental implementation of active isolation indicates its strong potential for seismic protection of important buildings.

9.2 Future Studies

Some recommendations for future studies related to this work are:

- Active isolation systems have been verified under the bi-directional excitations. To fully represent these systems against earthquakes, this control strategy should be assessed under fully 3-dimensional ground motion, particularly the impact due to the vertical excitation.
- Active isolation systems, which employ hydraulic actuators, require a power source to maintain the hydraulic pressure. Once power is unavailable during earthquake events, these hydraulic actuators may not be functioning properly. In the context of this shortcoming, a backup control strategy for these hydraulic actuators, such as using an accumulator to hold the hydraulic pressure for a short time, should be developed.
- The active isolation of the six-story building has been already assessed for excitations up to 0.2-g. the limits of performance for this active isolation system should be examined under larger excitations.
- Semi-active base isolation (i.e., isolation bearings with magnetorheological dampers) has the advantage of requiring very low power (most can run on battery backup if power to the system is cut) and intrinsic stability. Such isolation systems using the current setup should be investigated to fully understand the potential of active isolation systems.
- This research implemented laboratory-scaled active isolation systems using shake table testing. Although this research has demonstrated successful implementations of active isolation for the model buildings, larger-scale experiments should be conducted in the future.

- This research implemented active isolation systems when the isolated buildings were undamaged. The buildings might be possibly damaged during severe earthquake events. Hence, the robustness of the designed controllers based on the advanced H_2/LQG control methods should be investigated.

REFERENCES

Auweraer, H. V. D., Guillaume, P., Verboven, P., Vanlanduit, P. (2001). "Application of a fast-stabilizing frequency domain parameter estimation method." Journal of Dynamic Systems, Measurement, and Control, 123, 651-658.

Barbat, A. H., Rodellar, J., Ryan, E. P., Monlinares N. (1995). "Active control of nonlinear base-isolated buildings." Journal of Engineering Mechanics, 121(6), 676-684.

Bayard, D. S. (1994). "High-order multivariable transfer function curve fitting: Algorithms, sparse matrix method, and experimental results." IEEE Automatica, 30(9), 1439-1444.

Buckle, I., Nagarajaiah, S., Ferrell, K. (2002). "Stability of elastomeric isolation bearings: Experimental study." Journal of Structural Engineering, 128(1), 3-11.

Carrion, J. E., Spencer, B. F., Jr. (2007). "Model-based strategies for real-time hybrid testing." NSEL Report, Series 006, University of Illinois at Urbana-Champaign, http://hdl.handle.net/2142/3629.

Casciati, F., Yao, T. (1994). "Comparison of strategies for the active control of civil structures." Proc., First World Conference on Structural Control, WA1, 3-12.

Chen, C. T. (1998). Linear system theory and design. Oxford University Press, Inc., New York.

Chung, L. L., Reinhorn, A. M., Soong, T. T. (1988). "Experiments on active control of seismic structures.: Journal of Engineering Mechanics, 114(2), 241-256.

Chung, L. L., Lin, R. C., Soong, T. T., Reinhorn, A. M. (1998). "Experimental study of active control for MDOF seismic structures." Journal of Engineering Mechanics, 115(8), 1609-1627.

Constantinou, M. C., Symans, M. D. (1992). "Experimental and analytical investigation of seismic response of structures with supplemental fluid viscous dampers." NCEER Rep. 92-0032, State Univ. of New York at Buffalo, New York.

Datta, T. K. (2003). "A state-of-the-art review on active control of structures." Journal of Earthquake Technology, 40(1), 1-17.

Dickinson, B. W., Morf, M., Kailath, T. (1974). "Minimal realization algorithm for matrix sequences." IEEE Transactions on Automatic Control, AC19(1), 31-38.

Dyke, S. J., Spencer, B. F., Jr., Quast, P., Kaspari, D. C., Sain, M. K. (1994a). "Implementation of an active mass driver using acceleration feedback control." Microcomputers in Civil Engineering: Special Issue on Active and Hybrid Structural Control, 11, 305-323.

Dyke, S. J., Spencer, B. F., Jr., Quast, P., Sain, M. K., Kaspari, D. C., Soong, T. T. (1994b). "Experimental verification of acceleration feedback control strategies for an active tendon system." NCEER Rep. 94-0024, State Univ. of New York at Buffalo, New York.

Dyke, S. J., Spencer, B. F., Jr., Quast, P., Sain, M. K. (1995). "Role of control-structure interaction in protective system design." Journal of Engineering Mechanics, 121(2), 322-338.

Dyke, S. J., Spencer, B. F., Jr., Sain, M. K., Carlson, J. D. (1996a). "Modeling and control of magnetorheological dampers for seismic response reduction." Smart Materials and Structures, 5, 565-575.

Dyke, S. J., Spencer, B. F., Jr., Sain, M. K., Carlson, J. D. (1996b). "Seismic response reduction using magnetorheological dampers." Proc., IFAC World Congress, Vol. L., Int. Fed. of Automatic Control, 145-150.

Feng, M. Q. (1993). "Application of hybrid sliding isolation system to buildings." Journal of Engineering Mechanics, 119(10), 2090-2108.

Feng, Q., Shinozuka, M. (1990). "Use of a variable damper for hybrid control of bridge response under earthquake." Proc., U.S. National Workshop on Structural Control Research, USC Publication, CE-913.

Fu, K. S. (1971). "Learning control systems and intelligent control systems: An intersection of artificial intelligence and automatic control." IEEE Transactions on Automatic Control, 16, 70-72.

Fur, L. S., Yang, H. T. Y., Ankireddi, S. (1996). "Vibration control of tall buildings under seismic and wind loads." Journal of Structural Engineering, 122(8), 948-957.

Higashino, M., Aizawa, S. (1993). "Application of active mass damper system in actual buildings." Proc., Int. Workshop on Structural Control, 194-205, Los Angeles.

Housner, G. W., Bergman, L. A., Caughey, T. K., Chassiakos, A. G., Claus, R. O., Masri, S. F., Skelton, R. E., Soong, T. T., Spencer, B. F., Jr., Yao, J. T. P. (1997). "Structural control: Past, present, and future." Journal of Engineering Mechanics, 123(9), 897-971.

Inaudi, J. A., Kelly, J. M. (1990). "Active isolation." U.S. National Workshop on Structural Control Research, Los Angeles, 125-130.

International Conference of Building Officials (ICBO). (1994). Uniform building code, earthquake regulations for seismic-isolated structures, vol. 2, Appendix Chapt. 16, Whittier, CA.

Kaufman, H., Bar-Kana, I., Sobel, K. (1994). Direct adaptive control algorithm. Springer-Verlag New York, Inc., New York.

Kelly, J. M., Leitmann, G., Soldatos, A. G. (1987). "Robust control of base-isolated structures under earthquake excitation." Journal of Optimization Theory and Applications, 53, 159-180.

Kelly, J. M. (1997). Earthquake resistant design with rubber. 2nd ed., Springer, New York.

Kelly, J. M. (1999). "The role of damping in seismic isolation." Earthquake Engineering and Structural Dynamics, 28, 3-20.

Kim, S. B., Spencer, B. F., Yun, C. B. (2005). "Frequency domain identification of multi-input, multi-output systems considering physical relationships between measured variable." Journal of Engineering Mechanics, 131(5), 461-472.

Kobori, T., Koshika, N., Yamada, N., Ikeda, Y. (1991). "Seismic response controlled structure with active mass driver system. Part 1: Design." Earthquake Engineering and Structural Dynamics, 20, 133-139.

Kobori, T., Inou, Y., Seto, K., Imura, H., Nishitani, A. (1998). Proc., 2nd World Conference on Structural Control, Wiley, New York.

Lee-Galuser, G. J., Ahmadi, G., Horta, L. G. (1997). "Integrated passive/active vibration absorber for multistory buildings." Journal of Structural Engineering, 123(4), 499-504.

Lin, P. Y., Rosche, P. N., Loh, C. H. (2007). "Hybrid base-isolation with magnetorheological damper and fuzzy control." Journal of Structural Control and Health Monitoring, 14, 384-405.

Loh, C. H., Chao, C. H., (1996a). "Effectiveness of active tuned mass damper and seismic isolation on vibration control of multi-story building." Journal of Sound and Vibration, 193(4), 773-792.

Loh, C. H., Ma, M. J. (1996b). "Control of seismically excited building structures using variable damper systems." Engineering Structures, 18(4), 279-287.

Madden, G. J., Symans, M. D., Wongprasert, N. (2002). "Experimental verification of seismic response of building frame with adaptive sliding base-isolation system." Journal of Structural Control, 128(8), 1037-1045.

Madden, G. J., Wongpraser N., Symans, M. D. (2003). "Analytical and numerical study of a smart sliding base isolation system for seismic protection of building." Computer Aided in Civil Infrastructure Engineering, 18, 19-30.

Makris, N. (1997). "Rigidity-plasticity-vicosity: Can electrorheological dampers protect base-isolated structures from near-source earthquakes." Earthquake Engineering and Structural Dynamics, 26, 571-591.

MATLAB (2011), The Math Works, Inc., Natick, Massachusetts.

Meirovitch, L., Stemple, T. J. (1997). "Nonlinear control of structures in earthquakes." Journal of Engineering Mechanics, 123(10), 1090-1095.

Moog (2011). East Aurora, New York. http:/www.moog.com/, 1951-present.

Naeim, F., Kelly, J. M. (1999). Design of seismic isolated structures: From theory to practice. Wiley, Chichester, England.

Nagarajaiah, S., Riley, M. A., Reinhorn, A. M. (1993). "Control of sliding-isolated bridge with absolute acceleration feedback." Journal of Engineering Mechanics, 119(11), 2317-2332.

Nagarajaiah, S. (1994). "Fuzzy controller for structures with hybrid isolation system." Proc. 2nd World Conference on Structural Control, Wiley, New York, TA2, 67-76.

Nagarajaiah, S., Ferrell, K. (1999). "Stability of elastomeric seismic isolation bearings." Journal of Structural Engineering, 125(9), 946-954.

Nagarajaiah, S., Sahasrabudhe, S., Iyer, R. (2000). "Seismic response of sliding isolated bridges with MR dampers." Proc., American Control Conference.

Nagarajaiah, S., Narasimhan, S. (2006). "Smart base-isolated benchmark building. Part II: Phase I sample controllers for linear isolation systems." Journal of Structural Control and Health Monitoring, 13, 589-604.

Nagayama, T., Spencer, B. F., Jr. (2007). “Structural health monitoring using smart sensors.” NSEL Report, Series 001, University of Illinois at Urbana-Champaign, http:/hdl.handle.net/2142/3521.

Narasimhan, S., Nagarajaiah, S., Johnson, E. A., Gavin, H. P. (2006). "Smart base-isolated benchmark building. Part I: Problem definition." Journal of Structural Control and Health Monitoring, 13, 573-588.

National Instruments Corporation. (2011). Austin, TX. http://www.ni.com/

Newell, D. P. Dai, H., Sain, M. K., Quast, P., Spencer, B. F., Jr. (1995). "Nonlinear modeling and control of a hydraulic seismic simulator." Proc., American Control Conference, Seattle, WA.

Nikon Metrology NV. Http://us.nikonmetrology.com/home.php (2011).

Nishimura, H., Kojima, A. (1998). "Active vibration isolation control for a multi-degree-of-freedom structure with uncertain base dynamics." JSME Int. Journal Series C-mechanical Systems Machine Elements and Manufacturing, 41(1), 37-45.

Ober, R. J. (1991). "Balanced parametrization of classes of linear-systems." SIAM Journal of Control and Optimization, 29(6), 1251-1287.

Ohtori, y., Christenson, R. E., Spencer, B. F., Jr., Dyke, S. J. (2004). "Benchmark control problem for seismically excited nonlinear buildings." Journal of Engineering Mechanics, 130(4), 366-385.

Park, K. S., Jung, H. J., Lee, I. W. (2003). "Hybrid control strategy for seismic protection of a benchmark cable-stayed bridge." Engineering Structures, 25(4), 405-417.

Park, K. S., Jung, H. J., Yoon, W. H., Lee, I. W. (2005). "Robust hybrid isolation system for a seismically excited cable-stayed bridge." Journal of Earthqukae Engineering, 9(4), 497-524.

Patten, W., Sun, J., Li, G., Kuehn, J., Song, G. (1999). "Field test of an intelligent stiffener for bridges at the I-35 Walnut Creek Bridge." Earthquake Engineering and Structural Dynamics, 28(2), 109-126.

PCB Piezotronics, Inc. (2011). Depew, NY. http://www.pcb.com/

Pozo, F., Montserrat, P. M., Rodellar, J., Acho, L. (2008). "Robust active control of hysteretic base-isolated structures: Application to the benchmark smart base-isolated building." Journal of Structural Control and Health Monitoring, 15(5), 720-736.

Pu, J. P., Kelly, J. M. (1991). "Active control and seismic isolation." Journal of Engineering Mechanics, 117(10), 2221-2236.

Quast, P., Spencer, B. F., Jr., Sain, M. K., Dyke, S. J. (1995). "Microcomputer implementation of digital control strategies for structural response reduction." Microcomputers in Div. Eng., 10, 13-25.

Ramallo, J. C., Johnson, E. A., Spencer, B. F., Jr. (2002). "Smart base isolation systems." Journal of Engineering Mechanics, 128(10), 1088-1099.

Reinhorn, A., Riley, M. A. (1994). "Control of bridge vibrations with hybrid devices." Proc. First World Conference on Structural Control, TA2, 50-59.

Riley, M. A., Reinhorn, A. M., Nagarajaiah, S. (1998). "Implementation issue and testing hybrid sliding isolation system." Engineering Structures, 20(3), 144-154.

Rofooei, F. R., Tadjbakhsh, I. G. (1993). "Optimal control of structures with acceleration, velocity, and displacement feedback." Journal of Engineering Mechanics, 119(10), 193-201.

Sahasrabudhe, S., Nagarajaiah, S. Hard, C. (2000). "Experimental study of sliding isolated buildings with smart dampers subjected to near source ground motion." Proc., 13th Engineering Mechanics Conference, Reston.

Sahasrabudhe, S., Nagarajaiah, S. (2005a). "Effectiveness of variable stiffness systems in base-isolated bridges subjected to near-fault earthquakes: An experimental and analytical study." Journal of Intelligent Material Systems and Structures, 16, 743-756.

Sahasrabudhe, S., Nagarajaiah, S. (2005b). "Experimetnal study of sliding base-isolated buildings with magetorheological dampers in near-fault earthquakes." Journal of Structural Engineering, 131(7), 1025-1034.

Sener, M., Utku, S. (1998). "Adaptive base isolation system for the control of seismic energy flow into buildings." Journal of Intelligent Material Systems and Structures, 9, 104-115.

Shook, D., Lin, P. Y., Lin, T. K., Roschke, P. N. (2007). "A comparative study in the semi-active control of isolated structures." Smart Materials and Structures, 16, 1433-1446.

Shore Western Manufacturing (2010). Monrovia, CA. http://www./shorewestern.com/

Skinner, R. I., Robinson, W. H., McVerry, G. H. (1993). An introduction to seismic isolation. Wiley, Chichester, England.

Soong, T. T., Manolis, G. D. (1987). "Active structures." Journal of Structural Engineering, 113, 2290-2301.

Soong, T. T. (1988). "Active structural control in civil engineering." Engineering Structures, 10, 74-84.

Soong, T. T., Reinhorn, A. M. (1993). "An overview of active and hybrid structural control research in the U.S." The Structural Design of Tall Buildings, 2, 192-209.

Soong, T. T., Grigoriu, M. (1993). Random vibration of mechanical and structural systems, Prentice-Hall, Englewood Cliffs, N.J.

Soong, T. T., Constantinou, M. C. (1994). Passive and active structural vibration control in civil engineering. Springer-Verlag New York, Inc., New York.

Soong, T. T., Dargush, G. F. (1997). Passive energy dissipation systems in structural engineering. John Wiley & Sons, Inc., New York.

Spectral Dynamics, Inc. (2007). San Jose, CA. http://www.spectraldynamics.com/

Spencer, B. F., Jr., Suhardjo, J. Sain, M. K. (1994). "Frequency domain optimal control strategies for aseismic protection." Journal of Engineering Mechanics, 120(1), 135-158.

Spencer, B. F., Jr., Sain, M. K. (1997). "Controlling buildings: A new frontier in feedback." IEEE Control Systems Magazine, 17(6), 19-35.

Spencer, B. F., Jr., Dyke, S. J., Deoskar, H. S. (1998). "Benchmark problems in structural control - Prat I: active mass driver system." Earthquake Engineering and Structural Dynamics, 27, 1127-1139.

Spencer, B. F., Jr., Yang, G. (1998). "Earthquake simulator control by transfer function iteration." Proc. of the 12th ASCE Engineering Mechanics Conference, San Diego, CA.

Spencer, B. F., Jr., Johnson, E. A., Ramallo, J. C. (2000). ""Smart" isolation for seismic control." JSME, Int. J., Der. C, 43(3), 704-711.

Spencer, B. F., Jr., Nagarajaiah, S. (2003). "State of the art of structural control." Journal of Structural Engineering, 120(7), 845-856.

Suhardjo, J., Spencer, B. F., Jr., Kareem, A. (1992). "Frequency domain optimal control of wind-excited buildings." Journal of Engineering Mechanics, 118(12), 2463-2481.

Symans, M. D., Constantinou, M. C. (1999). "Semi-active control systems for seismic protection of structures: A state-of-the-art review." Engineering Structures, 21(6), 469-487.

Tsai, M. H., Chang, K. C., and Wu, S.Y. (2006). "Seismic isolation of a scaled bridge model using rolling-type bearings." 4th International Conference on Earthquake Engineering, Taipei, Taiwan.

Tsuchimoto, K., Kitagawa, Y., Shinozaki, Y., Nagashima, I., Sanui, Y., Komatsu, H., and Kobayashi, T. (2005). "A design of advanced base-isolation system for asymmetrical building." The 2005 World Sustainable Building Conference, Tokyo, Japan.

van Overschee, P., de Moore, B. (1994). "N4ID: Subspace algorithms for the identification of combined deterministic-stochastic systems." IEEE Automatica, 30, 75-93.

Vargas, R. and Bruneau M. (2009). "Experimental Response of Buildings Designed with Metallic Structural Fuses. II." Journal of Structural Engineering, 135(4), 394-403.

Whittaker, A. S., Bertero, V. V, Thompson, C. L., Alonso, L. I. (1993). "Seismic testing of steel plate energy dissipation systems." Earthquake Spectra, 7(4), 563-604.

Williams, D. M., Williams, M. S., Blakeborough, A. (2001). "Numerical modeling of a servohydraulic testing system for structures." Journal of Engineering Mechanics, 127(8), 816-827.

Wongprasert, N., Symans, M. D. (2005). "Experimental evaluation of adaptive elastomeric base-isolated structures using variable-orifice fluid dampers." Journal of Structural Engineering, 131(6), 867-877.

WorkSafe Technologies (2011). Valencia, CA. http://www.worksafetech.com/

Xu, K. Q. (1997). "Frequency domain modal parameter identification of high order systems in a numerically stable way." Journal of Vibration and Acoustics, 119, 265-270.

Yang, J. N., Li, Z., Liu, S. C. (1992). "Stable controllers for instantaneous optimal control." Journal of Engineering Mechanics, 118(8), 1612-1630.

Yang, J. N., Vongchavalitkul, S. (1994). "Stochastic hybrid control of hysteretic structures." Probabilistic Engineering Mechanics, 9(1-2), 125-133.

Yang, J. N., Wu, J. C, Kawashima, K., Unjoh, S. (1995). "Hybrid control of seismic-excited bridge structures." Earthquake Engineering and Structural Dynamics, 24, 1437-1451.

Yang, J. N., Wu, J. C., Reinhorn, A. M., Riley, M. A. (1996). "Control of sliding-isolated buildings using sliding-mode control." Journal of Structural Engineering, 122(2), 179-186.

Yoshida, K., Kang, S., Kim, T.,(1994). "LQG control and H-infinity control of vibration isolation for multi-degree-of-freedom systems." Proc., First World Conference on Structural Control, TP4, 43-52.

Yoshioka, H., Ramallo, J. C., Spencer, B. F., Jr. (2002). ""Smart" base isolation strategies employing magnetorheological damper." Journal of Structural Engineering, 128(5), 540-551.